Johannes Gutenberg-Universität Mainz
Institut für Physik
Dissertation

Precise muon momentum calibration and Z mass measurement with the ATLAS experiment, using pp collisions at $\sqrt{s}$ =13 TeV

Dissertation
zur Erlangung des akademischen Grades
Doktorat in Physik

vorgelegt von
Dionysios Fakoudis

Betreuer:	Stefan Tapprogge
Zweiter Betreuer:	Maarten Boonekamp
Datum der Untersuchung:	17/12/2024

Contents

Abstract in German

Das Standardmodell ist die Grundlage der modernen Teilchenphysik. Präzise Messungen stehen im Mittelpunkt wichtiger Studien. Mit der Entdeckung des Higgs-Bosons werden weitere Messungen des elektroschwachen sektors durchgeführt, um die Konsistenz des Modells zu überprüfen. ATLAS ist ein Mehrzweckdetektor und eines der Experimente am LHC des CERN. Mit einem speziellen detector- und Magnetsystem erzielt das Experiment hochpräzise Messungen des Myonenimpulses im Endzustand.

In diesem Zusammenhang ist die Messung der Z-Masse in ATLAS ein Teil dieser Bemühungen. Die Masse des Z-Bosons wurde mit hervorragender Genauigkeit im LEP-Experiment am CERN gemessen, ohne dass die systematischen Unsicherheiten bei der Rekonstruktion berücksichtigt werden mussten. In ATLAS beinhaltet die Messung die Rekonstruktion von finalen Myonenobjekten, was entsprechende Verzerrungen mit sich bringt. Der Vergleich zwischen den beiden Messungen ist von hohem wissenschaftlichen Interesse und ein Test für die Fähigkeiten von ATLAS.

Die Arbeit untersucht die Kalibrierung des Myonenimpulses im ATLAS-Experiment mit proton-proton-Kollisionen bei der Schwerpunktsenergie $\sqrt(s) = 13$ TeV. ATLAS verwendet Standardkerzen"-Resonanzen für die Kalibrierung, das J/psi-Meson und das Z-Boson. Durch den Vergleich des Di-Muonen-Massenspektrums in der Simulation und in den Daten für die beiden Resonanzen wird die Kalibrierung abgeleitet.

Die Kalibrierung in dieser Arbeit steht im Zusammenhang mit den offiziellen ATLAS-Empfehlungen, aber auch für die Z-Massenmessung in erster Linie, aber auch für andere elektroschwache Messungen, wie z.B. die W-Massenmessung.

Die Arbeit konzentriert sich auf die Herausforderungen bei der Kalibrierung mit den offiziellen ATLAS-Werkzeugen, wobei die Ergebnisse in zwei Hauptabschnitte unterteilt sind. Der erste Abschnitt befasst sich mit Kalibrierungsarbeiten, die für das ATLAS-Experiment durchgeführt wurden. Konkret wird die relative Impulsauflösung von Myonen in ATLAS für den Inner Detector (ID), das Muon Spectrometer (MS) und die Combined (CB) Spuren untersucht. Aus diesen Studien werden Karten der relativen Impulsunsicherheit von Myonen sowohl für die Simulation als auch für die Daten erstellt. Diese Karten zeigen systematische Mängel in den Untersystemen des Detektors und falsche Modellierungen in den Simulationen auf. Die Karten werden dann in den offiziellen ATLAS-Kalibrierungs-software integriert, um ihr Potenzial zur Verbesserung der Kalibrierungsgenauigkeit zu bewerten, wobei die Ergebnisse mit und ohne diese zusätzlichen Informationen verglichen werden. Abschließend werden der Prozess und die Ergebnisse der bestimmung der offiziellen ATLAS-Kalibrierungsempfehlungen vorgestellt. Diese Empfehlungen werden getrennt für die ID-, MS- und CB-Spuren entwickelt.

Der zweite Teil dieser Arbeit befasst sich mit der Kalibrierung im Zusammenhang mit der Z-Massenmessung, einschließlich einer detaillierten Analyse einer Z-Massenmessung mit der angewandten Kalibrierung. Der Kalibrierungsprozess wird so verändert, dass er die Z-Boson-Resonanz nicht berücksichtigt. Kalibrierungskorrekturen werden nur mit dem J/psi-Meson abgeleitet.

Unter Verwendung offizieller ATLAS-werkzeuge wird die Kalibrierung für Prompt- und Nicht-Prompt-J/ψ-Mesonen verglichen. Die kinematischen Verteilungen für beide Typen wer-

den analysiert, und die Unterschiede zwischen den Kalibrierungen werden diskutiert. Die Kalibrierungsparameter werden als Funktion der Pseudorapidität des Detektors und des Transversalimpulses des Myons abgeleitet.

Schließlich wird nach Anwendung der abgeleiteten Kalibrierung auf Myonen aus Z-Kandidaten-Zerfällen eine Bewertung der erwarteten Unsicherheiten für die Z-Bosonen-Masse mit Hilfe eines Likelihood-Fits mit dem Di-Muon-Kanal extrahiert.

Résumé étendu en français

Le Modèle Standard constitue la base de la physique des particules moderne. Des mesures précises sont au cœur des études majeures. La découverte du boson de Higgs ouvre la voie à des mesures électrofaibles supplémentaires pour tester la cohérence du modèle.

ATLAS est un détecteur polyvalent et l'une des expériences menées au LHC du CERN. Grâce à un système de suivi et de magnétisme dédié, l'expérience atteint une grande précision dans la mesure de l'élan des muons à l'état final. Dans ce contexte, la mesure de la masse du boson Z avec ATLAS fait partie de ces efforts. La masse du boson Z a été mesurée avec une excellente précision lors de l'expérience LEP au CERN, sans aborder les incertitudes systématiques liées à la reconstruction.

Dans ATLAS, cette mesure implique la reconstruction des objets muons finaux, introduisant des biais correspondants. La comparaison entre les deux mesures suscite un grand intérêt scientifique et constitue un test des capacités d'ATLAS. Enfin, après application de la calibration dérivée aux muons issus des désintégrations de candidats bosons Z, une évaluation des incertitudes attendues sur la masse du boson Z est extraite à l'aide d'un ajustement de vraisemblance, dans le canal di-muon. Cette thèse porte sur la calibration de l'élan des muons dans l'expérience ATLAS, avec des collisions pp, à une énergie dans le centre de masse de $\sqrt{s} = 13$ TeV.

ATLAS utilise des résonances, appelées "bougies étalon", pour la calibration, comme le méson J/ψ et le boson Z. En comparant le spectre de masse di-muon en simulation et en données pour ces deux résonances, la calibration est établie.

La calibration dans cette thèse s'inscrit dans le cadre des recommandations officielles d'ATLAS, mais également dans le contexte de la mesure de la masse du boson Z, ainsi que pour d'autres mesures électrofaibles, comme celle de la masse du boson W

Le travail se concentre sur les défis de calibration à l'aide des outils officiels d'ATLAS, avec des résultats divisés en deux sections principales. La première section traite des travaux de calibration réalisés pour l'expérience ATLAS. En particulier, la résolution relative de l'élan des muons dans ATLAS est étudiée pour le détecteur interne (Inner Detector, ID), le spectromètre à muons (Muon Spectrometer, MS), et les trajectoires combinées (Combined, CB). Ces études permettent de générer des cartes des incertitudes relatives de l'élan des muons pour les simulations et les données.

Ces cartes révèlent des déficiences systématiques dans les sous-systèmes du détecteur ainsi que des désaccords dans les simulations. Elles sont ensuite intégrées dans le cadre de calibration officiel d'ATLAS afin d'évaluer leur potentiel pour améliorer la précision des calibrations. Une comparaison des résultats est effectuée, avec et sans ces informations supplémentaires. Enfin, le processus et les résultats permettant d'établir les recommandations officielles de calibration pour ATLAS sont présentés, séparément pour les trajectoires ID, MS et CB.

La seconde partie de cette thèse se concentre sur la calibration dans le contexte de la mesure de la masse du boson Z, incluant une analyse détaillée d'une mesure de cette masse avec la calibration appliquée. Le processus de calibration est modifié pour exclure la résonance du boson Z. Les corrections de calibration sont obtenues à partir du méson J/ψ.

À l'aide des outils officiels d'ATLAS, la calibration est comparée pour les mésons J/ψ Prompts et Non Prompts. Les distributions pour les deux types sont analysées, et les différences

entre leurs calibrations sont discutées. Les paramètres de calibration sont déterminés en fonction de la pseudorapidité du détecteur et de l'élan transverse des muons.

Les paramètres d'étalonnage sont dérivés en fonction de la pseudorapidité du détecteur et du impulsion transversal du muon.

Enfin, une évaluation des incertitudes d'étalonnage sur la masse du boson Z est extraite à l'aide d'un ajustement de vraisemblance, avec le canal di-muon.

Abstract in English

Standard Model is the foundation of modern particle physics. Precise measurements are in the center of major studies. The Higgs boson discovery probes for further Electro-Weak measurements, to test the consistency of the model. ATLAS is a multi-purpose detector and one of the experiments at the CERN LHC. With a dedicated tracking and magnetic system, the experiment achieves high precision measurements of the muon momentum at the final state.

In that context, the Z mass measurement in ATLAS is part of these efforts. The Z boson mass has been measured with excellent accuracy in the LEP experiment at CERN, without delving into reconstruction systematic uncertainties. In ATLAS, the measurement involves the reconstruction of final muon objects introducing corresponding biases. The comparison between the two measurements is of high scientific interest and a test for ATLAS capabilities.

The thesis investigates muon momentum calibration in the ATLAS experiment, with pp collisions, at center of mass energy $\sqrt{s} = 13$ TeV. ATLAS uses "standard candles" resonances for the calibration, J/ψ meson and Z boson. By comparing di-muon mass spectrum in simulation and data, for the two resonances, the calibration is derived.

The calibration in this thesis is in the context of official ATLAS recommendations but also for Z mass measurement primarily, but also other Electro-Weak measurements, such as the W mass measurement.

The work focuses on calibration challenges using official ATLAS tools, with results divided into two main sections. The first section addresses calibration work performed for the ATLAS experiment. Specifically, the relative momentum resolution of muons in ATLAS is investigated for the Inner Detector (ID), the Muon Spectrometer (MS), and the Combined (CB) tracks. From these studies, maps of the muon relative momentum uncertainty are generated for both simulation and data. These maps reveal systematic deficiencies in the detector subsystems and mis-modelings in the simulations. The maps are then integrated into the official ATLAS calibration framework to assess their potential for improving calibration precision, with a comparison of results both with and without this additional information. Lastly, the process and outcomes of deriving the official ATLAS calibration recommendations are presented. These recommendations are developed separately for the ID, MS, and CB tracks.

The second part of this thesis focuses on calibration in the context a the Z mass measurement, including a detailed analysis of a Z mass measurement with the applied calibration. The calibration process is altered so it does not include the Z boson resonance. Calibration corrections are derived with the J/ψ meson.

Using official ATLAS tools, the calibration is compared for Prompt and Non-Prompt J/ψ mesons. Kinematic distributions for both types are analyzed, and the differences between their calibrations are discussed. The calibration parameters are derived as a function of detector pseudorapidity and muon transverse momentum.

Lastly, an assessment of the calibration uncertainties on the Z boson mass is extracted using a likelihood fit, with the di-muon channel.

Introduction

In this thesis, the Z mass is measured in the ATLAS experiment, using proton proton collisions, at $\sqrt{s} = 13$ TeV. ATLAS is a generic high energy physics experiment, operating in the LHC. One of the main objectives of the ATLAS experiment is to test the consistency of the Standard Model. ATLAS has performed a series of Standard Model (SM) precise measurements, and notably, in the electro weak sector the m_W has been measured with excellent accuracy for Run-1. This thesis aims to push the boundaries of current methodologies by deriving a Z boson mass measurement with a low uncertainty. The measurement is performed through reconstructing final state muons. Therefore, understanding and correcting detector biases introduced at the reconstruction is crucial. Specifically, this thesis is focusing in charge independent effects on muon transverse momentum p_T^μ. Through the calibration procedure, which is the main theme of this thesis, these biases are corrected.

In Chapter 1, the SM is presented with a focus on the derivation of the Z mass through the Higgs mechanism. Fundamental particles, fermions and bosons, and their interactions are presented. Moreover, the derivation of the Z boson through the Electro-Weak unification is shown. The Z boson properties are presented and finally the LEP measurement is outlined to motivate the current thesis.

In Chapter 2, the experimental apparatus is presented. First, the LHC is presented alongside the proton filling scheme. ATLAS detector is introduced with the corresponding coordinates and different detector regions. The magnetic field is presented, with a brief introduction on magnetic field measurement non closures. Furthermore, the Inner Detector, the Muon Spectrometer and the Calorimeter systems are presented, with a focus on muon detection and interaction with the subsystems. Trigger algorithms and data acquisition are presented. Finally, track reconstruction, muon interaction with the detector and muon track types are presented.

In Chapter 3, the official ATLAS calibrations tools are presented with technical details. Two kind of momentum measurement biases are presented. First, charge dependent biases, also referred as saggita biases are outlined. Their source and their effect is presented. Secondly, non-charge dependent biases are presented. Their origin is presented, alongside the derivation of the corresponding corrections. The corrections are derived through a dedicated algorithm, and the parametrization of the momentum with scale and resolution parameters. The effect of these parameters is shown on $m_{\mu\mu}$ distributions, corresponding to the J/ψ and Z resonances. Lastly, the J/ψ background derivation is presented.

In Chapter 4, calibration studies done for the Qualification Task (QT) and the Muon Momentum Calibration group of ALTAS are presented. For the QT, the *pre-smearing* procedure was performed. Detector η and ϕ maps of $\frac{\sigma_{p_T^\mu}/p_{T\,Data}^\mu}{\sigma_{p_T^\mu}/p_{T\,MC}}$ are derived for different p_T^μ bins. Profiles of $\sigma_{p_T^\mu}/p_T^\mu$ are studied as a function of p_T^μ for simulation and data. Momentum resolution parametrization is tested by fitting a parametric function to these profiles. Lastly, from the $\frac{\sigma_{p_T^\mu}/p_{T\,Data}^\mu}{\sigma_{p_T^\mu}/p_{T\,MC}^\mu}$ maps a correction is derived and injected in the calibration procedure. In the second part of Chapter 4, the results of the official muon momentum calibration are presented. Finally, a validation is conducted to assess the quality of the calibration across detector η, ϕ, and p_T^μ.

In Chapter 5, the calibration in the context of the Z mass measurement is presented. First, the overall strategy is discussed alongside challenges. The primary strategy involves deriving calibration corrections as a function of detector η, using the J/ψ resonance, specifically for the barrel region of the Inner Detector. First, a study is conducted to calibrate muons from J/ψ mesons produced either near or displaced from the Interaction Point. Secondly, the calibration as a function of η is presented, alongside the validation of the process. Finally, the p_T^μ dependence of the calibration parameters is derived, accounting for the fact that muons originating from the Z resonance decay exhibit a different p_T^μ spectrum compared to those from the J/ψ.

Finally, in Chapter 6, the Z mass measurement is derived using the calibration corrections for the J/ψ. The simulation and data samples are presented. Systematic uncertainties are outlined. The decay channel $Z \to \mu\mu$ is used to derive signal templates for different m_Z and width Γ_Z values. By morphing between the templates and a dedicated likelihood fit the final result is derived, with a blinded m_Z central value.

Chapter 1

The Standard Model and the Z Boson

Contents

1.1 Standard Model of elementary particles

The Standard Model (SM) is the basis and foundation of modern particle physics. It describes three of the four fundamental forces of particle interactions. It's framework give an accurate description of electromagnetic, weak and strong nuclear force. With the discovery of the Higgs boson by ATLAS and CMS experiments at the Large Hadron Collider, the SM puzzle got completed. Theoretical predictions and experimental data are in excellent agreement up to the current date, making the SM the best description of the universe until now.

Despite the success of the SM, there are still phenomena that remain unexplained. The most important is gravity. The fourth fundamental force, is significantly weaker compared to the other forces, making it difficult to probe SM predictions in relation to it. Furthermore, it is unable to explain the imbalance of matter and anti-matter in the universe. Additionally, it does not include a coherent mechanism for neutrino oscillations or the way their acquire mass.

Due to these persistent questions a large part of the research is focused on beyond to the SM theories.

The SM is based on Quantum Field Theory (QFT), which is relativistic quantum mechanics where the Hilbert space of particles is called Fock space of quantum fields. In this framework particles and their interactions are a result of field excitations. The dynamics of the quantized fields is described by the Lagrangian density $\mathcal{L}(v, \dot{v})$, where v is the local function of the field and it's derivative $\dot{v}$. The equation of motion is derived from the principle of least action:

$$\frac{d}{dt}\frac{\partial \mathcal{L}}{\partial \dot{v}} - \frac{\partial \mathcal{L}}{\partial v} = 0 \tag{1.1}$$

The core of the SM is the fundamental particles and their interactions. The elementary particles are displayed in the Figure 1.1. There are two large group of particles: fermions and bosons. Fermions form matter and bosons are mediators of the fundamental forces.

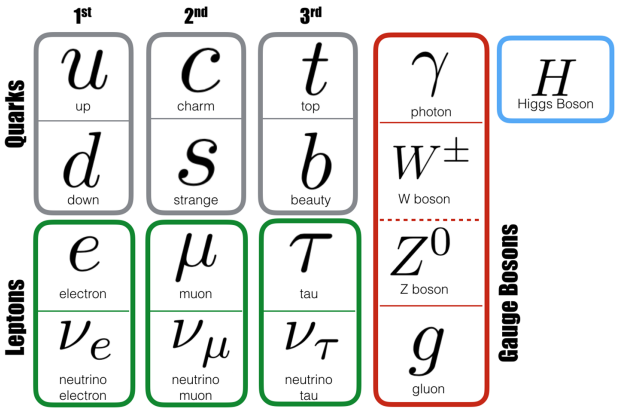

Figure 1.1: Elementary Particles of the SM, taken from ref.[1]

SM is a gauge theory based on Quantum Field Theory (QFT) that describes interactions between fundamental particles by the exchange of bosons. These bosons come forward from demanding local gauge symmetry of the theory. The three symmetries governing the SM are:

$$\mathcal{G}_{\text{SM}} = SU(3)_C \otimes SU(2)_L \otimes U(1)_Y \tag{1.2}$$

where

- $SU(3)_C$ is a special unitary group with three elements, representing the **strong interaction** (quantum chromodynamics, QCD) and is associated with the **color charge**.
- $SU(2)_L \otimes U(1)_Y$ represents the electro-weak interactions and is associated with the **weak isospin** and **weak hyper-charge**.

SM is separated in three sections. The quantum electron dynamics (QED), the weak interactions and the Quantum Chromo Dynamics. Also, a unification of QED and weak interaction has been proved experimentally and it is called electroweak.

In the context of this chapter, for simplicity, the anti-particle notations is equal to the particle one.

Natural Units In the context of high energy physics, the natural units scheme is used to simplify the notations. This involves the setting of fundamental constants of physics equal to 1. The standard natural units, which are also used in the thesis is the following:

- speed of light **c=1**
- reduced Planck constant $\hbar = 1$

This allows for quantities like mass to be written for example $GeV/c^2 \rightarrow GeV$ or momentum $GeV/c \rightarrow GeV$, whereas energy remains unchanged.

1.1.1 Fermions

Fermions are separated in quarks (left top group of Figure 1.1) and leptons (left bottom group of Figure 1.1). Depending on their type, fermions interact with different fundamental forces. They are characterized by half integer spin, therefore due to Dirac - Fermi statistics, they can not occupy the same quantum state. Free fermions are solutions to the relativistic wave equation of Dirac:

$$(i\gamma^\mu \partial_\mu - m)\psi = 0 \tag{1.3}$$

where: ψ is the wave function of the fermion, or Dirac spinor. γ^μ are the *gamma matrices*, which encode the spin structure. ∂_μ represents the four-derivative with respect to spacetime coordinates. m is the mass of the fermion. i is the imaginary unit.

Quarks are referred often as "building blocks" of matter. They form hadrons, such as protons and neutrons, and therefore are the basis of atoms. They interact with all fundamental forces but their unique characteristic is the interaction with the strong force, allowing the creations of hadrons. Due to the potential of the strong force the quarks are never found in isolation but always form bound states. This phenomenon is called color confinement and it is analyzed further in Section 1.3.

The six flavors of quarks are divided in three generations:

- **Up (u)** and **Down (d)**: The lightest and most stable quarks, up and down quarks are found in protons and neutrons, which make up ordinary matter.
- **Charm (c)** and **Strange (s)**: Heavier and less stable quarks. Strange quarks play a role in the formation of strange particles, such as kaons, while charm quarks are produced in high-energy collisions. Charm quarks are particularly relative to this thesis as one of their main bound states, J/ψ charmonium ($c\bar{c}$), is used extensively in the thesis . Also strange hadrons as Kaons are used in modern particle physics to study violations of fundamental physics symmetries to probe matter anti-matter asymmetry.
- **Top (t)** and **Bottom (b)**: The heaviest of the quark flavors. The top quark is the most massive elementary particle observed, while the bottom quark is significant in heavy mesons such as B-mesons. The later play a significant role in ATLAS experiment. Due to their large lifetime they have a distinct detector signature, allowing for their easy identification. Also in the context of the thesis they play an important role as they allow for the distinction of Prompt J/ψ and Non Prompt J/ψ in Chapter 5. Prompt J/ψ produced directly near the Interaction Point, whereas Non Prompt J/ψ originate from the decay of B-mesons and are typically produced at a measurable distance from the interaction point. Top quarks are connected to crucial SM properties as the W and the Higgs boson mass through higher order diagrams.

The other group of fundamental fermions are the leptons. Their main distinction from the quarks is that they don't interact with the strong force. There are six leptons and they are grouped into three generations, each consisting of a charged lepton and it's corresponding neutrino.

- **Electron (e)**: It is the lightest and most stable of the charged leptons. Electrons are found at atoms, orbiting around the nucleus. They are produced in abundance in the universe.
- **Muon (μ)**: A second-generation charged lepton. The muon has a much greater mass (105.66 MeV). It decays into an electron and neutrinos via the weak interaction. Muons are relevant in the context of their thesis as they are the decay channel that the Z mass is measured. Muons have a larger lifetime than τ and they do not decay in the ATLAS detector making it possible to be easily identified by a dedicated detector system.
- **Tau (τ)**: The heaviest of the charged leptons, the tau is a third-generation particle. Due to its large mass, the tau is unstable and decays quickly into lighter particles, including electrons, muons, and neutrinos through the week force. Due to their short lifetime, τ leptons decay almost instantaneously, complicating their differentiation from other processes that also produce leptons in the final state. As a result, τ tagging represents one of the primary challenges faced by the ATLAS experiment. In the context of this thesis, tau leptons are particularly significant as they contribute to the background for the signal process $Z \to \mu\bar{\mu}$.
- **Neutrinos, electron, muon, tau (ν_e, ν_μ, ν_τ)**: The corresponding neutrinos to electron, μ and τ respectively. They have an extremely low mass and only interact elusively via the weak force and gravity. Neutrinos are notoriously difficult to detect.

Particle	**Mass (GeV)**	**Charge (e)**	**Spin**
Quarks			
Up (u)	0.0022	$+\frac{2}{3}$	$\frac{1}{2}$
Down (d)	0.0047	$-\frac{1}{3}$	$\frac{1}{2}$
Charm (c)	1.28	$+\frac{2}{3}$	$\frac{1}{2}$
Strange (s)	0.096	$-\frac{1}{3}$	$\frac{1}{2}$
Top (t)	173.1	$+\frac{2}{3}$	$\frac{1}{2}$
Bottom (b)	4.18	$-\frac{1}{3}$	$\frac{1}{2}$
Leptons			
Electron (e)	0.000511	-1	$\frac{1}{2}$
Electron Neutrino (ν_e)	$< 2.2 \times 10^{-6}$	0	$\frac{1}{2}$
Muon (μ)	0.1057	-1	$\frac{1}{2}$
Muon Neutrino (ν_μ)	$< 0.17 \times 10^{-3}$	0	$\frac{1}{2}$
Tau (τ)	1.7769	-1	$\frac{1}{2}$
Tau Neutrino (ν_τ)	$< 18.2 \times 10^{-3}$	0	$\frac{1}{2}$

Table 1.1: Fermions in the Standard Model, taken from ref.[2].

1.1.2 Bosons

Bosons have integer spin. They follow Einstein - Bose statistics, meaning they can occupy the same quantum state. This allows them to be mediators of fundamental particles between the fermions.

Bosons are solutions to different equations. Higgs, which is a scalar boson, is a solution to the Klein Gordon equation, where the other bosons W,Z, γ are produced through interaction with local gauge symmetries and the corresponding formalism is more complicated.

Scalar bosons are solutions to the relativistic wave equation of Klein Gordon:

$$\left(\Box + \frac{m^2c^2}{\hbar^2}\right)\phi = 0 \tag{1.4}$$

where ϕ is the field representing the boson, $\Box \equiv \partial_\mu \partial^\mu$ is the d'Alembertian operator, or the wave operator in spacetime, m is the mass of the boson, c is the speed of light, $\hbar$ is the reduced Planck constant.

- **Gauge Bosons (Spin 1)**: The fundamental forces are mediated by gauge bosons, all of which have spin 1.
  - **Photon (γ)**: The photon mediates the electromagnetic force. It has spin 1 and is massless.
  - **W and Z Bosons**: The W^+, W^- bosons mediate the weak force. The Z^0 bosons mediate the electroweak force. They are vector bosons with spin-1.
  - **Gluons (g)**: Gluons are responsible for mediating the strong force between quarks. They have spin 1 and are massless.
- **Higgs Boson (Spin 0)**: The Higgs boson has spin 0. Its spinless nature allows it to couple uniformly to other particles. It is connected to the Higgs mechanism, through which particles acquire mass.
- **Graviton (Hypothetical, Spin 2)**: In theoretical models of quantum gravity, the graviton is proposed as the mediator of the gravitational force. It's spin is hypothesized to be 2. The graviton has not yet been experimentally observed.

Particle	Interaction	Mass (GeV)	Spin
Photon (γ)	Electromagnetic	0	1
W Boson ($W^\pm$)	Weak	80.379	1
Z Boson (Z^0)	ElectroWeak	91.1876	1
Gluon (g)	Strong	0	1
Higgs (H)	Mass	125.1	0

Table 1.2: Bosons in the Standard Model, taken from ref.[2]

1.2 QED

Quantum Electro Dynamics (QED) is the one of the most important parts of the SM, ref. [3]. It consists of the foundations of the more complicated interactions (Weak and Strong). It describes electromagnetic interactions between electrically charged particles.

Main foundation of QED is the notion that electrically charged particles, when interacting, exchange photons. The photons, γ, are the mediators of the electromagnetic force and they arise from local gauge symmetry.

In QED, a key principle, inspired by classical electromagnetism, is the introduction of an additional field. Specifically the electromagnetic gauge field ensures that the fundamental

laws of physics remain unchanged under local transformations. This concept preserves gauge symmetry and allows for the consistent description of interactions between charged particles and the photon field.

QED is required to preserve gauge invariance, local and global. In simpler terms, the theory is required to hold in space-time transformations. This means that fundamental physics properties of the system remain unchanged when the fermion wave function is transformed under a space-time shift :

$$\psi(x) \rightarrow \psi'(x) = e^{i\alpha(x)}\psi(x) \tag{1.5}$$

The transformation changes the Dirac Lagrangian:

$$\mathcal{L}_{\text{fermion}} = \bar{\psi}(i\gamma^\mu\partial_\mu - m)\psi \rightarrow \bar{\psi}'(i\gamma^\mu\partial_\mu - m)\psi' = e^{-i\alpha(x)}\bar{\psi}(i\gamma^\mu\partial_\mu - m)e^{i\alpha(x)}\psi \tag{1.6}$$

where m is the fermion mass. The effect of the derivative on the transformed wave function will add a term $(\partial_\mu\alpha)\psi$ which breaks the local symmetry:

$$\partial_\mu\psi \rightarrow \partial_\mu(e^{i\alpha(x)}\psi) = e^{i\alpha(x)}(\partial_\mu\psi + i(\partial_\mu\alpha)\psi) \tag{1.7}$$

To treat this additional term introducing an additional gauge field is required A_μ, which is essentially the photon. The interaction with the gauge field is introduced with covariant derivative D_μ:

$$D_\mu = \partial_\mu + iqA_\mu \tag{1.8}$$

where q is the charge of the fermion. The photon field A_μ must be transformed the following way under a local transformation:

$$A_\mu(x) \rightarrow A_\mu(x) - \frac{1}{q}\partial_\mu\alpha(x) \tag{1.9}$$

This additional term will cancel the one presented in Relation 1.7.

To describe fully the QED, another term is needed for the Lagrangian. This which is a kinematic term of the photon. It is the equivalent of Maxwell laws in Quantum Field Theory (QFT). The term introduced is called **field strength tensor** $F^{\mu\nu}$ and is defined as:

$$F^{\mu\nu} = \partial^\mu A^\nu - \partial^\nu A^\mu \tag{1.10}$$

Finally the QED Lagrangian, which is local and globally phase transformation symmetric is:

$$\mathcal{L}_{QED} = -\frac{1}{4}F^{\mu\nu}F_{\mu\nu} + i\bar{\psi}\gamma^\mu D_\mu\psi - m\bar{\psi}\psi \tag{1.11}$$

In conclusion, the QED Lagrangian has three terms. First a kinematic term without a mass for the photon, the field tensor, a term of interaction of fermions with the photon gauge field through the covariance derivative and a mass term for the fermions. It is important to note that the field tensor term does not include photon self interactions, which is in contrast to what occurs in both QCD and the weak interactions, where self-interactions are present.

1.3 QCD

Quantum Chromodyamics (QCD) is a gauge theory of the SM using $SU(3)_C$ symmetries, ref. [4]. The theory describes the interactions of quarks, using the colour charge, by the exchange of the gauge boson of QCD, gluons.

The langrangian for free quarks, using equation 1.3, is:

$$\mathcal{L} = \sum_j \bar{q}_j (i\gamma^\mu \partial_\mu - m_j) q_j \tag{1.12}$$

for j=1,2..,6 for the six quarks. The wave functions of the QCD are vectors in the colour space (red, green blue), therefore: $q_j = (q_r, q_g, q_b)$. Similarly to QED and the U(1) the QCD theory must be invariant under $SU(3)$ local gauge transformations. The transformation is:

$$q^{'} = q e^{i\alpha_s \vec{\lambda} \theta(\vec{x})} \tag{1.13}$$

with α_s the coupling to the strong force, λ are the Gell Mann matrices and $\theta(x)$ is a vector of functions taking different values for space time x, with 8 elements. The eight elements are the eight gluons required for the exchange of the colour charge between the quarks. The gluon field tensor is:

$$G^a_{\mu\nu} = \partial_\mu A^a_\nu - \partial_\nu A^a_\mu + g f^{abc} A^b_\mu A^c_\nu \tag{1.14}$$

where f_{abc} are the structure constants of the $SU(3)$ algebra.

The final QCD Lagrangian is:

$$\mathcal{L}_{\text{QCD}} = \bar{q} \left(i\gamma^\mu D_\mu - m \right) q - \frac{1}{4} G^a_{\mu\nu} G^{a\mu\nu} \tag{1.15}$$

In conclusion the QCD gauge boson, the gluons are produced from requiring $SU(3)$ gauge invariance for colour triplets. The resulting Lagrangian 1.15 has a field strength tensor term for the gluon field, which reflects the gluon kinematics and self interactions. In contrast with QED, the gauge field is allowed to have self interactions due to the $g f^{abc} A^b_\mu A^c_\nu$ term of the Relation 1.14. They arise from the third term of 1.14, which reflect the non abelian structure of the QCD.

The most important feature of the strong force is the corresponding potential. The potential has two terms corresponding to two different regimes of the force. The first term corresponds to high energies and small distances and is similar to electromagnetic potential:

$$V(r) \sim -\frac{\alpha_s}{r} \tag{1.16}$$

In this regime α_s becomes small and the quarks behave as they are almost "free". This property is called asymptotic freedom. The second term corresponds to low energies and is more significant in larger distances:

$$V(r) \sim r \tag{1.17}$$

The potential there becomes linear with distance which leads to the phenomenon of colour confinement. Due to this term the quarks are not observed in colour singlet state, but always bound in hadrons. Consequently the potential function makes QCD precision different in the two energy regimes.

There are two kind of energy regimes where QCD goes into effect. One is the perturbative regime where the coupling of the strong force α_s is small, meaning the energy is high enough, where the Feynman's formalism can work and the matrix element of the interaction can be expanded in orders of α_s. The non perturbative regime is at effect in low energies or high distances. There the α_s is high enough to be unable to expand in orders of α_s. The phenomena at non perturbative QCD are hadronization and confinement of quarks in the hadrons. For this QCD regime there are models such as lattice QCD and effective theories but Feynman formalism do not work. Therefore the simulation of non perturbative QCD is of limited capabilities.

1.3.1 Parton Distribution Functions

An important factor, which influences the results of hadron collider experiments like ATLAS, is the proton structure. At small energies the proton is mainly described by the valence quarks. The momentum of the proton is divided in it's parton. This division is not a simple 1/3 for every parton, due to interactions between the partons, but the momentum of every parton is described by a function. Additionally with increasing energy gluon-gluon pairs are creating sea quarks. Therefore the distribution of the momentum in the proton becomes complicated. The distribution of parton momentum is called Parton Distribution Functions (PDFs).

The PDFs are used in the cross sections of deep inelastic scattering calculations to account for this effect. The functions used are based at the DGALP approach ref.[5], which accounts for the running of α_s.The equations are:

$$\frac{\partial f_i(x,Q^2)}{\partial \ln Q^2} = \sum_j \int_x^1 \frac{dz}{z} P_{ij}\left(z, \alpha_s(Q^2)\right) f_j(\frac{x}{z}, Q^2) \tag{1.18}$$

where $f_i(x,Q^2)$ is the PDF, corresponding to the probability of parton i carrying moment x for energy scale Q. and the splitting function. $P_ij(z,\alpha_s(Q^2))$ is the splitting function describing the propability of parton j splitting into a parton i carrying a fraction z of the original parton's momentum. The splitting function takes into account the running of α_s with Q^2. The limits of the integration are $(x,1)$ to cover for all possible values of z of the original parton's momentum. In Equation the sum is integrating over all parton types j.

PDF calculation is a complicated problem because of their connection with non perturbative QCD regime. Therefore their effects are studied through global fits with data from several high energy physics experiments that involve deep inelastic scattering in QCD. These fits use the Q^2 and the x parametrization of the PDFs, to constrain different PDF models into data. Notable eaxmples are the NNPDF approach which implements neural network models to interpolate PDFs mainly from LHC ref.[6], CTEQ ref.[7]-[8], MSTW/MMHT ref.[10] which use data from LHC, Tevatron and HERA.

In Figure 1.2, PDF model CT10 is displayed, which is used for the Z mass analysis. The graphs illustrate the behavior of the PDFs as a function of the momentum fraction x for different Q. It is evident that for different Q, meaning a energetic scattering on the partons, the sea contribution by quarks and gluons is increasing for low momentum fraction x. The valence quark contribution is slightly decreasing with Q.

In physics analysis, the PDF uncertainty is important to aces the effect of theoretical uncertainty of parton momentum. They are usually by comparing the effect of different PDF models to the kinematic variables. A common procedure is taken the envelope of the effect as the uncertainty.

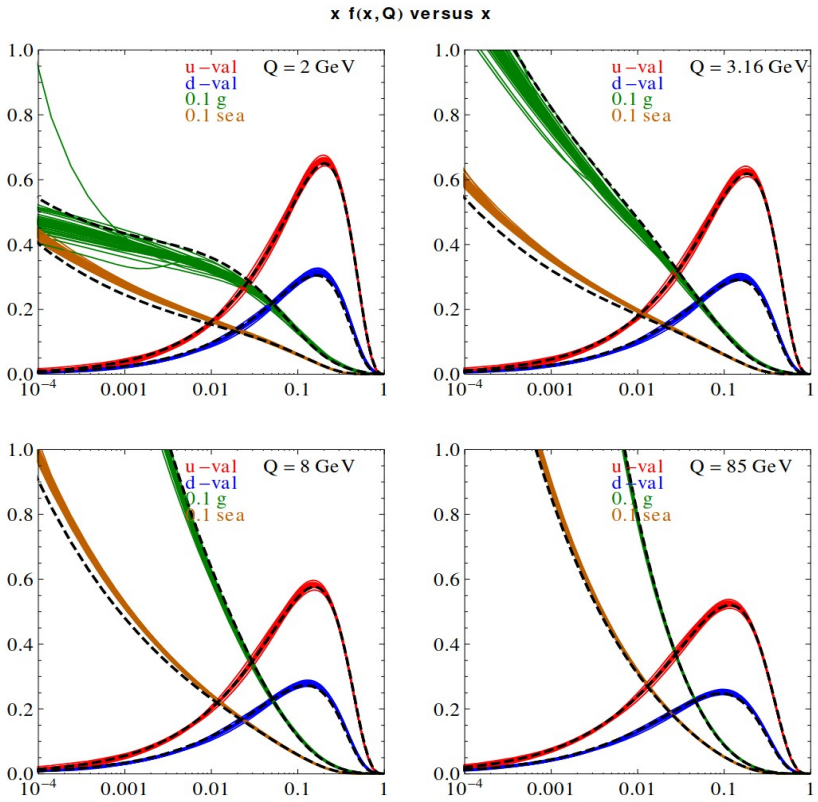

Figure 1.2: CT10NNLO parton distribution functions for different Q. Valence u,d and sea gluon, quark PDFs are displayed as a function of x. The values of Q are 2, 3.16, 8, 85 GeV. The dashed curves are the central CT10 NLO fit. Taken from ref. [8]

1.4 Weak Interaction

The weak interaction came as necessity at the SM to explain experimental data. It explains a variety of physical processes with radiation and nuclear decay being one of the most significant. The most notable experiments to probe the search for the weak force is the Wu experiment.

In 1956, Chien-Shiung Wu conducted an experiment that provided evidence for the violation of parity symmetry in weak interactions, ref. [11]. At the experiment cobalt-60 atoms nucleus spin were aligned with a strong magnetic field. By observing the direction of the electrons originating from β decay, she was able to prove the parity violation. Main proof of the violation was that the electrons emitted had a preferred direction relative to the nuclear spin.

From that moment various experiments replicated similar results. The weak force has to violate parity. This means that the interaction vector term presented in Dirac equation 1.3 has to be altered to include a parity violation term in the equation. To include this kind of term the probability current must use a vector - axial vector term:

$$j^{\mu} = \bar{\psi}\gamma^{\mu}(1-\gamma^{5})\psi \tag{1.19}$$

with $\gamma^5 = i\gamma^0\gamma^1\gamma^2\gamma^3\gamma^4$. This kind of term will appear naturally after interacting with the gauge fields of the weak force.

An important aspect of the weak force is the coupling of different flavour fermions and for specific chirality configurations. A new symmetry is defined for the weak interaction, the weak isospin I_W^3. Since weak force is known to interact only with left handed (LH) fermions and

right handed (RH) anti-fermions, particles will carry different I_W^3 depending on their chirality. Left handed fermions have absolute value of $I_W^3 = 1/2$ and right handed fermions have isospin $I_W^3 = 0$, not interacting therefore with the weak force. For this reason left handed fermions are grouped into I_W^3 doublets:

$$\Psi_L = \begin{pmatrix} \psi_{I_W^3=1/2} \\ \psi_{I_W^3=-1/2} \end{pmatrix}, \quad \begin{pmatrix} \nu_e \\ e_L \end{pmatrix}, \quad \begin{pmatrix} \nu_\mu \\ \mu_L \end{pmatrix}, \quad \begin{pmatrix} \nu_\tau \\ \tau_L \end{pmatrix}, \quad \begin{pmatrix} u_L \\ d_L \end{pmatrix}, \quad \begin{pmatrix} c_L \\ d_L \end{pmatrix}, \quad \begin{pmatrix} t_L \\ b_L \end{pmatrix} \tag{1.20}$$

Right handed fermions are represented by singlets of SU(2).

Weak interaction bosons arise with a similar fashion as a photon in QED, by demanding a local gauge invariance. The Weak Interaction arises from $SU(2)$ local phase transformations:

$$\psi \rightarrow \psi^{'} = \psi e^{i\vec{\alpha}(x)\cdot\frac{\vec{\sigma}}{2}} \tag{1.21}$$

where $\vec{\alpha}(x)$: These are the local gauge transformation parameters, which depend on the space-time position x and $\frac{\vec{\sigma}}{2}$: The Pauli matrices $\vec{\sigma} = (\sigma_1, \sigma_2, \sigma_3)$ are the generators of the $SU(2)_L$ group. The factor of $\frac{1}{2}$ accounts for spin-$\frac{1}{2}$ particles.

By doing an expansion of the exponential with a negligible constant g:

$$e^{i\vec{\alpha}(x)\cdot\frac{\vec{\sigma}}{2}} = \lim_{g\rightarrow 0}[I + \left(ig\vec{\omega}(x)\cdot\frac{\vec{\sigma}}{2}\right) + \cdots] \tag{1.22}$$

Similarly to QED a covariance derivative is defined:

$$D^\mu = \partial^\mu + i\frac{g}{2}\vec{W}^\mu \cdot \vec{\sigma}, \tag{1.23}$$

with $\vec{W}^\mu$ the gauge field associated with the gauge bosons. By requesting the following for the covariance derivative:

$$\Psi'\gamma^\mu D'_\mu \Psi' = \Psi\gamma^\mu D_\mu \Psi \tag{1.24}$$

three boson gauge fields arise: W_1^μ,W_2^μ,W_3^μ. The interaction term of the gauge fields with the fermions has the following form:

$$\frac{g}{2}\Psi\gamma^\mu\vec{W}^\mu \cdot \vec{\sigma}\Psi \tag{1.25}$$

The two physical bosons W^+ and W^- can be written as linear combinations of W_1 and W_2: $W^\pm = \frac{W_1 \pm W_2}{\sqrt{2}}$. The corresponding probability currents can be written:

$$j_\pm^\mu = \frac{g}{\sqrt{2}}\bar{\Psi}_L\gamma^\mu\sigma_\pm\Psi_L \tag{1.26}$$

with $\sigma_\pm$ the spin ladder operators. For simplicity the doublet is replaced with:$\Psi = \begin{pmatrix} \nu \\ l \end{pmatrix}$. Equation 1.26 can be transformed into a vector-axial vector form (Equation 1.19) to probe parity violation:

$$j_+^\mu = \frac{g}{\sqrt{2}}\bar{\nu}\gamma^\mu\frac{1}{2}(1-\gamma^5)l \tag{1.27}$$

$$j_{-}^{\mu} = \frac{g}{\sqrt{2}} \bar{l} \gamma^{\mu} \frac{1}{2}(1-\gamma^{5})\nu \tag{1.28}$$

There are are though two open questions. One is the W_3^{μ}, which has not been used until now. It will be used for unification of the weak force with electromagnetism to form electroweak theory. The second one is the mass term of the Diran equation, which has been ignored until now.

1.4.1 Mass Term-Gauge Invariance

The mass term from dirac equations can be written as:

$$m\bar{\psi}\psi = m(\bar{\psi}_L\psi_R + \bar{\psi}_R\psi_L)$$

where:

- $\psi_L = \frac{1}{2}(1-\gamma^5)\psi$ is the left-handed component of the fermion.
- $\psi_R = \frac{1}{2}(1+\gamma^5)\psi$ is the right-handed component of the fermion.

The mass term $m(\bar{\psi}_L\psi_R + \bar{\psi}_R\psi_L)$ mixes the left-handed and right-handed fermions. However, under the gauge transformations introduced in Section 1.4, these two components transform differently. The left handed fermion wavefunction is a I_W^3 doublet where the right handed fermion is a singlet with I_W^3. One term will transform under the $SU(2)_L$ and the other not. Therefore the mass term is not gauge invariant. This problem will be fixed with the Higgs mechanism which is going to be discussed in Section 1.5.1.4.

1.5 ElectroWeak Sector

Electroweak (EW) theory is the unification of two of the four known fundamental forces: the electromagnetic force and the weak nuclear force. In the 1960s, Sheldon Glashow (ref. [12]), Abdus Salam (ref. [13]), and Steven Weinberg (ref. [14]) independently proposed a unified theory Their work showed a unification of forces at higher energies.

EW theory is very important in the scope of this thesis because the Z boson arises from the unification but also the interference between Z and γ is used to produce variations of the m_Z distribution to measure the Z mass.

The mathematical formalism of EW sector is part of the $SU(2) \otimes U(1)$ gauge group, with generators the weak isospin T and weak hypercharge Y. The generators give rise to three W bosons of weak isospin(W_1, W_2, W_3) and the B boson of weak hypercharge. These bosons are "massless" and they correspond to non physical fields. The physical bosons $W^{\pm}$, Z^0 and γ^0 are produced after the spontaneous symmetry breaking of the EW symmetry to $SU(2) \times U(1)_Y$ to $U(1)_{em}$ through the Higgs mechanism. The W_3^{μ} gauge field predicted by weak theory gives a probability current:

$$j_{W_3}^{\mu} = g \begin{pmatrix} \bar{\nu} & \bar{l} \end{pmatrix}_L \gamma^{\mu} \frac{\sigma_3}{2} \begin{pmatrix} \nu \\ l \end{pmatrix}_L \tag{1.29}$$

$$\rightarrow j_{W_3}^{\mu} = \frac{1}{2} g \left(\bar{\nu}\gamma^{\mu}\nu - \bar{l}\gamma^{\mu}l \right) \tag{1.30}$$

The field W_3^μ notably is associated with neutral current and has a similar structure as QED. But still does not have a mass and does not explain massive neutral current.

To solve the mass problem which was also discussed in Section 1.4 Glashow proposed the existence of massless Goldstone-like bosons B_μ. The new field will be connected to a new gauge symmetry, similar to that of electromagnetism, weak hypercharge $U(1)_Y$. And hypercharge is given by:

$$Y = 2Q - I_W^3 \tag{1.31}$$

where Q us the electromagnetic charge and I_W^3 the z component of the weak isospin. The weak hypercharge is notable having different values for left handed and right handed particles due to the I_W^3 term.

The physical boson γ and Z will be a combination of W_μ^3 and B_μ:

$$A_\mu = B_\mu \cos\theta_W + W_3^\mu \sin\theta_W \quad \text{(photon, } \gamma\text{)} \tag{1.32}$$

$$Z_\mu = W_3^\mu \cos\theta_W - B_\mu \sin\theta_W \quad \text{(Z-boson)} \tag{1.33}$$

where θ_W is the Weinberg angle which mixes the physical fields A_μ,Z_μ with the gauge fields W_3^μ and B^μ. By convention the coupling of the B_μ to fermions will be given by: $\frac{1}{2}g^{'}Y$

An important aspect of the model is the interdependence of SM parameters and the association of arbitrary gauge field properties to the physical field ones. By requesting:

$$j_\mu^{em} = j_\mu^Y \cos\theta_W + j_\mu^{W_3} \sin\theta_W \tag{1.34}$$

and

$$j_\mu^Z = -j_\mu^Y \sin\theta_W + j_\mu^{W_3} \cos\theta_W \tag{1.35}$$

ones derives:

$$e = g\sin(\theta_W) = g^{'}\cos\theta_W \tag{1.36}$$

and for a $g_z = \frac{g_w}{\cos\theta_W}$:

$$e = g_Z \cos\theta_W \sin\theta_W \tag{1.37}$$

The Equation (1.37) is important as it connects the coupling of electromagnetism to an EW coupling of the Z boson and the weak mixing angle.

By advancing the probability current Equation (1.35) for the Z boson:

$$J_Z^\mu = g_Z \left(I_W^3 - Q\sin^2\theta_W\right)[\bar{\psi_L}\gamma_\mu\psi_L] - g_Z Q\sin^2\theta_W[\bar{\psi_R}\gamma_\mu\psi_R] \rightarrow \tag{1.38}$$

$$J_Z^\mu = g_Z c_L[\bar{\psi_L}\gamma_\mu\psi_L] - g_Z c_R[\bar{\psi_R}\gamma_\mu\psi_R] \tag{1.39}$$

Which means that the Z boson couples differently with left handed and right handed fermions. The W_3 part of Z couples only to LH components (similarly to $W^\pm$) and the B_μ part couples equally LH, RH components. This gives a property for the Z boson which is called **Asymmetry**.

The probability current for the Z can also be expressed with the vector $c_V = c_L + c_R$ and axial vector $c_A = c_L - c_R$ couplings:

$$J_Z^\mu = \frac{g_Z}{2}\bar{\psi}\gamma_\mu[c_V - c_A\gamma_5]u \tag{1.40}$$

At the Appendix A are presented the couplings and the hypercharge for all fermions.

Finally EW Lagrangian, by ignoring mass terms, is derived:

$$\mathcal{L}_{\text{EW}} = -\frac{1}{4}W^a_{\mu\nu}W^{a\mu\nu} - \frac{1}{4}B_{\mu\nu}B^{\mu\nu} + i\bar{\Psi}\gamma^\mu D_\mu\Psi \tag{1.41}$$

In conclusion it is important to analyze the EW probability currents and Lagrangian. The EW Lagrangian has multiple terms with different interpretations. The two first ones:$W^a_{\mu\nu}W^{a\mu\nu}$ and $B_{\mu\nu}B^{\mu\nu}$, are kinematic terms of EW bosons and allow for self interaction W and Z. Also through the mixing, interaction is allowed between the boson themselves. The third term $\bar{\Psi}_L i\gamma^\mu\partial_\mu\Psi_L$ is the EW interaction term with the fermions. From this term W probability currents emerged in Equations 1.27 1.28. From these probability currents it is visible that W boson change the flavour of the lepton. Therefore, they couple netrinos with the corresponding leptons. Finally from the probability current of Z in Equation 1.39, it is clear that the Z couples differently to left handed and right handed particles. Also it decays similarly to a photon in e,μ,τ or quark, but also it can decay to neutral netrinos.

Finally, there is still a problem with the mass terms in the Lagrangian, which does not the respect gauge invariance. This will be solved with Higgs mechanism at the Section 1.5.1.

1.5.1 Higgs Mechanism

Higgs mechanism is a solution to the mass problem of EW boson and fermions. By adding a scalar field at the Lagrangian and the spontaneous symmetry breaking, the particles acquires mass.

First the Goldstone model is going to be presented which is a simple basis on the higgs mechanism. Then the more complex higgs mechanism will be presented, the procedure for acquiring the higgs mass is going to be discussed and finally the coupling of bosons and fermions to the higgs field.

1.5.1.1 The Goldstone Model

In the Goldstone model, ref. [15], the Lagrangian has a kinematic term of complex scalar field ϕ and a corresponding potential V:

$$\mathcal{L} = (\partial_\mu\phi)^*(\partial^\mu\phi) - V(\phi), \tag{1.42}$$

where V is the potential:

$$V(\phi) = \mu^2|\phi|^2 + \lambda|\phi|^4, \tag{1.43}$$

Here, μ^2 and λ are constants, with $\lambda > 0$ ensuring the potential is bounded from below. The sign of μ^2 will determine whether symmetry breaking occurs. If $\mu^2 > 0$, the potential has a minimum at $\phi = 0$, and no symmetry breaking occurs. However, if $\mu^2 < 0$, the minimum occurs at a non-zero value of ϕ, and the symmetry is spontaneously broken.

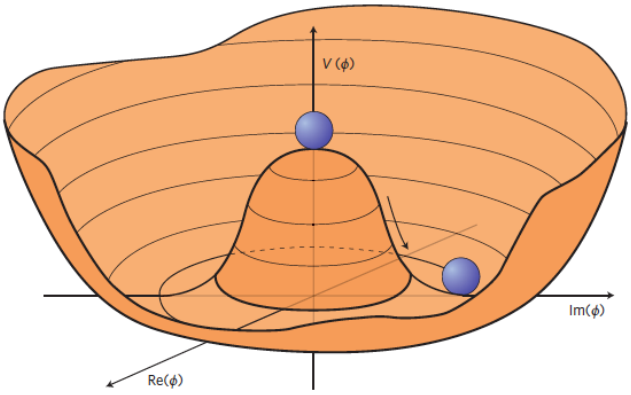

Figure 1.3: Functional form of the potential V in Relation 1.43 as a function of imaginary and real part of the complex scalar field ϕ for $\mu < 0$. Taken from ref. [16]

When $\mu^2 < 0$, the potential takes the form of the "Mexican hat" potential. By analytically minimizing the potential, the vacuum expectation value (VEV) of the field ϕ is found.

To find the minimum of the potential, the derivative of $V(\phi)$ with respect to ϕ is calculated and required to be to zero. And by solving for $|\phi|^2$:

$$\frac{dV(\phi)}{d\phi} = 0 \rightarrow |\phi|^2 = -\frac{\mu^2}{2\lambda}. \tag{1.44}$$

For $\mu^2 < 0$, this gives a positive value for $|\phi|^2$, and the vacuum expectation value (VEV) of ϕ is defined as:

$$\eta^2 = \frac{-\mu^2}{\lambda}. \tag{1.45}$$

Thus, the VEV is:

$$\eta = \sqrt{-\frac{\mu^2}{\lambda}}. \tag{1.46}$$

This shows that the field acquires a non-zero vacuum expectation value, spontaneously breaking the U(1) symmetry.

Since the potential only depends on the magnitude of ϕ, and not on its phase, the vacuum is degenerate. The set of possible vacua forms a circle, parameterized by the phase θ. The vacuum configuration can be written as:

$$\langle\phi\rangle = \frac{\eta}{\sqrt{2}} e^{i\theta} \tag{1.47}$$

where $0 \leq \theta \leq 2 * \pi$ is an arbitrary constant phase, indicating the degeneracy of the vacuum. The physical vacuum can reside in any place in the degenerate vacua. By choosing a particular one (a value for the θ of equation 1.47), U(1) symmetry is broken.

According to the *Goldstone theorem*, the spontaneous breaking of a continuous global symmetry leads to the existence of massless scalar particles, called *Goldstone bosons*. In this example, the U(1) symmetry is spontaneously broken, and one massless Goldstone boson is expected.

The Goldstone model scalar field, shown here, is mass less, but the Higgs boson is not massless. By combining the spontaneous symmetry breaking, a gauge field and a scalar field, the later can acquire mass, which is going to be presented in Section 1.5.1.2.

1.5.1.2 The Higgs model and coupling to gauge fields

In the following analysis section the coupling of the higgs field with a arbitrary gauge field R_μ is going to be displayed. The process of acquiring mass for the scalar field ϕ is going to be presented.

Similarly to QED in Section 1.2, local gauge invariance is requested and therefore an associated gauge field is defined R_μ. The Lagrangian is:

$$\mathcal{L} = (D_\mu \phi)^\dagger (D^\mu \phi) - V(\phi) - \frac{1}{4} F^a_{\mu\nu} F^{a\,\mu\nu} \tag{1.48}$$

where $F^a_{\mu\nu}$ is the field strength tensor associated with the gauge field, D_μ is the *covariant derivative*: $D_\mu = \partial_\mu - ieR_\mu$.

By demanding the local gauge invariance:

$$\phi(x) \to \phi^{'}(x) = e^{ia(x)}\phi(x) \tag{1.49}$$

and for a small a_x:

$$\phi^{'}(x) = \phi(x) + ia(x)\phi(x) \tag{1.50}$$

Without loss of generality the field can be set to be real:

$$\phi = \eta + \frac{\sigma(x)}{\sqrt{2}} \tag{1.51}$$

with $\sigma(x)$ a real scalar field. By substituting the 1.51 in the Lagrangian of 1.48:

$$\mathcal{L} = \frac{1}{2}\partial_\mu \sigma \partial^\mu \sigma - \frac{1}{2} 2\lambda \eta^2 \sigma^2 - \frac{1}{4} F^a_{\mu\nu} F^{a\,\mu\nu} + \frac{1}{2} 2e^2 \eta^2 R_\mu R^\mu \tag{1.52}$$

In equation 1.52 new terms emerged with the coupling of the scalar field with the gauge field. The first term is the kinematic term of the scalar field. The second term is the mass term that emerged by adding the gauge field to the lagrangian, with mass $2\lambda\eta^2$. The third term is the kinematic term of the gauge field Similarly with QED and Weak interactions. Finally a mass term arises for the gauge field with a mass: $2e^2\eta^2$.

In conclusion, adding a gauge field to the Goldstone model discussed in Section 1.5.1.1, with the spontaneous symmetry breaking generates massive scalar and gauge fields. In this section the gauge field was an arbitrary one. In Section 1.5.1.3 the higgs field with the $SU(2)_L \otimes U(1)_Y$ symmetry is discussed.

1.5.1.3 The Higgs field and $SU(2)_L \otimes U(1)_Y$

Using the EW Lagrangian 1.41 with the higgs model presented in Section 1.5.1.2 and the spontaneous symmetry breaking, the W and Z bosons can acquire mass.

The fields can be written as:

$$Z_\mu = \frac{1}{\sqrt{g^2 + g'^2}} \left(g W^3_\mu - g' B_\mu \right) \tag{1.53}$$

$$A_\mu = \frac{1}{\sqrt{g^2 + g'^2}} \left(g' W^3_\mu + g B_\mu \right) \tag{1.54}$$

By substituting at the EW Lagrangian with the new field definitions, the mass terms of the new fields are:

$$\mathcal{L}_{\Updownarrow\dashv\int\int} = \frac{1}{2}\left(\frac{g\eta}{2}\right)^2 \left(W_\mu^+\right)^2 + \frac{1}{2}\left(\frac{g\eta}{2}\right)^2 \left(W_\mu^-\right)^2 + \frac{1}{2}\left(\frac{\eta\sqrt{g^2+g'^2}}{2}\right)^2 Z_\mu^2 + 0 \cdot A_\mu^2 \tag{1.55}$$

In conclusion the SM boson mass is parameterized by the same parameter of the Higgs model, VEV η, as portrayed in Table 1.3.

Field	**Mass**
H	$\sqrt{2\lambda}\eta$
W_μ^+	$\frac{g\eta}{2}$
W_μ^-	$\frac{g\eta}{2}$
Z_μ	$\frac{\eta\sqrt{g^2+g'^2}}{2}$
A_μ	0

Table 1.3: Masses of the gauge bosons after EW symmetry breaking.

Moreover, the relation connecting W and Z boson mass and weak mixing angle is given by:

$$m_Z = \frac{m_W}{\cos\theta_W} \tag{1.56}$$

Testing the consistency of the SM is crucial for the modern physics. This can be done by measuring SM parameters as θ_W, couplings and boson masses independently probing the way for precision and the discovery of potential new physics. In the ATLAS context there two parallel analyses in Run-2 which have a common ground, the W and Z mass measurements.

1.5.1.4 Yukawa couplings

Fermions also acquire mass through the higgs field. This is reflected to the mass Yukawa terms of the Lagrangian:

$$\mathcal{L}_Y = -y_f \bar{\psi}_L \phi \psi_R \tag{1.57}$$

for ϕ the higgs field. The left-handed doubletψ_L transforms as a doublet under $SU(2)_L$. The Higgs Field Φ also transforms as a doublet under $SU(2)_L$. The right handed singlet ψ_R transforms as a singlet under $SU(2)_L$, therefore it does not transform. By using the unitary gauge for the higgs field:

$$\Phi = \begin{pmatrix} 0 \\ \frac{v+\sigma(x)}{\sqrt{2}} \end{pmatrix} \tag{1.58}$$

the mass term becomes gauge invariant the fermions can acquire mass.

1.5.1.5 Higgs Discovery

Higgs discovery ref.[17] by ATLAS and CMS in 2012 was one of the most important events in particle physics. The discovery confirmed the mechanism of symmetry breaking and mass generation for fundamental particles. The measurement was done using proton proton collisions with integrated luminosities of approximately $4.8 fb^-1$ collected at $\sqrt(s) = 7$ TeV in 2011 and 5.8 fb^-1 at $\sqrt(s) = 8$ TeV in 2012. The discovery had a magnificent significance of 5.9 σ. The mass of higgs was measured: $m_H = 126.0 \pm 0.4\,(\text{stat}) \pm 0.4\,(\text{sys})$ GeV.

Channels that had a main role in the discovery are: $H \to \gamma\gamma$, $H \to ZZ \to 4l$ and $H \to WW \to l\nu l\nu$.

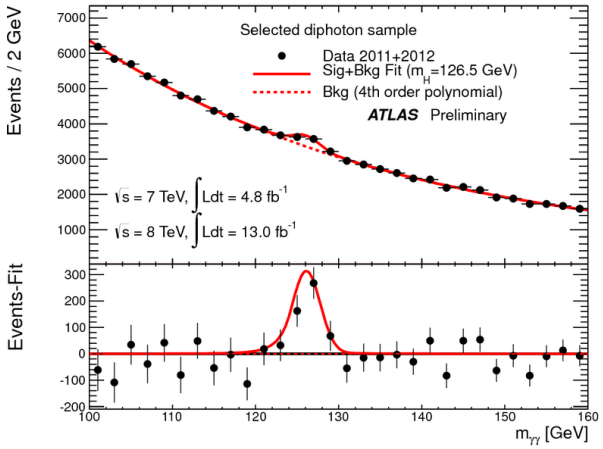

Figure 1.4: Number of events as a function of $mass_{\gamma\gamma}$. Taken from ref.[17].

1.5.2 Z Bosons

1.5.3 W and Z bosons

As shown in Section 1.5.1.3 the SM observables are correlated. Moreover, the higher order diagrams can contribute to processes, correlating SM observables, through loop diagrams. To verify the consistency of the Standard Model, measurements of its parameters must be conducted both independently and in combination with one another.

The most prominent example, important in the context of the thesis is the W mass. The W mass analysis in ATLAS is running parallel to the Z mass analysis and their work is intertwined, especially in the calibration part. The W mass (m_W) is related to other parameters, such as (m_Z), the α_{em}, and the Fermi constant (G_F). The relationship is corrected by radiative effects, summarized in the Δr parameter. This correction origins from the contributions of loops diagram from various particles, with the most influential being the top quark and the Higgs boson. The $m_W^2 s$ parametrization from m_Z, and Δr is given by the Relation 1.59:

$$m_W^2 = \frac{C}{\left(1 - \frac{m_W^2}{m_Z^2}\right)(1 - \Delta r)} \tag{1.59}$$

with C constant dependent on the electromagnetic and weak coupling. In Relation 1.60 the Δr term is analysed in the contributions of top and Higgs mass + other high order terms:

$$\Delta r = \Delta r_t + \Delta r_H + \Delta r_{\text{others}} \approx C_1 M_t^2 + C_2 \ln\left(\frac{m_H^2}{m_Z^2}\right) + \text{others} \tag{1.60}$$

with C_1, C_2 constants dependent from couplings. From Relations 1.59 and 1.60 is evident the dependence of m_W directly from m_Z but also from m_t and m_H. Since m_Z has been measured precisely in various experiments, the dependence from m_t and m_H has a bigger effect on m_W.

In the Figure 1.5, the most recent M_W measurement of ATLAS displayed in comparison of other notable results from similar experiments. The ATLAS 2024 measurement of m_W ref.[18] is one of the most recent and indicates consistency with earlier measurements while being the most precise to date.

In the Figure 1.5 (b), the 68% and 95% confidence level integrals for m_W and m_t comparison for two different fits are displayed. First fit is the global ElectroWeak Fit and the second fit is the latest m_W ref.[18] ATLAS measurement after the LHC m_H and m_t measurements. Notably

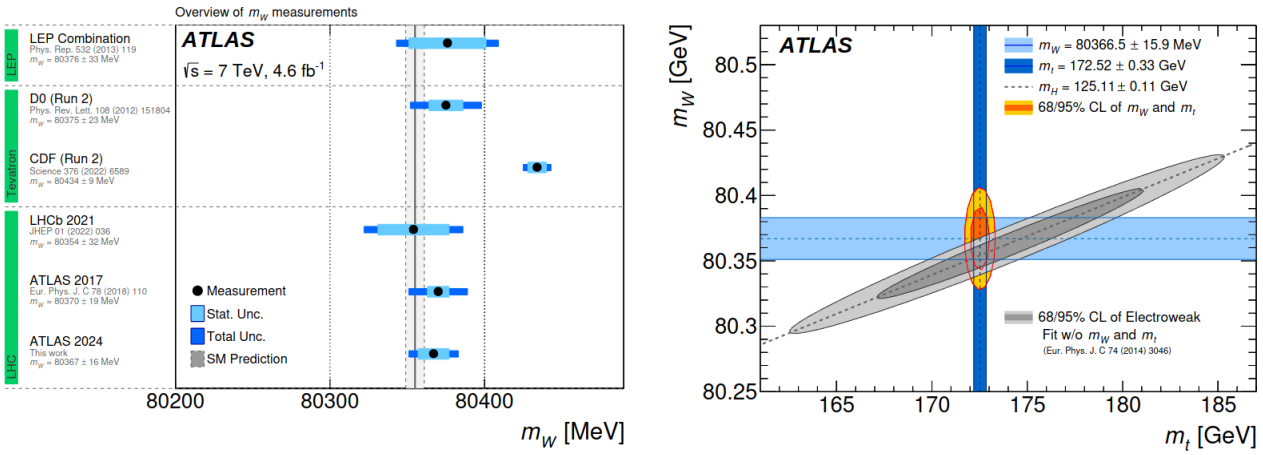

(a) (b)

Figure 1.5: (a) Present measured value of M_W , compared to SM prediction from the global electroweak fit, and to the measurements of LEP, Tevatron and the LHC. (b) The 68% and 95% confidence level integrals of m_W and m_t for the electroweak global fit and the ATLAS $\sqrt{s} = 7$ TeV measurement. Taken from ref.[18].

at the ElectroWeak fit the unknown mass of the Higgs gives the high correlation shape. Through the measurements of m_H and m_t, the m_W correlation with the other masses got contained.

1.5.3.1 Z Boson Properties

Z Branching Ratios:

Decay Channel	Branching Ratio (%)
$Z \to e^+e^-$	3.3632
$Z \to \mu^+\mu^-$	3.3662
$Z \to \tau^+\tau^-$	3.3696
Total Leptonic Decays	**10.1**
Total Neutrino Decays	**20**
$Z \to$ hadrons	69.987

Table 1.4: Z boson decay branching ratios into leptons, neutrinos, and hadrons. Taken from ref.[19].

LineShape: Z Lineshape is formed by multiple parameters. The peak is described by a Breit Wigner distribution with an energy-dependent total width. The shape is defined by three parameters, position of the peak, the width, and the height which are connected to physical parameters of the boson, Z boson mass m_Z, width of Z boson Γ_Z and branching ratio $\Gamma(l_{in}l_{in}) \times \Gamma l_{out}l_{out}$.

Cross section of $q\bar{q} \to l\bar{l}$ for a given boson mass and width is proportional to the following terms:

$$\hat{\sigma}(\hat{s}) \propto \sum_{i,j} \alpha_i \alpha_j V_i V_j B_{ij} P_{ij}(\hat{s}) \tag{1.61}$$

where α_i and α_j are the coupling constants associated with particles i and j, V_i and V_j are generation mixing terms, B_{ij} is the coupling factor for the initial and final states, and $P_{ij}(\hat{s})$

is the propagator term, which relies on the the Breight Wigner parametrization and $\hat{s}$ is the available energy for the parton-level process. The sum runs over the propagators, in this case: γ, Z and the interference Z/γ. The $\hat{s}$ in practise is the boson mass at generator level for a specific event.

Coupling factor is given by:

$$B_{ij} = (v_i v_j + a_i a_j)_{\text{in}} (v_i v_j + a_i a_j)_{\text{out}} \tag{1.62}$$

with v the vector couplings. And the propagator - Breit Wigner terms are given by:

$$P_{ij}(\hat{s}) = \frac{\hat{s}\left[(\hat{s} - m_i^2)(\hat{s} - m_j^2) + m_i m_j \Gamma_i \Gamma_j\right]}{\left[(\hat{s} - m_i^2)^2 + (m_i \Gamma_i)^2\right]\left[(\hat{s} - m_j^2)^2 + (m_j \Gamma_j)^2\right]} \tag{1.63}$$

By using this parametrization the interference between Z and γ is taken into account. The Lineshape of Z with all of the propagators contributing is displayed in Figure 1.10.

Also Lineshape is influenced by radiation in the initial or final state. This radiation is called initial and final state radiation. It's nature can be QED or QCD depending on the initial and final state particles. It can influence heavily the tails of the Z mass distribution.

Asymmetry: In equation 1.39 the probability current of the Z boson decay at two leptons reflects an asymmetry in the way the Z boson interacts with left and right handed fermions. This leads to an angular asymmetry in the cross section with respect to the scattering angle θ, relative to the axis of the incoming particles.

The matrix element of $l_{in} l_{in} \to Z \to l_{out} l_{out}$ using the EW probability current of 1.39 can be expressed as:

$$\left\langle |M_{fi}|^2 \right\rangle \propto \left[\left(c_L^{in}\right)^2 + \left(c_R^{in}\right)^2\right]\left[\left(c_L^{out}\right)^2 + \left(c_R^{out}\right)^2\right](1 + \cos^2\theta) + \left[\left(c_L^{in}\right)^2 - \left(c_R^{in}\right)^2\right]\left[\left(c_L^{out}\right)^2 - \left(c_R^{out}\right)^2\right]\cos\theta \tag{1.64}$$

In Equation 1.64 there are two terms in orders of $\cos\theta$ with different constants. This creates the cross section behavior seen in Figure 1.7 for two hemispheres, Forward: $0 \leq \cos\theta \leq 1$ Backward: $-1 \leq \cos\theta \leq 0$. Two corresponding cross sections are defined: $\sigma_B = \int_{-1}^{0} \frac{d\left\langle |M_{fi}|^2 \right\rangle}{d\cos\theta} d\cos\theta$ and $\sigma_F = \int_{0}^{1} \frac{d\left\langle |M_{fi}|^2 \right\rangle}{d\cos\theta} d\cos\theta$

An EW observable is defined, called Forward Backward asymmetry:

$$A_{FB} = \frac{\sigma_F - \sigma_B}{\sigma_F + \sigma_B} \tag{1.65}$$

Measuring A_{FB} can be expressed in terms of EW couplings and therefore is a critical component of the SM. The A_{FB} has been measured by several experiments. Notable examples are JADE ref.[20] and LEP ref.[21]. The differential cross section $\frac{d\sigma}{d\cos\theta}$ as a function of $\cos\theta$ is displayed in Figure 1.7, from JADE experiment. The plot displays two predictions, one solid line which is the QED only prediction and the dashed line including the Z contribution. The dashed line is not symmetric with $\cos\theta$ describing the data. LEP measured: $A_{FB} = 0.0171 \pm 0.0010$ ref.[21].

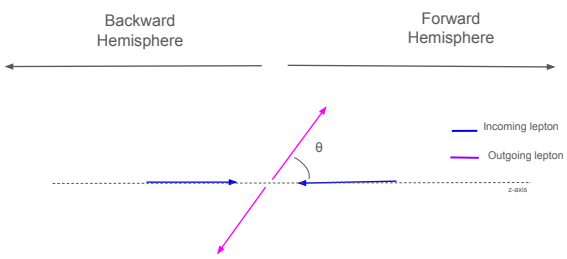

Figure 1.6: Hemisphere definition in the rest frame of the Z boson. Forward and backward hemispheres are defined to denote the asymmetry of the Z boson decay products, respect to the decay angle θ.

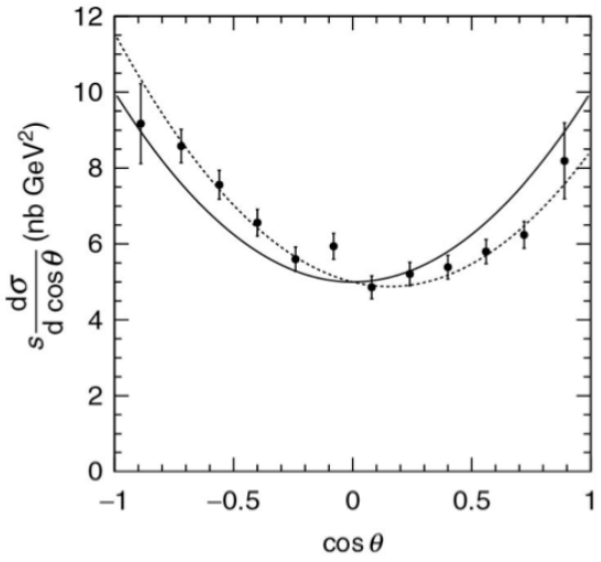

Figure 1.7: Differential cross section from process: $ee \to \mu\mu$, JADE experiment. Solid line is prediction calculated away from Z boson mass pole, with contribution only from QED, where dashed line includes Z boson pole. Data are described from dashed line. Taken from ref.[20]

1.5.3.2 Z boson at Hadron Colliders

Most common process of producing Z boson at hadron colliders is the Drell-Yan process. It involves the annihilation of a quark and an anti-quark from two different hadrons, the creation of a Z/γ propagator and finally the decay to two leptons of opposite charge. Quarks have to carry the same charge and flavor, but they can be either valence or sea quarks.

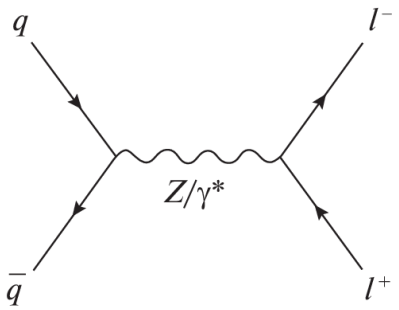

Figure 1.8: Drell-Yan process Feynmann diagram for $qq \to Z \to l^+l^-$.

Z is produced in an abundance of di-muon processes in a hadron collider. A mass spectrum of di-muon processes in ATLAS at $\sqrt{s} = 7$ TeV is displayed in Figure 1.9. There is a Drell-Yan continuum thought the whole mass spectrum where γ dominates. At low energies there is domination of QCD resonances (such as ω, ϕ, J/ψ and Υ). Above ≈ 10 GeV the γ contribution from Drell-Yan falls as a power-law until the Z mass regime, where the Z mass peak is found. Irelaxing musicn Figure 1.9 there is also contribution from di-boson processes which contribute to the continuum but their cross section is too small to have a visible effect here.

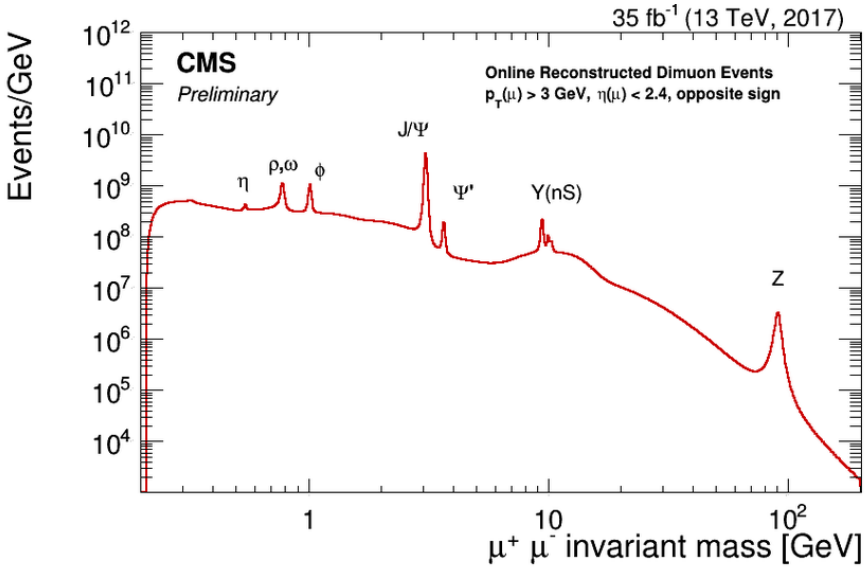

Figure 1.9: Di-muon mass spectrum in CMS from Run-2 (2017 and 2018 campaigns). Taken from ref. [22].

At Figure 1.10 the interference of Z and γ production through Drell-Yan process is plotted. At low invariant masses (below 60 GeV), the production is dominated by the γ contribution, as the Z boson does not contribute significantly at those energies. Around 80–100 GeV, Z contribution dominates and shapes significantly the cross section. At high mass the Z contribution is diminishing until the γ contribution becomes dominant again.

Around 80–100 GeV, the interference becomes large, both positive and negative, as the Z boson contribution interferes with the photon.

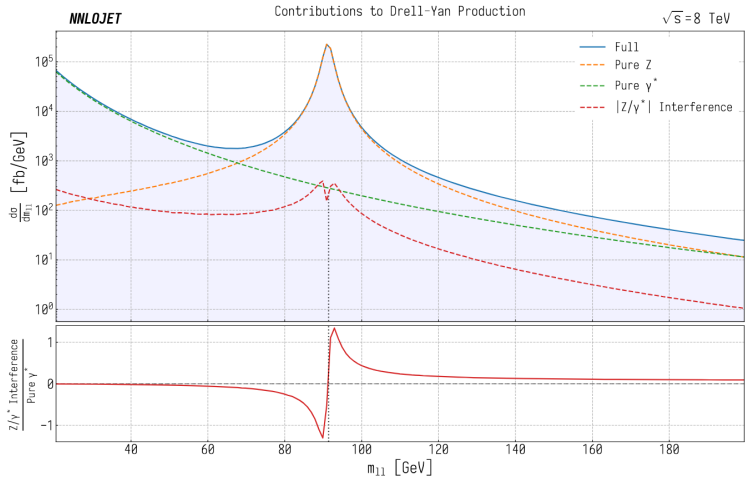

Figure 1.10: Theoretical prediction of Z, γ interference as a function of m_{ll} at Drell-Yan process, in the context of a hadron collider, calculated at LO in QCD. Top panel shows absolute values of pure Z, pure γ and Z/γ interference. The bottom plot shows ratio of $Z\gamma$ to γ pure contributions. Black dotted line is at $\approx m_Z$ pole. Taken from ref.[23].

Experimentally is not possible to distinguish from the final di-muon state the pure Z and Z/γ interference contribution so the signal modeling have to take into account interference terms.

1.5.3.3 Previous Measurements of Z boson properties

In the following sub-section previous measurements of the Z boson are going to be presented, such as the one of LEP in CERN. This subsection motivates this thesis since at the end of the thesis the reader can compare the LHC - ATLAS precision with the LEP one. Main difference between the two is the type of particles collided. LEP used electrons and positrons which have by default a "clean" signal compared to complex processes happening though QCD at the LHC. LEP achieved a highly precise measurement by carefully calibrating the beam energy and conducting detailed scans of the beam energy around the Z pole. In contrary, in ATLAS, the scope is to reconstruct the final state objects, reconstruct the di-muon mass distribution and therefore introduce reconstruction systematic uncertainties. The comparison of a precise beam calibration and a detector calibration process, in the context of a Z mass measurement, is deemed to be of large scientific interest.

Properties of Z the boson have been at the center of many physics analyses. EW unification was one of the major breakthroughs of modern particle physics. The first experiment to find experimental evidence of a unification of electrodynamics and weak force was at the Gargamelle bubble chamber at CERN ref.[24], by identifying weak neutral current. This paved the way for the discovery of the Z boson at Super Proton Synchrotron (SPS) of CERN, from the experiments UA1 and UA2 ref.[25].

Later, W and Z bosons got studied extensively at LEP. At CERN, where the Large Hadron Collider resides now, the LEP collider was based. LEP was a 27 kilometers long electron positron collider and operated as a "factory" of Z boson for the experiments located at it's ring. These four experiments, ALEPH, DELPHI, L3 and OPAL, took data from 1989 to 1995 contributed to precise measurements of the resonance.

Main attribute of the measurements was the fact that the collider center of mass energy was scanned at values near the Z mass resonance peak 88-94 GeV. By performing a cross section the experiments were able to provide a precise result on Z mass and width. At the same time, SLD experiment with the linear collider, SLAC, provided Z properties measurements. For the

context of the thesis the focus will be on the LEP experiments.

For the beam energy calibration several methods were used. The most significant, contributing to the precision of the final result is the Resonant Depolarization, which is going to be analyzed in short here. Basic principle was the de-polarization of transverse polarized (compared to the beam axis) electrons, in a controlled way with an oscillating horizontal magnetic field. By observing the effects of this controlled de-polarization, the beam energy can accurately be determined. This is possible because the frequency of the spin precession (the rate at which the spins rotate) is directly related to the energy of the particles. The number of spins precessions per revolution, the spin tune ν_s, is related to the beam energy with the relation:

$$E_{beam} = \frac{\nu_s \times m_e c^2}{(g_e - 2)/2} = 0,440648\text{GeV} \times \nu_s \tag{1.66}$$

with $(g_e - 2)/2$ the magnetic moment anomaly of the electron, m_e is the electron mass and c is the speed of light. The de-polarizing field is applied to the electrons once per turn in the ring. So once per turn the depolarizing field is in phase with the spin precession. The depolarization then will occur with an independent rate from the integer part of the spin tune. The depolarizing magnetic field is applied at a frequency that matches the fractional part of the spin tune. Specifically, the resonance happens at the fractional part of $\nu_s - int(\nu_s)$ multiplied by the revolution frequency of the of the particles f_{rev}:

$$f_{dep} = (\nu_s - int(\nu_s)) \times f_{rev} \tag{1.67}$$

where f_{rev} is known from the beam energy. The experiment locates the resonance by varying the frequency of the depolarizing field within successively smaller ranges to match the fractional spin tune and determine the beam energy with high precision.

The LEP measurement, ref.[21], included the simultaneous determination of different EW parameters related to the Z boson. The basic principle of the measurement was the scanning of the center of mass energy around the Z pole and doing a cross section measurement. This method resulted in a measurement with minimal uncertainties, independent from the reconstruction of the final state particles. The great advantage of the electron positron beam is the fact that beam energy and initial state energy can be known very precisely. Therefore, the error on the mass was dominated by the uncertainty in the absolute energy scale and the difference between the scans of the energy.

The cross section of Equation (1.61) was used for $e\bar{e} \to f\bar{f}$ with the Brei-Wigner parametrization of Equation (1.63). By fitting the observed cross section data to the Breit-Wigner resonance curve, and utilizing the precise knowledge of the center-of-mass energy, the mass of the Z boson can be determined with high accuracy. The measurement procedure is displayed in Figure 1.11.

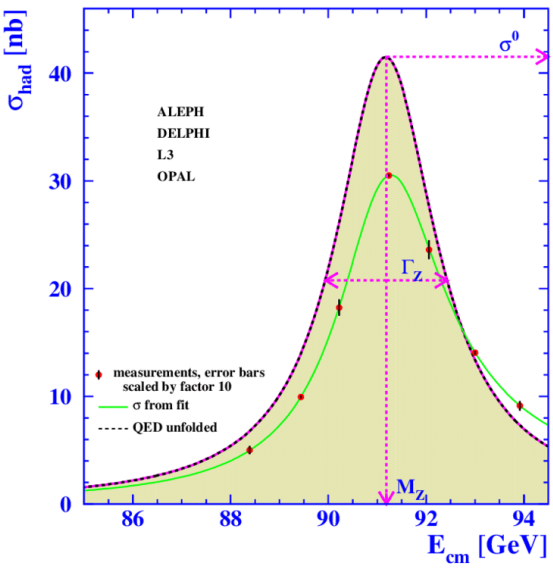

Figure 1.11: LEP hadronic cross-sections, as a function of centre-of-mass energy. The points correspond to the cross scection measurments parametrized by the Breit-Wigner distribution and the centre-of- mass energy. The shaded area represents the cross-section, deconvoluted for the effects of QED. Taken from ref. [21].

The combined results from the 4 experiments and the combination of all leptons channels are presented in Table 1.5. The combined LEP measurement achieved an excellent result of $\sigma_{m_Z} = 0.002$ GeV.

Parameter	Value	m_Z	Γ_Z	σ_h^0	R_ℓ	$A_{\rm FB}^{0,\ell}$
m_Z [GeV]	91.1875 ± 0.0021	1.00				
Γ_Z [GeV]	2.4952 ± 0.0023	-0.023	1.00			
σ_h^0 [nb]	41.540 ± 0.037	-0.045	-0.297	1.00		
R_ℓ	20.767 ± 0.025	0.033	0.004	0.183	1.00	
$A_{\rm FB}^{0,\ell}$	0.0171 ± 0.0010	0.055	0.003	0.006	-0.056	1.00

Table 1.5: Results for the m_Z measurement with correlations and uncertainties.

Other than the Z value it self an interesting aspect of the LEP experiments is the correlation of the parameters fitted. Specifically, since the m_Z and Γ_Z shape $m_{\mu\mu}$ distribution the correlation between them will be also discussed in the context of the thesis.Consequently, comparing the correlations between the Lineshape method used by LEP and the approach adopted in this thesis offers a interesting field for analysis. In the Table 1.5 the post fit correlation between EW observables is displayed. The most interesting correlation in the context of the thesis is the one of m_Z and Γ_Z. It is evident that there is a small anti-correlation effect $\approx 2\%$.

LEP measurement utilized all available Z decay channels, hadronic and leptonic. In total available events were $\approx 17,221,000$. For ATLAS the available Z, without cuts, in data are: $\approx 41,000,000$ million. Even though ATLAS has a larger sample, the process of reconstructing the final state objects is expected to increase the systematic uncertainty contribution.

Chapter 2

LHC and the ATLAS Detector

Contents

In this Section the experimental setup is going to be analyzed. The analysis starts from the creation of the protons beams to be injected into the particle collider. Then a detailed examination of the ATLAS detector and its subsystems will be presented. Additionally, the interactions of particles with various detector components will be examined, with a special focus on muons. The reconstruction of muon candidates and the analysis of their tracks will also be thoroughly explored. Also trigger systems and data acquisition will be discussed.

2.1 The Large Hadron Collider

Large Hadron Collider(LHC) and ATLAS are experimental high energy physics machinery located in Genena Switzerland. LHC accelerates and collides hadrons and experiments like ATLAS analyze the outcome of the collisions, ref. [26]. In the LHC ring reside four particle

detector experiments: ATLAS, CMS, ALICE and LHCb. A small analysis of the LHC and the beam formation will take place in this subsection.

The collider resides in a circular tunnel, with a circumference of 26.7 km , at a depth from 50 to 175 mm underground. In the tunnel used to operate the Large Electron Collider (LEP). LHC operates from 2008 to today. It had delivered protons at different energies depending on the data taking period. During the first period (Run 1) the LHC derived protons at center of mass (c.o.m) energy of 7 and 8 TeV, the second period (Run 2) at c.o.m of 13 TeV and the third one at c.o.m. of 13.6 TeV.

For the protons to be collided in the LHC and at the position of the experiments a big chain of events take place. Beam has to be created, formulated in order to be stable in the ring and then accelerated to the energies required. Injection scheme is presented graphically in 2.1. First a cloud of protons is created by stripping the electrons from the atoms of a hydrogen gas using a strong electric field. Secondly, the protons are injected into linear particle accelerator Linac4, where they are accelerated to 160 MeV (red line in Figure 2.1). Next, they pass to Proton Synchrotron Booster (PSB), accelerated to 2 GeV and injected to Proton Synchrotron (PS) and accelareated to 26 GeV (green and blue circles in Figure 2.1). Before LHC, they are injected to Super Proton Synchrotron (SPS) to increase their energy to 450 GeV (red circle in 2.1). At LHC (blue circle in 2.1) they are accelerated to 13 TeV in the course of the Run-2 (7 and 8 TeV in Run-1 and 13.6 in Run-3).

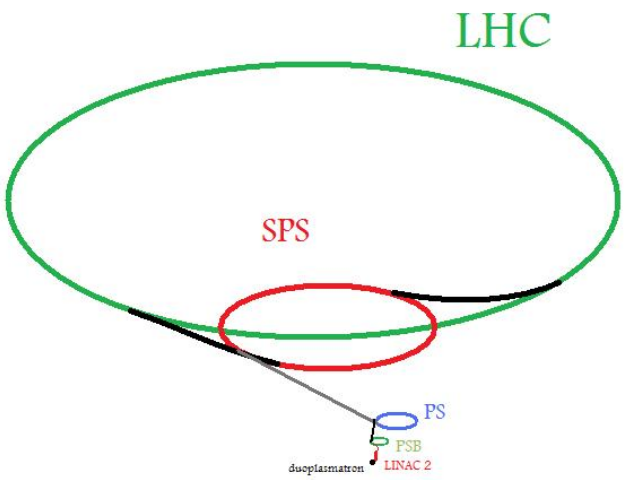

Figure 2.1: Proton injection scheme from Linac to LHC, taken from ref.[27]

In LHC there are two anti-parallel beam pipes, with beams traveling in the opposite direction. To accelerate and formulate the beam a complex system of magnet dipoles and quadruples is used. Dipoles are used for acceleration in each turn in the LHC where the quadruples are used for focusing. Also higher order magnets are used to correct beam imperfections.

The magnets are operating in superconducting phase in order to deliver the high values of magnetic field. Superconductivity is succeeded with cooling them at a temperature of 1.9 K using superfluid Helium-4.

2.2 ATLAS Detector

2.2.1 General Introduction

The ATLAS detector in LHC is a multipurpose subatomic particles detector based on energy and track reconstruction of charged particles passing though it's various sectors. ATLAS is

having three large subsystems: Inner Detector(ID), Calorimeters and Muon Spectrometer(MS). The detector is one of the largest in the world, it is composed from a barrel cylindrical section around the Interaction Point(IP) and two Endcaps an the detector proximity, having a total length of 46m and a radius of 25m. To measure the charged particle energy two magnet systems are used, which bend the charged particles. Energy is measured from the track curvature. To measure the energy of photons and other not charged particles a calorimeter system is used. All of these systems will be discussed thoroughly below. Since muons are interacting mainly in the Inner Detector and the Muon Spectrometer focus will be given on these systems.

There are three Runs, meaning three large data taking periods, in the history of ATLAS. Run 1 of the LHC spanned from 2009 to 2013 and achieved center of mass energy of 7 and 8 TeV. With the data collected (25 fb^{-1}) in Run 1 higgs boson was announced. Then Run 2 spanned from 2015 to 2018 which took place after upgrades both in detector, luminosity, software and algorithm level. Run 2 data (150 fb^{-1}) are going to be used in the context of this thesis. Run 2 achieved a center of mass energy of 13 TeV. Run 3 which is currently running achieved increased luminosity and center of mass energy 13.5 TeV. In the context of this thesis also shifts have been done in the experiment in Run 3 in trigger and run control desks.

The detector main parts are:

- **Inner Detector** is a tracker, which measures the bent trajectory of charged particles under the magnetic field and the primary and secondary interaction vertices.
- **Electromagnetic Calorimeter and Hadronic Calorimeter** are used for the detection of showers and jets, electromagnetic and hadronic respectively.
- **Muon Spectrometer** is a tracking detector of muons, consists mainly of Trigger systems.
- **Solenoid magnet** to bend the charged particles in the Inner Detector.
- **Toroid magnet** is used to bend muons in the Muon Spectrometer.

A rough analysis of the particle interaction is the following one. Charged particles transverse through the tracker, Inner Detector, leaving track hits. Then depending on their nature they are stopped in the Calorimeter. Electrons and pions are stopped almost completely in the Electromagnetic calorimeter. Hadrons deposit their energy in the Hadronic calorimeter. Photons do not interact with the tracker and leave a signal only in the calorimeter. Muons leave a track in the Inner Detector. Then interact faintly with the calorimeter depositing a small amount of energy and then leaving a clear signal in the muon spectrometer. The momentum measurement of the charged particles is possible by the usage a magnetic field in the Inner Detector and the Muon Spectrometer. Lastly, neutrinos escape the detector undetected, and their momentum and energy are measured indirectly. This is achieved by analyzing the final state signatures of the other particles involved in the interaction.

2.2.2 Coordinate System of ATLAS and associated variables

ATLAS coordinates is a very basic concept in order to understand the analysis as the kinematics of the reconstructed particles are based on the ATLAS coordinate system. In this subsection coordinates of ATLAS and associated variables used in the context of the thesis are presented.

ATLAS coordinate system is based on a right handed system with the origin at the Interaction Point(for x-y axis) and z axis along the beam pipe. At the transverse plain, the y axis points upward and the x axis from the Interaction Point to the center of LHC. The coordinate system is shown graphically in Figure 2.2.

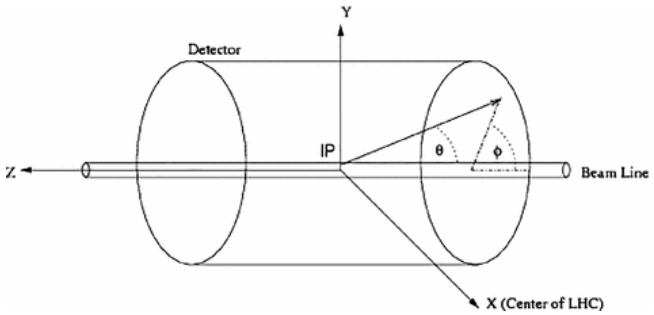

Figure 2.2: Coordinates System of ATLAS. IP at the center of the cylinder is the Interaction Point. θ is the angle from the beam z-axis. ϕ is the azimuthal angle in the transverse $\chi - y$ plane, with X pointing to LHC ring center, taken from ref.[28]

Usually, in ATLAS the analysis is performed in terms of angles. For the transverse plain, the angle ϕ is measured around the beam axis (z-axis) and has values: $0^o < \phi < 360^o$. The θ is the angle from the z-axis and has values: $0^o < \phi < 90^o$. Instead of θ ATLAS analyses usually use rapidity (Y) and pseudo-rapidity (η). Y advantage is it's invariance under Lorentz boosts along the beam axis. η is an approximation of rapidity, and under circumstances (when particle energy is significantly larger from it's mass) also is invariant under Lorentz boosts along the beam axis.

Rapidity is defined as:

$$Y = \frac{1}{2}\ln(\frac{E + p_Z}{E - p_Z}) \tag{2.1}$$

with E and p_Z energy and p_Z momentum at beam axis. Pseudo-rapidity is defined as:

$$\eta = \ln\tan(\frac{\theta}{2}) \tag{2.2}$$

where θ is the polar angle with respect to the beam axis. Pseudo-rapidity is important in the context of the ATLAS detector as detector systems have a strong dependence from η in terms of structure, performance, and reconstruction capabilities.

Other important variables used in ATLAS is the impact parameters: d_0 and z_0. They are defined as the perpendicular distance of the closest approach of a particle track to the primary vertex in the transverse plane (d_0) and along the beam axis (z_0). They are computed by using Inner Detector information.

The detector's performance varies across different segments, with certain regions excelling or under performing under specific conditions. The most significant distinction is among different η regions. This phenomenon originates in differences of the detector's structure and configuration across η regions, which also varies the precision of track reconstruction between these regions. Broadly, the detector can be grouped into three big η regions. Roughly the detector has three regions in η:

- Barrel: $|\eta| < 1.05$. It is the central part of the detector. It surrounds the beamline and at it's center is the interaction point.
- Intermediate: $1.05 < |\eta| < 1.4$. This intermediate region serves as a transition between the barrel and endcap regions. It handles particle trajectories that are at a moderate angle relative to the beamline. Measurements providing a blend of the measurement qualities from barrel and endcaps. Also magnetic field complicated shape makes the intermediate regions harder to simulate.

- Endcaps: $|\eta| > 1.4$. Systems positioned at the ends of the detector, the endcaps cover the forward and backward directions. They are optimized for tracks that are more parallel to the beam axis and play an important role in extending the detector's coverage to higher η values.

2.2.3 Magnetic Field

To measure the momenta and the charges of final state particles a magnetic field apparatus is used, ref.[29]. The magnetic systems have two geometries as displayed in Figure 2.3. It consists of a central superconductive solenoid and superconductive toroid systems:

- **Central Solenoid**: Cylindrical coil surrounds the Inner Detector, as shown in Figures 2.3a and 2.3b. It's axial length is 5.3 m and it's diameter 2.56 m. It's center coincides with the beam axis. It provides an axial magnetic field of 2 Tesla for the bending of charged particles in the Inner Detector. Particles from such a field are deflected in the transverse plain. The solenoid has been measured with a precise dedicated system inserted in the solenoid apparatus, ref. [30]. Due to the nature of the measurement one side of the structure was open, making the measured magnetic field asymmetric in the z (or η) direction. Corrections of magnetic field residuals are inserted, but a part of this asymmetry can be also absorbed in momentum calibration. Also according to experts the magnetic field in the solenoid is known to a precision of 0.5 mTesla and for a magnetic field of 2 Tesla, this means that the magnetic field is calculated with a precision of about 2%. This is also something to be addressed by the momentum calibration.

- **Toroid Magnets**: Toroid magnets have two different geometries as shown in Figure 2.3a. At the barrel $|\eta| < 1$, magnetic bending is provided by the large barrel toroid and at the endcaps $1.4 < |\eta| < 2.7$ two smaller toroid systems are added. The barrel and endcap magnets consists of eight superconductive coils each. The barrel coil length is 35.3 m and 5.4 m in height. In the end-cap there are two toroid systems positioned beyond the forward hadronic calorimeter. Toroid magnet systems generate a corresponding magnetic field in order to bend particles in the Muon Spectrometer, in the azimuthal plain. The main advantage of such a field is that it's direction is perpendicular to the direction of flight of the particles and deflects the particles in the η plain. The field varies in η due to interaction of the detector and support systems with the magnetic field. The shape of the magnetic field is displayed as a function of η in Figure 2.4. At the region $1 < |\eta| < 1.4$, usually referred as the transition region, muon tracks are deflected by a combination of the barrel and the endcap fields. The complex nature of the magnetic field in ATLAS increases the sensitivity of this region to potential mis-simulation of the magnetic field. Notably, there is a region, at $\eta \approx 1.4$ and ≈ 1.6 where the magnetic field reaches almost 0. This complex nature of the field in these regions is expected to be affecting also the muon momentum calibration, which is a main theme for this thesis.

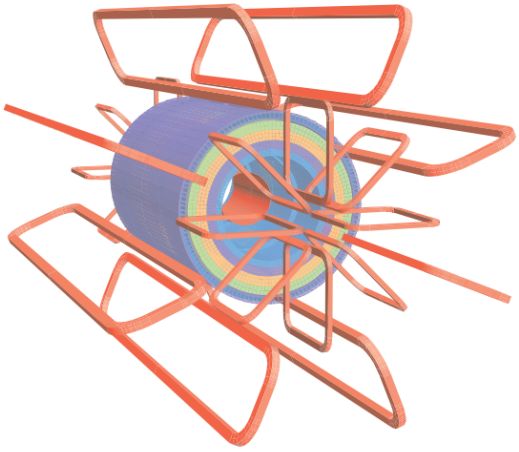

(a) Geometry of magnetic systems in ATLAS

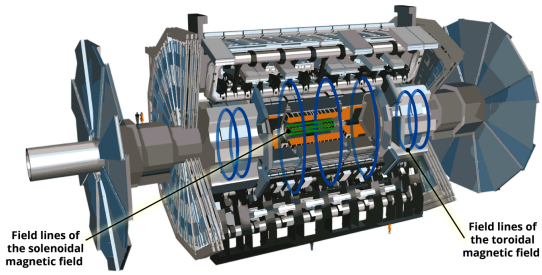

(b) Field Lines for the solenoid and toroidal field

Figure 2.3: Magnet systems a) and field lines b) in ATLAS, taken from ref.[31]

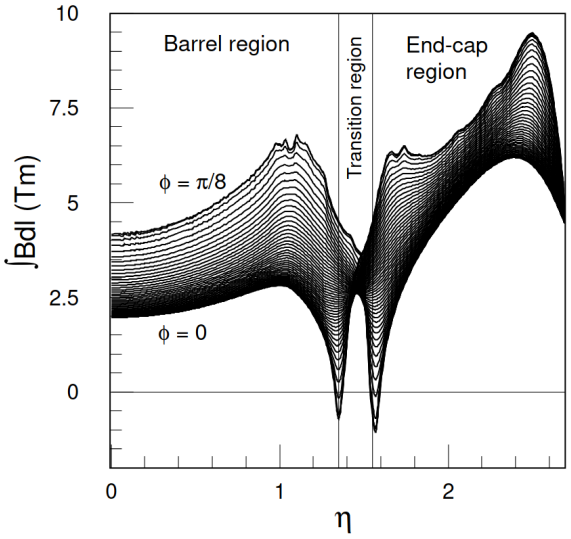

Figure 2.4: Toroid magnetic field integral as a function of detector η for different ϕ. Taken from ref. [32]

The magnetic field is calculated through a complicated procedure which is outside the scope of the thesis. It's precision influences the absolute accuracy of the momentum scale. In the muon spectrometer, the field is highly non-uniform, making it's calculation there particularly challenging. Non closures can introduce both strong muon momentum scale and resolution effects.

2.2.4 The Inner Detector

The Inner Detector (ID) is one of the most essential components of the ATLAS detector. It is designed for precise tracking and momentum measurements of charged particles and it is characterized of high spacial granularity. It's sub-systems in order from the inner to the outer part are : the Pixel Detector, the Semiconductor Tracker (SCT), and the Transition Radiation Tracker (TRT), each of these systems will be analyzed thoroughly in this subsection.

The ID has four main features are:

- Precise measurement of transverse momentum charge and impact parameter of the particles.
- Reconstruction of the primary and secondary vertex.
- Discrimination between electrons and photons, as the photon will not interact with the ID, in contrast with the electron which will be bent from the magnetic field and will give signal.
- Tagging of the b-jets and τ leptons.

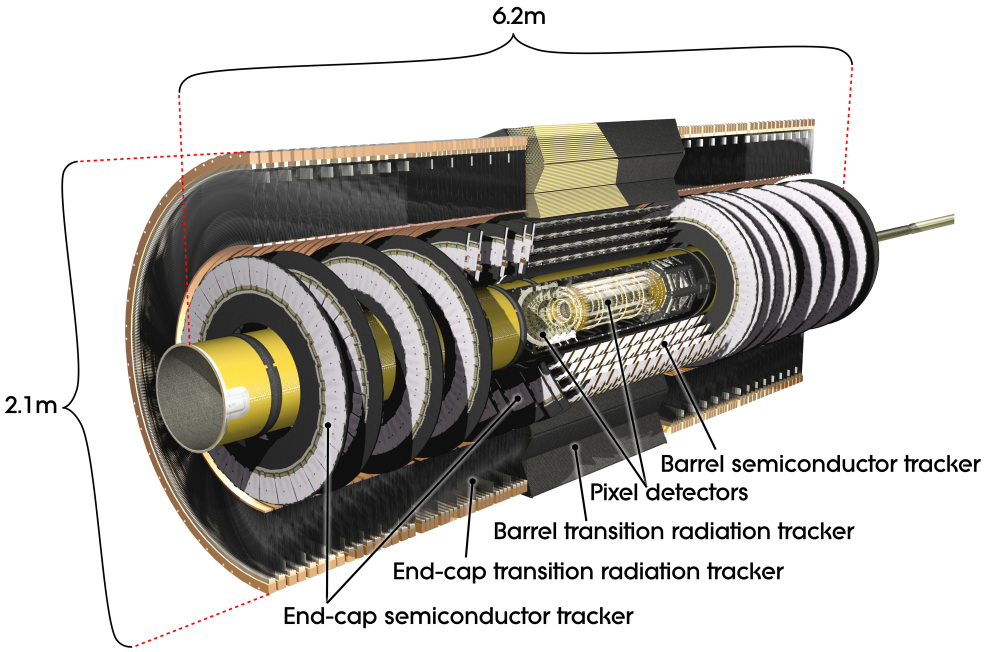

Figure 2.5: Inner Detector Graphic Representation, taken from ref. [33]

In the Figure 2.5 a detailed view of the Inner Detector is presented. Inner Detector shape is cylindrical with two distinct regions, the barrel and the endcaps. Diameter is 2.1 meters and length is 6.2 meters. Modules in the barrel are cylindrical where in the endcaps systems have disk structure. Barrel systems are the Pixel, Semiconductor tracker and Transition radation tracker.

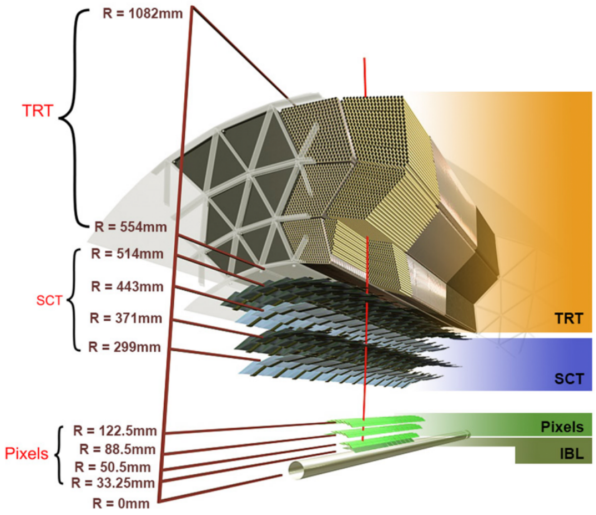

Figure 2.6: Detailed graphics of the barrel Region Modules in the Inner Detector, taken from ref. [52]

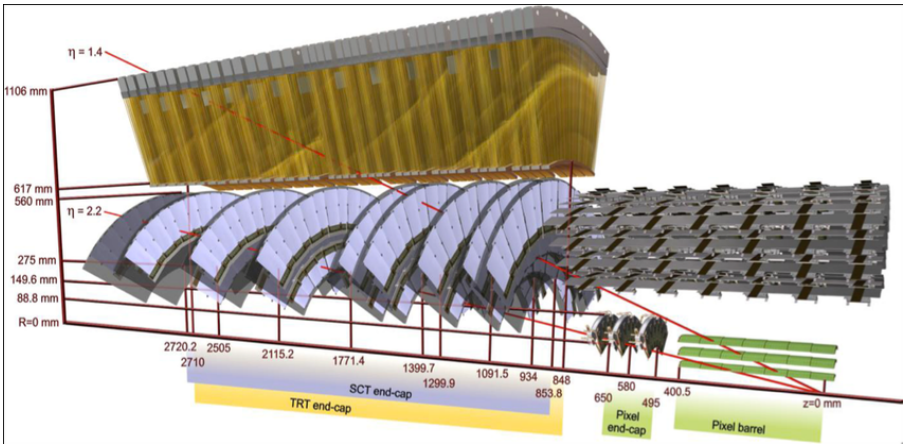

Figure 2.7: Detailed graphics of the End Caps Region Modules in the Inner Detector, while a 10 GeV charged particle transverse through it for different pseudorapidity values: 0.3, 1.4, 2.2, taken from ref. [34]

In Figure 2.6 the four layers of the Pixel detector is presented with green color starting only at 33.25 mm from the beam pipe center. Then the four layers of the SCT and finally the straws of the TRT are the largest in volume part of the Inner Detector.

Figure 2.7 provides a detailed representation of the Inner Detector in the endcaps, illustrating examples of a particle traversing through the detector. In the endcaps there are three Pixel disks near the interaction point. The structure of the SCT also changes at the end-caps at disk modules. The TRT being the outermost part does not have a different structure between barrel and endcaps.

2.2.4.1 Subsystems

All sub-systems are used for track reconstruction but only TRT give also particle identification information. Pixel and SCT use silicon 285 mm thick p^+ on n^- silicon sensors which give excellent track position information. TRT utilize gaseous detectors and transition material to obtain information on the particle type.

The **Silicon Pixel Detector** has the purpose of high precise measurements of tracks of charged particles at the proximity of the interaction point, only 3.3 mm from the LHC beam line. It consists from four layers of silicon pixels, 92 million overall, giving high spacial granularity, needing 1736 sensor modules for the Read Out. Pixel size is 50 x 400 μm^2 for the external layers and 50 x 250 μm^2 for the innermost layer (IBL). It's shape is cylindrical at the barrel region and it consists of five disks to cover the acceptance at the end-caps. In order to ensure the performance of the detector in conditions of heavy radiation the whole system of the Silicon Pixel Detector is cooled to $-10C^o$

The **Semiconductor Tracker** is made from 4088 modules of silicon strips grouped in four concentric layer-barrels and nine disks at the end-caps. In order to define a track point each barrel or disk gives two strip signals at a stereo angle which are combined to build a space-point. SCT outputs four space-points for the particles originating from the interaction region.

SCT consists of the barrel and the endcaps different sub-systems. In the barrel part it is consisted from 4 layers of silicon-strip sensors, with cylindrical models homocentric with their center being the the interaction point. At the endcaps region the SCT consists from 9 disks in each side.

Both Pixel and SCT suffer from radiation damage due to the pixel detector structure. Radiation can lead to damaged or dead pixels which reduces the efficiency of over times during ATLAS lifetime. Especially, during Run-2 which had elevated luminosity compared to Run-1 this effects was more significant. For example in the end of Run-2 charge collection efficiency at the Pixel detector dropped from 99 % to around 80% at the start of the Run-2.

The **Transition Tracker** is the third and outermost segment of the Inner Detector. The transition tracker is consisted from 300,000 drift tubes. The drift tubes contain a gas mixture of 70% Xe, 27% CO2 and a grounded wire. Passing charged particles ionise the gas and free electrons absorbed by the wire give rise to an electrical signal. The TRT information is used for track reconstruction but also provides information of the type of the particle passing. The spaces between the tubes are filled with polymer fibres (barrel) and foils (endcaps) to create transition radiation. The high relativistic particles have a probability of radiation emission as they transverse different material boundaries. This effect depends on the relativistic factor $\gamma = \frac{E}{m}$ and can be used for particle identification. In the context of ATLAS this is useful especially for charged pions and electrons passing through TRT, as the two type of particles have distinct response. For muons this feature is not that relevant since muons also have a reconstructed track in the muon spectrometer.

2.2.4.2 τ and b tagging

τ tagging is an important feature of the ID and is essential in the context of this thesis. Decays of Z bosons in $\tau\bar{\tau}$ events can influence heavily the Z mass measurement as their background shape in $m_{\mu\mu}$ distributions are similar to the signal shape.

The Inner Detector provides excellent and precise secondary vertex reconstruction. The τ has a short lifetime and decays in electrons and muons. Electrons deposit all their energy in the calorimeters so only the $\tau \to \mu$ is a plausible background. The τ events can't be identified by the displayed secondary vertex compared to the primary one due to their short τ lifetime. Therefore it is challenging with the current algorithms to differentiate $Z \to \tau t\bar{a}u$ from $Z \to \mu\bar{\mu}$ events.

b tagging is also essential for many physics analyses in ATLAS and also particularly in the context of this thesis, which is done by using primarily ID information. b-tagging, in this thesis, is useful as it enables differentiating between J/ψ mesons produced near the interaction point from direct gluon gluon fusion from J/ψ mesons produced at a displaced vertex originated from b physics. The above influence the calibration procedure used in the context of this thesis as

analyzed in Chapter 5.3. The procedure of b tagging is essential then to be understood in a primary level. b tagging is based on the properties of b-hadrons, lifetime and high mass.

High mass of b-hadrons lead to larger multiplicity in in final state compared to other processes. Furthermore, their lifetime: $\tau \approx 1.5$ ps lead to a decay length of $\approx 450\ \mu m$. Therefore, they travel several milliliters in the laboratory frame, before decaying, giving a largely displaced secondary vertex. To identify these displaced second vertices variables like the impact parameters are used. Impact parameter is the distance of closest approach of the track to the collision point— of the tracks of the charged particle decay products. They are calculated from the Inner Detector apparatus since it consists of the most precise tracking system of ATLAS. Their precise measurement is essential for the accurate reconstruction of kinematics and b tagging. The measurement uncertainty depend on the algorithm it self, the detector capabilities and the detector damage over time.

2.2.5 The Muon Spectrometer

The Muon Spectrometer (MS) resides at the the outermost part of the ATLAS detector. It's purpose is the muon identification, reconstruction and it is connected to dedicated triggers for muon detection. It's coverage is extended at forward regions of $\eta = 2.7$. Detector size is approximately 22 m in diameter and 44 m in length.

The MS consists of four types of sub-detectors. It's dedicated systems can do muon momentum measurements with a relative resolution of about 3% at low p_T^μ and about 10% for muons of $p_T^\mu \approx 1TeV$. Its operation is based on the magnetic deflection of muon tracks within a system of three superconducting air-core toroidal magnets. The magnetic field generated is toroidal, effectively deflecting particles in the $R - z$ plane.

The MS has two main purposes:

- Muon triggering and identification.
- Muon track reconstruction.

To achieve that, there are dedicated sub-detector systems consisting of precision and trigger systems. The detector systems in MS are: Resistive Plate Chambers (RPS), Thin Gap Chambers(TGC), Small-Strip Thin-Gap Chambers and Monitored Drift Tubes(MDT).

In the Figure 2.8 the MS structure in $x - y$ and $z - y$ plains is shown.

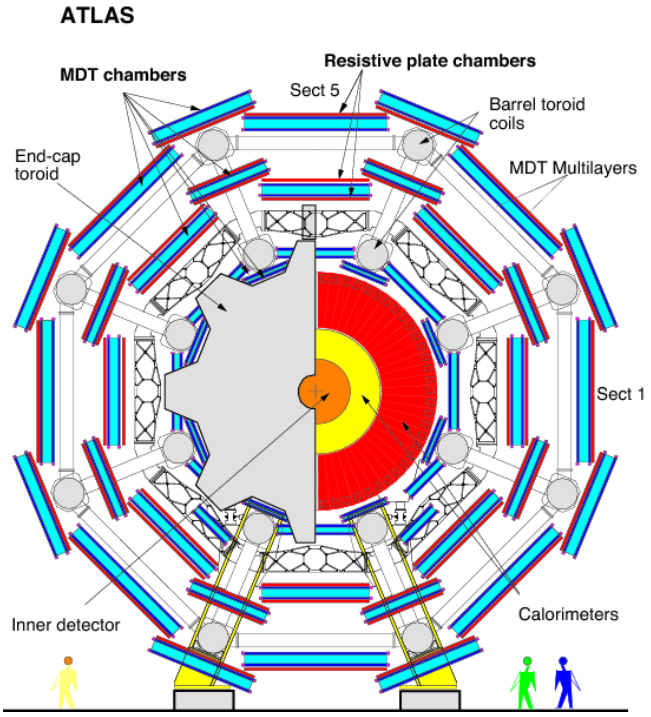

(a) Large Sectors

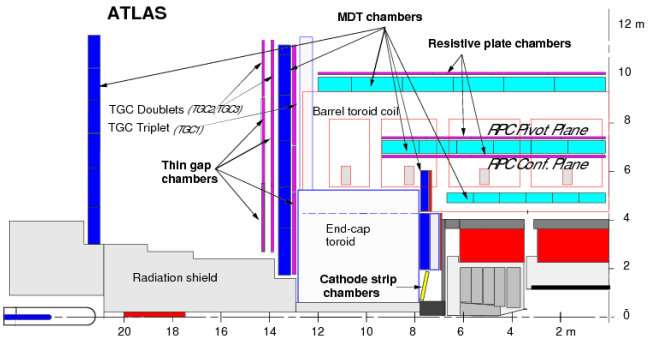

(b) Small Sectors

Figure 2.8: Schematic view of the muon spectrometer in the x-y (top) and z-y(bottom). Taken from ref. [35]

As shown in the Figure, the MS has an η and ϕ structure. It is separated in two group of systems geometrically. In η it consists of the barrel systems ($-1.05 < \eta < 1.05$) and the end-cap ($1.05 < |\eta| < 2.7$) systems. In Figure 2.8 (bottom) the barrel systems as designated with light blue and end-caps with deep blue.

The **barrel** systems have three stations, consisted from MDT and RPS chambers. The three cylindrical stations have a radius 5, 7.5 and 10 m respectively for the inner middle and outer stations. The **end-cap** systems are organized in concentric disks modules around the beam axis. Distance from interaction point is 7.4, 10.8 and 21.5 m. In the azimuth plane MS consists of 16 fold segments as shown in Figure 4.20a. The structures are arranged in Small and Large Sectors to follow the magnet arrangement. The Large Sectors cover the region between toroid coils in the barrel where the Small Sectors cover the azimuthal range of the coils.

In the barrel region, the precision measurement of the muon tracks is performed by the MDT's. Three stations of RPCs are used for trigger function, bunch-crossing identification and the second coordinate measurements. RPCs lie on the two sides of the MDT or only on the side below or above the outer MDT. This is presented in the top graph of Figure 2.8 with red lines as the RPC systems residing above the outermost blue squares(MDT) for the large sectors and below for the small sectors.

2.2.5.1 The Precision Chambers

The **MDT** system can detect the position of the muon as it transverses the tube with an accuracy of less than a 0.1 mm. They are composed of 3 cm wide aluminum tubes filled with a gas mixture. Muons ionize the gas as they transverse, producing a signal. The tubes are assembled into modules, with each module containing several layers of tubes to provide multiple measurements of the muon's position. Each MDT module provides 6 to 8 measurements in η along the muon track with a single hit resolution in the precision (r z bending) plane of about 80 μm. MDT is the main provider of muon tracks for the MS and it covers all the detector as shown in 4.20b.

The **CSC** are multi-wire proportional chambers with multiple layers of anode wires between cathode planes. CSC are filled with a gas mixture for the charged particle to ionize. Their key functions are triggering, precise spacial and time measurements. The measurement is done in r-z plane with a single hit resolution of about 60 μm and can provide a time measurement with a resolution of 3.6 ns. CSC are important at the forward region providing high granularity measurements for muons with small angles with respect to the beam axis.

2.2.5.2 The Trigger Chambers

The **RPC** systems are used for fast muon triggering and precise timing. They lie in the barrel region and the effectively cover the MDT modules. They consist from two charged parallel resistive plates, with a gas volume in between. Their fast response time allows correlation of detected particles with specific collision events. RPC also used for calculation of time of flight of muons in the detector.

The **TGC** are used mainly for Level 1 triggering in the forward η region: $1 < |\eta| < 2.4$. Also they are used for η, ϕ position measurements with an average spatial resolution of 5-10 mm. Their structure is similar to the CSC. The timing resolution of the TGCs, approximately 4 ns, is crucial for identifying bunch crossings.

2.2.5.3 Muon Triggers

The trigger coverage is shown at the Figure 4.20b. The trigger system achieves 99% coverage in the end-cap region but only 80% coverage in the barrel region ($|\eta| < 0.1$). This reduced coverage in the barrel is due to limited detector presence in areas occupied by cabling and channel-processing technical machinery. In the barrel region the muon trigger is based at the hits in the RPC. In the end-cap the muon trigger is based on the hits in the TGC of the middle layer, called the Big Wheel.

The high p_T^μ triggers are used for single muon signatures, while the low p_T^μ triggers are used in coincidence with other trigger objects to select multi-muon events. In the context of this thesis, di-muon triggers are the most essential, due to the signal: $Z \to \mu\mu$.

There is a series of background processes firing muon triggers in the Muon Spectrometer. These processes can be showers not fully contained in the calorimeter, cosmic rays, low momentum charged particles originating from the end-cap toroid magnets and beam shielding. All these processes have different time characteristics compared to muons produced in the pp collisions. Therefore to reduce background to the L1 system coincidence algorithms are applied. To suppress the background there is a coincidence requirement between the Big Wheel TGC and end-caps TGC.

2.2.6 Calorimeters

The ATLAS calorimeters play a important role for the precise measurement of particle energies and identification. Particles loose energy as they transverse the calorimeters with various way depending on particle type and energy. This energy lost is measured providing information on the particle kinematic properties. Using different techniques and materials calorimeters measure electron, pion, jets and photon energy. Total calorimeter coverage in ATLAS is $|\eta| < 4.9$, with various subsystems included.

Calorimeter technology is based on a simple principle. The particles charged or not charged enter a dense material, where they are forced to decay and create showers. Secondly, there is also "active" material, which collect the energy emitted through ionization of the charged final state particles, mostly electrons. This kind of calorimeter is called sampling calorimeter. Depending on experimental apparatus also the dense material can be dropped and only an "active" one can be used. These calorimeters are called uniform. There two kind of showers, electromagnetic and hadronic ones. In the electromagnetic, main mechanism is the pair production of photons and the ionization and Bremsstrahlung from electrons. In the ATLAS energy regime, main mechanism being Bremsstrahlung for electrons at the start of the electromagnetic shower and ionization for the ones produced at the end of it. In hadronic showers main mechanism is QCD interactions between the hadron and the nucleus of the dense material. Hadronic showers are more complex and have a non trivial internal structure. They also include smaller electromagnetic showers from photons and electrons emitted. Different kind of materials and different kind of configurations promote electromagnetic or hadronic showers. In ATLAS there two different systems for the two kind of showers: the Electromagnetic Calorimeter (ECAL) and the Hadronic Calorimeter(HCAL).

Active materials used in the calorimeters are Liquid Argon(LAr) and Crystal scintillators. Each with individual advantages and drawbacks. LAr offers detector uniformity, radiation resistance, high granularity. Drawbacks are of technical nature with the most significant being the fact that LAr must be kept in extremely low temperature to remain liquid. Advantages of Crystal scintillators are also mainly of technical nature. Their cost being the most important. One problem they encounter is the damage done to the crystal and it's scintillation capabilities deterioration in hard radiation environments.

General structure of the whole calorimeter system from the center to the outermost part is:

1. Presampler: Active Material to correct for energy loss before the calorimeter.
2. Strip Layer: Active Material strips with high spatial granularity.
3. ECAL: Electromagnetic calorimeter.
4. HCAL: Hadronic calorimeter.

Presampler is a system positioned in front of the calorimeters, surrounding the Inner Detector, to correct for energy lost by the particles before they enter in the calorimeter. Presampler is essential to measure accurately the total energy of the particles which deposit their energy in the calorimeter. It consists of a thin layer of active material (Liquid Argon). By measuring energy deposited in the Presampler and combining information from Inner Detector trajectories an estimation is derived on the particle energy before it enter the calorimeter. The exact algorithm is outside the scope of this thesis.

Second in order is the **Strip Layer**. This is a thin layer of fine cells of active material of Liquid Argon which provide high spatial granularity. Strip layer provides the connection of energy bulks in the calorimeter with particle individual trajectories. One of the most significant functions of the Strip Layer is the separation of π^0 and γ. π^0 decay into two photons. If the

granularity is not high enough the two photons can be identified as one single photon. Strip Layer allows for that separation. Strip layer cover only the region: $|\eta| < 1.8$.

The **ECAL**, third in order, is responsible for the measurement of the energies of electrons, pions and photons. It is a sampling calorimeter and consists of layers of lead absorbers interleaved with layers of active material, Liquid Argon (LAr), which produces signals proportional to the energy deposited by particles. Photons are forced to pair production and the electrons to emit Bremm radiation in the dense lead. Electrons and photons as they interact with ECAL create electromagnetic showers, and therefore their whole energy is deposited in the calorimeter. ECAL is divided in small cells which provide a three-dimensional granularity. It is divided into barrel ($|\eta| < 1.475$) and two endcaps ($1.375 < |\eta| < 3.2$) parts. It's structure is often mentioned as accordion like. Cells are placed in alternating order in respect with lead absorbers, read out electrodes and liquid argon in order to ensure there are no cracks in azimuth plain.

The **HCAL** surrounds the ECAL and it is designed to measure the energy of hadrons such as protons, neutrons, and mesons. The HCAL utilizes dense materials such as steel or scintillating tiles interspersed with layers of active material, typically either scintillating plastic or gaseous detectors, to capture and measure the energy of hadronic showers. Further analysis of the hadronic showers are considered out the context of the thesis.

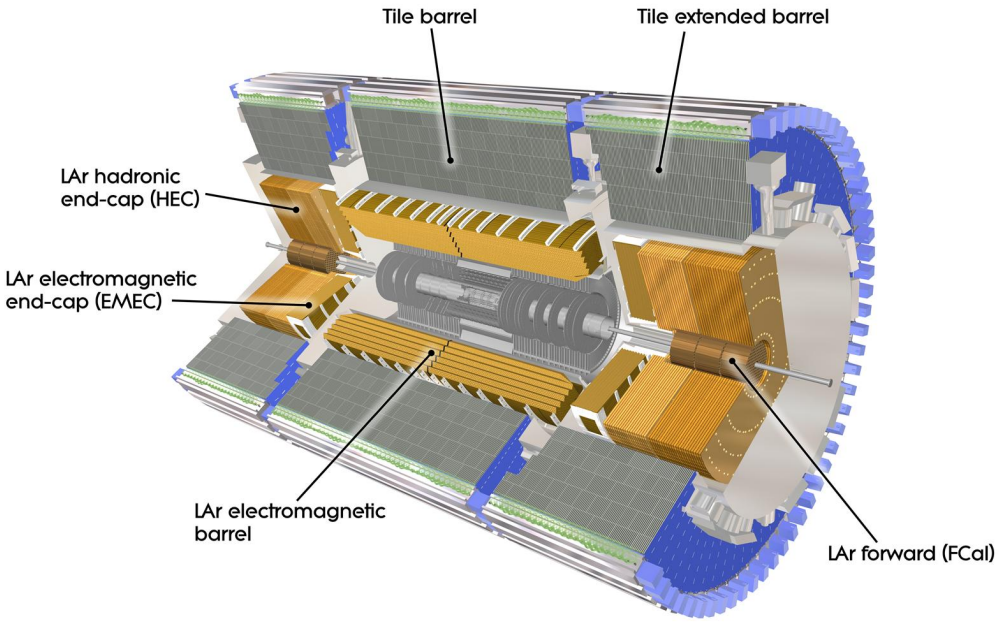

Figure 2.9: ATLAS Calorimeter systems. Taken from ref.[37]

When a muon passes through the calorimeter system, it typically leaves behind a small amount of energy due to ionization and minimal electromagnetic interactions. This energy deposition is usually much smaller compared to that of electrons or hadrons, making muons appear as minimally ionizing particles within the calorimeter. The usual ammount of energy deposit in ≈ 3 GeV.

2.3 Trigger and Data Acquisition

In the context of particle physics, a "trigger" is a system designed to select interesting events from the vast number of final state particles occurring after the initial state collisions. A trigger is a mixture of hardware and software algorithms that decides which events are to be kept in the

data storage. The trigger system also categorizes events into different groups based on specific physics analysis goals, streamlining the final analysis process. This categorization ensures that data relevant to various research objectives are grouped, making the final physics analysis more manageable and effective. The Trigger in the Run-2 configuration have two levels:

- **Level 1 (L1)**: The first stage of event selection in ATLAS. It's purpose is to make quick decisions using information from the Calorimeters and the Muon Spectrometer. It's primary use is the fast decision making. The L1 trigger is capable of making rapid decisions within a small time margin of about 2.5 μs per event, corresponding to the bunch crossing rate of 40 MHz at the LHC. At it's hardware side it uses Field-Programmable Gate Arrays (FPGAs) and Application-Specific Integrated Circuits (ASICs) to achieve the required speed and flexibility.

- **High-Level Trigger (HLT)**: The second level of trigger. Receives the events selected by the Level-1 trigger and utilizes detector information from all sub-detectors, including the calorimeters, muon systems, tracking detectors, and other specialized detectors. The HLT is doing a more sophisticated analysis of each event and it is capable of running on more complex algorithms to distinguish between different processes. The HLT is running using CPUs (Central Processing Units) and GPUs (Graphics Processing Units) for its computations.

HLT plays a crucial role as it can categorize the events based on their signature to different physics streams. That way events can be categorized for different research purposes as b-physics, Higgs physics, SM and all the categories ATLAS experiment is interested in.

In the context of this analysis, single and double muon trigger are of interest and Physics Main B physics streams, as Physics Mains includes a lot of Z events and B Physics stream is rich in J/ψ and Υ mesons.

One significant aspect of the trigger system is the pre-scale system. Pre-scale method is an algorithm which selectively reduce the rate at which certain types of events are recorded. Some processes which are not interesting to new physics in the context of ATLAS are considered not essential and therefore not all of them are recorder. A pre-scale is essentially a number which indicates how many candidate events are going to be rejected and not recorded. A pre-scale is applied on a specific trigger which is sensitive to the "uninteresting" processes. It can vary within a single run and across different data-taking campaigns. As the trigger definitions evolve, pre-scales are adjusted accordingly to optimize the data collection process. Pre-scale is a fraction: $\frac{1}{X}$ which means that one event is going to be recorder for every X event candidates firing the trigger.

In Figure 2.10 the comparison of Physics and B-Physics streams in terms of output rate, as a function of different campaigns of Run-2 (2016,2017,2018). In 2016 the relevant triggers for b-physics are heavily pre-scaled making the contributions from Physics Main and B Physics comparable. In 2017 and 2018 triggers related to b-physics are not pre-scaled and therefore the contribution of B Physics Stream is larger compared to Physics Main one.

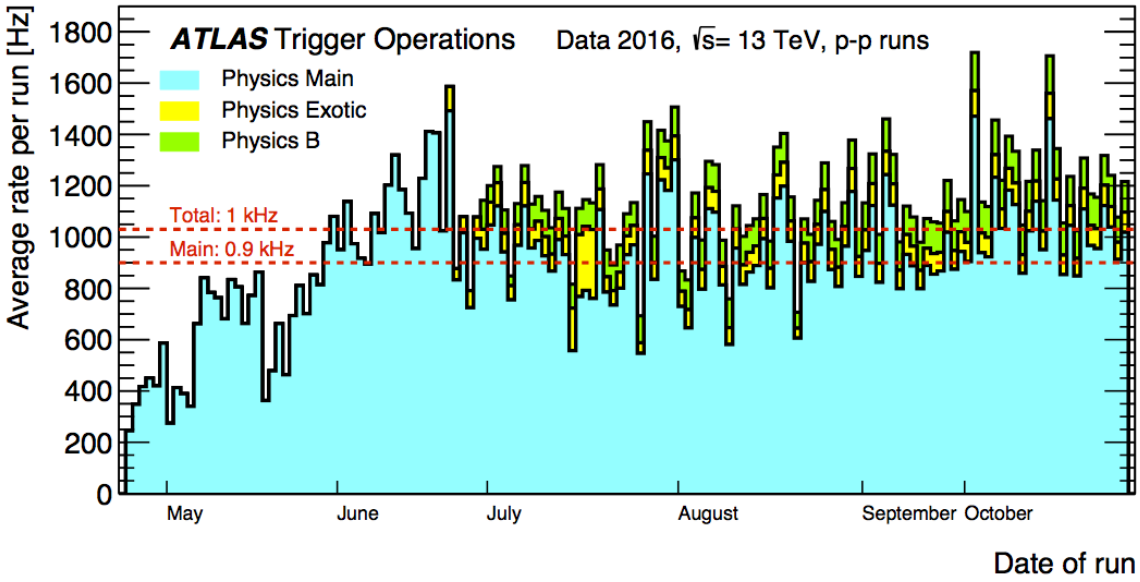

(a) Physics Main, B Physics and Exotic streams rates per run for 2016

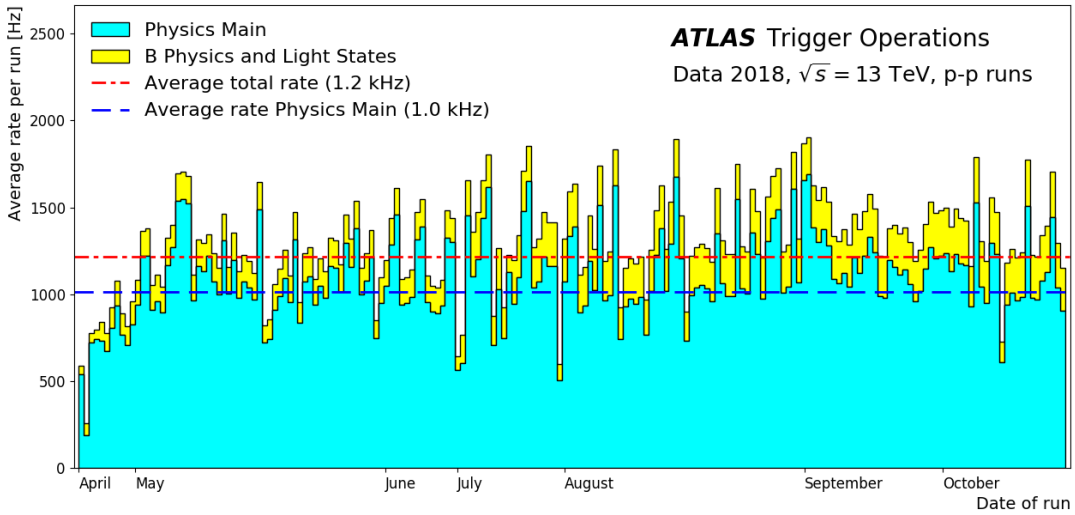

(b) Physics Main, B Physics streams rates per run for 2018

Figure 2.10: Physics Main and B Physics streams for Run-2 taken from ref.[38]. 2017 is displayed as it is similar to 2018.

2.3.0.1 Trigger Matching and Passing

Trigger passing and matching are two offline selections connected to trigger configurations.

Trigger passing: Trigger passing refers to the kinematic selection corresponding to the trigger. In the context of ATLAS the majority of triggers have a p_T^{μ} selection. Also a trigger can have a selection on the number of final state particles in a process or a mass selection. When an event is selected by the trigger then it means it "passes" the kinematic selection. The trigger passing can influence heavily kinematic distributions.

Trigger Matching: Trigger matching is a process of matching objects in an event that have passed the trigger system with objects that are reconstructed offline during the event reconstruction stage. For this process dedicated algorithms are utilized. The trigger matching

mainly influences the normalization and has little effect on kinematic distributions.

2.4 Track Reconstruction

2.4.1 Helix Parameters

In this subsection a small introduction on general track reconstruction is going to take place. Electron reconstruction is going to be discussed shortly and a detailed muon reconstruction is presented in Chapter 2.5.

Tracks in the context of the ATLAS experiment are particle trajectories as they are reconstructed after passing the detector. Track is, in principle, a mathematical representation of the trajectory, derived using information from various detector parts. Direct track information in ATLAS are provided by the Inner Detector and the Muon Spectrometer. Utilizing different algorithms and considering different detector parts, the fitted track can vary.

Track reconstruction of a particle passing through the detector is parameterized by 5 parameters, which are necessary for describing a helix trajectory. In the ATLAS terminology, these parameters are commonly referred to as the helix parameters. As the particle leave hits-signals in the detector and it's trajectory is bent by the magnetic field the following parameters are fitted during tracking:

- Curvature $\frac{q}{|p|}$. This represents the charge divided by it's reconstructed momentum and it is equal to $\frac{q}{|p|} = \frac{1}{B \times r}$, where B is magnetic field strength and r radius of particle helix movement in magnetic field.
- Transverse impact parameter d_0. This represents the distance of the particle vertex from the beam axis in the transverse plain, as shown in Figure 2.11.
- Longitudinal impact parameter z_0. This represents the distance of the particle vertex from the interaction point in the longitudinal plain, as shown in Figure 2.11.
- ϕ_0 represents the azimuth angle.
- θ represents the polar angle.

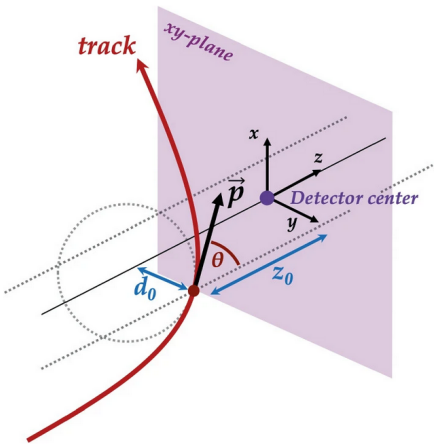

Figure 2.11: Impact Parameters sketch: transverse d_0 and longitudinal z_0, with the atlas coordinate system, Taken from ref.[39].

As particles traverse the detector, they leave a track path. From this track, the helix parameters are determined using a global χ^2 fit. The uncertainties in these parameters are estimated from the covariance matrix of the fit.

2.4.2 Track Reconstruction in the Inner Detector

Track reconstruction in the Inner Detector measures the impact parameters and momentum of charged particles. Main algorithm works from the center of the detector to the outermost parts and it is usually referred as inside-out. It associates first the silicon hits and then extrapolating the trajectory to the TRT. Tracks with a minimum number of silicon hits and the ones passing a cut in the transverse and longitudinal impact parameter are kept. Main steps in the inside - out algorithm is :

1. Formation of Space Points: Creation of clusters of hit space points of Pixel, SCT and TRT detectors.

2. Track reconstruction seeded by space points: First space points are grouped in sets. Sets of three space-points form a seed using information either from Pixel-only, SCT-only or Pixel and SCT mixed seed. A selection is implemented in each seed depending on p_T^{μ}, impact parameter resolution criteria. Seeds track are required to match a forth point with an extrapolated trajectory.

3. Out of all the seeds tested, many are excluded. Among those that are selected, some are more likely to correspond to an actual trajectory. Seeds are getting ranked based on the probability to correspond to a real track. This systems favors tracks with a higher score. An additional neural network clustering algorithm has been implemented for the Pixel clusters to separate multiple particle tracks in dense environments.

4. TRT track extension: Candidate trajectories with the highest ranking score are extrapolated to TRT and a valid set of matching drift circles is matched to the trajectory, if they exist. To improve the momentum resolution the track is refitted using all information from Pixel, SCT and TRT combined hits.

2.4.3 Track Extrapolation

In order to match muon tracks through different detector segments there is a dedicated track extrapolation algorithm ref.[40]. This algorithm "transports" the muon track through the magnetic field by solving the equation of motion of the particle.

$$\frac{d^2\mathbf{r}}{ds^2} = \frac{q}{p}\frac{d\mathbf{r}}{ds} \times \mathbf{B}(\mathbf{r}) + g(p, \mathbf{r})\frac{d\mathbf{r}}{ds}, \tag{2.3}$$

where represents the position of the particle along the trajectory s, s is the trajectory, q is the muon (or anti-muon) charge, B is the magnetic field and g(p,r) is an energy loss function. As the muon transverses through intermediate material the algorithm takes into account the augmentation of the error of track parameters from material effects.

2.4.4 Muon momentum resolution

Muon momentum measurement has a corresponding uncertainty. This uncertainty is parametrized by the experiments special conditions. In ATLAS a standard high energy physics experiment is followed, ref.[41].

Ionization Muons deposit energy as they transverse material through ionization. Muons in the energy range of ATLAS are considered minimum ionizing particles. Their energy loss depends on the material. In the inner detector the energy loss in insignificant. In the calorimeters, where denser material is present, they can loose up to 3 GeV through ionization. The energy loss of charged particles is given by the simplified Bethe Bloch formula ref. [42]:

$$-\frac{dE}{dx} = C_1\beta^2 \cdot \left(\ln\left(C_2 \cdot \beta^2\gamma^2\right) - \beta^2\right) \tag{2.4}$$

with C_1 and C_2 constants connected to material and electromagnetic interaction, β the fraction of speed of light of the particle and γ the relativistic Lorentz factor. For small energies this term is dominant and tends to be constant in larger energies.

Multiple Scattering Charged particles scatter in material, interacting electromagnetically with the nucleus of the material. It has been proven that multiple scattering is independent from energy of the charged particle and it is dependent from the thickness and the radiation length of the material, ref.[43].

Magnetic Field The magnetic field is utilized to bend the particles, allowing their momentum to be calculated from the curvature of their trajectory. For particles with lower energy and in the presence of a stronger magnetic field, the curvature is larger, leading to a more accurate momentum measurement. Conversely, for particles with higher energy or in a weaker magnetic field, the curvature is smaller, resulting in less accurate momentum measurements. This resolution term is called also intrinsic resolution term. The momentum and it's uncertainty of a charged particle is measured through the Sagitta s:

$$p = \frac{L^2qB}{8s} \rightarrow \sigma_p = \sqrt{\left(\frac{p}{2L}\sigma_L\right)^2 + \left(\frac{p}{s}\sigma_s\right)^2 + \left(\frac{p}{B}\sigma_B\right)^2} \tag{2.5}$$

where L is the is the distance between the outermost measurements of the tracking system and B the magnetic field strength. By assuming that the uncertainty of the magnetic field strength and the distance L is negligible:

$$\sigma_p = \sqrt{\left(\frac{p}{s}\sigma_s\right)^2} \rightarrow \frac{\sigma_p}{p} = \frac{8p}{L^2qB}\sigma_s \tag{2.6}$$

Therefore, the relative momentum uncertainty is proportional to the momentum of the muon and inverse proportional to the magnetic field.

Combining ionization, multiple scattering and magnetic field effects, the relative uncertainty of transverse momentum is:

$$\frac{\sigma_{p_T^\mu}}{p_T^\mu} = \sqrt{\left(\frac{r_0}{p_T^\mu}\right)^2 + r_1^2 + (r_2 \cdot p_T^\mu)^2} \tag{2.7}$$

Relative momentum uncertainty of ATLAS is about 3% over a wide range of p_T^μ, reaching 10% at $p_T^\mu = 1$ TeV. Depending on the detector part used for the track reconstruction the relative uncertainty can vary, as explained in Section 2.5.

2.5 Muons in ATLAS, tracking and reconstruction

Muons are charged particles which transverse the whole detector and they exit without decaying. Their track is reconstructed by using their hits in the Inner Detector and the Muon Spectrometer. Also they interact with the electromagnetic and hadronic calorimeters leaving a minimum amount of energy. In the context of this analysis the understanding of the muon properties and their interaction with ATLAS is essential as both the J/ψ (which is going to be used for calibration in the context of this thesis) and the Z resonances, decay to muon pairs. In the following subsection the reconstruction and the identification of muon objects in ATLAS are presented. Muon reconstruction in the Inner Detector is analyzed thoroughly in the Chapter 2.2.4.

Muon originate from various processes, including Drell-Yann or b- physics. They transverse through the detector interacting with multiple parts while their trajectories are bent from the magnetic field. In the Inner Detector they leave track signals but they loose almost no energy. As they pass from the calorimeter system they deposit a small amount of energy and finally they leave track hits in the Muon Spectrometer System.

Muons can loose energy with ionization, Brehmsstralung and pair production. In ATLAS, muons loose a small percentage of their energy in calorimeters with ionization. For the muons investigated in this thesis which is above 4 GeV, the muon energy is enough to have reached the plateau of the Beth-Bloch formula and therefore the contribution of this is almost independent with the p_T^μ of the muon.

2.5.1 Muon Track Types

Different components of the detector and various reconstruction algorithms yield distinct muon track types, such as Inner Detector (ID), Muon Spectrometer (MS or ME), and Combined (CB) tracks. This diversity affects the analysis by influencing the physics objects themselves, reconstruction efficiency, and background rejection. The choice of detector components used for muon track reconstruction directly impacts the precision and accuracy of muon measurements, which are critical for achieving reliable analysis results. Each part of the ATLAS Detector has its strengths and limitations in terms of spatial resolution, momentum resolution, and coverage. The Inner Detector provides excellent momentum resolution for low momentum muons and precise tracking information in the barrel region of the detector but it's capabilities deteriorate in the end-caps. The Muon Spectrometer is specifically designed for detecting and measuring the momentum of muons and have advanced muon reconstruction capabilities in the end-caps regions.

Also discriminating signal muons from background particles is crucial for any muon analysis. Different detector parts have different capabilities in identifying and rejecting background particles. For instance, the Inner Detector can provide precise track reconstruction and vertexing, allowing for efficient rejection of background tracks originating from proton-proton collisions. Meanwhile, the Muon Spectrometer can identify muons based on their energy deposition and track curvature in the magnetic field, aiding in the rejection of non-muon background particles.

In order to achieve the precision goal of the Z boson mass measurement the reconstruction of muons and the efficiency of the various ATLAS detector parts have to be understood. The muon candidates tracks can be reconstructed in the following ways:

- Inner Detector(ID): Hits used only from the Inner Detector to reconstruct tracks pointing to muon chamber hits.
- Muon Spectrometer(MS and ME): **MS**:Hits used only from the Muon spectrometer to reconstruct track. MS is the track as it is fitted in the Muon Spectrometer. Close hits in

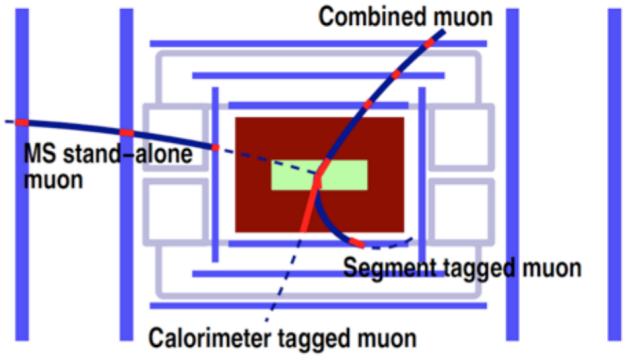

Figure 2.12: Muon reconstruction algorithm examples, red lines depict the track hits used for the corresponding reconstruction algorithm. Taken from ref.[44].

the MDT chambers are fitted to produce segments. Each chamber produce a segment. Finally the segments from three chambers are used to reconstruct a track. **ME**: MS tracks are projected back to the interaction point and refitted with a relaxed constraint, incorporating the energy loss in the calorimeter.

- Combined(CB): Combined muons are reconstructed by matching ME tracks and ID tracks, combining them with a global χ^2 fit. The algorithm is following an *outside-in* path. The information from MS is used to begin the muon reconstruction seed algorithm and at as a second step the algorithm moves to the ID part. In order to achieve the best possible momentum resolution, the hits at the muon system are updated using information from the combined fit. This improves the the expected errors of the hits and finally the CB muon is reconstructed.

- Segment tagged(ST): muons consist of a fitted ID track and a MS segment track

- Calorimeter tagged(CT): muons consist of a fitted ID track and an energy deposit in the calorimeters.

In Figure 2.12 these reconstruction algorithms examples are displayed for hypothetical muons passing through the detector.

In Figure 2.13 the relative uncertainty on p_T^{μ} using cosmic rays data is compared for ID, CB and MS tracks.

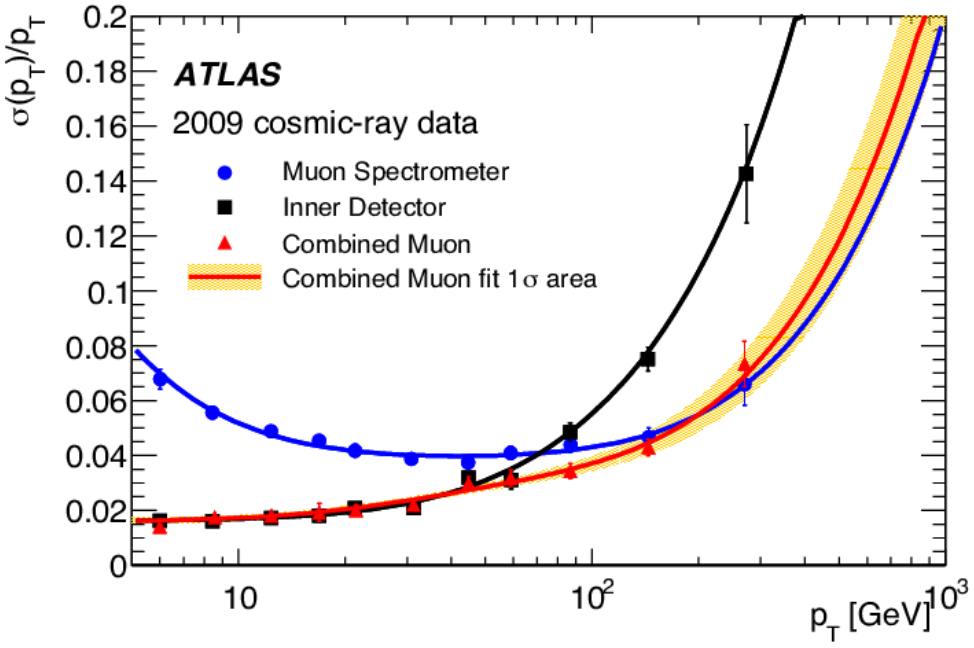

Figure 2.13: Comparison of ATLAS muon track relative uncertainty for 2009 cosmic muon rays for different reconstruction algorithms, ID, MS and CB. Taken from ref.[45].

ID tracks (black dots) in smaller energies (from $p_T^\mu = 0$ to $\approx$ 70 GeV) have a better p_T^μ resolution compared to CB and MS tracks. In Figure 2.13 it is evident that the ID is the best option in the p_T^μ regime ($6GeV < p_T^\mu < 100GeV$) of the analysis (for J/ψ calibration and Z mass measurement). CB tracks in low p_T^μ are comparable to the ID ones. Depending on the detector region and p_T^μ regime, CB tracks show similarities to either the ID or the MS. In the barrel region, where the ID performs better, CB tracks resemble the ID tracks. In the end-cap, where the MS demonstrates better performance, the CB behavior resembles the MS tracks.

The combined reconstruction using information from both the ID and MS, exploiting their complementary advantages, improves the overall muon reconstruction efficiency and accuracy. The CB tracks then use the advantages of both. CB tracks are excellent for generic studies which include muons. For the level of precision required, however, their dependence on MS tracks makes them unsuitable for this analysis.

Chapter 3

Muon Calibration in ATLAS

Contents

Muon momentum measurement is a crucial part in ATLAS analyses. However, the accuracy of these measurements can be sensitive to biases due to detector imperfections, reconstruction algorithms and false simulation of the detector properties. Understanding and correcting these biases is essential for ensuring the precision of physics results obtained. Biases in muon momentum measurements can have significant implications for physics analyses. They can distort the shape of invariant mass distributions, affect the reconstruction efficiency of certain decay channels, and introduce systematic uncertainties in cross-section measurements. Inaccurate momentum measurements can lead to misinterpretation of physics signals, "hide" the discovery potential of new particles, and decrease the precision of fundamental parameter measurements. For sensitive measurements, such as the Z mass measurement, accuracy and precision are crucial.

Addressing muon momentum biases requires a multi step procedure involving detector calibration, alignment procedures, and advanced reconstruction algorithms, ref. [46]. Calibration techniques use known particle resonances to validate the result of the muon momentum measurement, known also as "standard candles". Alignment procedures ensure the proper alignment of detector components, reducing spatial distortions and mis-alignments. Advanced reconstruction algorithms, including track fitting and momentum estimation techniques, aim to minimize biases introduced during track reconstruction.

During alignment a correction is derived by minimizing a global χ^2 of track-hit residuals. After alignment, where the track has been corrected ensuring that the particle track has a spiral path, there are still remaining biases to be addressed. This method is "blind" to misalignment called "weak modes". These biases are addressed by momentum calibration. In calibration, there two groups of biases that are corrected, one charge dependent due to rotations of the detector, and charge independent effects which are mostly due to magnetic field mis-modeling and stochastic nature of processes such as muon energy losses in the calorimeter and multiple scattering.

3.1 Charge Dependent effects

A crucial bias is the charge dependent bias due to detector rotations in the transverse plain. These distortions introduce a bias to the Sagitta measured during tracking, which due to the influence of the magnetic field have opposite effects on negative and positive charged particles. This bias is corrected by introducing Sagitta bias correction. Essentially the assumed position of different detector parts are shifted and rotated in order to measure afterwards the correct position of the particle. In practice, the correction corrects the p_T^{μ} charged particle tracks in data, as if the detector was not rotated.

The Sagitta correction is a complicated process since different detector parts in the Inner Detector and the Muon Spectrometer can be shifted in different angles. Therefore, maps of the corrections are extracted with a dedicated fit and a fine η and ϕ binning. The maps correct the momentum independently of ID, CB and ME tracks. Essentially the correction is the angle of the rotation.

Due to the magnetic field, a rotation of the detector has an opposite effect on the negative and positive muons. One has a reconstructed track with lesser curvature and one with larger curvature than the real track. This leads to a charge dependent effect.

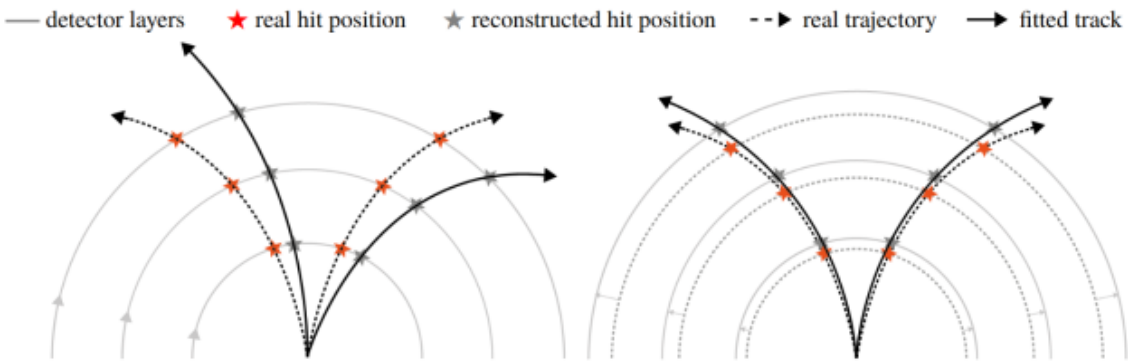

Figure 3.1: Two different kind of distortion effects on the transverse plain of the detector. The left one corresponds to sagitta bias, charge dependent and rotation effects. The right one corresponds to charge-independent, radial displacement and magnetic field effects. Taken from ref. [47]

In figure 3.1 the effect of the sagitta bias on the track reconstruction is shown on the left graph. The rotation angle between the two daughter particles in the graph is the same, but because one will get reconstructed with less curvature (left black line) and the other one with more curvature (right black line) the effect will be opposite on the two opposite charged particles.

If one detector module is rotated with a small rotation a the unbiased Sagitta is connected with the biased one with the relation:

$$s^{bias} = s + qda$$

where q is the charge of the track, and d is the distance from the origin to the second layer of the detector. The radius of the track ρ, is going to be biased ρ_{biased} in the following way:

$$\frac{1}{\rho_T} = \frac{1}{\rho} + q\frac{8da}{l^2}$$

Since p_T^{μ} is proportional to the magnetic field and the radius of the track $B \times \rho$ and if ignoring magnetic field biases the biased p_T^{μ} of the particle can be expressed as:

$$\frac{1}{p_T^{biased}} = \frac{1}{p_T} - q * \delta_s$$

where δ_s is a quantity that corresponds to the impact of the Sagitta bias measurement to the q/p_T and p_T^{biased} is the p_T is the one measured from the detector. Therefore, the **corrected transverse momentum** can be written as:

$$p_T^{corrected} = \frac{p_T^{biased}}{1 + q\delta_s(\eta, \phi)p_T^{biased}} \tag{3.1}$$

where the δ_s is the bias introduced by the rotations in the momentum which will be η and ϕ dependent. ATLAS standard methods produce maps of δ_s with a binning of 24×24 for η and ϕ.

Effect of Sagitta bias corrections on the mass distributions are displayed on Figure 3.2, using barrel muons. The sagitta bias corrections used correspond to the official ATLAS recommendation of sagitta bias.

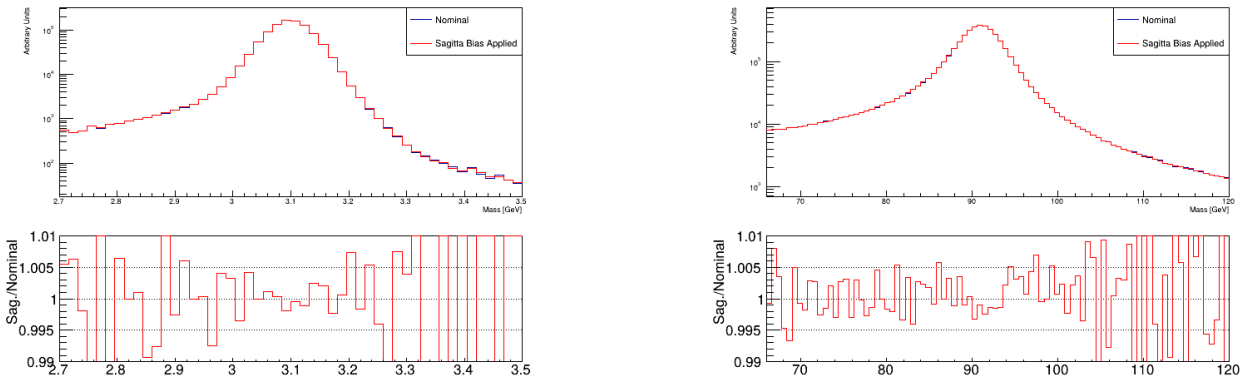

(a) J/ψ (b) Z

Figure 3.2: Examples of effect of Sagitta bias correction at the $m_{J/\psi}$ and m_Z distributions, using barrel muons. Samples used for the plots are simulation. a) J/ψ Parameters. b) Z. The corrections used in this example are the ones used in the thesis for all studies, for charge dependent effects.

3.2 Non-charge dependent effects

The correction of non-charge dependent biases are the second step of the muon momentum calibration procedure. There are two kind of biases. First, the momentum scale biases, which influence primarily the mean of the mass distribution and secondly the resolution effects, affecting primarily the tails of the mass distribution. Their origin is usually hard to disentangle. Main source is the complex magnetic field, inaccurate magnetic field measurement, as mentioned in Chapter 2.2.3. The magnetic field data is subject to biases. On the other hand, the magnetic field used for the reconstruction of MC is a "perfect" calculation of the magnetic field using Biot Savart law. Another source is detector deformations not addressed by the Sagitta corrections and alignment. The resolution biases smear the muon momentum, widening the distributions. Their effect is the miss simulation of the stochastic nature of interaction of particles with the detector. These effects are primarily, energy loss and multiple scattering.

This section focuses on the standard ATLAS calibration procedure and it's variations used in the context of the thesis. For muon momentum calibration a dedicated framework is used. The program applies the desired selection and produces templates of mass distributions for the three ID, CB and ME track types. The framework nominally performs joint calibrations fits of

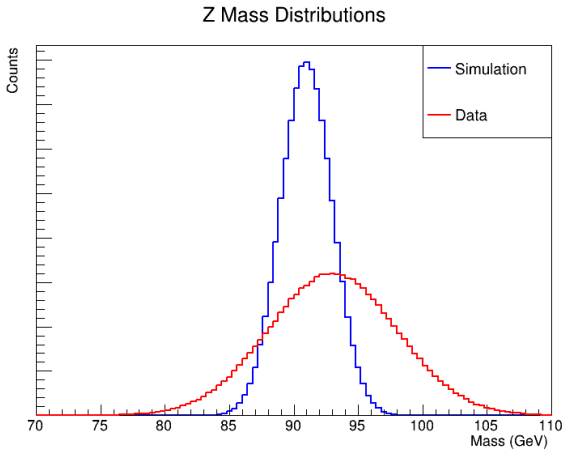

Figure 3.3: Exaggerated sketch for display purposes. Overlayed histograms, of hypothetical simulation and data, showing the mass distributions of the Z boson. The simulation does not include biases. Data is subject to biases, scale effects which move the mean of the distribution and resolution effects, due to stochastic effects in the calculation of muon resolution, as explained in 2.4.4.

J/ψ and Z mass distributions. Finally, the framework with applying variations of the selection, produces systematic estimations on the calibration parameters. The fit process is done with a dedicated minimizing algorithm using templates and a minimum likelihood estimation by interpolating between the templates.

3.3 Scale and Resolution Calibration in ATLAS

The two effects to be corrected are scale effects, which bias mainly the mean of the distribution where the resolution effects make the distributions wider. An exaggerated sketch of the effects, for a Z mass example, is displayed in Figure 3.3.

Each track type ID, CB and ME the calibration parameters are derived independently. The reconstructed momentum of the muon p_T^μ is parametrized as follows: For **ID** tracks:

$$p_{T,ID}^{Calibrated} = \frac{p_T^{\mu\,MC} + ds_1 * p_T^{MC}}{1 + \sqrt{(g_1 * dr_1)^2 + (g_2 * dr_2 * p_T^{MC})^2}} \tag{3.2}$$

For **CB** tracks:

$$p_{T,CB}^{Calibrated} = \frac{p_T^{MC} + ds_0 + ds_1 * p_T^{MC}}{1 + \sqrt{(g_1 * dr_1)^2 + (g_2 * dr_2 * p_T^{MC})^2}} \tag{3.3}$$

For **ME** tracks:

$$p_{T,ME}^{Calibrated} = \frac{p_T^{MC} + ds_0 + ds_1 * p_T^{MC}}{1 + \sqrt{(g_0 * \frac{dr_0}{p_T^{MC}})^2 + (g_1 * dr_1)^2 + (g_2 * dr_2 * p_T^{MC})^2}} \tag{3.4}$$

with:

- ds_0: constant scale correction accounting for low p_T^μ energy loss effects, only for MS and CB tracks calibrations since there is not material budget before the ID where the muon looses energy
- ds_1: scale correction term accounting for radial distortions and magnetic field mis-modeling

- dr_0: resolution correction term accounting for fluctuation of the energy loss the muon as it goes through the calorimeter. Needed only for MS and CB tracks.
- dr_1: constant resolution correction term accounting for multiple scattering.
- dr_2: resolution term accounting for residuals mis-alignments and mis-modeling of the magnetic field, also for the intrinsic resolution of the detectors.
- $g_i, i = 0, 1, 2$ are Gaussian terms that smear the distribution. With mean 0 and $\sigma_{gaus} = 1$.

The correction relation is slightly different for ID and MS tracks. In the Inner Detector there is no energy loss from the muons corresponding terms. Therefore, ds_0 and dr_0 are set to 0 when calibrating the ID tracks.

In the Figure 3.4, examples of effects of calibration parameters on the $m_{J/\psi}$ and m_Z distributions. A nominal, without any corrections template, is compared to templates corrected for the calibration parameters. All parameters are set to the same value to compare the effects. Since J/ψ and Z have different p_T^μ distributions the effect of one parameter, for the same value, can have different impact on the mass distribution. Examples of p_T^μ originating from J/ψ and Z distributions are displayed in Appendix

$_T distributions sec : J/Psi and Z sigma^\mu_{p_T} distributions) and (c) represent the effects of the scale parameter$

and m_Z, respectively. These two parameter effects can be readily disentangled: the ds_0 parameter introduces a tilt in the distributions, while the ds_1 parameter shifts the entire distribution. ds_1 has a larger contribution as it is multiplied with p_T^μ

(c) and (d) correspond to the resolution parameters. The effect of the dr_0 as it is multiplied to ${p_T^\mu}^{-1}$ it is more relevant to J/ψ than Z. The dr_2 has a larger effect on the m_Z distribution as it is multiplied with p_T^μ.

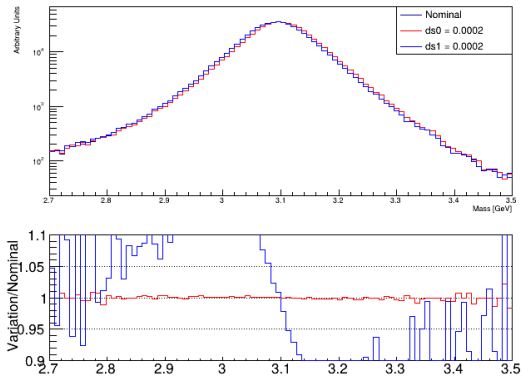

(a) Scale Parameters effect on $m_{J/\psi}$

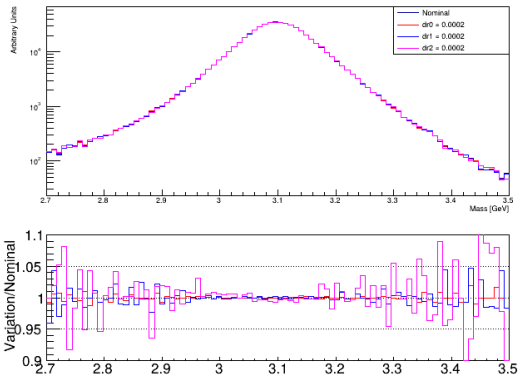

(b) Resolution Parameters effect on $m_{J/\psi}$

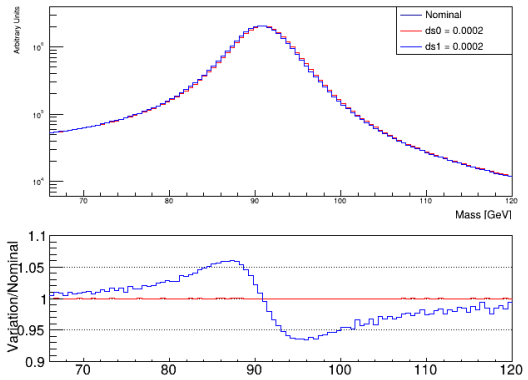

(c) Scale Parameters effect on m_Z

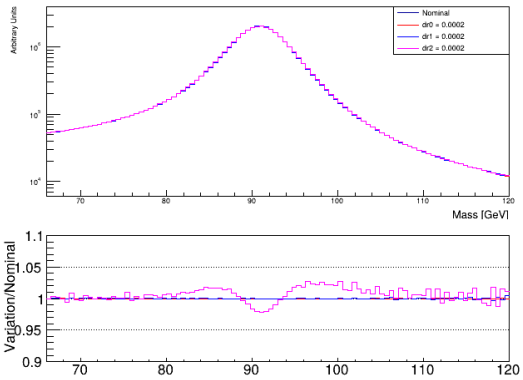

(d) Resolution Parameters effect on m_Z

Figure 3.4: Examples of effect of calibration parameters at the $m_{J/\psi}$ and m_Z distributions. (a) and (c) Scale Parameters. (b) and (d) Resolution Parameters

3.3.1 Iteration Scheme

Calibration is η, ϕ and p_T^μ dependent. The phase space is divided in regions calibrated depending on the configuration. The calibration phase space dependence is presented for the different calibrations taking place in this thesis in Table 3.1.

Track Type	**Official ATLAS**	**Z Mass**
ID Tracks	η	$\eta_{(p_T^\mu\ intergrated)}$ | $p_{T\ (\eta\ integrated)}^\mu$
CB Tracks	η, ϕ	
MS Tracks	η, ϕ	

Table 3.1: Calibration phase space binning for official ATLAS and Z mass measurement calibrations.

In the official ATLAS algorithm depending on the track type, the fit is sensitive to different phase space observables. For ID tracks, there is a negligible ϕ dependence expected, as ID is uni-some in ϕ. Therefore, the ID calibration is fitting parameters as a function of η. For the CB and ME tracks a different approach is used. Due to the ϕ structures of the Muon Spectrometer, which are the Small and the Large sectors, the fit includes the ϕ direction. The algorithm separates muons belonging in Small and Large sectors for each η region. The Small and Large sectors are fitted independently for each η bin.

Calibration parameters take different values on different regions of the phase space. If a mother particle (J/ψ or Z) decays to muons belonging in two different phase space regions, the fit has to handle two sets of calibration parameters. Therefore, each histogram for a region of

interest will contain muons originating from multiple regions and finally a matrix of multiple set of calibration parameters have to be calculated simultaneously. To solve the this problem an iterative procedure is followed.

In the first iteration only muons belonging to the same region of phase space are selected. The phase space regions used are broad enough, to have sufficient event yield. This way a calibration is derived for all the phase space. In the next iterations, by having an estimation for all phase space regions, finer regions are used and the muons can belong to multiple regions of the phase space. The detailed procedure is presented in Appendix B.

3.3.2 Fit Methodology

In summary the framework follows this algorithm in each iteration:

1. **Corrections Applied**: At the start of each iteration there are two kind of corrections applied to the p_T^μ on the sample (data or MC). If it is data the p_T^μ is corrected with the sagitta bias correction. If it is MC the muon p_T^μ is corrected for scale and resolution parameters with the values obtained from the previous iteration.

2. **Selection**: Apply selection on MC (signal and background) and data. Selection is using an η,ϕ and p_T^μ scheme. Depending on the track fitted the ϕ dependency is dropped. ID calibration uses only an η dependence and CB, ME include a ϕ one. Nominally there are 18 regions fitted in η and if there is a ϕ dependence all the Large Sectors in an η region will be fitted simultaneously and all the Small Sectors will be fitted simultaneously in a separate fit independently from the Large Sectors.

   On top of that, there is an additional p_T^μ based selection. The framework uses nominally 4 p_T^μ bins to build 4 templates per detector region calibrated, 2 J/ψ originated and 2 Z originated muon p_T^μ bins. In the selection there is a fundamental difference in the method between J/ψ and Z. For the J/ψ the algorithm builds two histograms based on the sub-leading muon p_T^μ and for the Z it builds 2 histograms based on the leading muon p_T^μ.

3. **Selection of muons to fit**: If the MC muon falls in the η,ϕ region of interest it is not corrected from the previous iteration (from step 1). The values obtained from the previous iteration will be used a starting value for the current iteration. If the muon falls outside the region of interest, it's p_T^μ is corrected according to the values of the previous iteration (step 1).

4. J/ψ **Background Estimation**:After the data, signal and Z background histograms have been filled per region, the J/ψ background has to be evaluated. For the background of J/ψ using a parametric function fit of signal plus background with a data driven method the background shape and number of events is extracted. The procedure of J/ψ background fit is presented in Section 3.3.3.

5. **Minimization**: A simple minimizing algorithm provides the first estimation for the parameters. These values are injected into a dedicated likelihood minimization algorithm, which uses signal simulation templates with varying correction parameters and interpolation between them.

For the minimization procedure and the parameters calculation the calibration framework uses Minuit ref.[48]. The code uses two kind of minimizers:

- Simplex: First a SIMPLEX (algorithm implemented in Minuit ref.[48]) minimizer is used. This minimizer consists of three stages. In the first step it computes scale parameters my comparing the mean between data and MC with χ^2. Secondly, it computes the resolution parameters by comparing again by a χ^2 the mean and the Standard Deviation between the two distributions. This first two stages are called High Level χ^2. Finally the minimizer uses a binned χ^2 to correct all the parameters simultaneously.

- GridScan: GridScan provides a higher precision minimization. This algorithm takes as input the Simplex minimization of the parameters creating a "grid" of templates. To create the grid it reads the input minimized value for each calibration parameter and it creates reference values of the parameters around the input values. The reference values are chose by the user. By applying the reference values of the calibration parameters to the MC samples a 3D grid of templates is created. Finally it calculates a negative log likelihood for each point of the grid and interpolates between the likelihood values. This was there is a continuous value of the likelihood in the calibration parameters space. The minimization is handled by Minuit. The algorithm is based movement morphing methods already implemented in other ATLAS analyses ref. [49].

3.3.3 J/ψ Background

J/ψ background is fitted with a parametric analytical fit and it is not taken from simulation. The background corresponds to a continuum, which receives contributions from the Drell-Yan process and hadron decays that is difficult to simulate due to non perturbative QCD regime dominating. By considering an analytical model for the signal and the background and fitted them both at the data distribution an estimation is derived for the background shape and yield.

Given the good resolution mainly in the barrel region the final state radiation tail of the J/ψ mass distribution has to be accounted for by the parametric fit of the signal model of the J/ψ. Therefore, the model used for the signal model sum of a Crystal Ball and a Gaussian function to account for additional resolution effects. Crystal Ball and Gaussian share the same mean:

$$N_{signal} = N * (Gauss(\mu, \sigma) + CB(\mu, \sigma, \alpha, \eta))$$

where N is a normalization factor between Crystal Ball and Gauss. The Crystal Ball function combines a Gaussian core for the central peak region and a power-law tail for deviations. The function is ideal for asymmetric distributions. The Crystal Ball function ref.[50] is defined as follows:

$$f(x; \alpha, n, \bar{x}, \sigma) = \begin{cases} \exp\left(-\frac{(x-\bar{x})^2}{2\sigma^2}\right), & \text{for} \quad \frac{x-\bar{x}}{\sigma} > -\alpha \\ A\left(B - \frac{x-\bar{x}}{\sigma}\right)^{-n}, & \text{for} \quad \frac{x-\bar{x}}{\sigma} \leq -\alpha \end{cases} \tag{3.5}$$

Where:

- x: the variable of interest (e.g., energy or mass),

- $\bar{x}$: the peak position or mean of the Gaussian part,

- σ: the standard deviation of the Gaussian core,

- α: defines the point where the Gaussian core transitions into the power-law tail (on the left-hand side of the peak),

- n: the exponent that controls the shape of the power-law tail,
- A: normalization factor ensuring continuity between the Gaussian and power-law regions, $A = \left(\frac{n}{|\alpha|}\right)^n \exp\left(-\frac{|\alpha|^2}{2}\right)$,
- B: a parameter that ensures the continuity of the function and its derivative at the transition point, $B = \frac{n}{|\alpha|} - |\alpha|$.

The model is fitted to the simulation to calculate shape parameters and finally only the mean and the sigma of the Crystal Ball are allowed to float when fitting the data sample. The di-muon background of the J/ψ is non resonant and parametrized using either an exponential or a Chebysev of the second order. The official ATLAS calibration uses nominally the exponential model and the calibration parameters derived by using the Chebysev are used as a systematic uncertainty.

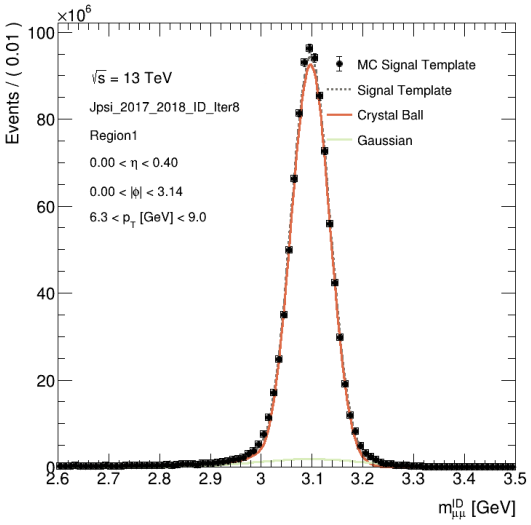

(a) Signal Model Parametric fir for $6.3 < p_T^{sub-leading} < 9$ GeV

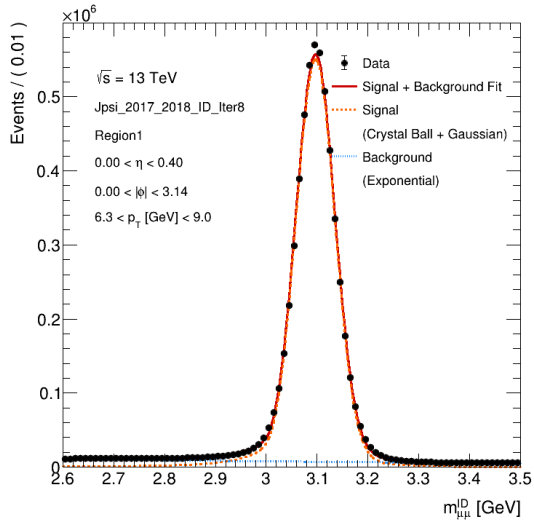

(b) Signal and Background to Data Model Parametric fit for $6.3 < p_T^{sub-leading} < 9$ GeV

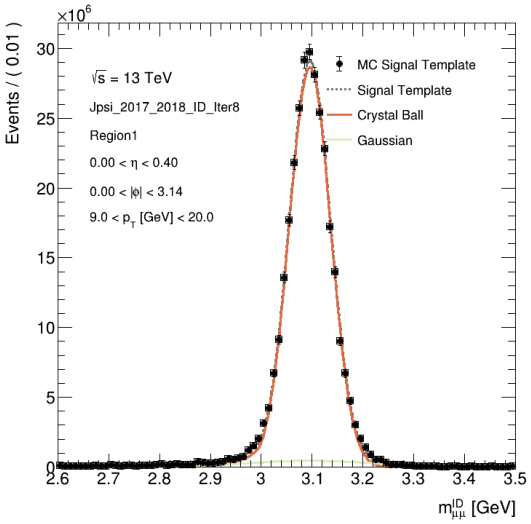

(c) Signal Model Parametric fir for $9 < p_T^{sub-leading} < 20$ GeV

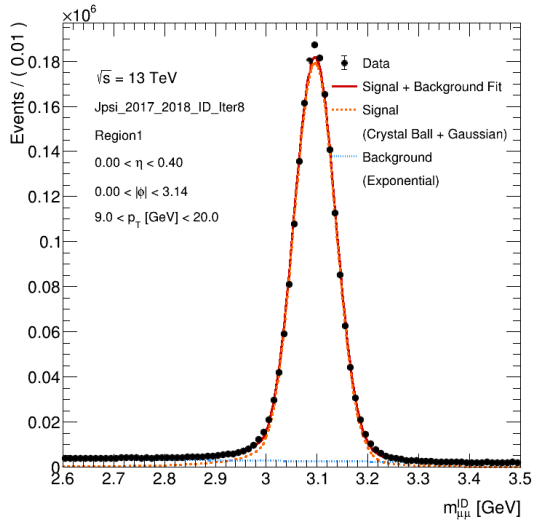

(d) Signal and Background to Data Model Parametric fit for $9 < p_T^{sub-leading} < 20$ GeV

Figure 3.5: Examples of analytical parametric fits of signal and background in order to derive the background component, produced in the context of thesis. First, the fit is performed on the signal mass templates (a and c) with a sum of a Crystal Ball and a Gauss. In the next step the fit is performed on the data(b and d) with an exponential model for the background. Distributions shown use Inner Detector muons and one of the muons belonging to the interval: $0 < \eta < 0.4$

In Figure 3.5 the analytical fit procedure for the J/ψ background estimation is shown.

J/ψ background and signal analytical functions parameters are re-evaluated in each iteration. As corrections parameters fluctuate in each iteration the $m_{\mu\mu}$ signal distributions vary as well. This can lead to parametric analytical fits changing from iteration to iteration. Therefore, in each iteration the templates are corrected with the calibration parameters of the previous iteration and the signal+background analytical fit takes place on the corrected template.

3.3.4 Z background

The Z background is calculated through simulation. The main background processes are di-boson, top anti-top pair and $Z \to \mu\mu$

In the Table 3.2 the background processes are presented.

Table 3.2: Z Background Processes for $Z \to \mu\mu$

Background Processes
$W + \mu + \nu$
$Z \to \tau^+\tau^-$
$W^- \to l^-\nu$ and $W^+ \to l^+\nu$
$WZ \to l\nu ll$
$ZZ \to llll$
$ZZ \to \nu\nu ll$
$WZ \to qqll$
$ZZ \to qqll$
$t\bar{t}$

3.4 Calibration Validation

In the context of the thesis a calibration validation framework was developed. The framework is inspired by codes already used by ATLAS for the calibration. Purpose of the validation is to compare the calibration as a function of multiple parameters. The goal is to test the calibration method and its accuracy and find non closures or mis-modelings to be taken further into consideration. The calibration framework will also be used further in the Z mass measurement analysis for comparison of calibration methods.

After the calibration parameters are derived for the needs of the thesis they are injected in the validation framework. The framework algorithm has the following structure:

1. Simulation samples are corrected for non-charge dependent effects. The simulation is re-weighted with a di-muon $p_T - Y$ re-weighting map, to match p_T distribution of simulation to the data one. The data samples are corrected for charge dependent biases.

2. Distributions are produced using for the selection a kinematic variable. This kinematic variable are η, ϕ p_T^μ of the leading muon or the di-muon.

3. (Only for the J/ψ) The background yield and shape of the J/ψ is derived from a parametric fit, as described in the Section 3.3.3. The background distribution derived is added to the signal.

4. The core of the di-muon distribution is fitted with the convolution of a Crystal Ball and a Gaussian function, for both MC and data. The two functions share a common mean and a different variance. The common mean and the σ of the Crystal ball are plotted as a function of the selection kinematic variable.

   The above are repeated for nominal, up and down systematic variations of the calibration parameters. The contributions are added in quadrature to evaluate the uncertainties.

An advantage of the validation framework is the testing of the calibration in finer binning than the calibration one. This way shapes and non-closures in fine detector regions can be detected and treated accordingly.

The validation framework is under development. The σ of the Crystal Ball is used to study the effect of the calibration in the smearing of the mass distributions. The σ of the Gaus is ignored for now, in the future the two σ will used for the validation.

3.5 Samples

In this Section, are presented the technical details over the samples used in the official ATLAS calibration scheme.

The data belong to full Run-2 luminosity with pp collisions. They are derived from Physics Main and B Physics data streams.

Physics main contains higher p_T^μ triggers and is suitable for Z analysis and J/ψ ones with very energetic muons. B Physics having lower p_T^μ triggers is suitable for a J/ψ analysis.

For the Z MC generation information can be found at the Chapter 6.1. For the J/ψ are produced using Pythia 8 ref.[51] with CTEQ6L1 PDF set ref.[7].

The pre-selection in sample level is:

Pre-Selection	**Values**
Quality Working Point	Medium
Vertex Cut	$\frac{\lvert d_0\rvert}{\sigma(d_0)} < 3$, $\lvert z_0 \times \sin\theta\rvert < 0.5$ mm
Pre-selection Resonances mass cut	Z: $66 < m_{\mu\mu} < 125$ GeV J/ψ: $2.6 < m_{\mu\mu} < 3.5$ GeV

Table 3.3: Pre-selection for pre-smearing studies.

Trigger choice for the official calibration procedure is:

Table 3.4: HLT triggers that are used to select Z boson candidates.

Year	**Trigger**
2015	HLT_mu20_iloose_L1MU15 —- HLT_mu40
Rest	HLT_mu26_ivarmedium —- HLT_mu50

Table 3.5: HLT triggers that are used to select J/ψ boson candidates.

Year	**Main Trigger**	**Alternative Trigger**
2015	HLT_2mu4_bJpsimumu	-
2016	HLT_2mu6_bJpsimumu —- HLT_2mu6_bJpsimumu_delayed	-
2017	HLT_2mu6_bJpsimumu_Lxy0_L1BPH-2MU6_2DR15_2MU6	HLT_mu11_mu6_bJpsimumu
2018	HLT_2mu6_bJpsimumu_Lxy0_L1BPH-2MU6_2DR15_2MU6	HLT_mu11_mu6_bJpsimumu

Chapter 4

General Studies in Calibration

This chapter is split of two parts. Both correspond to studies and work done on muon momentum calibration but not for the Z mass analysis.One focus is the pre-smearing correction study, while the other is the 2017 calibration results for the ATLAS Run-2 new samples release of data and simulation. Both studies focus on the non charge dependent bias part of momentum calibration. The charge dependent biases corrections have been already pre-applied in the samples.

In the first part, the effect of the muon momentum uncertainty at the calibration is studied as part of the ATLAS Qualification Task. Distributions of relative p_T^μ uncertainty are presented and the process of deriving them is explained. Furthermore, 2D maps in η and ϕ of muon momentum relative uncertainty are studied, for different p_T^μ bins. A hypothesis is proposed suggesting that the calibration exhibits non-closure due to observed differences in relative muon momentum uncertainty between MC and data. To address this, these differences are mapped and incorporated into the calibration procedure. The calibration results are then compared with and without the inclusion of these maps to evaluate their impact.

In the second part, the calibration results are presented using the official ATLAS calibration method. Samples calibrated belong to a new release of data and simulation, with improved reconstruction with respect to the previous release. A description of the systematic uncertainties is given and the distributions before and after calibration are presented for ID, CB and ME track. Subsequently, the corrections and the χ^2 per degree of freedom post-calibration are plotted as functions of η. Finally, validation graphs are provided, examining non-closures and the efficiency of the calibration as a function of muon kinematic variables.

4.1 Pre-Smearing Corrections

4.1.1 Calibration Implementation on Relative p_T Uncertainty

To justify this study, the impact of the calibration on the relative uncertainty distributions is analyzed. Main point of this subsection is to give a short insight on the process from ATLAS sample level of $\sigma_{q/p}$ to $\frac{\sigma_{p_T}}{p_T}$ distributions Additionally, the goal is to show that the p_T^μ calibration is not capable to match $\frac{\sigma_{p_T}}{p_T}$ distributions between simulation and data. This difference is assumed to be a source of additional uncertainty. Addressing this issue potentially can help the calibration fit to converge further. Relative uncertainty distributions in ID, CB and MS and profiles with η and p_T^μ calibrated MC and data are going to be displayed.

4.1.1.1 $\sigma_{q/p}$ distributions

Initially, three distributions of absolute uncertainty—corresponding to the ID, MS, and CB—for both J/ψ and Z will be presented. These distributions are selected from the barrel, the intermediate region, and the end-cap. Relative momentum uncertainty is determined following the helix parameter fit detailed in the Chapter 2.4.1. The J/ψ and Z studies are shown separately as the p_T^μ distribution of the muons originating from the two resonances differentiate distinctively, as shown seen in Appendix D.2. The muons from J/ψ and Z decays are differentiated by adding a selection for the $m_{\mu\mu}$: $2.8 < m_{\mu\mu} < 3.3$ GeV for the J/ψ, and $70 < m_{\mu\mu} < 110$ GeV for the Z. The sole purpose of the Figures 4.1, 4.3, 4.4 and 4.6 is to demonstrate the differences in MC and data that exist in sample level, before transforming $\sigma_{q/p}$ to σ_{p_T}/p_T. The distributions of $\sigma_{q/p}$ are displayed and commented in more detail for all track types and η bins where for the other distributions only some examples will be displayed and the rest are provided on the Appendix D.1 - D.2.

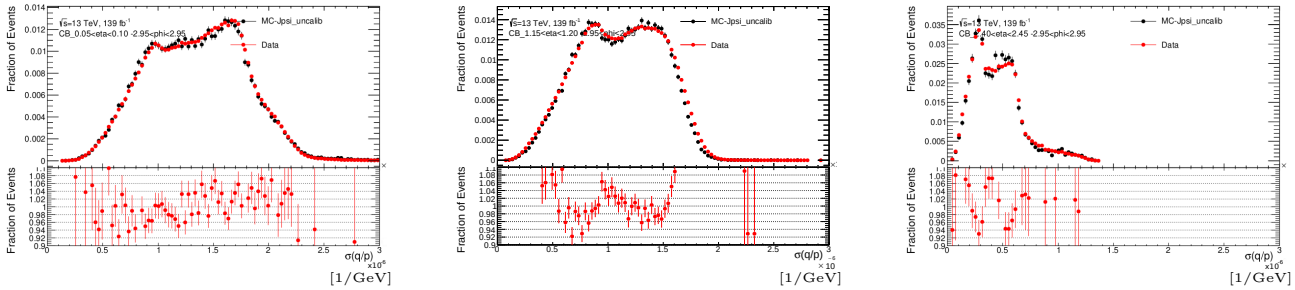

(a) $0.05 < \eta < 0.10$ (b) $1.15 < \eta < 1.20$ (c) $2.40 < \eta < 2.45$

Figure 4.1: Distributions of $\sigma_{q/p}$ for **CB** muons in the J/ψ mass region $2.8 < m_{\mu\mu} < 3.3$ GeV in three η ranges.

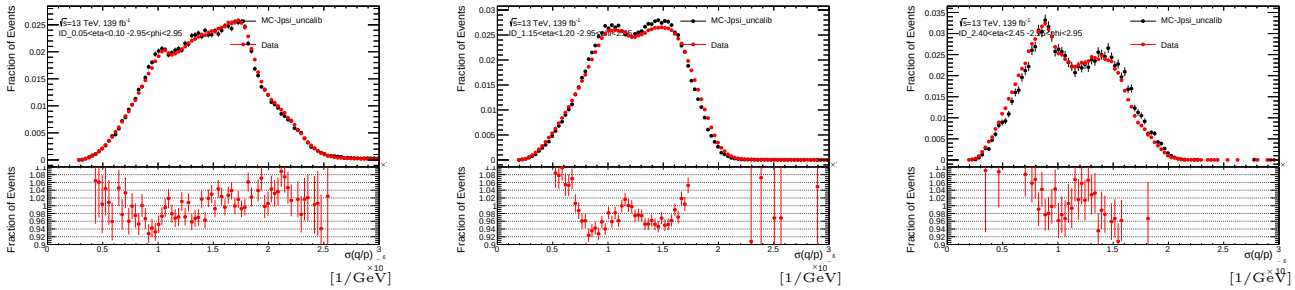

(a) $0.05 < \eta < 0.10$ (b) $1.15 < \eta < 1.20$ (c) $2.40 < \eta < 2.45$

Figure 4.2: Distributions of $\sigma_{q/p}$ for **ID** muons in the J/ψ mass region $2.8 < m_{\mu\mu} < 3.3$ GeV in three η ranges.

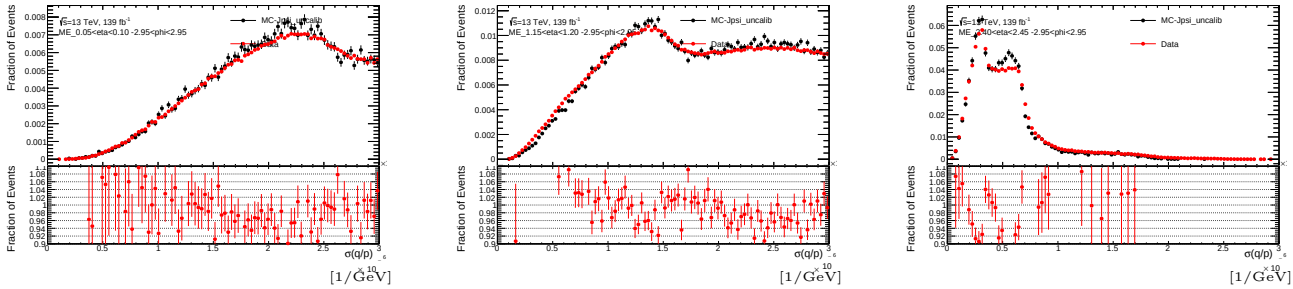

(a) $0.05 < \eta < 0.10$ (b) $1.15 < \eta < 1.20$ (c) $2.40 < \eta < 2.45$

Figure 4.3: Distributions of $\sigma_{q/p}$ for **ME** muons in the J/ψ mass region $2.8 < m_{\mu\mu} < 3.3$ GeV in three η ranges.

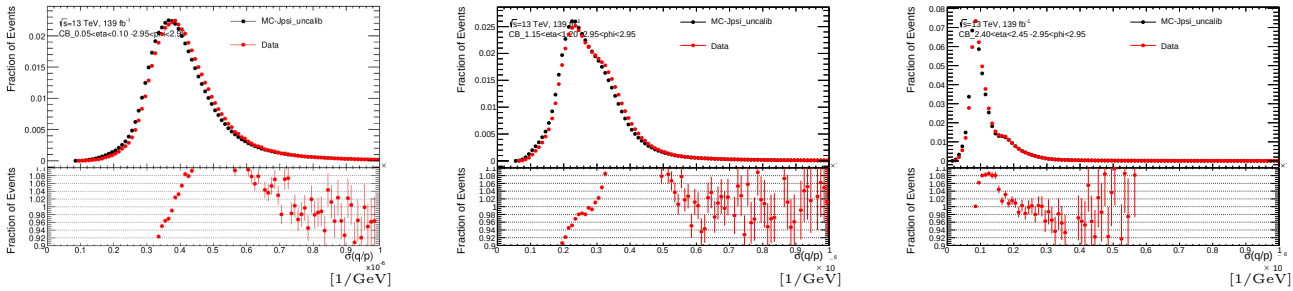

(a) $0.05 < \eta < 0.10$ (b) $1.15 < \eta < 1.20$ (c) $2.40 < \eta < 2.45$

Figure 4.4: Distributions of $\sigma_{q/p}$ for **CB** muons in the Z mass region $70 < m_{\mu\mu} < 110$ GeV in three η ranges.

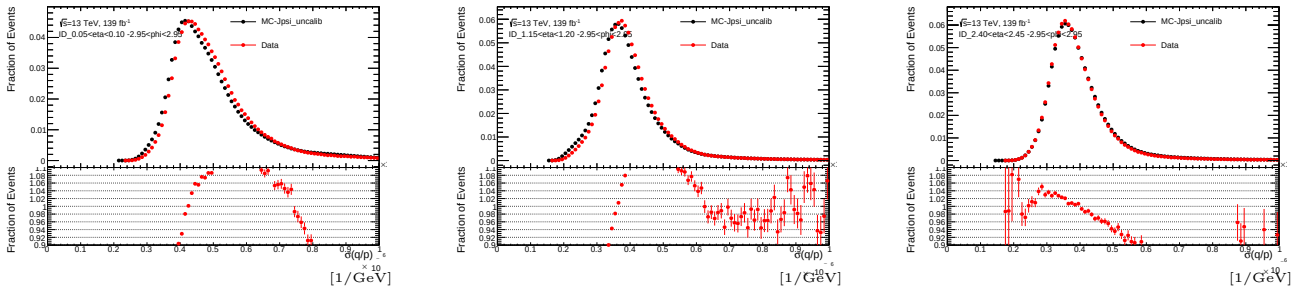

(a) $0.05 < \eta < 0.10$ (b) $1.15 < \eta < 1.20$ (c) $2.40 < \eta < 2.45$

Figure 4.5: Distributions of $\sigma_{q/p}$ for **ID** muons in the Z mass region $70 < m_{\mu\mu} < 110$ GeV in three η ranges.

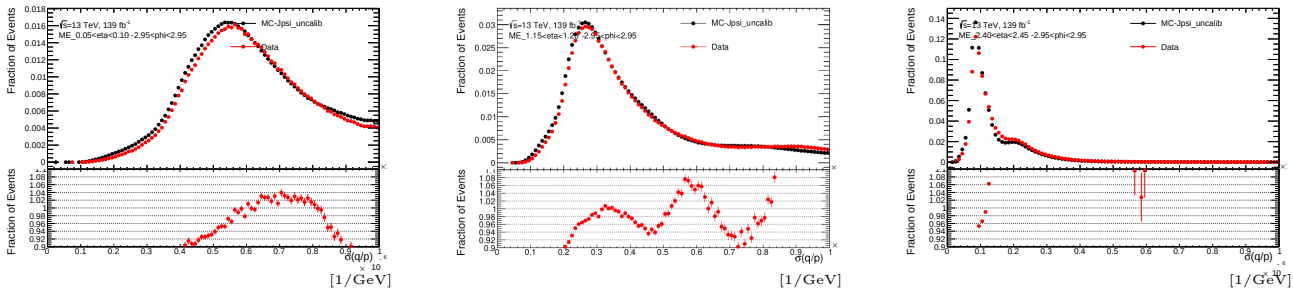

(a) $0.05 < \eta < 0.10$ (b) $1.15 < \eta < 1.20$ (c) $2.40 < \eta < 2.45$

Figure 4.6: Distributions of $\sigma_{q/p}$ for **ME** muons in the Z mass region $70 < m_{\mu\mu} < 110$ GeV in three η ranges.

In the Figures 4.1, 4.3, 4.4 and 4.6, the CB and ME case for muons coming from Z and J/ψ resonances are displayed. There are no distinct peaks in the distributions, this comes from not including ϕ dependence in these plots, since CB and ME subsystems have a corresponding dependence. For the purpose of this simple display of distributions only the η dependence is considered enough, as detailed maps will be shown later.

Regarding the CB case, it is evident that it exhibits a better performance than ID and ME. In the barrel, the CB distribution has a shape close to the ID one, where in the end-cap the shape is closer to the ME case. In the J/ψ case the agreement between data and MC is better than the Z.

An increase of this disagreement with p_T^μ is hinted from comparing J/ψ and Z plots. Since J/ψ has a peak in $p_T^\mu \approx$ 6-8 GeV and Z $\approx$ 44 GeV this signals a deterioration of the agreement with p_T^μ, something to be discussed thoroughly later in the chapter. Also in the Z case, it is prominent that the uncertainty in the simulation is pushed to lower values as shown in Figures 4.4 - 4.6.

Regarding ME, Figures 4.3, 4.6 (a) and (b) the distribution is broader compared to the corresponding plots in the ID and CB case (4.1, 4.2, 4.4 and 4.5) due to the increased muon momentum resolution. This originates from the ME tracks reconstruction. In the ME case, there is the contribution of energy loss uncertainty in low p_T^μ (relevant for the J/ψ) which broadens the distribution relatively to the other cases. Moreover, this contribution is influenced by additional effects, as it depends on the material budget the muon traverses before reaching the Muon Spectrometer. The observed broadening also arises from the poorer performance of the Muon Spectrometer (ME) in the barrel region compared to the Inner Detector (ID), as analyzed in Chapter 2.5.

4.1.1.2 σ_{p_T} distributions

To derive the $\sigma_{p_T^\mu}$ distributions the following transformation took place:

$$\sigma_{p_T} = \frac{1}{(q/p)\sin\theta}\sqrt{\left(\frac{\sigma_{q/p}}{q/p}\right)^2 + \left(\frac{\cos\theta}{\sin\theta}\sigma_\theta\right)^2} \tag{4.1}$$

Secondly, the corresponding σ_{p_T} distributions are displayed, after the Relation 4.1 has been applied.

Regarding σ_{p_T}, only an example for J/ψ and one for Z are going to be displayed for barrel region, CB tracks. The rest of the distributions for intermediate and end-cap are in the Appendix D.1. CB is a combination of ID and ME tracks. Therefore, displaying ID and ME separately is considered unnecessary.

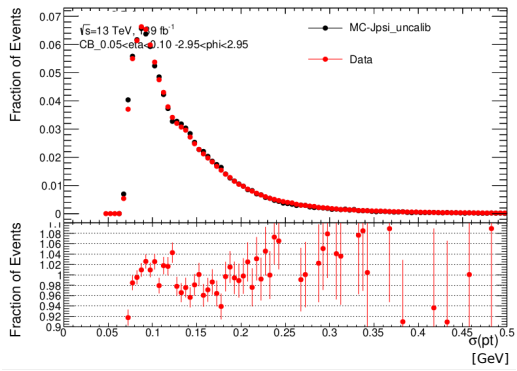

(a) J/ψ CB Barrel

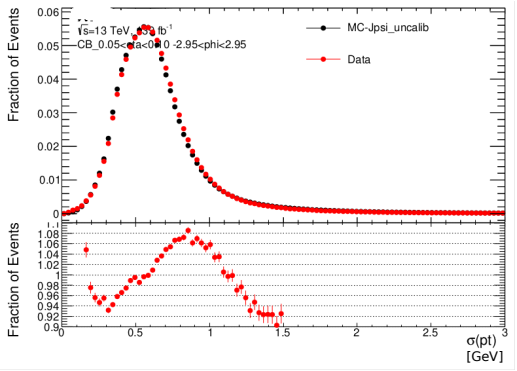

(b) Z CB Barrel

Figure 4.7: Distributions of σ_{p_T} for CB muons, with a $m_{\mu\mu}$ selection for the J/ψ resonance ($2.8 < m_{\mu\mu} < 3.3$ GeV) and the Z boson resonance ($70 < m_{\mu\mu} < 110$ GeV). $0.05 < \eta < 0.10$.

In this case, the shape differences between data and MC, observed in $\sigma_{q/p}$ (Figures 4.1-4.6), are propagated in the two Figures 4.7a and 4.7b. Primarily, it is evident that the J/ψ have peaks in lower values ($\approx 0.2-0.3$) than the Z ($\approx 0.4-0.6$). This originates to the dependence of σ_{p_T} with p_T^μ . Another critical aspect that influences the shape of the distributions is the trigger configuration. The double peak, in the J/ψ case, originates in the double trigger configuration used. While in the Z case 4.7b one muon trigger is used. Further commenting on these distributions and the CB histograms for three η ranges(barrel, intermediate and end-cap) are shown in Appendix D.1

4.1.1.3 Calibrated σ_{p_T}/p_T distributions

Finally, profiles of relative momentum uncertainty (*rel.unc.*) σ_{p_T}/p_T distributions in low η and ϕ are produced from low to high p_T^μ. For the subsection the muon momentum is corrected for biases. The calibrations used for this correction, are the official results coming from Muon Performance Group of ATLAS. The key observation here is that the calibration fails to account for the differences observed.

The profiles exhibited in this section were produce by a dedicated ATLAS framework for muon momentum uncertainty studies. In the context of this thesis, the framework was modified to apply calibration corrections directly to the samples.

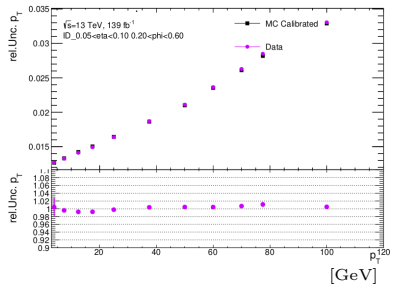

(a) $0.05 < \eta < 0.10$

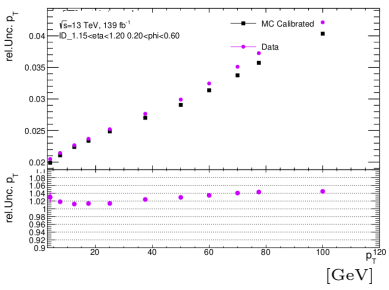

(b) $1.15 < \eta < 1.20$

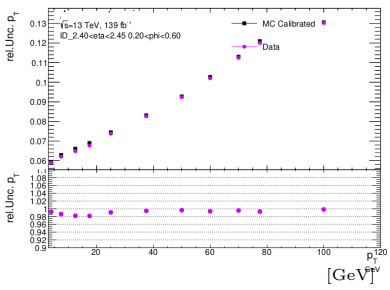

(c) $2.40 < \eta < 2.45$

Figure 4.8: Muon ID track profiles of σ_{p_T}/p_T as a function of p_T^μ, data and Calibrated MC

Primarily, it is important to highlight the behavior of the σ_{p_T}/p_T with p_T^μ in the Figures 4.8 - 4.10. In all cases, the relative uncertainty is rising with momentum. This originates from the third term of intrinsic resolution, r_2, of the Relation 2.7. The second, constant with p_T^μ, term of multiple scattering, is relevant for all cases. Therefore, all the graphs begin from non zero values for $p_T^\mu \approx 0$. Regarding ID, there is almost a linear rise with p_T^μ both in MC and

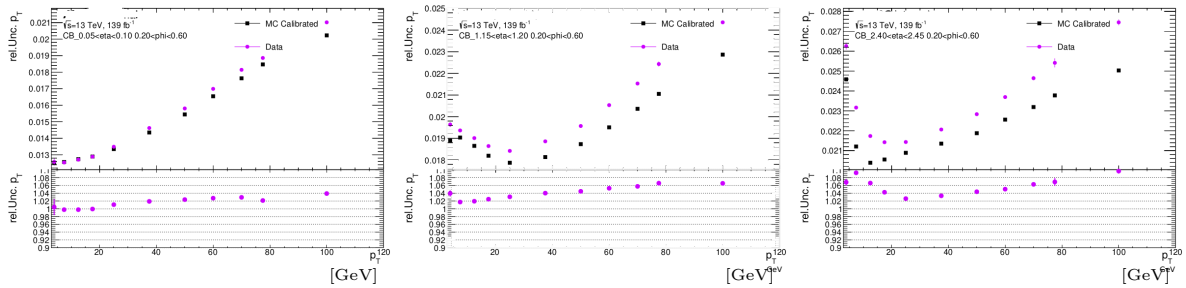

(a) $0.05 < \eta < 0.10$ (b) $1.15 < \eta < 1.20$ (c) $2.40 < \eta < 2.45$

Figure 4.9: Muon CB track profiles of σ_{p_T}/p_T as a function of p_T^μ, data and Calibrated MC.

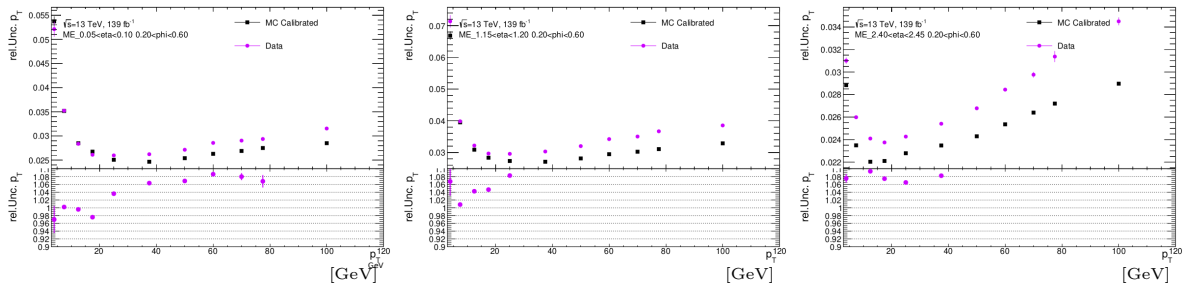

(a) $0.05 < \eta < 0.10$ (b) $1.15 < \eta < 1.20$ (c) $2.40 < \eta < 2.45$

Figure 4.10: Muon ME track profiles of σ_{p_T}/p_T as a function of p_T^μ, data and Calibrated MC.

data. This is what is expected from the Relation 2.7 since only the second and third term are relevant. Regarding ME (Figures 4.10 (a)-(c)), all three terms of Relation 2.7 are relevant. Therefore, at low p_T^μ, where the first inverse with p_T^μ term in Relation 2.7 is dominant, the relative uncertainty is starting from higher values. Afterwards, it decreases quadratically and at intermediate $p_T^\mu \approx 20GeV$, the third term starts being dominant. Finally, the uncertainty rises again with almost a linear behavior. Regarding CB (Figure 4.9), as expected, is a mixture of ID and ME behaviors.

In all cases (Figures 4.8 - 4.10, from (a) to (c)), the agreement progressively worsens as η increases toward the forward region. This behavior is anticipated, as the complexity of the magnetic field increases in the forward region, making its accurate calculation more challenging and leading to larger non-closure effects. Comparing the ID Figure 4.8, CB Figure 4.9 and ME Figure 4.10 for the same η bin it is evident that the ID has the best agreement. The CB has a similar behavior in barrel but the ratio plot is deviating from 1 moving forward in η. Finally the ME Figure 4.10 displays the worst agreement.

In Figures 4.8 - 4.10, the calibrated MC and the data display a difference persisting after applying the calibration. This suggests the possibility of a calibration non-closure. In the following sections, the pre-smearing method will be introduced as a targeted approach to address this issue.

4.1.2 Covariance Maps

In this Section, profile maps of $\frac{\sigma_{p_T}}{p_T}_{Data}/\frac{\sigma_{p_T}}{p_T}_{MC}$ are exhibited, produced in the context of the thesis.

The main challenge in this process is determining the optimal binning for the maps, ensuring that differences between MC and data are captured while avoiding low number of events in individual bins. After examining the distributions of $rel.unc.$ within each bin, it was concluded that a detector binning of 320 for ϕ, 108 for η, and 10 bins for p_T^μ is sufficient for the purposes of this analysis.

In the ratio maps of $rel.unc._{Data}/rel.unc._{MC}$ (Figures 4.11 - 4.13) there are structures between MC and data, in regions much finer than the regions used by the calibration.

An additional selection was applied to exclude muons with nonphysical, large relative uncertainties ($rel.unc.$). These muons, which can distort the mean of the $rel.unc.$ profile, predominantly appear in the ME tracks, less so in ID tracks, and rarely in CB tracks. The $rel.unc.$ values for these outliers range from approximately 100% to 200%. To mitigate their impact, a selection of $rel.unc. < 20\%$ was applied. These outliers, corresponding to muons with problematic tracking fits, are considered nonphysical and are therefore excluded from this study.

The maps include full Run-2. A minor study was done to investigate possible changes at the maps through the different campaigns. Since no significant effect was found, all the years were grouped to produce the maps.

Examples of ratio maps $rel.unc._{Data}/rel.unc._{MC}$ for MS, CB and ID are displayed, for three p_T^μ bins, in the Figures 4.11, 4.12 and 4.13.

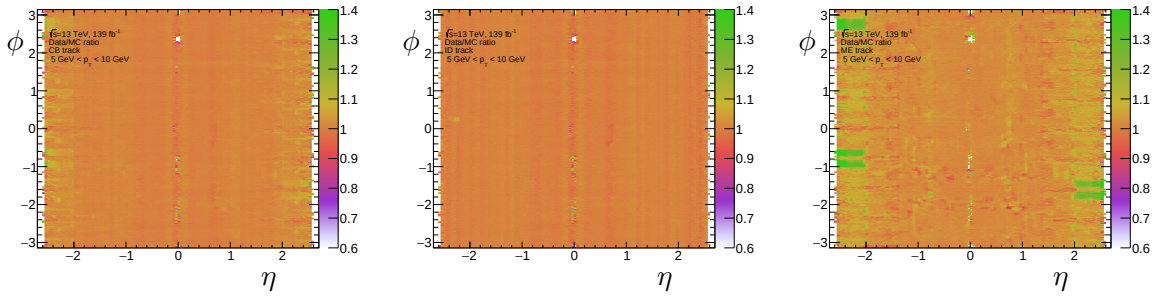

(a) CB (b) ID (c) ME

Figure 4.11: Map of: $rel.unc._{Data}/rel.unc._{MC}$ for $5 < p_T^\mu < 10$ GeV

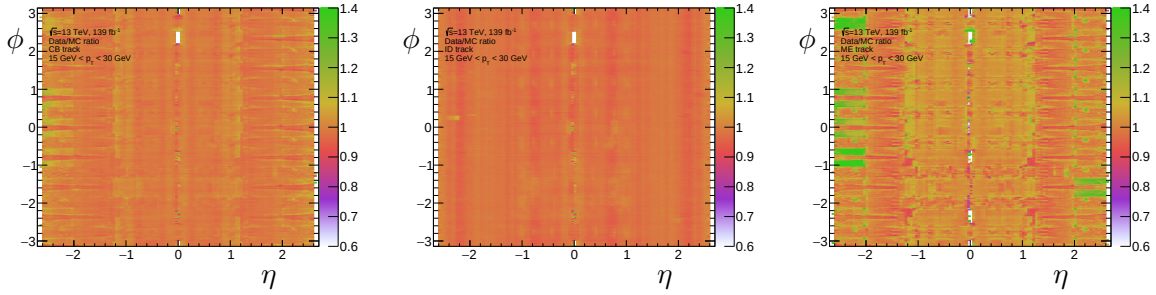

(a) CB (b) ID (c) ME

Figure 4.12: Map of: $rel.unc._{Data}/rel.unc._{MC}$ for $15 < p_T^\mu < 30$ GeV

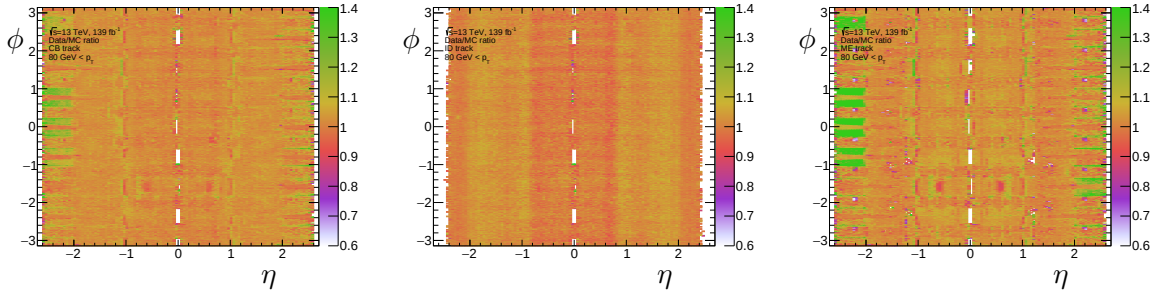

(a) CB (b) ID (c) ME

Figure 4.13: Map of: $rel.unc._{Data}/rel.unc._{MC}$ for $80 < p_T^\mu < 300$ GeV

In Figure 4.10 (and in Figures 4.14 - 4.15 in the following subsection 4.1.3), the relative uncertainty increases as a function of η. The ratio maps reveal distinct structures in the

detector, which correspond to specific subsystems. This suggests that the observed effect is not due to random mis-modeling but rather indicates a systematic mis-modeling of the detector. More structures are present in the ratio maps as the p_T^μ increases. This signals an increase of disagreement between MC and data with p_T^μ.

The ID is better simulated in comparison to the ME and CB track types, as less structures are present in the ratio data/MC maps. Furthermore, ID maps display a flat ratio in η and ϕ of one. For example, in the 4.13 at the 55 to 80 GeV p_T^μ bin, in both ME and CB, appear green bins (meaning a ratio above 1.4) where the ID display less structures and less bins with out of scale ratios. This is expected, as the Inner Detector has simpler systems and less complex magnetic field. Therefore, ID tracks, are less sensitive to mis-modeling.

Regarding the ID maps, the detector's uniform response in ϕ is shown clearly at the maps. With increasing p_T^μ there are structures appearing in ID maps. Notably, in the Figure 4.13 (b), the intermediate region, outside the barrel ($|\eta| > 1.05$) the *rel.unc.* disagreement increases significantly. This is due to change of the ID systems at that region, which have decreased performance, compared to the barrel region.

Regarding the CB and ME maps, the subsystems of the detector and support systems are visible in all the ratio maps. In contrast to the ID, both ME and CB exhibit a stronger ϕ dependence in the ratio of data/MC for the relative uncertainty (*rel.unc.*). This indicates a mis-modeling of the detector. The mis-modeling arises not only from the material itself but also from the inaccurate simulation of the magnetic field in the Muon Spectrometer.

In the CB and ME ratio maps there are eight structures at the region $1.4 < |\eta| < 2.7$. These structures correspond to the small end-cap toroid coils. These are related to mis-modeling of the coil material. Additionally, around the coils there are shapes of high ratios (with green color). This issue arises from two main sources. First, the magnetic field in these regions is highly complex due to the interference between the small toroid coils and the large ones, indicating potential mis-modeling of the magnetic field in the inter-coil regions. Second, these regions house the CSC detectors, which, for a significant portion of Run-2, were under-performing.

In the negative ϕ range ($\approx 1.4 - 1.9$), a shape is observed in the central η region (≈ -1 to 1), attributed to the mis-modeling of the metallic material in the support structures of the Muon Spectrometer and ATLAS. Additionally, repetitive shapes are visible across all ϕ at $|\eta| \approx 1.2$, which correspond to other supporting structures of the Muon Spectrometer. This hinders a material mis-modeling or a magnetic field mis-calculation around metallic supporting structures.

From Figures 4.11 to 4.13, and by comparing the CB (a) map with the ID (b) and ME (c), the behavior of CB tracks is clearly illustrated. In the barrel and intermediate regions, CB tracks are closer to the ID, while in the end-cap region, they more closely resemble the ME tracks.

4.1.3 Fitting of Relative Uncertainty

In this Section, a study of *rel.unc.* as a function p_T^μ is presented. As shown in Section 4.1.2, the ratio $\frac{rel.unc._{data}}{rel.unc._{MC}}$ has a p_T^μ, η and ϕ dependence. The study is presented for the first Large Sector and positive η. Further results, from other detector regions are not presented to avoid redundancy.

In Figures 4.14 and 4.15, the profile of the relative uncertainty (*rel.unc.*) is shown as a function of p_T^μ for different η bins. Additionally, a parametric fit is performed, utilizing the parametrization of *rel.unc.* with p_T^μ, Relation 2.7. Crucial points could be concluded about the calibration of "pre-smearing corrections" from the difference of the fit in MC and data. Examples of these fits are given for ME tracks. The CB tracks are not going to displayed since it is a mixture of ID and ME responses as discussed in Section 4.1.1. Examples of ID fits are

displayed in Appendix D.3.

The tables and the graphs of the fits are repeated for the cases where the muons originate from J/ψ or Z decay. This approach is employed because the J/ψ have falling p_T^μ distributions beyond approximately 10 GeV, whereas the p_T^μ distributions for the Z boson rise until around 44 GeV. Therefore, studying the behavior of muon resolution uncertainties from different sources as a function of p_T^μ is valuable for understanding the underlying trends and discrepancies. The distinction of muons originating in Z decay or J/ψ decay is done by implementing a mass cut.

The fit is performed in the first Large Sector, and for 50 η bins from 0 to 2.60. To avoid redundancy only ME tracks are displayed in this subsection.

Bin	$\frac{r_0^{MC}-r_0^{Data}}{r_0^{Data}}\%$	$\frac{r_1^{MC}-r_1^{Data}}{r_1^{Data}}\%$	$\frac{r_2^{MC}-r_2^{Data}}{r_2^{Data}}\%$
0.05< η <0.10	0	8	0
0.10< η <0.15	0	2	0
0.15< η <0.20	0	2	0
1.20< η <1.25	3	3	18
1.25< η <1.30	0	4.	60
1.30< η <1.35	0	2	1
2.45< η <2.50	8	13	96
2.50< η <2.55	21	19	96
2.55< η <2.60	96	-14	-73

Table 4.1: Difference of parametrization fits in MC and Data for ME muons coming from J/ψ resonance decay.

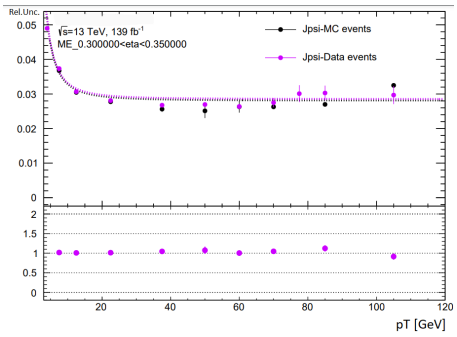

(a) $0.30 < \eta < 0.35$

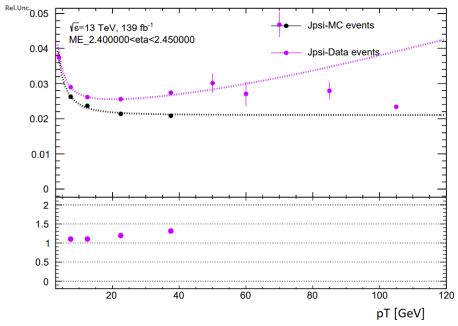

(b) $2.40 < \eta < 2.45$

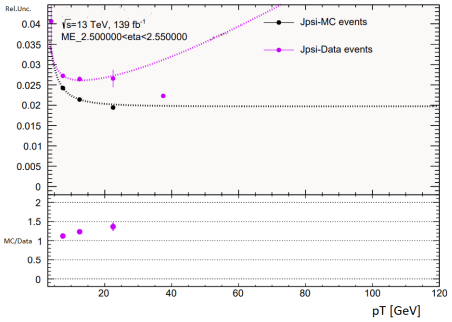

(c) $2.50 < \eta < 2.55$

Figure 4.14: Relative muon momentum uncertainty vs p_T^μ for MC and data using muons from J/ψ resonance decay for ME tracks

Muons from J/ψ decay-ME Table 4.1 displays the pull between MC and data of the fitted parameters r_0, r_1 and r_2, for ME muons originating from J/ψ resonance decay. Corresponding graphs of *rel.unc.* as a function of p_T^μ for data and simulation are displayed in the Figure 4.14. Both in the table and the relevant plots, the difference between simulation and data is increasing with η and p_T^μ.

Bin	$\frac{r_0^{MC}-r_0^{Data}}{r_0^{Data}}\%$	$\frac{r_1^{MC}-r_1^{Data}}{r_1^{Data}}\%$	$\frac{r_2^{MC}-r_2^{Data}}{r_2^{Data}}\%$
$0.05<\eta<0.10$	11	2	17
$0.10<\eta<0.15$	7	2	9
$0.15<\eta<0.20$	4	2	8
$1.20<\eta<1.25$	0	10	8
$1.25<\eta<1.30$	0	5	17
$1.30<\eta<1.35$	6	4	7
$2.45<\eta<2.50$	0	6	34
$2.50<\eta<2.55$	5	7	34
$2.55<\eta<2.60$	2	7	35

Table 4.2: Difference of parametrization Fits in MC and Data for ME muons coming from Z

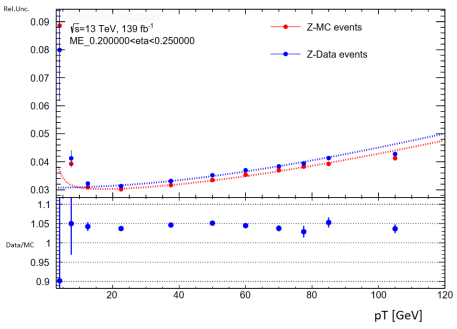

(a) $0.2 < \eta < 0.25$

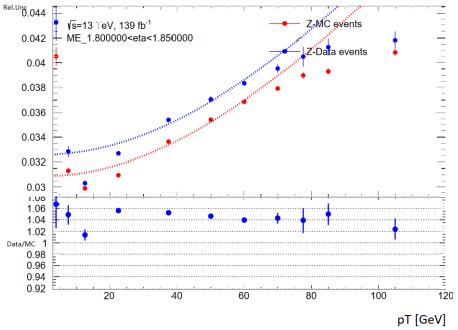

(b) $1.8 < \eta < 1.85$

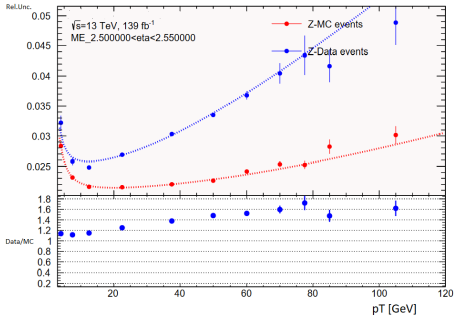

(c) $2.5 < \eta < 2.55$

Figure 4.15: Relative muon momentum uncertainty vs p_T^μ for MC and data using muons from Z resonance decay for ME tracks

Muons from Z decay-ME Table 4.2 displays the pull of the parameters r_0, r_1 and r_2, for ME muons originating from Z resonance decay. Corresponding graphs of *rel.unc.* as a function of p_T^μ for data and simulation are displayed in the Figure 4.15. Both in the table and the plots the difference between simulation and data is increasing with η and p_T^μ. In Figure 4.15, an example is displayed of failing fits ($1.8 < \eta < 1.85$), which fail to describe the points.

Failing fits exist in intermediate region. Due to complex magnetic field, the relative uncertainty parametrization deviates from standard form.

Notably, in the Figure 4.15, the difference between MC and data grows with p_T^μ and in the table 4.2 the parameter with the largest pull is the r_2, pointing at a mismatch at the r_2 parameter as also observed in Tables 4.1.

It is important to underline the fact that the difference seems larger for the third parameter r_2 of Relation 2.7 in the Tables 4.1 - 4.2, which is the one connected to the magnetic field. As expected, pulls are larger in regions where the magnetic field is complex.

Also by comparing the Z table and the J/ψ Table, from $1.4 < \eta < 1.45$ to $2.55 < \eta < 2.60$ the pull for r_2 between data and MC is larger for J/ψ case table ($\approx 70 - 80\%$) comparing to the Z case table ($\approx 30 - 50\%$).Since muons originating from the J/ψ decay have lower p_T^μ than those from the Z boson, this suggests that the pre-smearing correction may primarily benefit one of the two "standard candles." Consequently, the pre-smearing correction should be tested in calibrations involving only one of the resonances.

This discrepancy between the parameters fitted in data and MC in the ME fits signals a potential need to implement the pre-smearing corrections while fitting the dr_2 parameter.

4.1.4 Calibration with pre-smearing

4.1.4.1 Methodology

The dominant method used in this study is: derive a weight from the ratio maps and incorporate it in the correction calibration Relations 3.2, 3.3 and 3.4. The weight-correction derived is the bin content of the map that the muon belongs to. The correction is inserted in the calibration relation by multiplying it with a resolution calibration parameter during the fit. The study has been repeated for multiplying the correction with dr_1 and dr_2. As commented in Section 4.1.3, r_2 parameter deviates between MC and data, in parametric fits of $rel.unc.$ as a function of p_T^μ. Therefore, only the main results where the correction was multiplied with dr_2 parameter are going to be presented here. Rest of studies, including CB results and results of applying the corrections to dr_1 parameters, are not displayed here to avoid redundancy. The overall results were presented in the ATLAS Muon Performance Group to evaluate the method.

4.1.4.2 Results

Finally, in this section calibration results will be presented with the corresponding χ^2/Degrees of Freedom (D.o.F.). The $\chi^2/D.o.F.$ as a function of η is used as a validation of the overall method.

ID Results obtained from the ID tracks are displayed here.

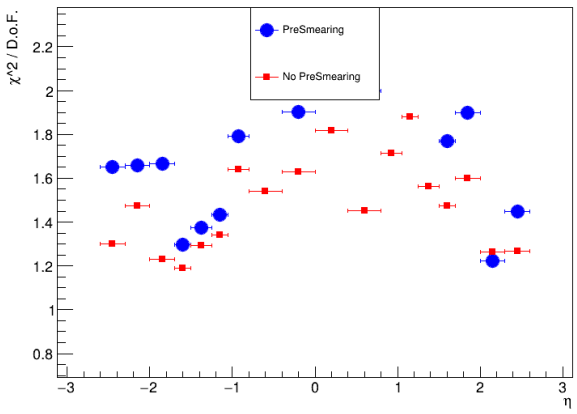

Figure 4.16: Nominal calibration and pre-smearing calibration χ^2/ Degrees of Freedom as a function of η for pre-smearing parameter dr_2, using J/ψ and Z, ID tracks

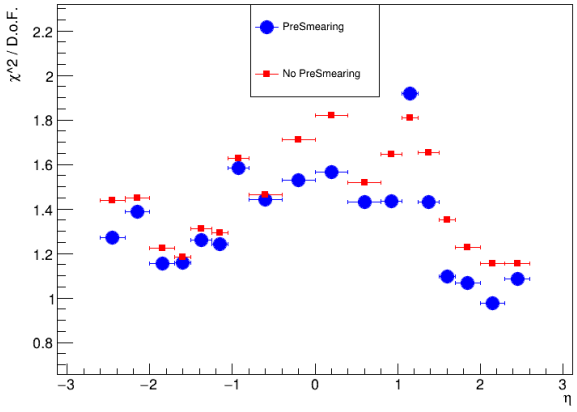

Figure 4.17: Nominal calibration and pre-smearing calibration χ^2/ Degrees of Freedom as a function of η for pre-smearing parameter dr_2, using Z, ID tracks

ME Results obtained from the ME tracks are displayed here.

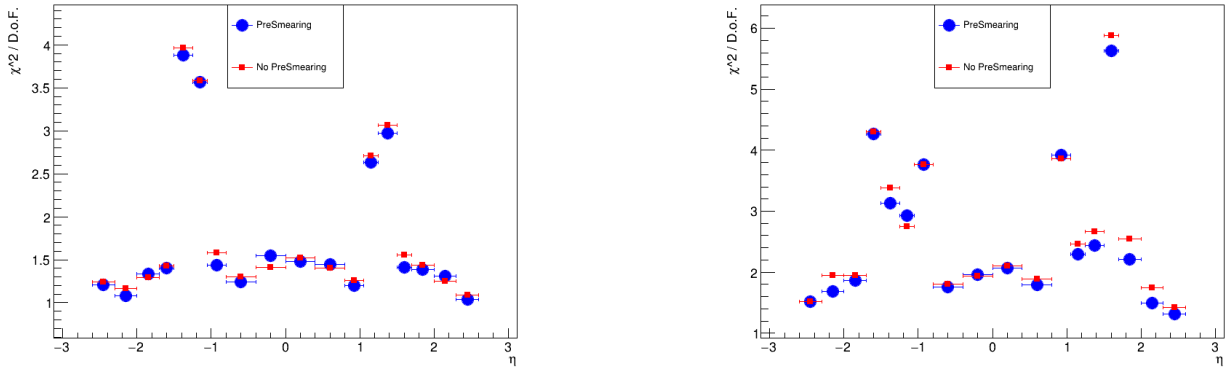

(a) Large Sectors

(b) Small Sectors

Figure 4.18: Nominal calibration and pre-smearing calibration χ^2/ Degrees of Freedom as a function of η for pre-smearing parameter dr_2, using Z, ME tracks

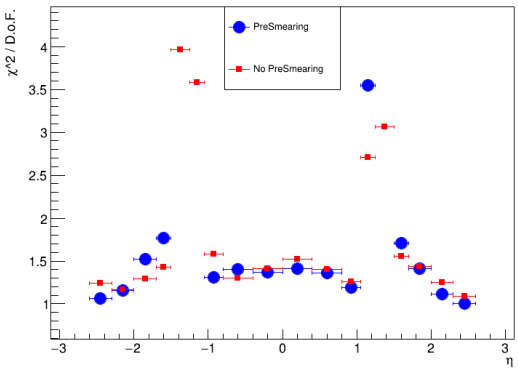

(a) Large Sectors

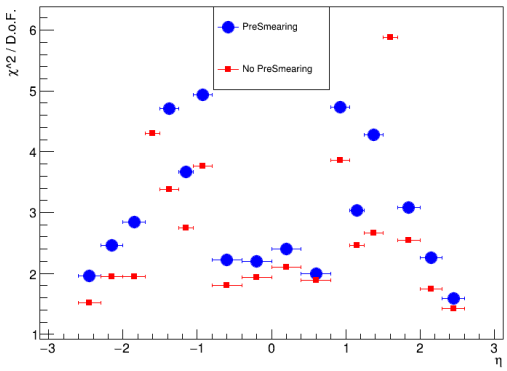

(b) Small Sectors

Figure 4.19: Nominal calibration and pre-smearing calibration χ^2/ Degrees of Freedom as a function of η for pre-smearing parameter dr_2, using Z and full Run-2 MC and Data, ME tracks

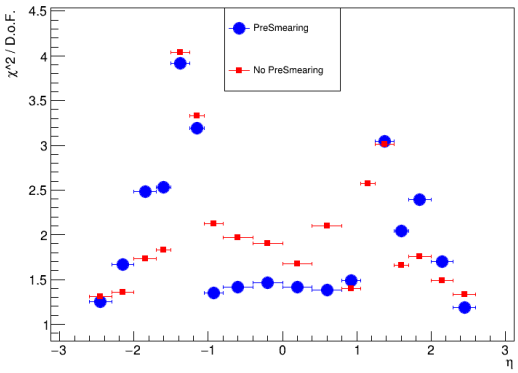

(a) Large Sectors

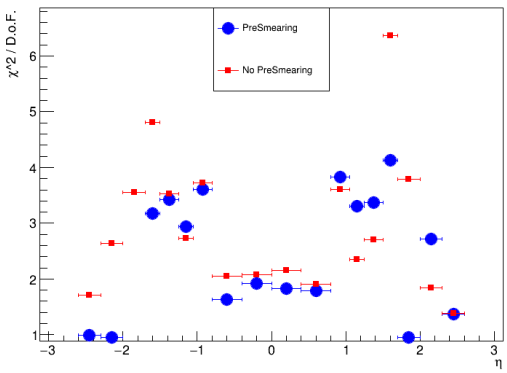

(b) Small Sectors

Figure 4.20: Nominal calibration and pre-smearing calibration χ^2/ Degrees of Freedom as a function of η for pre-smearing parameter dr_2, using J/ψ and Z, ME tracks

4.1.5 Conclusions

In the Section 4.1 the work performed in the context of QT for the ATLAS experiment, was presented. First, the derivation of muon *rel.unc.* was presented with corresponding graphs. Secondly, two dimensional maps (η, ϕ) of *rel.unc.* were presented, for different p_T^μ. Furthermore, the *rel.unc.* was studied as a function of p_T^μ. The difference between MC and data increased with p_T^μ. From parametric fits on the *rel.unc.* it was apparent that the r_2 parameter is the main parameter deviating between MC and data. For this reason the calibration dr_2 parameter was multiplied with the correction derived.

In the results presented in Section 4.1.4, a comparison between nominal and pre-smearing calibrations reveals that, in most cases, the method was unsuccessful. In some examples shown, there was notable improvement in the values of $\chi^2/D.o.F.$, such as applying the correction to Z resonance calibrations for the ID (Figure 4.17). Another example of reduced χ^2 is shown in the Figure 4.20 for calibrating Z and J/ψ for ME tracks. The results shown, were presented and passed to the experts for further analysis.

4.2 2017-Official Calibration Recommendations

In this Section, the results of the calibration, for the official recommendations of ATLAS Muon Performance group, are presented. The calibration is performed for the campaigns 2017 of ATLAS Run-2 and for all type of tracks: ID, CB and ME.

The calibration is fitting simultaneously the Z and J/ψ "standard candles". Goal is to have an accurate calibration for all η, ϕ and p_T^{μ}. Technical details and methodology of the ATLAS official calibration are presented in the Chapter 3. Selection and samples description are presented in the Chapter 3.5.

4.2.1 Data and simulation comparison

For completeness purposes, a set of kinematic variables is presented, for simulation and data. The distributions only for the J/ψ are presented in this Section. Regarding the Z samples the selection is similar to the one used for the main Z mass analysis of this thesis. Therefore, the display of kinematic variables in this Section is redundant. The corresponding plots are provided in Chapter 6.1.2.

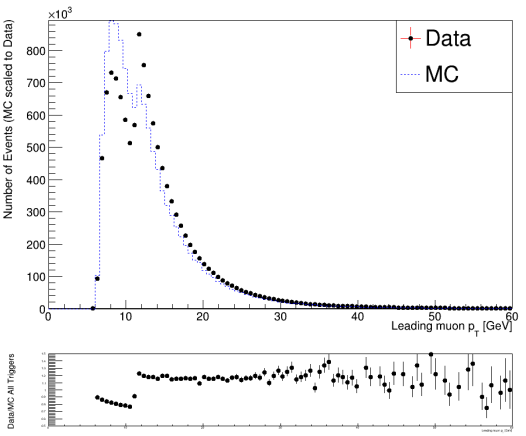

(a) Leading muon p_T^{μ}

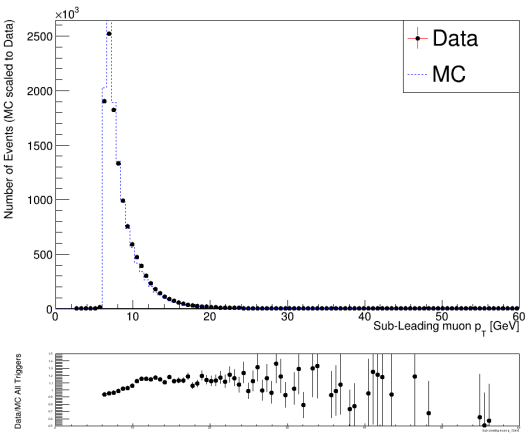

(b) Sub-leading muon p_T^{μ}

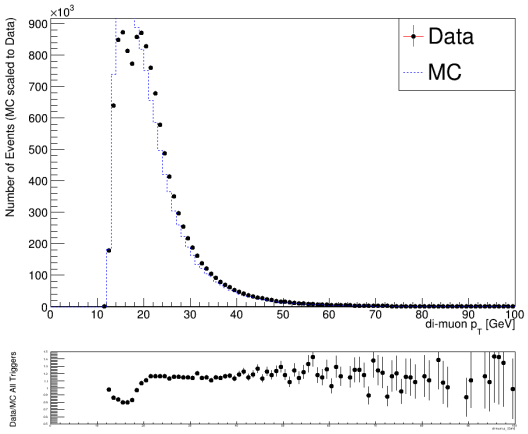

(c) di-muon $p_T^{\mu\mu}$

Figure 4.21: Comparison of data and simulation (J/ψ) for kinematic observables, for $2.8 < m_{\mu\mu} < 3.3$

In the Figure 4.21, kinematic distributions are displayed, in the mass integral $2.8 < m_{\mu\mu} < 3.3$, for simulation and data. In the Figure 4.21 (a), the $p_T^{leading-\mu}$ distributions is displayed. It is evident that there is a large effect in small $p^{leading-\mu_T} < 10$ GeV. The observed discrepancy

appears to be non-physical, likely resulting from unknown errors in the sample provided by the ATLAS Muon Momentum Calibration group. This error is believed to originate from an issue in the data distribution, potentially due to one of the triggers being unintentionally pre-scaled. Since the standard triggers used are typically not pre-scaled, this discrepancy suggests an error in the data preparation process. In the Figure 4.21 (b), the sub-leading p_T^{μ} distribution is displayed. The effect is negligible in this plot. In the Figure 4.21 (c), the $p_T^{\mu\mu}$ distribution is shown. The effect is again visible at values $p_T^{\mu\mu} < 20$ GeV.

4.2.2 Method

For the ID, CB and MS track types, different set of parameters are fitted as mentioned in Chapter 3. For ID and CB all parameters used in the track type are fitted during calibration, where in ME case the dr_2 is calculated with a tracking procedure and injected in the calibration procedure as constant.

The nominal case will be running until Iteration 20. From Iteration 1 to 8 is running on Simplex, and at Iteration 9 GridScan is added. The result from iteration 9-14 is averaged and the mean over iterations is used as input in iteration 15. This is expected to lead to the stabilization of the parameters in some regions. Finally, the average result from iteration 15 to 20 is taken as the nominal values of the parameters. For the systematic uncertainties, the iteration 12 to 20 is running and the average of even iterations is used as the value to be compared with the nominal. Finally to derive the systematic values for each region and for each parameter the distance of each systematic (average of even iterations 12-20) from the nominal (average iterations 15-20) is compared. The variation with the larger distance from the nominal will be regarded as the value of the systematic.

The list of calibration systematic uncertainties, along with the methodology used to derive them, is analyzed in Appendix C.

4.2.3 Results 2017

The Results from 2017 are presented here for the ID,CB and ME track types. For each track type, $m_{\mu\mu}$ distributions of barrel and end-cap regions are going to be presented. Only the Large Sector distributions of CB and ME are displayed here, to avoid redundancy. Additionally, the parameters of the calibration are going to be presented as a function of η for all track types.

4.2.3.1 ID

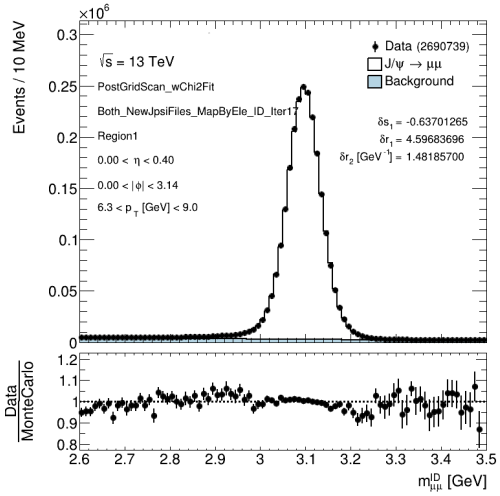

(a) J/ψ $6.3 < p_T^{sub-leading} < 9.0$ GeV

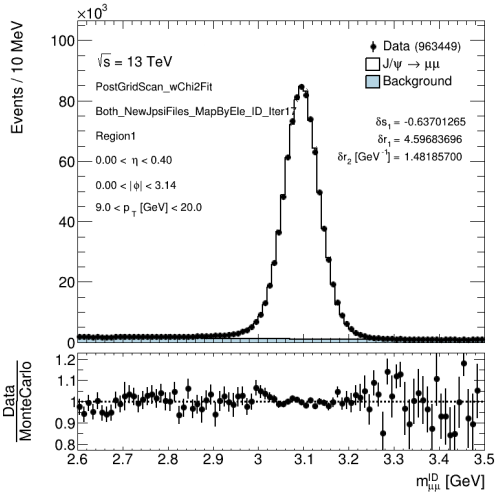

(b) J/ψ $9.0 < p_T^{sub-leading} < 20.0$ GeV

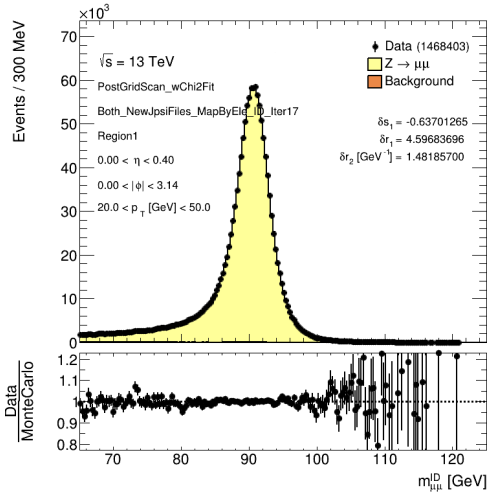

(c) Z $20.0 < p_T^{leading} < 50.0$ GeV

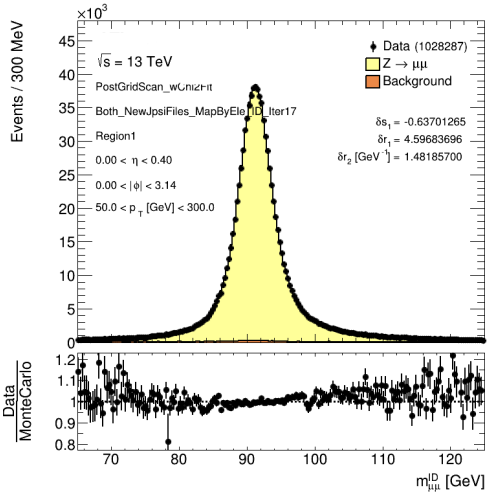

(d) Z $50.0 < p_T^{leading} < 300.0$ GeV

Figure 4.22: Region 1 ID: at least of the muons belong to the region $0 < \eta < 0.4$. $m_{\mu\mu}$ distributions for J/ψ and Z resonances, post GridScan distributions.

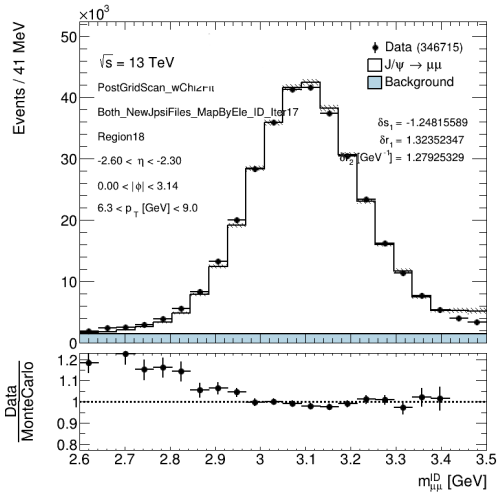

(a) J/ψ $6.3 < p_T^{sub-leading} < 9.0$ GeV

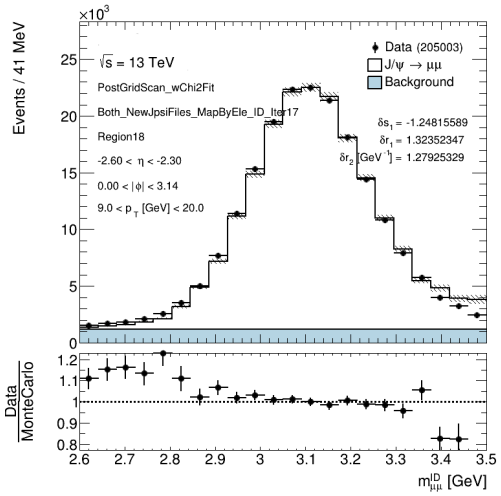

(b) J/ψ $9.0 < p_T^{sub-leading} < 20.0$ GeV

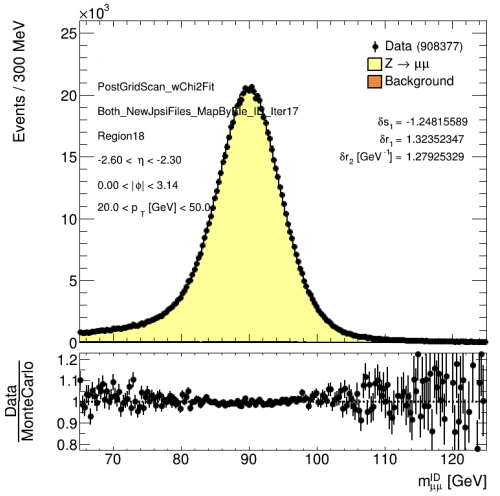

(c) Z $20.0 < p_T^{leading} < 50.0$ GeV

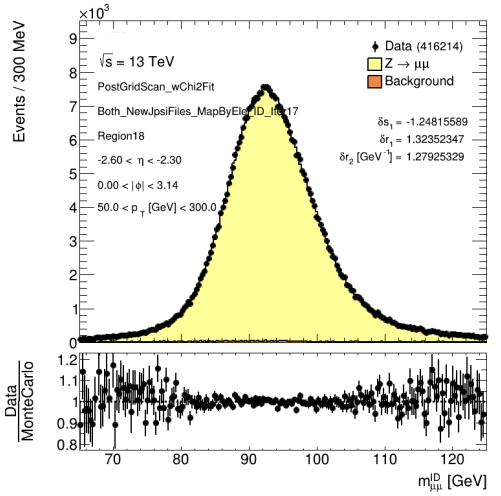

(d) Z $50.0 < p_T^{leading} < 300.0$ GeV

Figure 4.23: Region 18 ID: at least of the muons belong to the region $-2.6 < \eta < -2.3$. $m_{\mu\mu}$ distributions for J/ψ and Z resonances, post GridScan distributions.

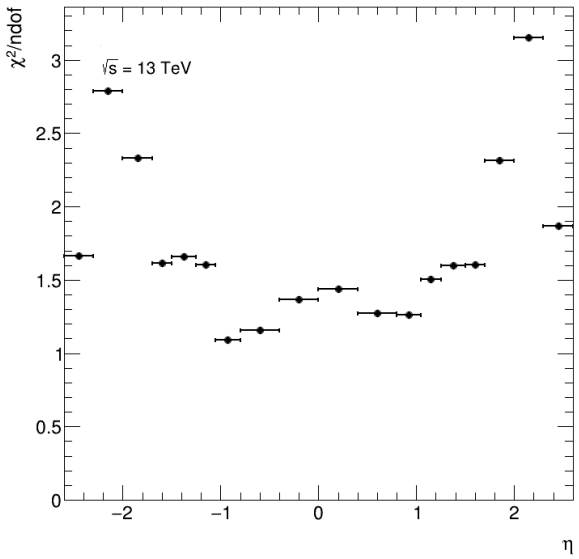

Figure 4.25: $\chi^2/D.o.F.$ between the signal+background and data mass distributions, after calibration, as a function of η, for 2017 ID tracks.

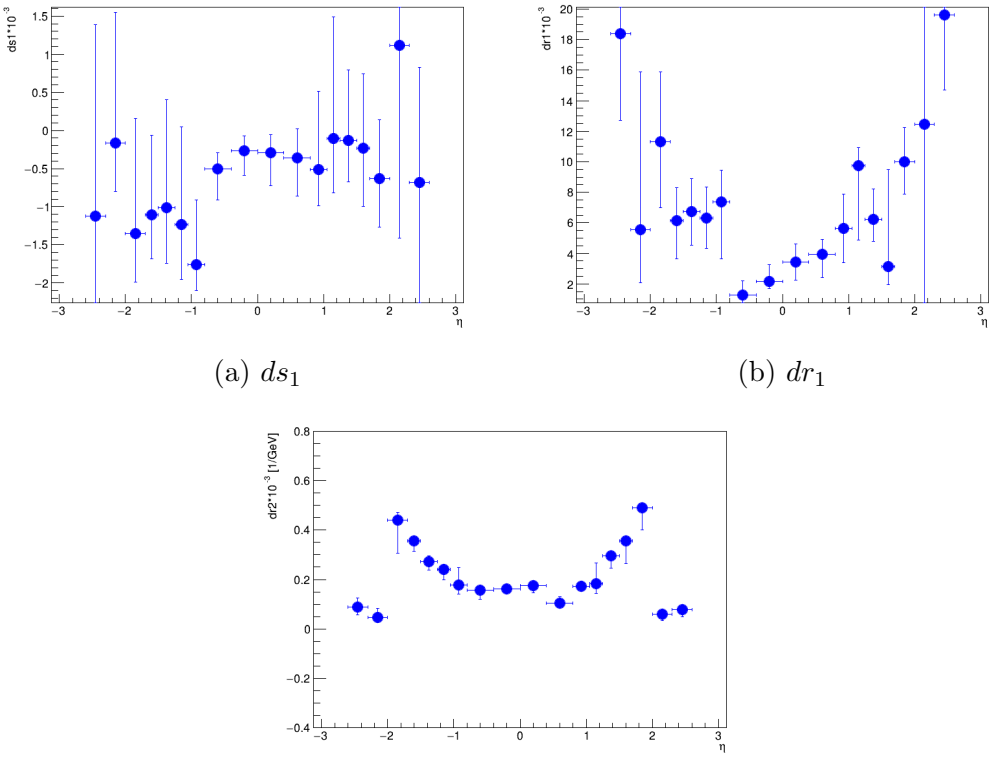

(a) ds_1 (b) dr_1

(c) dr_2

Figure 4.24: ds_1,dr_1 and dr_2 muon momentum calibration corrections as a function η for 2017 ID tracks. Points are average over iterations and error bars are systematic uncertainties.

In the Figures 4.22 and 4.23, two examples from ID track $m_{\mu\mu}$ distributions are displayed, for barrel and end-cap regions. There is a large widening of the distributions from the barrel to the end-caps. This originates in the poor momentum resolution of the ID for $|\eta| > 1.05$.

In the Figure 4.24 the calibration parameters ds_1, dr_1 and dr_2 are shown as a function

of η. The ds_1 exhibits small error bars in the barrel region, originating in the Z and J/ψ different scales systematic uncertainty. Where in more forward regions, outside the barrel, the ID tracks have a considerably worse performance. The fits at these regions are unstable leading to increased systematic uncertainties.

Notably there is an asymmetry in the scale as a function of η and specifically in the outermost barrel ($0.8 < |\eta| < 1.05$). The shapes seen in the negative values, at $\eta \approx -1.1$, originate from the measurement of the magnetic solenoid field. Due to an asymmetry in the way it was measured, the scale correction is larger for this region.

In Figure 4.24 (b), the dr_1 parameter is plotted as a function of η. In the forward regions, muons traverse more material and are consequently subjected to increased multiple scattering. As a result, muons in these regions require larger dr_1 corrections compared to those in the barrel region.

In the Figure 4.24 (c) the dr_2 parameters is shown as a function of η. The dr_2 behavior follows magnetic field patterns in the detector.

4.2.3.2 CB

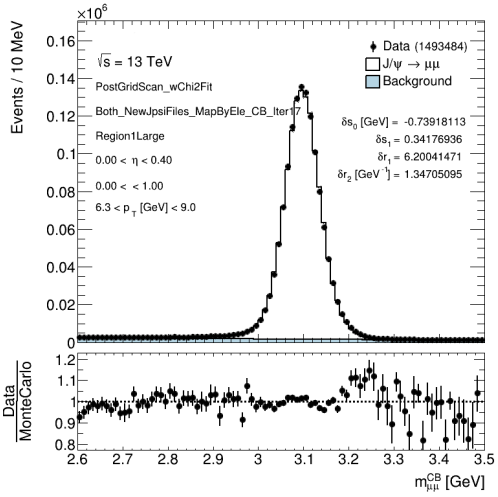

(a) J/ψ $6.3 < p_T^{sub-leading} < 9.0$ GeV

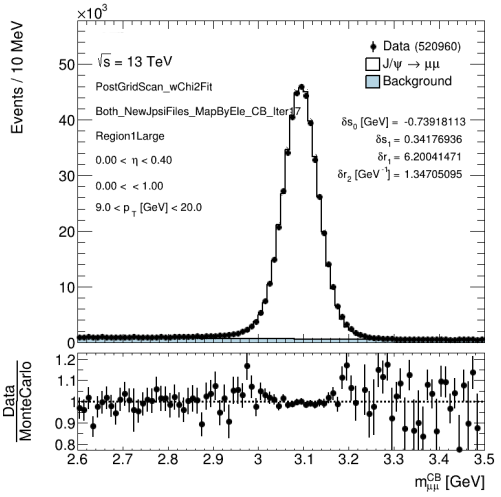

(b) J/ψ $9.0 < p_T^{sub-leading} < 20.0$ GeV

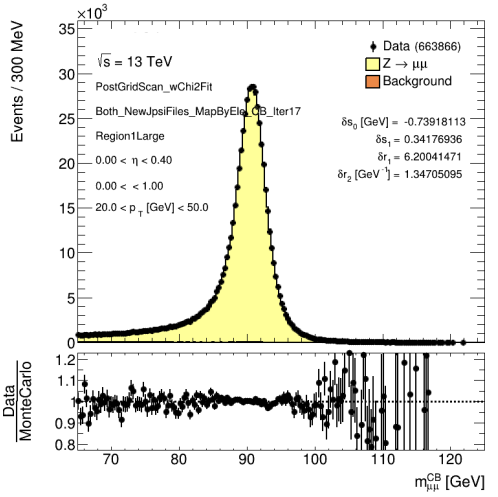

(c) Z $20.0 < p_T^{leading} < 50.0$ GeV

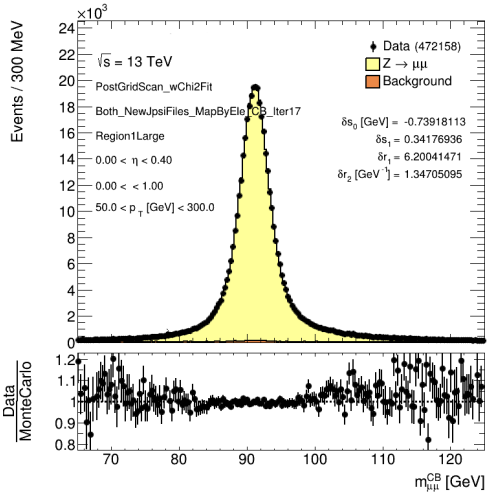

(d) Z $50.0 < p_T^{leading} < 300.0$ GeV

Figure 4.26: Region 1 Large CB: at least of the muons belong to the region $0 < \eta < 0.4$, First Large Sector. $m_{\mu\mu}$ distributions for J/ψ and Z resonances, post GridScan distributions.

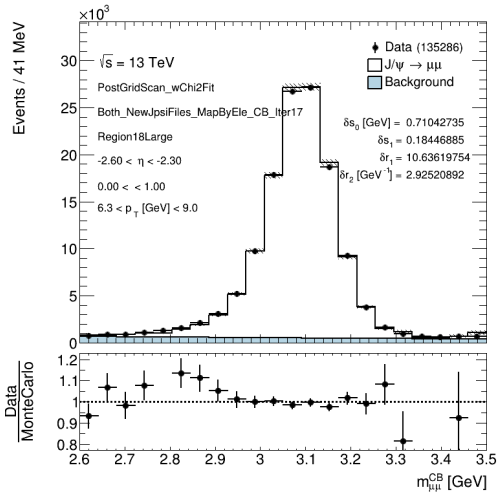

(a) J/ψ $6.3 < p_T^{sub-leading} < 9.0$ GeV

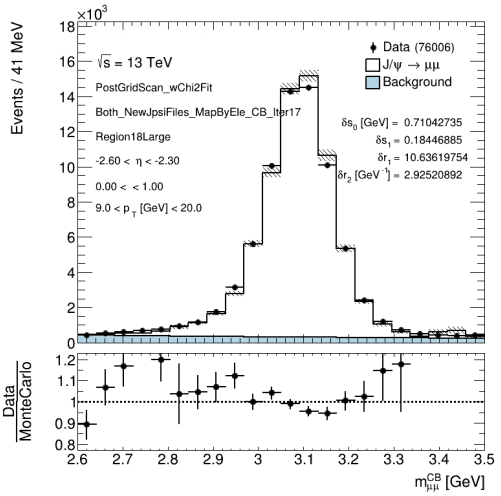

(b) J/ψ $9.0 < p_T^{sub-leading} < 20.0$ GeV

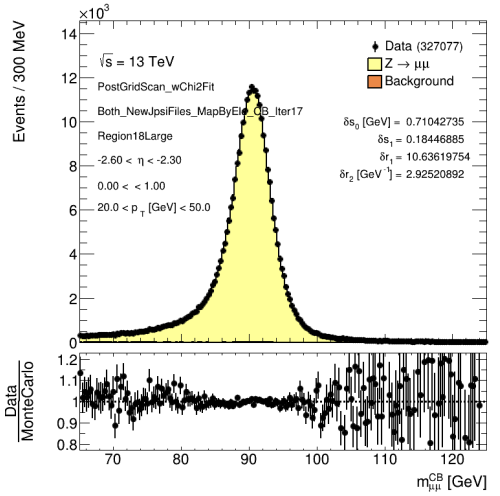

(c) Z $20.0 < p_T^{leading} < 50.0$ GeV

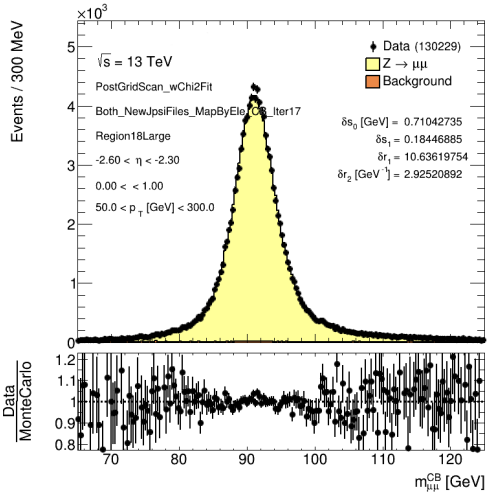

(d) Z $50.0 < p_T^{leading} < 300.0$ GeV

Figure 4.27: Region 18 Large CB: at least of the muons belong to the region $-2.6 < \eta < -2.4$, Large Sector. $m_{\mu\mu}$ distributions for J/ψ and Z resonances, post GridScan distributions.

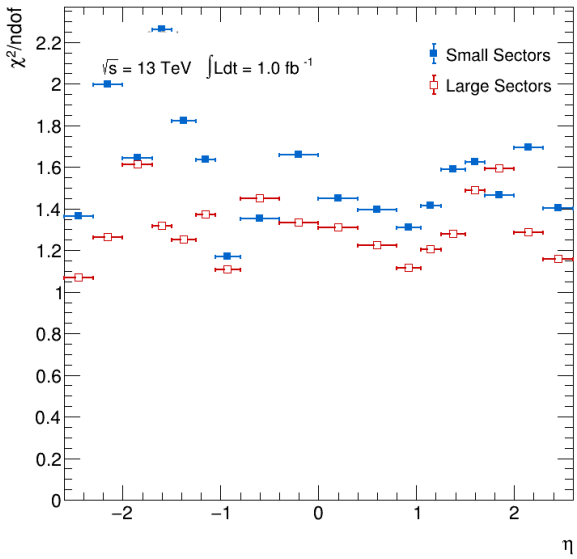

Figure 4.29: $\chi^2/D.o.F.$ between the signal+background and data mass distributions, after calibration, as a function of η, for 2017 CB tracks.

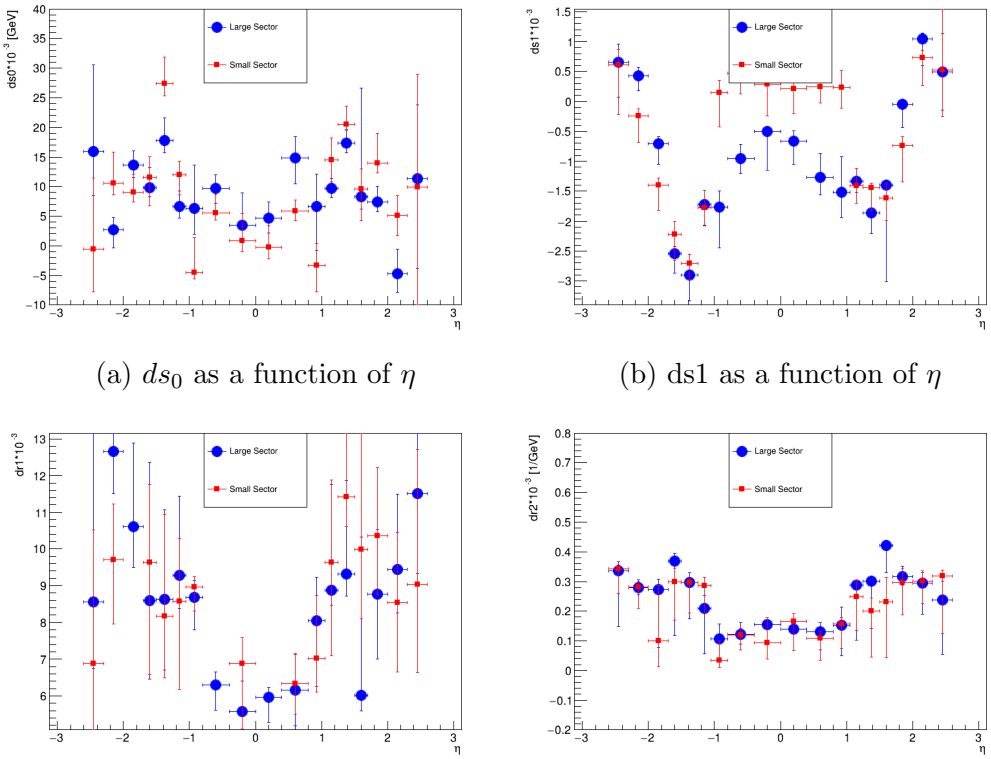

(a) ds_0 as a function of η

(b) ds1 as a function of η

(c) dr1 as a function of η

(d) dr2 as a function of η

Figure 4.28: ds_0, ds_1,dr_1 and dr_2 muon momentum calibration corrections as a function of η for 2017 CB tracks. Points are average over iterations and error bars are systematic uncertainties.

The $\chi^2/D.o.F.$ is displayed in the Figure 4.29, for the nominal calibration. The fit is less successful at the end-cap and the intermediate region than the barrel. Intermediate region has the larger values in $\chi^2/D.o.F.$. In these regions, the magnetic field exhibits complex structures, making it challenging for the fit to accurately account for them.

The graphs of muon momentum corrections for both scale and resolution, shown in Figures 4.28, indicate that the corrections are generally larger in the intermediate region compared to the barrel and end-cap. This observation aligns with the presence of more complex magnetic field structures in the intermediate region, as evidenced by the higher correction values.

In the Figure 4.28, the scale parameter ds_0 is plotted as a function of η for the Small and Large Sectors. The ds_0 parameter exhibits large systematic uncertainties, making it difficult to separate its dependence from η.

In the Figure 4.28 (b), the ds_1 scale is plotted as a function fo η for Small and Large Sectors.

In the barrel region, the large sectors require larger corrections compared to the small sectors. According to experts, this discrepancy arises from the challenges in accurately measuring the magnetic field in the large sectors of the barrel. Regarding larger η, Small and Large ds_1 corrections are converging. In both the cases there is a structure at ≈ 1.4, where a large absolute value of ds_1 is needed. In this region the magnetic field is particularly complex and hard to model. Also in this region the toroid field reaches 0 Tesla value, as mentioned in Chapter 2.2.3, making the region even more sensitive to mis-modelings.

In the Figures 4.28 (c) and (d), the resolution parameters dr_1 and dr_2 are plotted as a function of η, for Small and Large Sectors. The two sectors converge for the resolution parameters. Their dependence from η is almost uniform in the barrel regions. At intermediate regions there is an increase of the resolution parameters values, and it drops for high $|\eta| > 2$. Since the CB tracks are a combination of MS and ID tracks, and the two resolution parameters are highly correlated, disentangling and explaining this behavior becomes challenging.

4.2.3.3 ME

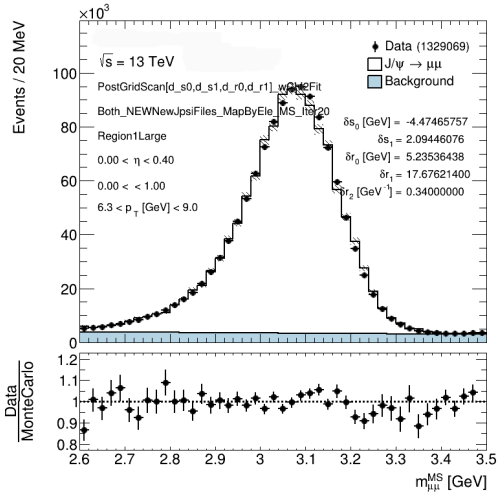

(a) J/ψ $6.3 < p_T^{sub-leading} < 9.0$ GeV

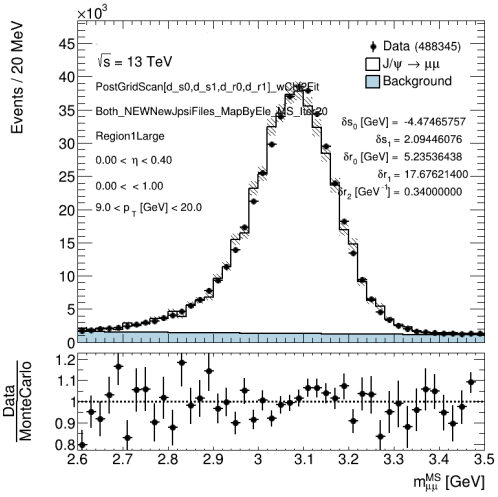

(b) J/ψ $9.0 < p_T^{sub-leading} < 20.0$ GeV

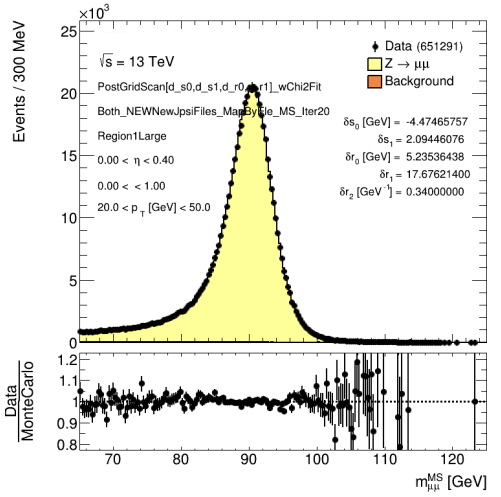

(c) Z $20.0 < p^{leading} < 50.0$ GeV

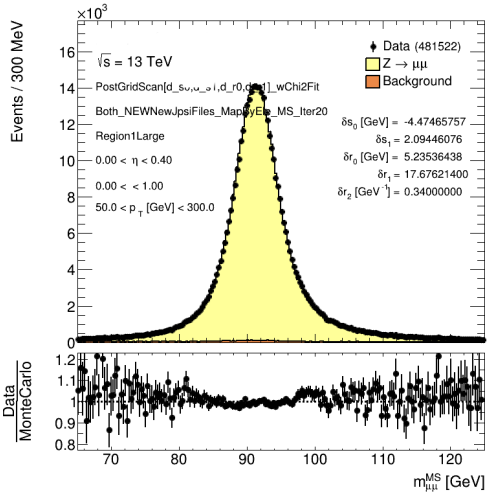

(d) Z $50.0 < p^{leading} < 300.0$ GeV

Figure 4.30: Region 1 Large ME: at least of the muons belong to the region $0 < \eta < 0.4$, First Large Sector. $m_{\mu\mu}$ distributions for J/ψ and Z resonances, post GridScan distributions.

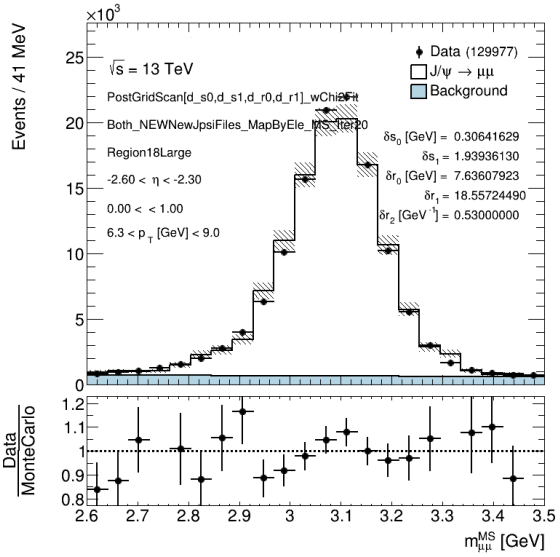

(a) Mass J/ψ, $6.3 < p_T^{\text{sub-leading}} < 9.0$ GeV

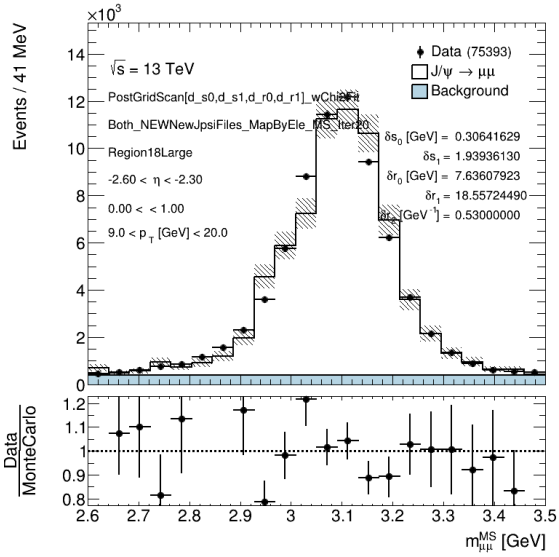

(b) Mass J/ψ, $9.0 < p_T^{\text{sub-leading}} < 20.0$ GeV

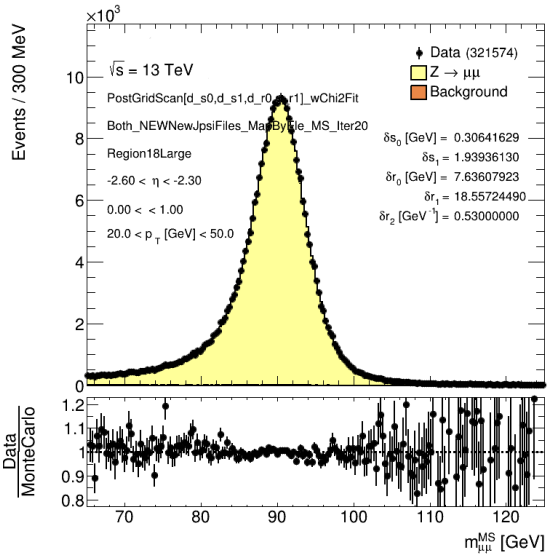

(c) Z boson, $20.0 < p_T^{\text{leading}} < 50.0$ GeV

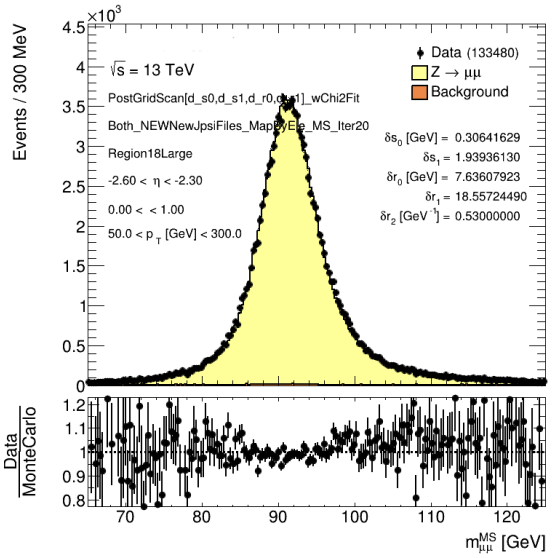

(d) Z boson, $50.0 < p_T^{\text{leading}} < 300.0$ GeV

Figure 4.31: Region 18 Large ME: At least one of the muons belongs to the region $-2.6 < \eta < -2.3$, Large Sector. $m_{\mu\mu}$ distributions for J/ψ and Z resonances, post GridScan distributions.

The correction parameters and the $\chi^2/D.o.F.$ as a function of η are displayed in the Figures 4.32 and 4.33.

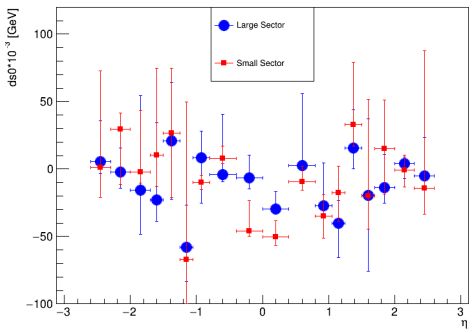

(a) ds_0 as a function of η

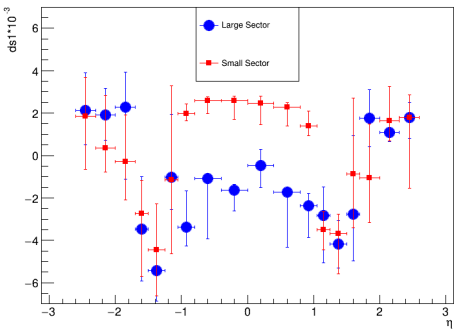

(b) ds_1 as a function of η

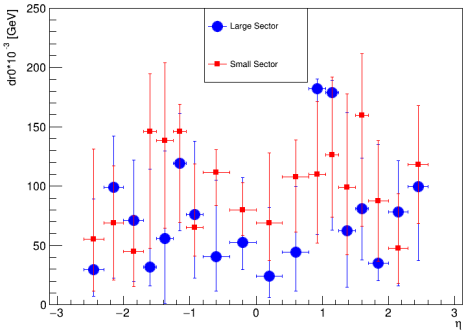

(c) dr_0 as a function of η

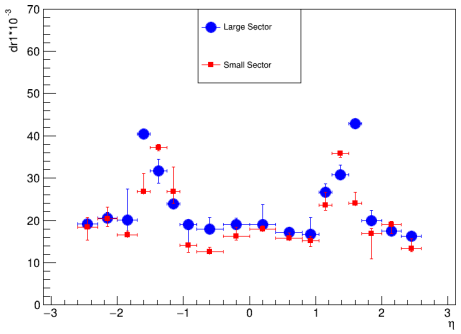

(d) dr_1 as a function of η

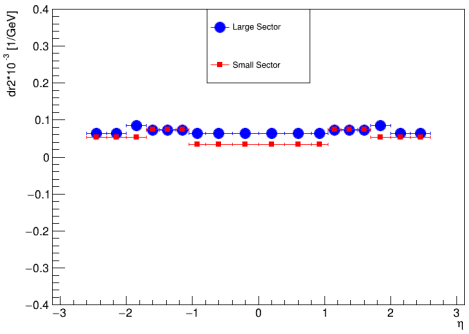

(e) dr_2 as a function of η

Figure 4.32: ds_0 and ds_1,dr_0 dr_1 and dr_2 muon momentum corrections as a function of η for 2017 ME tracks. Points are average over iterations and error bars are systematic uncertainties.

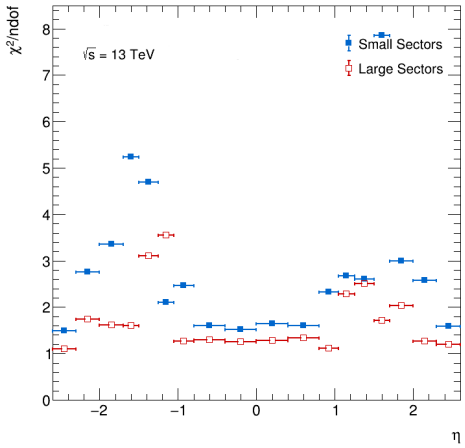

Figure 4.33: $\chi^2/D.o.F.$ between the signal+background and data mass distributions, after calibration, as a function of η, for 2017 ME tracks.

The results of the calibration for the MS are displayed for two examples of barrel and end-cap region in the Figures 4.30 and 4.31. The end-cap distributions, are comparable in variance with the barrel distributions, pointing to the relatively increased performance of MS at the end-cap compared to the ID.

In Figure 4.32 the scale parameters ds_0, ds_1 and the resolution parameters dr_0, dr_1 and dr_2 are displayed as a function of η for Large and Small Sectors. Their behavior is similar to the case of the Figure 4.28, for CB tracks. Therefore, their commenting is redundant and they are displayed for completeness.

In the $\chi^2/D.o.F.$ graphs for the CB (Figure 4.29) and the ME (Figure 4.33) the Small Sectors exhibits larger $\chi^2/D.o.F.$ values than the Large Sector. This discrepancy arises from the more complex magnetic field structures in the Small Sectors, which are more challenging to model accurately compared to the field in the Large Sectors.

In all post calibration $m_{\mu\mu}$ plots, a noticeable difference in the calibration quality is observed between the J/ψ and Z resonances. The Z plots exhibit a successful closure and the ratio plots are flat under the peak. In the J/ψ case, there are remaining structures in the ratio plots. This is connected to a major theme of this thesis, as it hinders the dependence of the scale from p_T^{μ}. As mentioned, the calibration is favoring the Z resonance due to the greater availability of simulated events. Consequently, a non closure in the J/ψ post fit plots is appearing. This is treated with a systematic of scale calibration in the official ATLAS algorithm.

4.2.4 Validation

Using the validation framework, the calibration is systematically evaluated for the Z resonance. The mean and variance of the $m_{\mu\mu}$ distributions, in simulation and data, are compared as functions of $\eta^{leading-\mu}$, $\phi^{leading-\mu}$, and $p_T^{leading-\mu}$, pre and post-calibration. Validation is displayed for CB tracks, other track types are not presented here to avoid redundancy, given their similarity to the CB track calibration results. The J/ψ validation is presented in the Appendix E. Non closures and problematic calibration regions will be reported to the corresponding muon calibration team of ATLAS.

4.2.4.1 CB Z

$\eta^{\mathbf{leading-\mu}}$: In Figures 4.34 and 4.35, the mean and the σ of the $m_{\mu\mu}$ distributions are displayed as a function of $\eta^{leading-\mu}$.

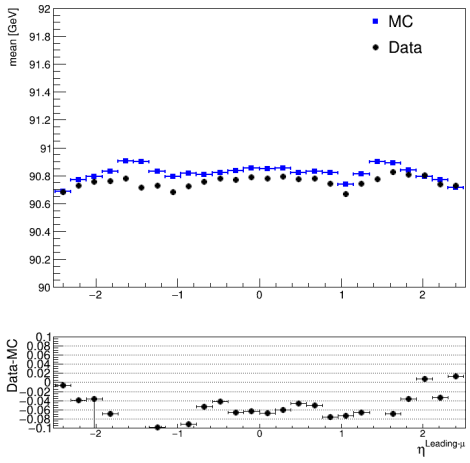

(a) Pre-calibration

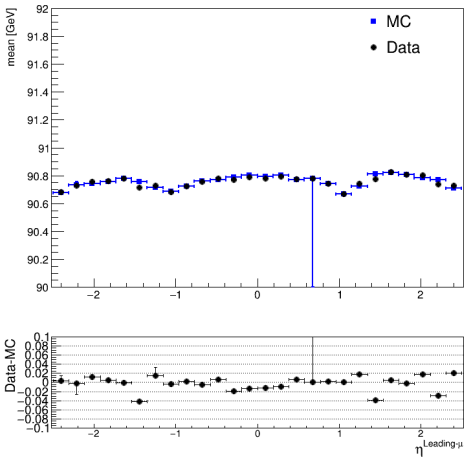

(b) Post-calibration

Figure 4.34: Pre and post calibration mean of $m_{\mu\mu}$ distribution ($70 < m_{\mu\mu} < 110$ GeV) as a function of $\eta^{leading-\mu}$.

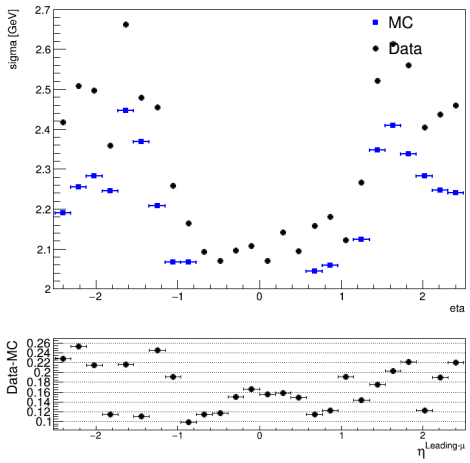

(a) Pre-calibration

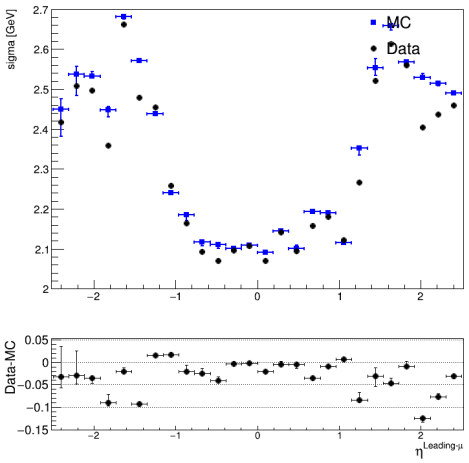

(b) Post-calibration

Figure 4.35: Pre and post calibration σ_{CR} of $m_{\mu\mu}$ distribution ($70 < m_{\mu\mu} < 110$ GeV) as a function of $\eta^{leading-\mu}$.

Regarding mean, a dependence with $\eta^{leading-\mu}$ is observed pre-calibration, both in simulation and data. This dependence originates primarily in the magnetic field in both cases. While the magnetic field shape is modeled in both data and MC samples, certain biases present in the data are absent in the MC. Consequently, the dependence of the mean on $\eta^{leading-\mu}$ appears smoother in the MC samples.

There is an approximately flat dependence of the mean in the barrel and at the intermediate region there is a clear structure for $1 < |\eta^{leading-\mu}| < 1.5$. This structure arises from the intricate nature of the toroidal magnetic field in this region. Before the calibration, the corresponding region has the largest difference between MC and data, and especially at $|\eta^{leading-\mu}| \approx 1.5$, more than 0.1%. This is caused by the magnetic field "hole" at the solenoid field and generally it's complex shape in that region, as mentioned in Chapter 2.2.3.

Post-calibration, the agreement reaches the level of 10^{-3} GeV in the majority of the regions, while in others it deteriorates up to 2×10^{-2} GeV. The intermediate region exhibits outliers

with significant non-closure. This is attributed to the complex magnetic field structures in this area, highlighting the need for finer binning in the calibration to capture all underlying effects. The high-uncertainty bin observed in the Figure 4.34 (b) originates from a failed parametric fit of the $m_{\mu\mu}$ distribution.

Regarding σ, a clear dependence with $\eta^{leading-\mu}$ is observed. This is primarily due to the varying resolution of the detector systems across different η regions, which affects the precision of muon momentum measurements. The barrel region exhibits the best resolution, as the CB tracks are closely aligned with the ID, where the Inner Detector provides high-precision measurements. In forward regions, the momentum resolution deteriorates, leading to a broadening of the $m_{\mu\mu}$ distributions. In very high $|\eta|$, the CB tracks increasingly resemble the ME tracks, resulting in a decrease in σ.

Before calibration, the agreement between data and MC is approximately 2×10^{-1} GeV. After calibration, it improves significantly to 1×10^{-2} GeV in the barrel region and 5×10^{-2} GeV in the forward regions. However, in the positive forward $\eta^{leading-\mu}$ region, outliers remain with discrepancies up to 10^{-1} GeV. These non-closures in $\eta^{leading-\mu}$ require further investigation by the ATLAS muon calibration group.

Overall, the majority of the regions exhibit a negative $\sigma_{data} - \sigma_{MC}$ after the calibration. Over smearing, is a known problem with the current calibration algorithm of ATLAS and there are active studies in the calibration group to address this issue.

$\phi^{\mathbf{leading-\mu}}$: In the Figures 4.36 and 4.37, the mean and the σ of the $m_{\mu\mu}$ distributions are displayed as a function of $\phi^{leading-\mu}$.

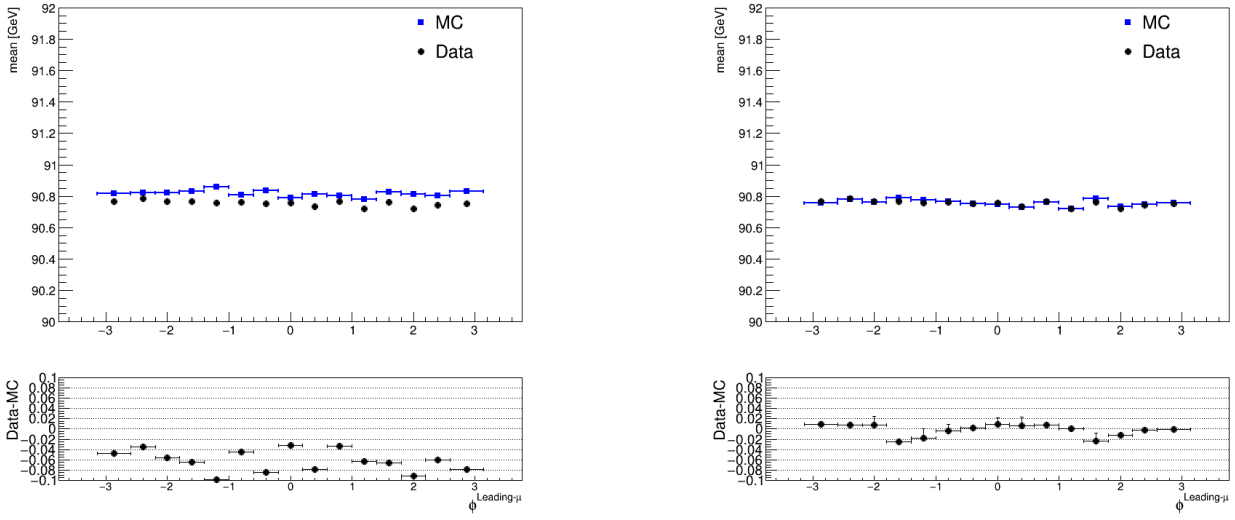

(a) Pre-calibration

(b) Post-calibration

Figure 4.36: Pre and post calibration mean of $m_{\mu\mu}$ distribution ($70 < m_{\mu\mu} < 110$ GeV) as a function of $\phi^{leading-\mu}$.

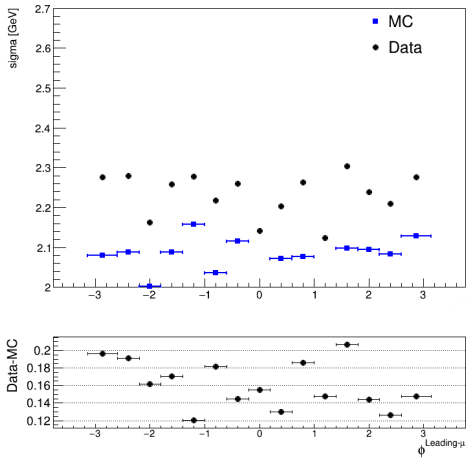

(a) Pre-calibration

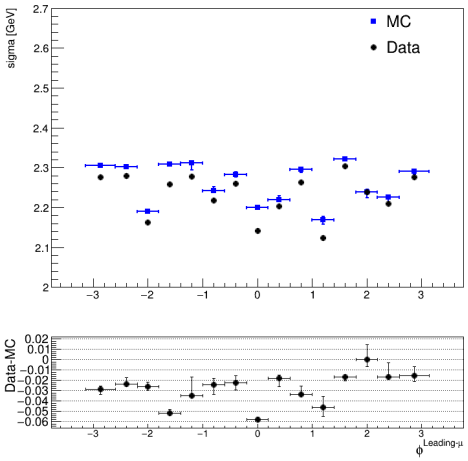

(b) Post-calibration

Figure 4.37: Pre and post calibration σ_{CR} of $m_{\mu\mu}$ distribution ($70 < m_{\mu\mu} < 110$ GeV) as a function of $\phi^{leading-\mu}$.

Overall, the mean and σ exhibit a weaker dependence on $\phi^{leading-\mu}$ compared to $\eta^{leading-\mu}$. This dependence arises from detector deformations and the complex structures of the toroid magnetic field between the large and small sectors.

Comparison of the mean figures, pre and post-calibration, reveals that the calibration effectively addresses the discrepancies observed prior to calibration. Before calibration, the difference between MC and data is approximately 5×10^{-2} GeV. Post-calibration, most regions exhibit an agreement within 10^{-3} GeV, with some outliers around -0.02 GeV. In these regions, the toroid magnetic field becomes complex, and the current calibration binning lacks the resolution to fully capture the underlying structures.

The σ exhibits a smaller dependence with $\phi^{\text{leading-}\mu}$ compared to the $\eta^{\text{leading-}\mu}$ case. Post-calibration, an over-smearing effect is observed in the $\sigma_{\text{data}} - \sigma_{\text{MC}}$ plot, similar to the one shown for $\eta^{\text{leading-}\mu}$, in Figure 4.35 (b).

$\mathbf{p_T^{leading-\mu}}$: In the Figures 4.38 and 4.39, the mean and the σ of the $m_{\mu\mu}$ distributions are displayed as a function of $p_T^{leading-\mu}$.

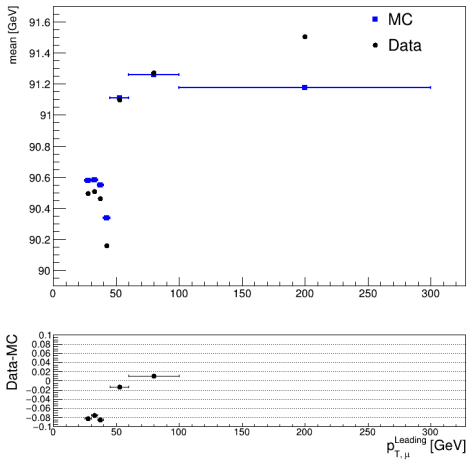

(a) Pre-calibration

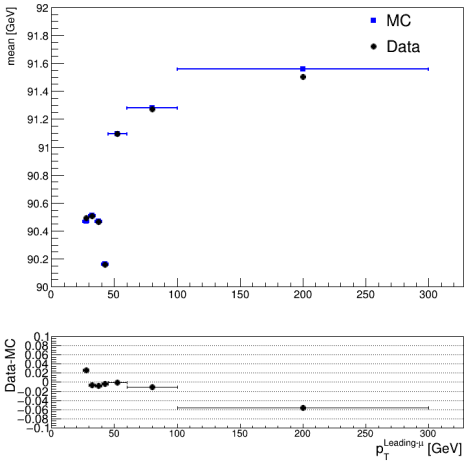

(b) Post-calibration

Figure 4.38: Pre and post calibration mean of $m_{\mu\mu}$ distribution ($70 < m_{\mu\mu} < 110$ GeV) as a function of $p_T^{leading-\mu}$.

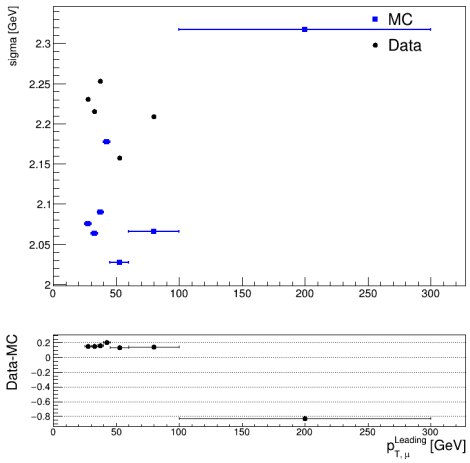

(a) Pre-calibration

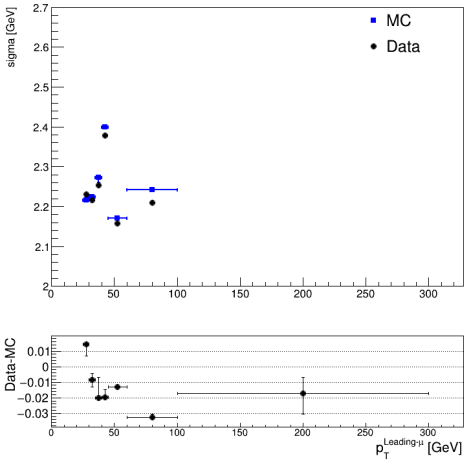

(b) Post-calibration

Figure 4.39: Pre and post calibration σ_{CR} of $m_{\mu\mu}$ distribution ($70 < m_{\mu\mu} < 110$ GeV) as a function of $p_T^{leading-\mu}$.

Regarding the mean, a distinct dependence of the mean with $p_T^{\text{leading-}\mu}$ is exhibited, in simulation and data. This dependence primarily arises from kinematic effects and the background mass distribution. Additionally, the agreement between MC and data also exhibits a $p_T^{\text{leading-}\mu}$ dependence. This is a known issue, originating from a non-closure of the calibration function, and is a major factor addressed in this thesis.

The $\text{mean}_{\text{data}} - \text{mean}_{\text{MC}}$, in the first bin $25 < p_T^{\text{leading-}\mu} < 30$ GeV, is positive. This phenomenon arises because the calibration is optimized to describe the data best around the Z p_T^{μ} regime (approximately 44 GeV). In subsequent bins, there is excellent agreement, within the order of 10^{-3} GeV. However, in the last bin, where $p_T^{\text{leading-}\mu} > 100$ GeV, the agreement deteriorates to 6×10^{-2} GeV. This discrepancy at high p_T^{μ} is treated as a systematic uncertainty in the standard ATLAS calibration approach.

4.2.5 Conclusions

In this section, the official recommendations for ATLAS muon momentum calibration were presented. In the first part, $m_{\mu\mu}$ distributions were presented for the different tracks, alongside with the fitted calibration corrections. The method showed a closure on the Z resonance. From the validation plots it is apparent that there is an average closure in the order of 10^{-3} GeV for the mean, and 10^{-2} GeV for the σ.

Lastly, a comparison is made between the recommendations prepared in this thesis and the official ones from ATLAS for another release of samples. In the Figure 4.40, the mean of $m_{\mu\mu}$ distributions is shown as a function of $\eta^{leading-\mu}$, using muons originating from Z resonance decay, for the two validations. A comparison demonstrates that the calibration developed in this thesis achieves a level of precision comparable to that of the previous ATLAS recommendations. There is a notable difference in the uncertainties between the two validations. The uncertainties presented in this thesis have smaller error bars, suggesting a potential underestimation of uncertainties. Since validation is an ongoing project, this is something to investigate further.

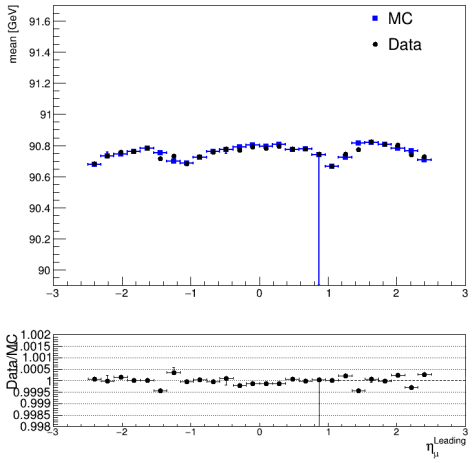

(a) Post calibration validation prepared in the context of the thesis and muon momentum group recommendations

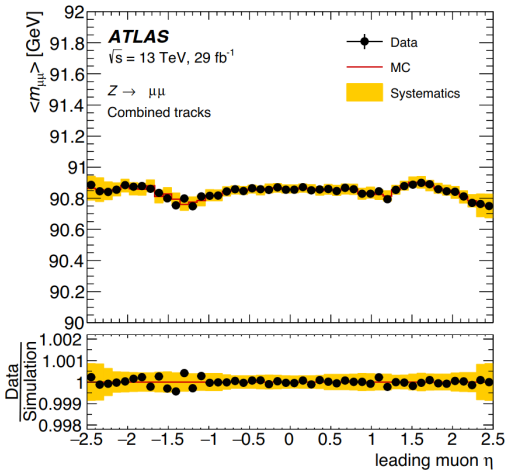

(b) Post calibration validation of ATLAS recommendation, taken from ref. [46]

Figure 4.40: Post calibration figures of mean$_{m_{\mu\mu}}$, as a function of $\eta^{leading-\mu}$, for the calibration recommendations prepared in this thesis and the official ATLAS recommendations of a previous release. Muons originate from the Z resonance decay.

Further non closures and discrepancies are to be reported in the Muon Momentum Calibration group of ATLAS, as the recommendations extraction is a project in progress.

Chapter 5

Calibration for Z Boson Mass

Contents

In this Chapter the calibration for the Z mass studies are going to be analyzed. First, the challenges and the overall strategy are going to be discussed. A study regarding the Prompt J/ψ, which are directly produced in the collision, and Non-Prompt J/ψ, which originate from the decay of longer-lived particles such as b-hadrons, is analyzed. This study influences the muon kinematic selection in the main calibration algorithm. The results of the calibration, in the context of the Z mass measurement, as a function of η^μ and p_T^μ separately are presented.

Results for the calibration as a function of p_T^μ are presented for different trigger configurations. Different trigger choices introduce different selections to the kinematic variables. This can influence heavily the kinematic distributions and their agreement between simulation and data. For the precision required for a Z boson mass measurement to include and study these effects is important.

5.1 Strategy for a Z Boson Mass Measurement Calibration

5.1.1 Introduction

The Z boson mass measurement in ATLAS requires a stable and accurate calibration, with as negligible uncertainty contribution as possible. The main challenge in the analysis is the reconstruction of the leptons which introduces reconstruction systematic effects in contrast with the LEP measurement which did not require such a procedure as described in the Chapter 1.

Therefore reconstruction related biases have to be corrected before moving to the measurement. This procedure is done through p_T^μ calibration. First, the calibration must account for charge dependent effects, which should, in principle, have minimal impact on the Z mass measurement, as they primarily affect the tails of the mass distribution. Second, the charge independent effects have to be corrected, which account primarily for magnetic field miss-modeling and multiple scattering. In the Inner Detector calibration configuration, there are three parameters, which account for scale and resolution effects, have to be calculated as mentioned in Equation 3.2, Chapter 3.3.

5.1.2 Available Resonances

ATLAS calibration frameworks and algorithms use a joint calibration of the "standard candles" J/ψ and Z. Calibration, in that case, is sensitive to Z mass value used in the simulation and it can bias the final measurement. Consequently the Z boson resonance has to be excluded from the calibration algorithm. Available di-muon resonances are Υ and J/ψ. Both resonances have a background contribution which is hard to simulate as it originates from hadron decays and Drell-Yan processes. Therefore, it is a non-resonant background. The background shape has to be modeled using an analytical function with a data driven method. Since there are three Υ mesons(1S,2S,3S), the calibration procedure is more complex as more parameters are needed for the analytical fit. This is due to the fact that the resolution of the Inner Detector is not low enough to distinguish efficiently between the three peaks. This poses significant challenges in achieving precise calibration of Υ. Moreover, the lower cross section of Υ, results in reduced number of Υ mesons compared to the J/ψ in data. The remaining J/ψ events can offer a more precise calibration, as the muon resolution enables a clear separation between the J/ψ (1S) and the excited ψ (2S) states.

5.1.3 Main Strategy and p_T^μ dependence

One significant aspect of the analysis is that the calibration is not constant with p_T^μ. The parametrization of p_T^μ, derived from the calibration parameters ds_1, dr_1, and dr_2 presented for the ID case in Equation 3.2, may not account for all the necessary effects, leading to a pronounced dependence of the scale on p_T^μ. Additionally, a dependence of the resolution parameters should not be excluded.

Main strategy for the calibration in the context of the Z mass analysis is calibrating the J/ψ resonance as a function η^μ. Secondly, extrapolating the calibration parameters from J/ψ p_T^μ regime (≈ 7 GeV) to the Z p_T^μ regime ≈ 44 GeV. Calibration will be carried out for ID track muons in the barrel region, where the Z mass measurement will also be conducted. Therefore, first an accurate and with negligible statistical uncertainty J/ψ has to be derived in η^μ. Next, the systematic uncertainties on that calibration have to be understood and studied. As discussed in Chapter 2.2.4, the Inner Detector does not have a significant ϕ^μ structure. This is reflected in the calibration, where a ϕ^μ dependence is not anticipated. Consequently, only

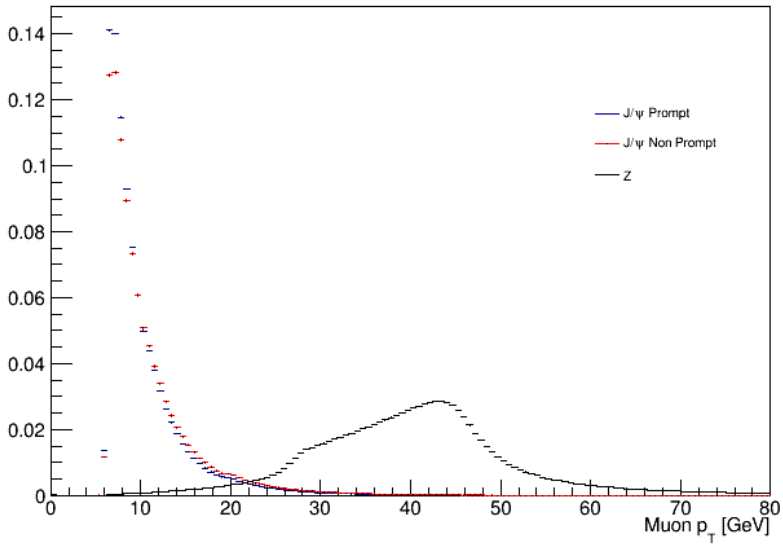

Figure 5.1: Muon p_T^μ in truth level, as generated from Monte Carlo generators before reconstruction, from three different decays, J/ψ Prompt, Non Prompt and Z. Only selection applied is: $p_T^\mu > 6.3$ GeV. Histograms are normalized to their own integral and secondly to the J/ψ Prompt Integral

the η^μ dependence will be examined at a primary level. Particular focus will be placed on the scale parameter ds_1, as it has a strong influence on the mean of the di-muon distributions. An incorrect calculation of its value could introduce a significant bias in the Z mass measurement. Additionally, the uncertainties in the scale parameter ds_1 are expected to significantly contribute to the uncertainty in the Z mass measurement. In contrast, the uncertainties in the resolution parameters are expected to have a lesser impact.

In the Figure 5.1, the truth level distributions of the p_T^μ originating from J/ψ (Prompt and Non Prompt) and Z are presented. The J/ψ and the Z have a significantly different p_T^μ distribution. The J/ψ resonance exhibits a peak at approximately 7 GeV, while the Z resonance peaks at around 44 GeV. The substantial "gap" between the dominant p_T^μ of the J/ψ and that of the Z resonance presents a significant challenge for accurate extrapolation. An overlap region exists in the intermediate range of p_T^μ, from 10 to approximately 24 GeV, where the Z boson contribution is negligible, and the area is dominated by J/ψ. The second overlap region lies above 24 GeV, where the contribution from J/ψ is minimal, and the area is predominantly influenced by Z bosons. The first one will be excluded off due to triggers after reconstruction which require both muon $p_T^\mu > 25$ GeV. Moreover, the Non Prompt are slightly more energetic, something to be discussed in the Chapter 5.3.

Another factor to investigate in the context of Z mass analysis calibration is the calibration of J/ψ produced in b hadron decays, far way from the interaction point, which is called Non Prompt J/ψ. The J/ψ produced directly from gluon gluon fusion are called Prompt, near the interaction point. Diagrams of the two production mechanisms are found in Section 5.3 and Figure 5.7. This study is necessary since Non Prompt J/ψ are more sensitive to background contribution leading to potential calibration non closures. Additionally, the p_T^μ distribution between the two production mechanisms is different in J/ψ and muons which could lead to non closures, if these differences are not understood. The corresponding study in Chapter 5.3 will influence muon selection for the main Z mass analysis calibration.

The main limiting factor of the calibration in the context of the Z mass analysis is the amount of simulated events. J/ψ simulation samples, used in the timeline of this thesis, have a

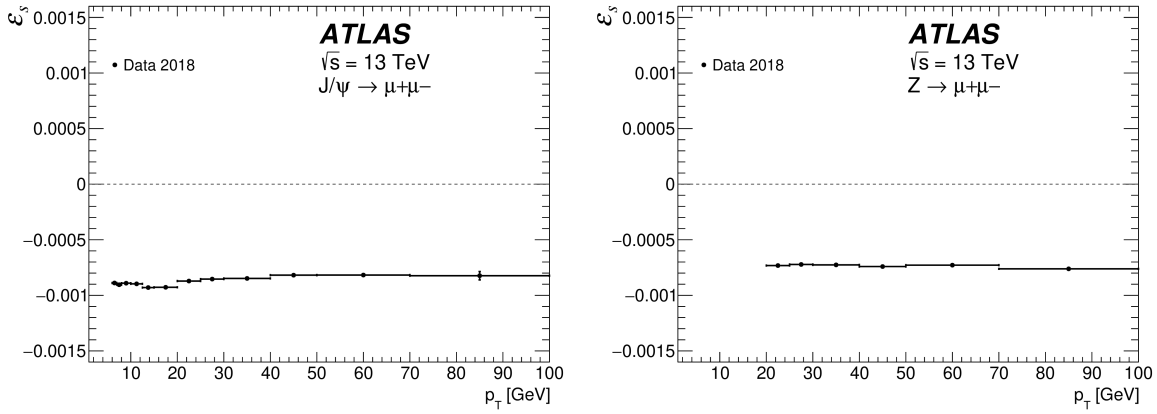

Figure 5.2: Global momentum scale ϵ_s as function of p_T^μ using muons from J/ψ decay and 2018 campaign Data. From ref.[52]

sufficient size for calibration as a function of η^μ, but for the p_T^μ it is not sufficient for a complete study. This influence the number of regions fitted in the calibration algorithm. By increasing the number of regions fitted finer corrections can be derived and therefore a more precise result. A balance should be found between amount of regions in p_T^μ fitted, to avoid having regions with too few events, which would make the calibration fit unstable and not precise. A strong dependence on p_T^μ is observed. Consequently, at large p_T^μ, where the number of J/ψ drops exponentially, a larger sample would permit more accurate studies. A large number of bins is required for p_T^μ extrapolation to study the p_T^μ dependence as accurately as possible, given the observed strong dependence.

In addition, another key point of the analysis is the trigger choice because it can influence the number of events, the shape of the distributions and consequently their agreement between simulation and data. The pre-scale factors in data samples, as they have been presented in Chapter 2.3, can influence the relative contribution of triggers in the p_T^μ distribution, leading potentially in an increase of disagreement between simulation and data.

5.1.4 Previous studies of muon momentum scale in ATLAS

Studies on dependence of scale from p_T^μ have been conducted before in the ATLAS experiment, paving a way for the Z mass analysis calibration. In the ref.[52], the scale, radial and longitudinal distortions are studied. The article utilizes 2018 campaign data to study the scale as a function of p_T^μ. The article looks into the ϵ_s and ϵ_z, ϵ_r, the absolute momentum scale and the scale originating from radial and longitudinal distortions respectively.

The method described in the article differs significantly from the one presented in this thesis. The article uses only data to derive the scale. Also the fit procedure is fitting all the p_T^μ simultaneously, similarly to the sagitta bias fit described in Chapter 3.1.In contrast, this thesis compares Monte Carlo simulations to data in order to derive the calibration corrections, employing an iterative procedure as outlined in Chapter 3.3. Consequently, the plots and results from the paper serve as a motivation for this research rather than influencing the central argument of the thesis. The dependence of scale from p_T^μ can be studied in a generic way from this study and inspire the Z mass analysis calibration. In the article, radial and longitudinal scale is found to be compatible to zero and global momentum scale is found to have a significant impact.

In the Figure 5.2, the scale as a function of p_T^μ is shown. At low p_T^μ (6 - 20 GeV) there are fluctuations and shapes which do not correspond to a clear dependence from p_T^μ. At 6 GeV to 10 GeV there is a limited plateau, between 10 and 20 GeV a dip is observed and for larger p_T^μ

values a slow rising trend which reaches a steady plateau at ≈ 45 GeV. The high p_T^μ plateau means that even if a stronger dependence and not clear shapes are expected in low p_T^μ, the momentum scale of muons at Z p_T^μ regime have relatively a flat dependence.

Moreover, in the article radial biases are considered compatible with zero using muons coming both from Z and J/ψ resonances separately. Therefore, the assumption in this thesis is that they are compatible with zero.

5.1.5 Alternative Calibration Strategies and methods

To attain the desired level of accuracy, the Z mass analysis explores various calibration methods that could offer greater precision than the official ATLAS tools utilized in this thesis. For the sake of completeness, some of these alternative calibration methods are presented here.

The calibration method of this thesis uses an iteration procedure as described in Chapter 3.3. This approach is taken to surpass the challenge of calibrating muons from the same di-muon pair that are located in different detector regions. Another method currently implemented by the analysis is to fit together all the regions of the detector in a joint fit. This is already done in Sagitta bias measurement as described in ref.[52]. The challenge of this method is to constraint the fit for all the regions of the detector and for multiple parameters, scale and resolution.

One approach to minimizing the number of floating parameters during the fit is to determine some of them using the J/ψ and fit the remaining parameters with a different particle. The Z mass analysis follows the scheme of simultaneously fitting both the scale and resolution parameters, where the resolution parameter originating from multiple scattering is derived from the J/ψ mass, while the resolution parameter associated with the magnetic field is obtained from the Z mass. To avoid m_Z dependence the later is measured using the Collins-Soper frame, which is the rest frame of the boson, and the pseudo-mass observable ref.[53]. That way the distribution fitted is independent from the value of m_Z.

To study the dependence of the scale with p_T^μ, the Z mass analysis is using a material budget systematic. The hypothesis is that the amount of material in the Inner Detector is miss-modeled leading to a dependence of the scale from the p_T^μ.

5.2 Data and Simulation Samples

5.2.1 Selection

Data originate from BPhysics and Physics Main data streams defined in Chapter 2.3, for all campaigns. MC was simulated using Pythia8 event generator ref.[51] with A14 add-on, a tune for ATLAS physics. To add the effect of QED final state radiation the samples were interfaced with Photos++ ref.[73]. Simulation samples ref.[74] were processed with Geant4 ref.[75] for the detector effects.

The triggers used belong to the general trigger list and the MCP trigger list found in Appendix I . The choice of trigger is an essential part of the calibration for the Z mass as it can influence heavily the p_T^μ distribution. The general trigger list provides a larger number of available events. However, the triggers used may be pre-scaled, making the calibration sensitive to any imperfections in the simulation of the trigger configuration in the MC.

In pre-selection phase, events with two muons are chosen and they are required to match and to pass one of the triggers, as defined in Chapter 2.3, in the trigger lists used. The kinematic selection is presented in the Table 5.2. This selection corresponds to main calibration in the context of the Z mass measurement: Section 5.4 and 5.5. Non Prompt and Prompt J/ψ calibration selection is specified in the Section 5.3.

MC 2015-16	17,000,000
Data 2015-16	71,000,000
MC 2017	20,000,000
Data 2017	84,000,000
MC 2018	25,000,000
Data 2018	133,000,000
MC overall	58,000,000
Data overall	280,000,000

Table 5.1: Available di-muon pairs for the three campaigns before trigger matching and passing, at the momentum range of the calibration studies: $p_T^\mu > 6.3$ GeV and the mass range of the J/ψ resonance: $2.6 < m_{\mu\mu} < 3.5$ GeV

Selection
$p_T^\mu > 6.3$ GeV
$2.7 < m_{\mu\mu} < 3.5$ GeV
$-1.05 < \eta^\mu < 1.05$
$\frac{d_0}{\sigma_{d_0}} < 3$
$z_0 \times \sin\theta < 0.5$ mm

Table 5.2: Kinematic selection criteria for muon events. This selection corresponds to the main calibration in the context of the Z mass measurement: Section 5.4 and 5.5. Non Prompt and Prompt J/ψ calibration selection is specified in the Section 5.3.

In the Figure 5.3, histograms of event yield during selection process are presented, for data and MC Prompt and Non Prompt J/ψ. The Prompt and the Non Prompt J/ψ are defined in Section 5.3.1. The simulation samples presented are not scaled to the corresponding cross section values and luminosity. The muons are restricted in the J/ψ mass range. Selection cuts are applied one after the other from the left to the right:

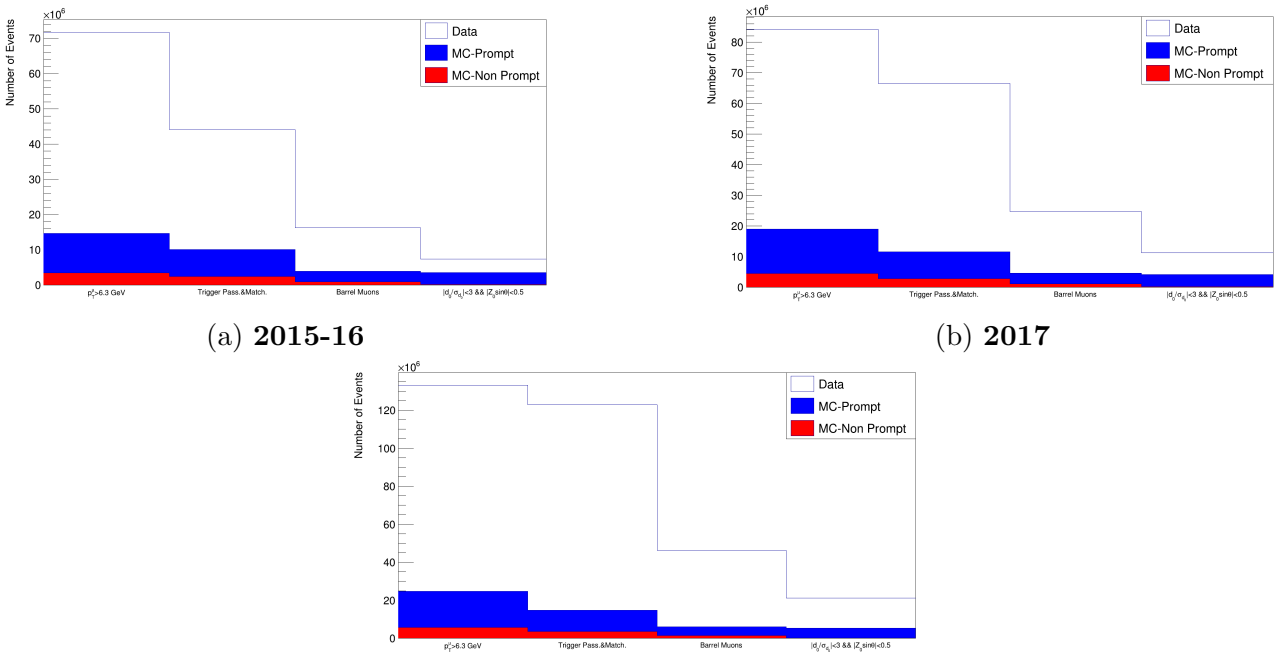

(a) **2015-16**

(b) **2017**

(c) **2018**

Figure 5.3: Cut flow histograms showing the number of events after each selection criteria for data, and MC Prompt and Non Prompt J/ψ. J/ψ definitions are presented in Section 5.3.1. The x-axis represents the selection criteria applied sequentially. First bin corresponds to signal dominant phase space region: $2.7 < m_{\mu\mu} < 3.5$ GeV and $p_T^{\mu} > 6.3$ GeV.

In the Figure 5.3, the number of events in the barrel region ($-1.05 < \eta^{\mu} < 1.05$) are shown in the final bin of each histogram. Due to the limited number of simulated events, the final selection contains a significantly low event yield. This poses a significant challenge for the analysis, as it limits the number of bins available for both calibration as a function of η^{μ} and p_T^{μ}. In η^{μ}, the ds_1 for barrel ID is expected to be relatively flat but for the p_T^{μ} extrapolation, where a strong dependence is expected, a low number of bins is possible to lead to an imperfect extrapolation.

5.2.2 Data and Simulation Comparison

Kinematic distributions are compared between simulation and data. The calibration required for this measurement's precision is sensitive to various simulation mis-modelings, such as detector distortions and mis-modeling of the magnetic field.

The results will be repeated for different trigger configurations, as these can significantly impact the kinematic distributions. As demonstrated in Section 5.5 of this chapter, the choice of trigger can strongly affect the p_T^{μ} dependence of the scale. For 2017 and 2018 there will be a comparison between the general trigger list and the MCP trigger list choice. For 2015-16 the MCP triggers are not present in the samples. As a result, such a comparison is not feasible. Therefore, for the 2015-16 data, only the general trigger list will be used. The general trigger list has a larger number of events both in simulation and in data. The selection used in the kinematic plots to be presented are relevant for the main study of η^{μ} and p_T^{μ} calibration in the context of the Z mass analysis. Only muons at the barrel region are relevant and di-muon events produced near the interaction point.

In the Figure 5.4, the leading muon p_T^{μ} is shown for the three campaigns. Regarding 2017 and 2018, there are trigger effects which can be seen at the ratio plots as shapes. These trigger effects occur in regions of $p_T^{leading-\mu}$ where key triggers impose thresholds in both configurations,

specifically at $p_T^{leading-\mu} \approx 11$ GeV and $p_T^{leading-\mu} \approx 20$ GeV. These effects are expected to have an effect on the calibration, and mostly in the calibration dependent from p_T^{μ} presented in section 5 of the chapter. Regarding 2015-16, the trigger effect is visible at $p_T^{leading-\mu} \approx 20$ GeV.

Using the MCP trigger list, a double trigger peak is observed at low $p_T^{\mu,leading}$, for the two triggers applied. Both triggers apply significantly different cuts on $p_T^{\mu,leading}$, resulting in the observed double peak. The general trigger selection has a clear peak followed by a declining distribution, with the exception of a slight rise observed at $p_T^{leading-\mu} \approx 20$ GeV.

The choice of trigger configuration, depending on the campaign, results in variations in the slope at high $p_T^{\mu,\text{leading}}$. In the 2018 histogram, the ratio plots show a flat trend in the high-p_T^{μ} region for the general trigger configuration, whereas the MCP trigger list exhibits a rising slope, reaching values of approximately 1.3. For the 2017 campaign, both configurations display a steadily rising trend in the corresponding ratio plots. Similarly, a rising trend is observed for the 2015–16 campaign.

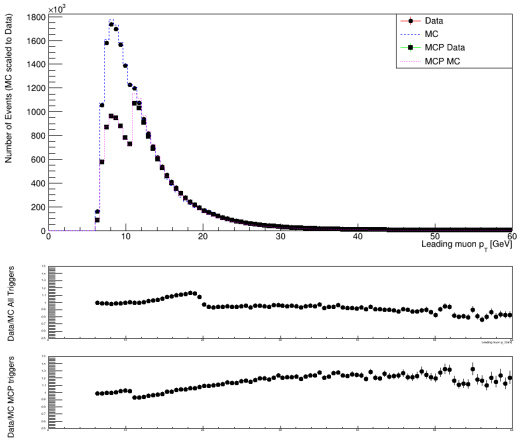

(a) 2018

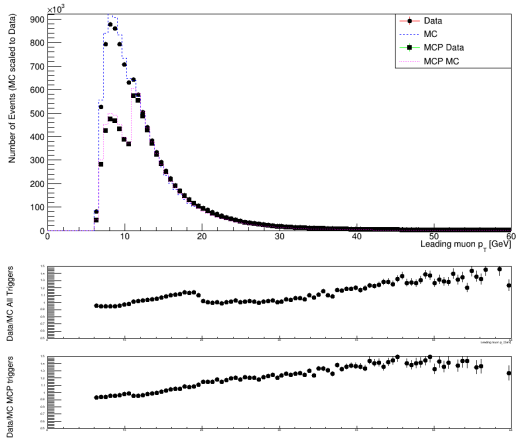

(b) 2017

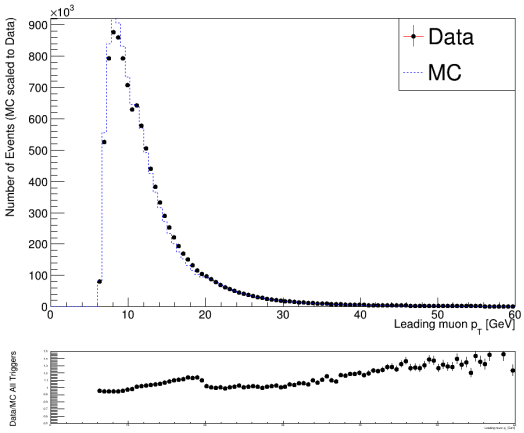

(c) 2015-16

Figure 5.4: Leading muon p_T^{μ} for simulation and data using different trigger lists: MC and Data for general trigger list, MCP MC and MCP Data for MCP trigger list. Selection applied is corresponding to Table 5.2

In the Figure 5.5, the sub-leading muon p_T^{μ} is shown for the three campaigns. Trigger effects are less visible in the ratio plots. Depending on the campaign the Data to MC agreement has opposite slides with $p_T^{\mu,subleading}$. The 2018 have a falling one and the 2017, 2015-16 have a steep rising one.

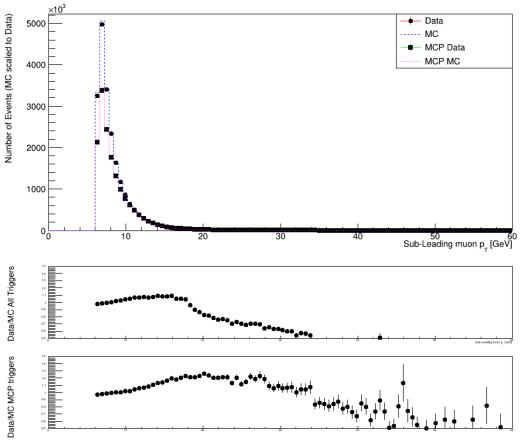

(a) 2018

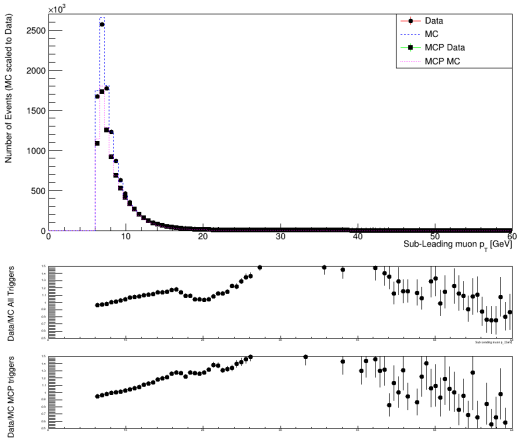

(b) 2017

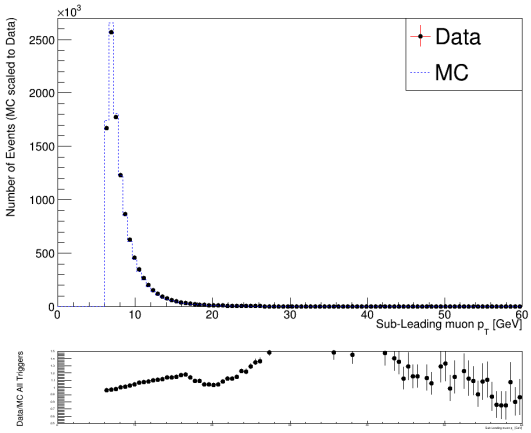

(c) 2015-16

Figure 5.5: Sub-leading muon p_T^{μ} for simulation and data using different trigger list: MC and Data for general trigger list, MCP MC and MCP Data for MCP trigger list. Selection applied is corresponding to Table 5.2

In the Figure 5.6, the $p_T^{\mu\mu}$ is shown for the three campaigns. These histograms are important because of the J/ψ $p_T^{\mu\mu} - Y^{\mu\mu}$ re-weighting used in the η^{μ} and p_T^{μ} calibration presented in this chapter on sections 4 and 5. Trigger effects are evident in the ratio plots, as well in the low $p_T^{\mu\mu}$ region. Different trends are observed depending on the campaign. Most important effect is on 2017 and 2015-16, where there is a large disagreement shape at the ratio plots above $p_T^{\mu\mu} \approx 60$ GeV. Since these ratios will be used in the re-weighting procedure, an effect is expected at the p_T^{μ} calibration.

The ultra high values observed are likely to originate in overlap of events in the data samples. Specifically, there are some events which overlap between the two data streams, Physics Main and BPhys. This effect was not possible to be corrected in the timeline of the thesis.

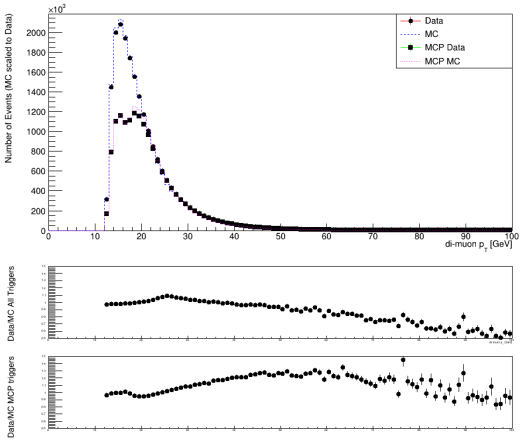

(a) 2018

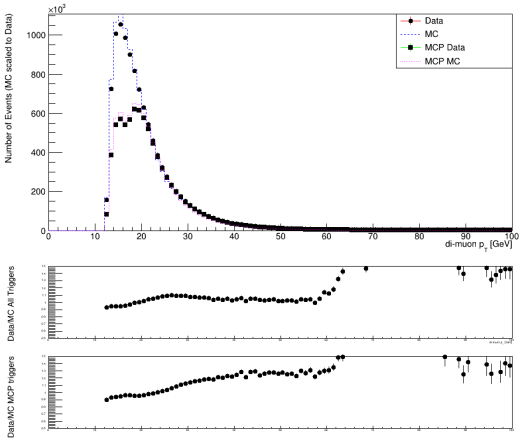

(b) 2017

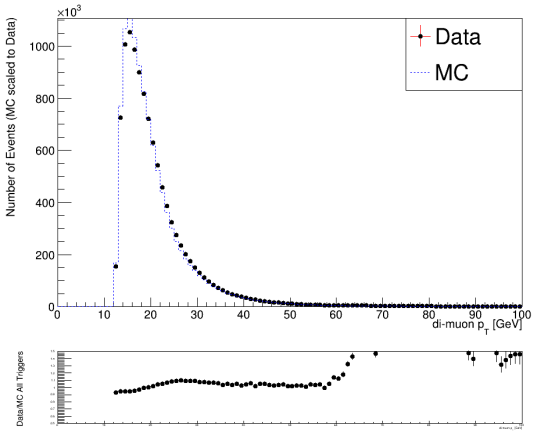

(c) 2015-16

Figure 5.6: Di-muon p_T for simulation and data for different using different trigger list: MC and Data for general trigger list, MCP MC and MCP Data for MCP trigger list. Selection applied is corresponding to Table 5.2

5.3 Prompt - Non Prompt J/ψ Calibration

In this Section, two different sets of calibrations are being compared, one for muons coming from Prompt J/ψ decays and one for Non Prompt J/ψ decays. Two studies are performed depending on the separation variable used between Prompt and Non Prompt J/ψ. One is a short study where the variables used for the separation are the standard ATLAS analysis ones (d_0 significance and $z_0 \times \sin\theta$) and a more complete study as separation variable the transverse decay length of the parent particle of the J/ψ. Only 2017 campaign samples were used in this section.

The main motivation for comparing muon calibration between Prompt and Non-Prompt J/ψ samples arises from the need to ensure precise and accurate calibrations. By adding the Non Prompt J/ψ in the calibration the statistics increase almost by a factor of two in simulated events and in data. Thus, one might anticipate a reduction in the statistical uncertainty of the fits during the calibration process. J/ψ mesons can originate either directly from the primary collision or from the decay of longer-lived particles such as b-hadrons. These two sources can exhibit different kinematic characteristics, potentially leading to discrepancies in the calibration process. By comparing the muon calibration between Prompt and Non-Prompt J/ψ samples, the aim is to identify and correct any biases or variations between the two. The result of this study gives a answer on the muon selection implemented to differentiate between Prompt and

Non Prompt in the Zmass analysis calibration .

5.3.1 Prompt - Non Prompt Mesons

Figure 5.7 illustrates the production of Prompt and Non-Prompt J/ψ. Prompt J/ψ are generated near the interaction point through various processes, including direct production from gluon-gluon fusion or decays of higher-mass excited charmonium states such as $\psi(2S)$ or χ_c. In contrast, Non-Prompt J/ψ originate from the decays of beauty mesons. The two categories can be experimentally distinguished, as Non-Prompt J/ψ are predominantly produced at a displacement from the interaction point due to the long lifetime of b-mesons.

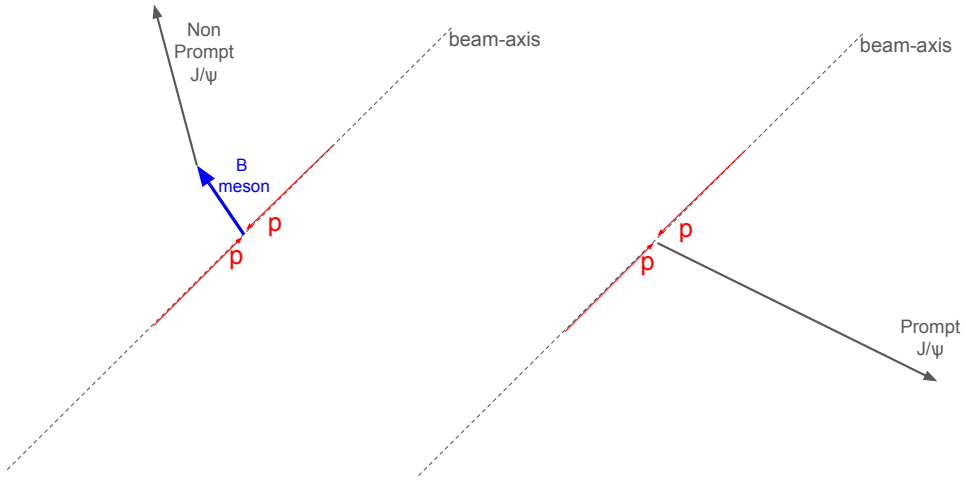

Figure 5.7: Sketch of Prompt and Non Prompt J/ψ production. Prompt J/ψ are produced close to the interaction point, where Non Prompt J/ψ are produced in majority displayed, after the decay of B mesons.

5.3.2 d_0/σ_{d_0} ,$|z_0 \times \sin\theta|$ study

The simulation and data distributions are influenced from multiple factors such as the η^μ, p_T^μ selection, separation variable between Prompt and Non Prompt and the triggers used. A key feature of this study is the separation variables used for the distinction of the two. A standard choose of selection is: $|\frac{d_0}{\sigma_{d_0}}| < 0.3$ and $|z_0 \times \sin\theta| < 0.5$ mm. Corresponding distributions are shown in the Figures 5.8a and 5.8b.

In the Figures 5.8a and 5.8b, data (red) is a mixture of the Prompt (blue) and Non Prompt (green) J/ψ distributions. The distributions correspond to full Run-2 merged and they are normalized to the data histogram. Regarding d_0/σ_{d_0}, a peak around 0 is observed, corresponding to J/ψ particles produced near the interaction point, originating from both Prompt and Non-Prompt processes. As expected, the contribution of Prompt around 0is larger compared to the Non Prompt, but the later exhibit also a lower peak. The Prompt J/ψ contributions becomes negligible at |4|. In larger values, the main contribution originates from Non Prompt J/ψ. In the Figure 5.8b the same behavior is observed. All distributions show a peak at 0, originating from muons produced near the interaction point, with the majority of the contribution coming from Prompt J/ψ. Around 0.2, the Prompt contribution nearly vanishes, and the Non-Prompt contribution becomes the dominant one.

These variables are used for the first study. Two sets of calibrations were produced depending on the Non Prompt J/ψ definition. The HLT triggers used for the short studies are the

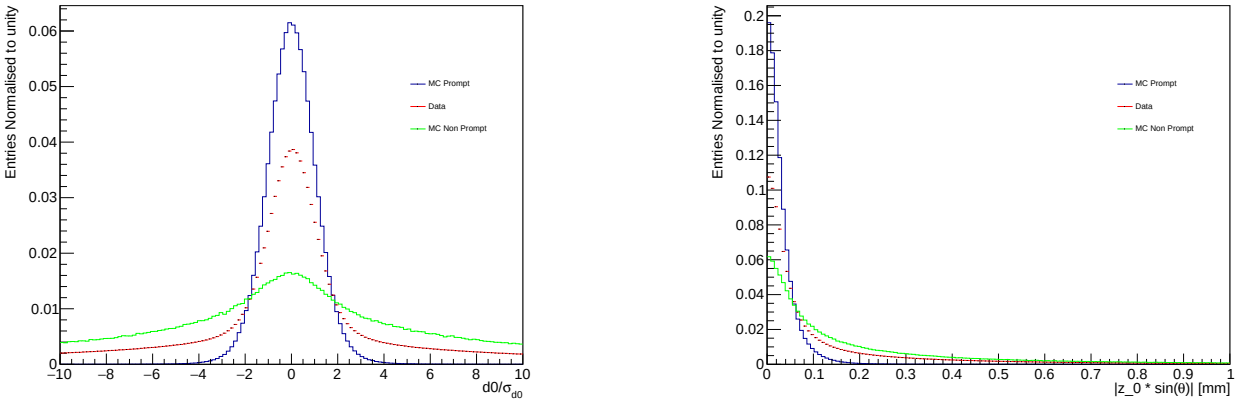

(a) d_0 significance

(b) $|z_0 \times \sin\theta|$

Figure 5.8: d_0 significance and $|z_0 \times \sin\theta|$ distributions for data, Prompt and Non Prompt MC. Only selection applied is $p_T^\mu > 6.3$ GeV and $2.7 < m_{\mu\mu} < 3.5$.

MCP trigger list, described in Appendix I. The triggers chosen are for the corresponding campaign (2017) are not pre-scaled, which lead to a better agreement of p_T^μ distributions between data and MC. The initial selection used to distinguish between Prompt and Non-Prompt J/ψ in the preliminary study is presented in the table 5.4.

Selection
$p_T^\mu > 6.3$ GeV
$2.7 < m_{\mu\mu} < 3.5$ GeV

Table 5.3: Selection criteria for muon events.

Prompt	**Non-Prompt**
$\lvert d_0/\sigma_{d0}\rvert < 3$	$\lvert d_0/\sigma_{d0}\rvert > 3$
$\lvert z_0 \sin\theta\rvert < 0.5$ mm	$\lvert z_0 \sin\theta\rvert > 0.5$ mm

Table 5.4: Selection applied to muons, to separate Prompt and Non Prompt J/ψ candidates for d_0 significance and $z_0 \sin\theta$ selection

The selection criteria in Table 5.4 are designed to minimize the contamination between Prompt and Non-Prompt J/ψ candidates in the samples. As a result, the number of Non-Prompt J/ψ candidates in the simulation is low, leading to a large statistical uncertainty in the corresponding calibrations.

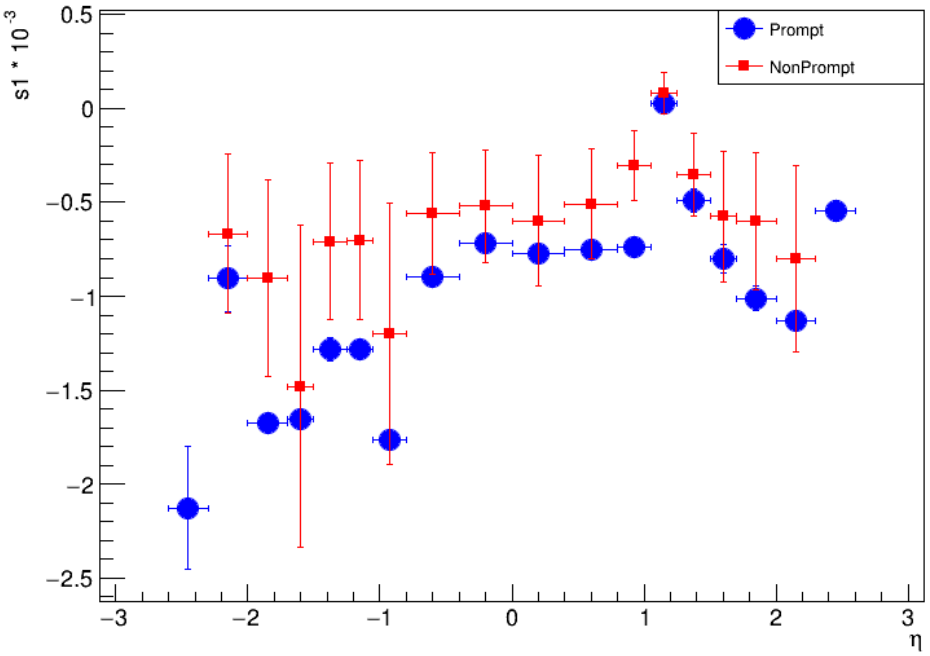

Figure 5.9: Scale as a function of η^{μ} for two different samples, Prompt and Non Prompt J/ψ, as described in the Table 6.14b156$\Gamma_Z$figure.caption.166ults are average over iterations and error bars are the standard deviation

In the Figure 5.9, the Non Prompt J/ψ calibration exhibits a large statistical uncertainty due to the low number of events in the corresponding simulation sample. A less negative scale is found for the Non Prompt than for the Prompt in all the η^{μ} bins. This is an indication of the scale dependence from the p_T^{μ} of the muons, as Non Prompt J/ψ tend to have larger p_T^{μ}.

5.3.3 L_{xy} study

L_{xy} variable and samples The main study of Prompt and Non Prompt J/ψ calibrations uses another variable for the separation of the two, the transverse decay length L_{xy}, where L_{xy} is the distance a particle travels in the transverse plane from the primary vertex to the secondary vertex where it decays. L_{xy} is computed as:

$$L_{xy} = \vec{\Delta S} \times \frac{\vec{p_T^{\mu\mu}}}{|p_T^{\mu\mu}|} = \cos\Phi \times |\vec{\Delta S}|$$

where $\vec{\Delta S}$ is the decay length of the parent particle or the three dimensional distance between primary secondary vertex, $\vec{p_T^{\mu\mu}}$ is the $p_T^{\mu\mu}$ candidate J/ψ transverse momentum and Φ is the angle between them, as shown in the Figure 5.10.

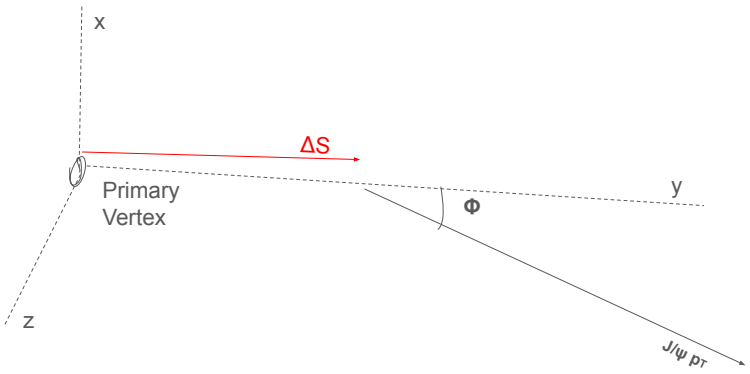

Figure 5.10: L_{xy} sketch in the x,y,z axis system of ATLAS. The red arrow corresponds to decay length of parent particle and the black arrow is the momentum of the J/ψ. IP corresponds to Interaction Point.

The L_{xy} distribution in Prompt and Non Prompt J/ψ simulation is shown in the Figure 5.11.

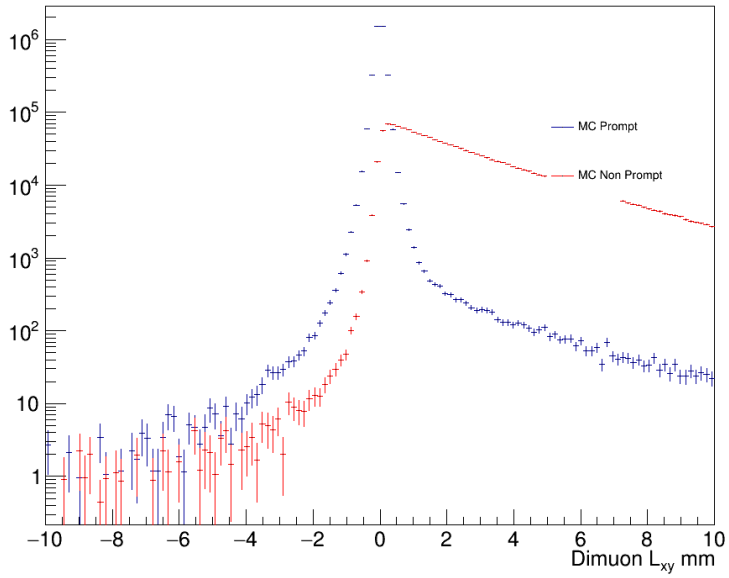

Figure 5.11: Prompt (blue) and Non Prompt (red) simulation histograms of J/ψ L_{xy}. Non Prompt histogram is normalized to Prompt.

The separation of Prompt and Non Prompt J/ψ is visually clearer than the one seen in the Figures 5.8a -5.8b, therefore the L_{xy} variable is chosen for the separation of two for the following study. Additionally, L_{xy} is a variable that describes the di-muon resonance itself, while the d_0 significance and $z_0 \times \sin\theta$ characterize the individual muons. Therefore, is worthwhile to explore L_{xy} as a separation variable between J/ψ events.

In the Figure 5.11, Prompt J/ψ exhibit a clear peak centered around 0. Prompt though has a negligible contribution towards positive values. This tail is originating to resolution effects but also to a reconstruction non closure. Both Prompt and Non Prompt have a minor negative tail which has an insignificant number of events below -4 mm. The negative values in majority

are present both in Prompt and Non Prompt due to resolution but as well could be in the cases the J/ψ candidate's momentum is pointing to the opposite direction from the $\vec{\Delta S}$ computed and the Φ angle is between $\frac{\pi}{2}$ and π. The Non Prompt distribution shows a small percentage of entries with negative values (around 1%), whereas the Prompt distribution is more symmetric around 0, with a slight preference for the positive side. This asymmetry arises because Non-Prompt J/ψ mesons are more energetic and boosted, causing their preferred flight direction to align with that of the parent particle.

A similar analysis could be performed using the d_0 significance and interaction point constraint, and a result similar to the one presented in this study is expected. Further information on the reconstruction of displaced secondary vertices and b-tagging can be found in Chapter 2.2.4.

The Prompt and Non Prompt J/ψ populations are separated in this study with the selection presented in the Table 5.6.

Selection
$p_T^\mu > 6.3$ GeV
$2.7 < m_{\mu\mu} < 3.5$ GeV

Table 5.5: Selection criteria for muon events.

-	**Prompt**	Non-Prompt
L_{xy}	< 0.2 mm	> 0.5 mm

Table 5.6: Selection applied to Prompt and Non Prompt J/ψ candidates for L_{xy} based selection

With this selection two well separated samples of Prompt and Non Prompt J/ψ are obtained. In the Prompt sample there is a low contamination of Non Prompt about 2% and in the Non Prompt sample there is a contribution of 1% in Prompt.

For the L_{xy} studies the general trigger list for 2017 campaign is used, presented in Appendix I. The triggers can include selection on L_{xy} and other kinematic variables. Therefore, they are a critical aspect of this study as they can shape the kinematic distributions such as J/ψ mass and p_T^μ, influencing the calibration comparison between Prompt and Non Prompt.

To justify the use of the general trigger list over the MCP list, kinematic distributions are compared and analyzed for both trigger configurations. In the following Figures, distributions of Prompt and Non Prompt are shown, for two different trigger configurations:

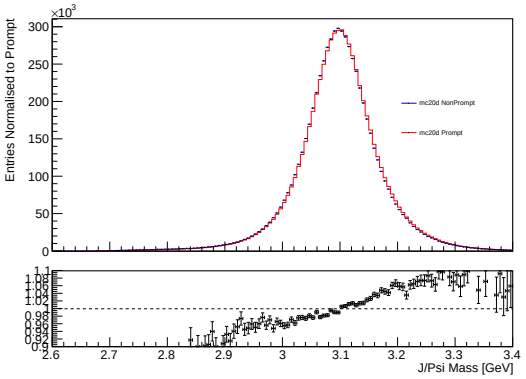

(a) Prompt and Non Prompt $m_{\mu\mu}$ with MCP trigger list

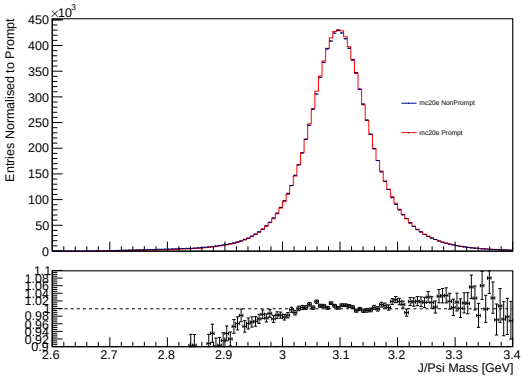

(b) Prompt and Non Prompt $m_{\mu\mu}$ with complete trigger list

Figure 5.12: Comparison of $m_{\mu\mu}$ distributions between Prompt and Non Prompt J/ψ simulation for two different trigger configurations. Non Prompt distributions are scaled to Prompt ones.

In the Figures 5.14a and 5.14b, the agreement between Prompt and Non Prompt $m_{\mu\mu}$ distributions depend on the trigger configuration chosen. The origin of this discrepancy can

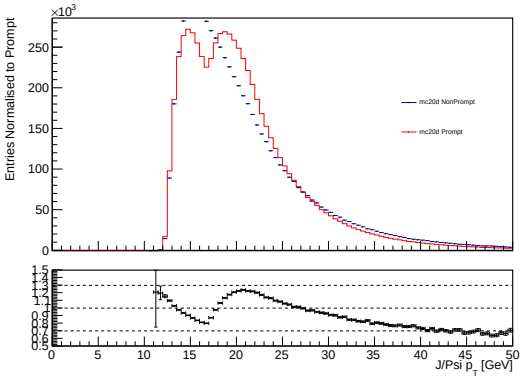

(a) Prompt and Non Prompt $p_T^{\mu\mu}$ with MCP trigger list

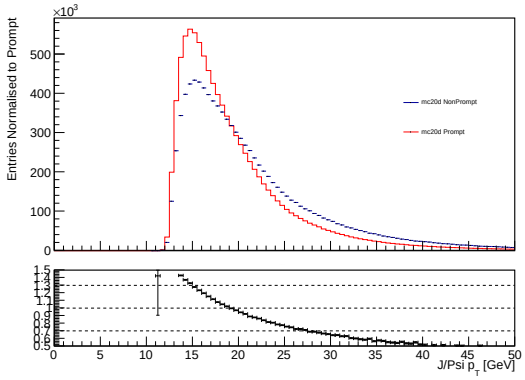

(b) Prompt and Non Prompt $p_T^{\mu\mu}$ with general trigger list

Figure 5.13: Comparison of $p_T^{\mu\mu}$ distributions between Prompt and Non Prompt J/ψ simulation for two different trigger configurations. Non Prompt distributions are scaled to Prompt ones.

be traced to the L_{xy} cuts applied to the di-muon in the MCP trigger list, which primarily affects the p_T^{μ} distributions originating from Non-Prompt J/ψ. This is clearly reflected in Figure 5.13, which shows the $p_T^{\mu\mu}$ distributions. One of the peaks, associated with the trigger `HLT_2mu6_bJpsimumu_Lxy0_L1BPH_2M9_2MU6_BPH_2DR15_2MU6`, is absent in the Non-Prompt J/ψ case. This absence is due to the L_{xy} selection present in the trigger. In the $p_T^{\mu\mu}$ distributions, where the general trigger list is utilized, shown in Figure 5.13b, the agreement between the two is better, making this configuration the most suitable for this study. It is advantageous to use the configuration in which the kinematic distributions align most closely between simulation and data, ensuring that any discrepancies observed between the two calibrations are well understood. In Figure 5.13, the choice of the L_{xy} cut on the Non-Prompt J/ψ favors more energetic Non-Prompt J/ψ, leading to a difference between the Prompt and Non-Prompt J/ψ kinematic distributions, such as the p_T^{μ} distributions.

Calibration Comparison As a first stage, the comparison of the calibration between Prompt and Non Prompt is investigated. No $p_T^{\mu\mu}$ re-weighting is applied, which is going to be used in the second part of the study. The full p_T^{μ} range is used, with three p_T^{μ} bins used per η^{μ} region based on the p_T^{μ} of the sub-leading: $6.3 < p_T^{subleading} < 9$ GeV, $9 < p_T^{subleading} < 20$ GeV and $20 < p_T^{subleading} < 60$ GeV.

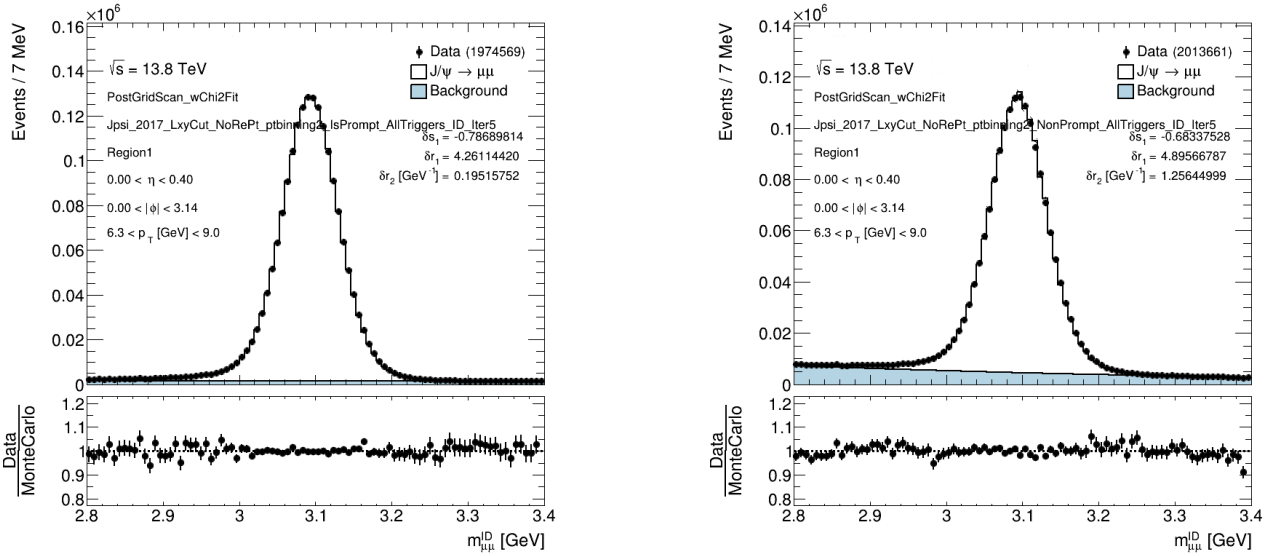

(a) Prompt J/ψ

(b) Non Prompt J/ψ

Figure 5.14: $m_{\mu\mu}$ post-calibration distributions for Prompt (a) and Non Prompt (b) J/ψ, 5th iteration. Example for first p_T bin: $6.3 < p_T^{subleading} < 9$ GeV and first η^μ bin: η^μ_{pos} or $\eta^\mu_{neg} \in 0 < \eta^\mu < 0.4$. Complete trigger list used.

In the Figure 5.14, Prompt and Non Prompt J/ψ are shown after the likelihood minimization algorithm for iteration 5 and for the first η^μ bin: η^μ_{pos} or $\eta^\mu_{neg} \in 0 < \eta^\mu < 0.4$. Only the first p_T bin here is shown $6.3 < p_T^{subleading-\mu} < 9$ GeV since a similar level of agreement is found in other

The post-calibration agreement between data and MC is successful below the peak for both the Prompt and Non-Prompt J/ψ cases, as shown in Figure 5.14. Non Prompt J/ψ is more sensitive to background contribution as observed in the Figure 5.14 (b). As an example for the η^μ region shown, the percentage of background yield fitted to the data yield for the three $p_T^{sub-leading}$ bins is presented in the table 5.7. Two observations are extracted from the table. First, the background contribution is nearly twice as large in the Non-Prompt case compared to the Prompt case. This makes the Non-Prompt calibration more sensitive to the background model, potentially introducing biases into the calibration process. In contrast, an incomplete background model for the Prompt J/ψ case is less likely to result in calibration inaccuracies, as the background contribution is limited. A second observation is the fact that background percentage is increasing with p_T^μ, which is an interesting observation for the calibration as a function of p_T^μ, to be presented later in this Chapter.

	N_{Bkg}/N_{Data}% Prompt	N_{Bkg}/N_{Data}% Non Prompt
$6.3 < p_T^{sub-leading} < 9$	7.2	20.1
$9 < p_T^{sub-leading} < 20$ GeV	8.7	20.1
$20 < p_T^{sub-leading} < 60$ GeV	12.5	21.4

Table 5.7: Percentage of background fitted to data yield for the three p_T bins used in the study.

A better pos-fit agreement is seen in the Figure 5.14 (a) (b) in the Prompt case compared to the Non Prompt one. This is considered mainly as a problem of the background fit non closure due to the larger background contribution.

The comparison of calibration results for the scale parameter as a function of η^μ are shown in the Figure 5.15a:

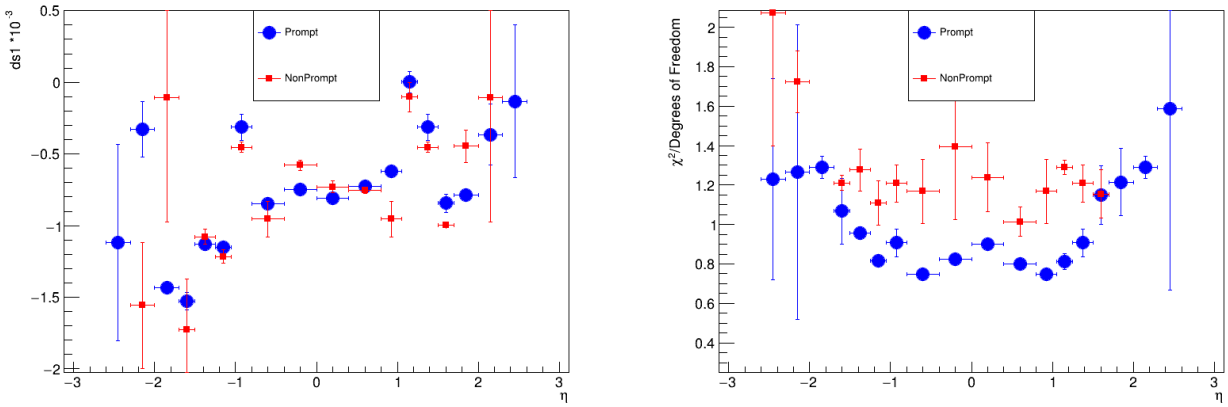

(a) Scale ds_1 (b) χ^2/(Degrees of Freedom)

Figure 5.15: Scale and χ^2/(Degrees of Freedom) between signal+background and data, as a function of η^μ, for Prompt (blue) and Non-Prompt (red) J/ψ samples, as defined in Table 5.6. χ^2/ computed by comparing MC and data histogram, post-calibration. ID tracks. Points are average over iterations and error bars are Standard Deviation.

In Figure 5.15a, the calibration parameter for scale is shown for both Prompt and Non-Prompt J/ψ. Large error bars are observed in the case of Non-Prompt J/ψ, which arise from two sources. The most significant reason is the low number of events at the simulated Non Prompt sample. The second reason is the large background contribution in Non Prompt resulting in some regions to a background shape fit fail in large η^μ regions. In the Prompt case similar behavior is observed in the large $|\eta^\mu|$ bins of 2.3 to 2.6. This behavior is rising due to low number of events and very high background contribution in the endcaps regions resulting in some background fails. Since the Z mass analysis is only using the barrel region the focus should be given to the six central points in the -1.05 to 1.05 η^μ. Overall Prompt calibrations has an excellent performance and a statistical uncertainty of the order of 10^{-5} in the barrel region. Non Prompt has slightly larger standard deviation over iterations due to the low number of events in the simulation and the fact that the background contribution is larger in the Non Prompt. Since the background shape is fitted using a parametric function rather than derived from simulation, its behavior is less well understood, especially when the background contribution is significant. This can increase the likelihood of inaccuracies in the calculation, potentially introducing additional instability in the iterative process.

The χ^2 to degrees of freedom (d.o.f.) as a function of η^μ is shown in the Figure 5.15b. The larger χ^2/d.o.f. for the Non-Prompt J/ψ calibrations suggests a potential non-closure in the calibration compared to the Prompt J/ψ. Given that the primary difference between the two is the background contribution, it is inferred that the discrepancy observed in this plot between the Prompt and Non-Prompt J/ψ calibrations is due to an imperfect representation of the background shape. It the central region there is a clear difference between the two distributions. The Prompt fits exhibit a better convergence as reflected by the χ^2 to degrees of freedom values. On the contrary at the intermediate regions ($1.5 < |\eta^\mu| < 2$) there is a tendency for agreement between the two calibrations regarding the quality of the fit. But in the endcap, the Non Prompt case have points which are far above 2 and are out of scale in the given graph.

A study was conducted to test the hypothesis of background non-closure in the calibration fit, which is presented in Appendix F.2. In this study, the nominal calibration is compared to an alternative one, which utilizes a more complex background model. Furthermore, in Appendix F.1 the comparison of the resolution parameters for the Prompt and the Non Prompt J/ψ

calibrations is presented.

Calibration Comparison, Re-weighting Study Finally, an additional study is conducted to further investigate the discrepancy between the two calibrations.The $p_T^{\mu\mu}$ distributions for Prompt data, Prompt simulation, and Non Prompt simulation are re-weighted to match the corresponding distributions in Non-Prompt data. The re-weighting is performed by a 2-dimensional re-weighting map of $p_T^{\mu\mu}$ and rapidity $Y^{\mu\mu}$. The process accounts for two effects, one is the higher p_T^{μ} of the Non Prompt J/ψ and the other is physics differences as mentioned earlier due to the two different production mechanisms. The re-weighting in data samples is not a common technique, as it changes the physics properties of the actual data collected from the detector. Therefore, this is just a trial study not to be used in the actual analysis calibration. The three maps are shown in the Figure 5.19.

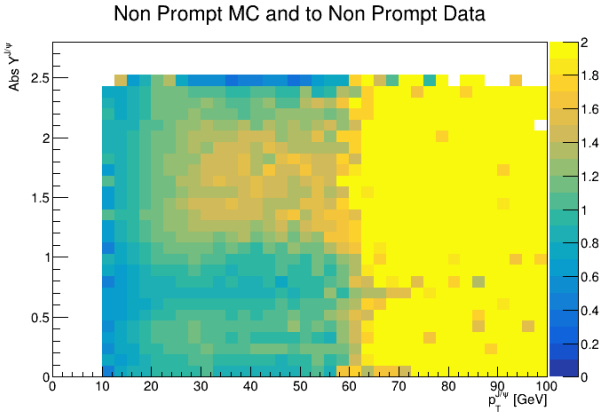

Figure 5.16: Non Prompt MC to Non Prompt data re-weighting map

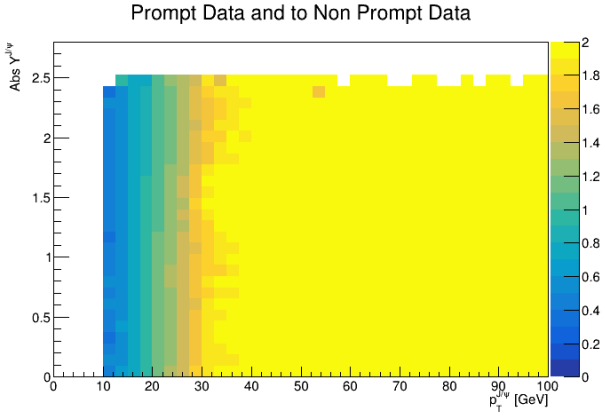

Figure 5.17: Prompt data to Non Prompt data re-weighting map

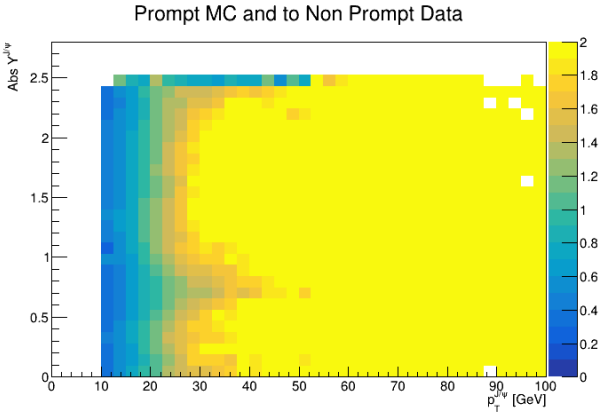

Figure 5.18: Prompt MC to Non Prompt data re-weighting map

Figure 5.19: Re-weighting maps to Non Prompt J/ψ data $p_T^{\mu\mu}$ and $Y_{\mu\mu}$ distributions.

In all the Figures 5.16, 5.17, and 5.18, Non-Prompt data exhibits higher $p_T^{\mu\mu}$ than the Prompt MC and data, as well as Non-Prompt MC, as indicated by the yellow zone on the right side of the maps. This phenomenon in the Prompt maps is explained by the fact that Non Prompt J/ψ, produced far from the interaction point, tend to be more energetic. In the Non Prompt MC maps, however, it suggests a mis-modeling of the $p_T^{\mu\mu}$ distribution.

In the two re-weighting map Figures 5.16 and 5.18, a structure is appearing in the 0.7 of Y from lower $p_T^{\mu\mu}$ to higher $p_T^{\mu\mu}$. In Figure 5.16, the $p_T^{\mu\mu}$ distribution of Non Prompt data exhibits a similar structure to that of Non Prompt MC, which remains visible up to approximately 60

GeV. In contrast, in the Prompt MC case shown in Figure 5.18, the structure is less apparent between 10 GeV and approximately 40 GeV. This difference arises due to the higher $p_T^{\mu\mu}$ of Non-Prompt data, which obscures the structure at higher $p_T^{\mu\mu}$ values. This structure is non present in data re-weighting map (Figure 5.17) therefore signaling that this structure is likely related to a detector effect. It's significance and origin are beyond from the scope of this study so as an effect it will be corrected by the $p_T^{J/\psi}$ re-weighting.

In the re-weighting procedure, a new weight is derived from these maps and multiplied with the existing event weight. For each event, the new weight is determined by identifying the bin corresponding to the event's $p_T^{J/\psi}$ and $|Y^{J/\psi}|$ values on the map. To ensure continuity between bins, a linear interpolation is carried out between the identified bin and its neighboring ones. To ensure there are no large weights which could affect the distributions in a un-physical manner weights are restricted to the range: [0.7,1.3].

The results from this study are exhibited in the Figures 5.20.

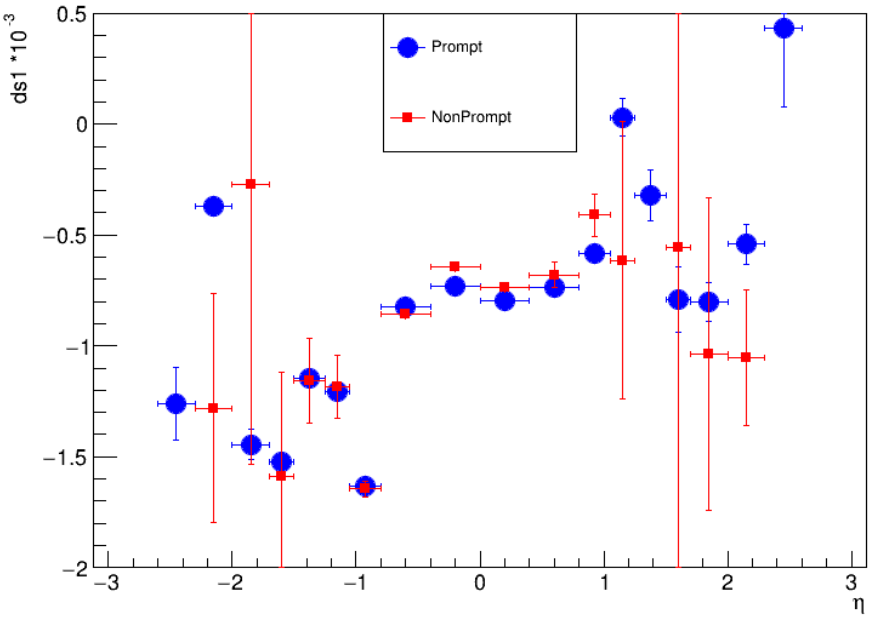

Figure 5.20: Scale as a function of η^{μ} for Prompt (blue) and Non Prompt(red) J/ψ samples, Prompt data and MC and Non Prompt MC are re-weighted to Non Prompt data as defined in Table 5.6. ID tracks. Points are average over iterations and error bars are Standard Deviation.

In the Figure 5.20 there is a clear difference between Prompt and Non Prompt calibrations persisting after the re-weighting. The two calibrations show a closer agreement in comparison to Figure 5.15a, where no re-weighting is applied. Notably, the issue of larger error bars persists. The larger background contributions in the Non-Prompt J/ψ sample significantly impact the understanding of the J/ψ p_T distribution. As a result, further studies on Non-Prompt calibrations are considered beyond the scope of this thesis. Given the sufficiently large Prompt J/ψ sample, which enables a calibration with minimal statistical uncertainty (approximately 10^{-5} for scale) in the barrel region, the inclusion of the Non-Prompt J/ψ sample is deemed unnecessary, as its addition does not enhance the precision of the calibration.

5.4 Calibration as a function of η^{μ}

In this Section, the muon momentum calibration as a function of η^{μ} in the context of the Z mass analysis is going to be analyzed. First, the method and technical details are presented. Examples of mass distributions are shown, pre and post calibration. Corrections of momentum scale and resolution as functions of η^{μ} and the process of deriving them are presented, with the corresponding systematic uncertainties.

Muon momentum calibration in η^{μ} is necessary to correct for non charge dependent bias effects. Since the calibration in Z mass analysis is focused in the ID tracks, there is no contribution from energy loss of the muons in these biases. The origin of the biases corrected are radial displacements, magnetic field miss-simulation and multiple scattering.

5.4.0.1 Method

After the Non Prompt Study of subsection 5.3 an exclusion of Non Prompt J/ψ is decided. L_{xy} variable is considered to have similar results with the d_0 significance and the $|z_0 \times \sin\theta|$ variables used frequently in ATLAS analyses for the separation of the Prompt and the Non Prompt J/ψ samples. Therefore, the d_0 significance and $|z_0 \times \sin\theta|$ will be used for the selection of Prompt and Non-Prompt J/ψ. To exclude the majority of Non Prompt J/ψ the kinematic selection of Table 5.2.

Deriving the calibration with different configurations as discussed in Chapter 3.3 produces systematic variations of the calibration parameters. A major challenge for the Z mass analysis is the calibration in η^{μ} and the extrapolation of correction parameters. Therefore, statistical uncertainty per region over iterations and the systematic uncertainties were analyzed thoroughly and understood during the thesis. The main source of systematic uncertainties are the ones obtained from technical changes in the calibration and selection, to ensure that the process is independent from the specific methodology chosen, as well as variations of the analytical background fit. A detailed analysis of the systematic uncertainties is provided in Chapter C. For this calibration algorithm, only the systematic uncertainties relevant to the J/ψ resonance will be considered:

- p_T^{μ} down: p_T^{μ} binning for the sub-leading muon (S.L.)is changed from $6.3 < p_T^{S.L.} < 9$ GeV and $9 < p_T^{S.L.} < 20$ GeV to $6.3 < p_T^{S.L.} < 8$ GeV and $8 < p_T^{S.L.} < 20$.
- p_T^{μ} up: p_T binning is changed from $6.3 < p_T^{S.L.} < 9$ GeV and $9 < p_T^{S.L.} < 20$ GeV to $6.3 < p_T^{S.L.} < 12$ GeV and $12 < p_T^{S.L.} < 20$ GeV.
- Background Parametrization: background model is changed from exponential to a Chebysev of the second order.
- Background Technique: Signal model is changed from a Gauss and a Crystal Ball to a double Crystal Ball one. The Crystal Balls share a common mean and a different σ, α and η^{μ}.
- J/ψ Bin Reduce: $m_{\mu\mu}$ histogram limits change from 2.8 to 3.4 GeV to 2.75 and 3.5 GeV.
- J/ψ Bins down: Number of bins are reduced from 90 to 60.

Systematic variations are calculated as follows: the nominal calibration is first performed for a sufficient number of iterations. Each systematic variation is run for the same number of iterations, with the mean over last ten iterations to be taken as the value for that systematic. The means of all systematic variations are compared to the nominal mean, and the variation

with the largest deviation from the nominal is identified as the systematic uncertainty. Depending on whether this difference is positive or negative, the systematic variation is categorized as either an "up" or "down" variation.

The η^{μ} calibration employs twelve regions within the barrel region. This number of regions is selected to ensure that each contains a sufficient number of events to allow for stable fits. Muons in the data samples are corrected for charge dependent effects with Sagitta bias produced by the ATLAS official recommendation. η^{μ} calibration is repeated for all campaigns.

A summary of the η^{μ} calibration procedure is the following:

- From Iteration 5 to Iteration 14, a likelihood minimization method is employed to estimate the calibration parameters.
- In Iteration 15, the average calibration parameters from Iterations 5 to 14 are used as input values instead of the results from Iteration 14. This approach helps stabilize the fit across iterations and minimizes the statistical uncertainty of the calibration parameters. The final results are derived from Iterations 15 to 20, with the calibration parameter values taken as the mean across these iterations and the statistical uncertainty calculated as their standard deviation.
- The iterative procedure also impacts the analytical fit used to estimate the background contribution, including the parameters of the Gaussian and Crystal Ball distributions. To aid convergence, the analytical fit parameters from one iteration are carried forward and injected as initial values for the next iteration. The results of the analytical fits are stored for each η^{μ} region in every iteration and used as input for subsequent iterations.

Finally, a re-weighting of the $p_T^{\mu\mu}$ distribution is applied, utilizing a $p_T^{\mu\mu} - Y^{\mu\mu}$ map to match the $p_T^{\mu\mu}$ distribution of the MC to that of the data. This re-weighting helps mitigate additional mis-modelings that could introduce calibration bias. The calibration is performed exclusively in the barrel region, as it is the focus of the Z mass analysis. The process is repeated separately for the 2015-16, 2017, and 2018 campaigns.

5.4.0.2 Results

Figures 5.21 and 5.22, present a comparison of the $m_{\mu\mu}$ distributions in data and MC, before and after the application of the calibration. One example is shown for the central barrel region, and another for the outermost barrel region.

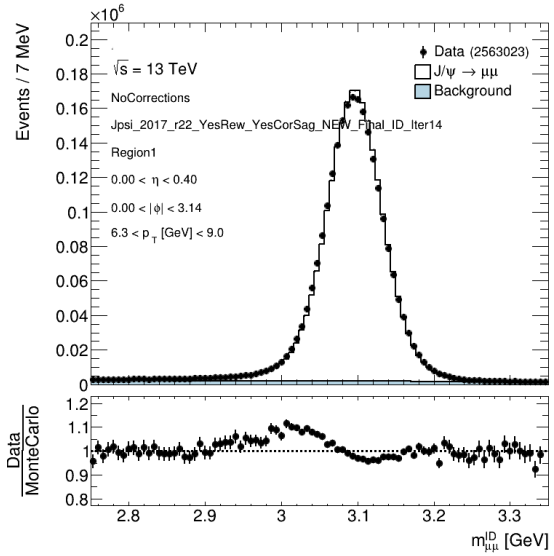

(a) Pre-Calibration distributions for the p_T bin :$6.3 < p_T^{sub-leading} < 9$ GeV

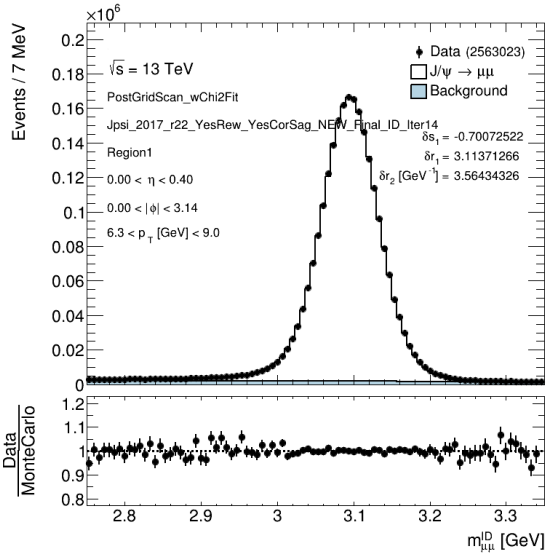

(b) Post-calibration distributions for the p_T bin :$6.3 < p_T^{sub-leading} < 9$ GeV

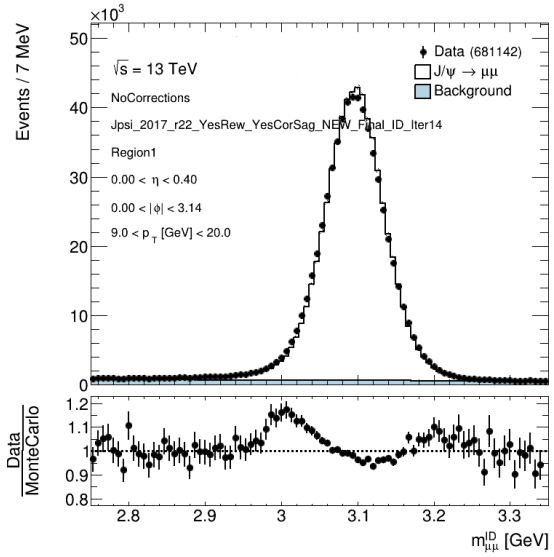

(c) Pre-calibration distributions for the p_T bin :$9 < p_T^{sub-leading} < 20$ GeV

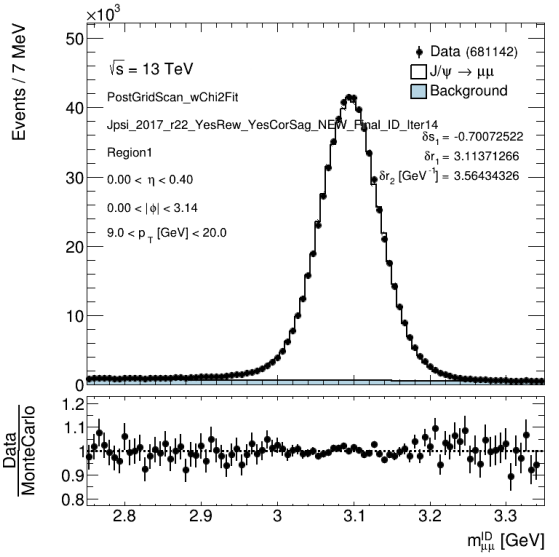

(d) Post-calibration distributions for the p_T bin :$9 < p_T^{sub-leading} < 20$ GeV

Figure 5.21: $m_{\mu\mu}$ distributions before (a and c) and after (b and d) calibration. One of the muons is required to be in η^μ region: $0 < \eta^\mu < 0.4$

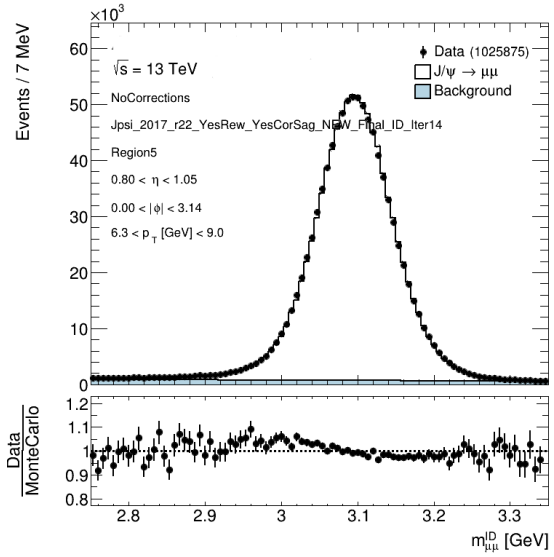

(a) Pre-Calibration, p_T bin :$6.3 < p_T^{sub-leading} < 9$ GeV

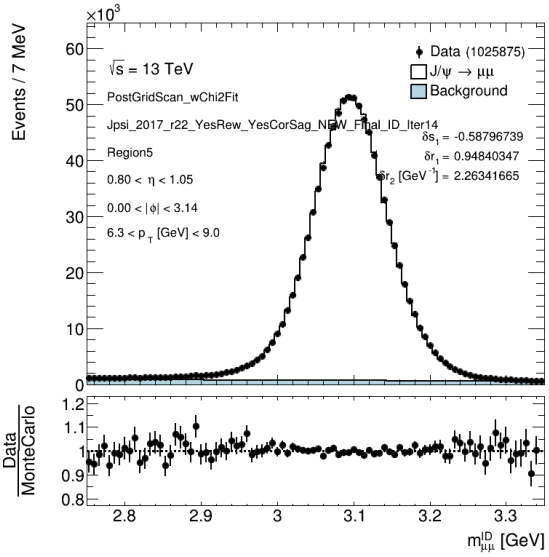

(b) Post-calibration, p_T bin :$6.3 < p_T^{sub-leading} < 9$ GeV

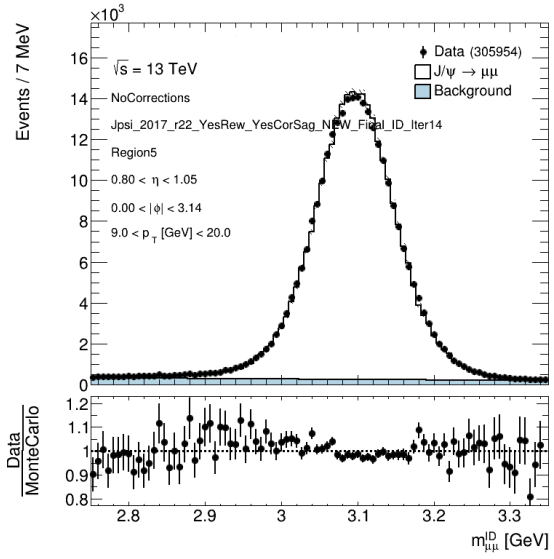

(c) Pre-calibration, p_T bin :$9 < p_T^{sub-leading} < 20$ GeV

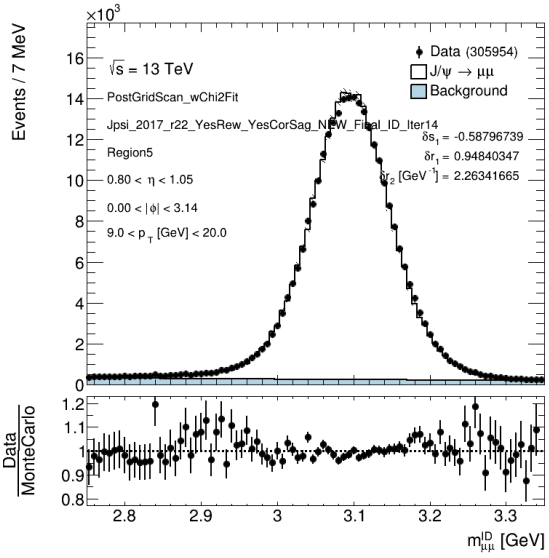

(d) Post-calibration, p_T bin :$9 < p_T^{sub-leading} < 20$ GeV

Figure 5.22: $m_{\mu\mu}$ distributions before (a and c) and after (b and d) calibration. One of the muons is required to be in η^μ region: $-1.05 < \eta^\mu < -0.8$

The mass distributions of $-1.05 < \eta^\mu < -0.8$ region in the Figure 5.22 are wider than the ones presented in the Figure 5.21 of $0 < \eta^\mu < 0.4$. This is pointing to the increase of the muon momentum resolution with η^μ. Post calibration agreement between calibrated MC and data mass distributions is larger in the first $6.3 < p_T^{sub-leading} < 9$ GeV bin in both Figures 5.21 b) and 5.22 (b) compared to the second $9 < p_T^{sub-leading} < 20$ p_T GeV bins 5.22 d) and 5.22 (d). This phenomenon is observed for two reasons. First, the second p_T bin has fewer number of events compared to the first one, leading to the fit prioritizing in the minimization the parameter values that describe the first p_T bin. Second, the phenomenon is pointing to a significant scale parameter ds_1 dependence with p_T^μ, which complicates the fit's ability to accurately calibrate both bins.

In both Figures 5.21 (b) and 5.22 (b), the ratio plots at the bottom of the figures are flat beneath the resonance peak, which confirms the accuracy of the scale calibration. However, in the tails of the distributions, the fit becomes less precise, and some structures are observed.

The observed discrepancies are attributed to imperfections in the calibration algorithm and the low number of events in the tails. The ds_1 scale parameter, which is the most significant for Z mass measurement, has a more pronounced effect on the position of the distributions. Consequently, the structures seen in the tails are considered to be non-closure effects, which are acceptable and do not require further attention within the scope of this study.

The scale ds_1, the resolution dr_1 and dr_2 are presented in the Figure 5.23.

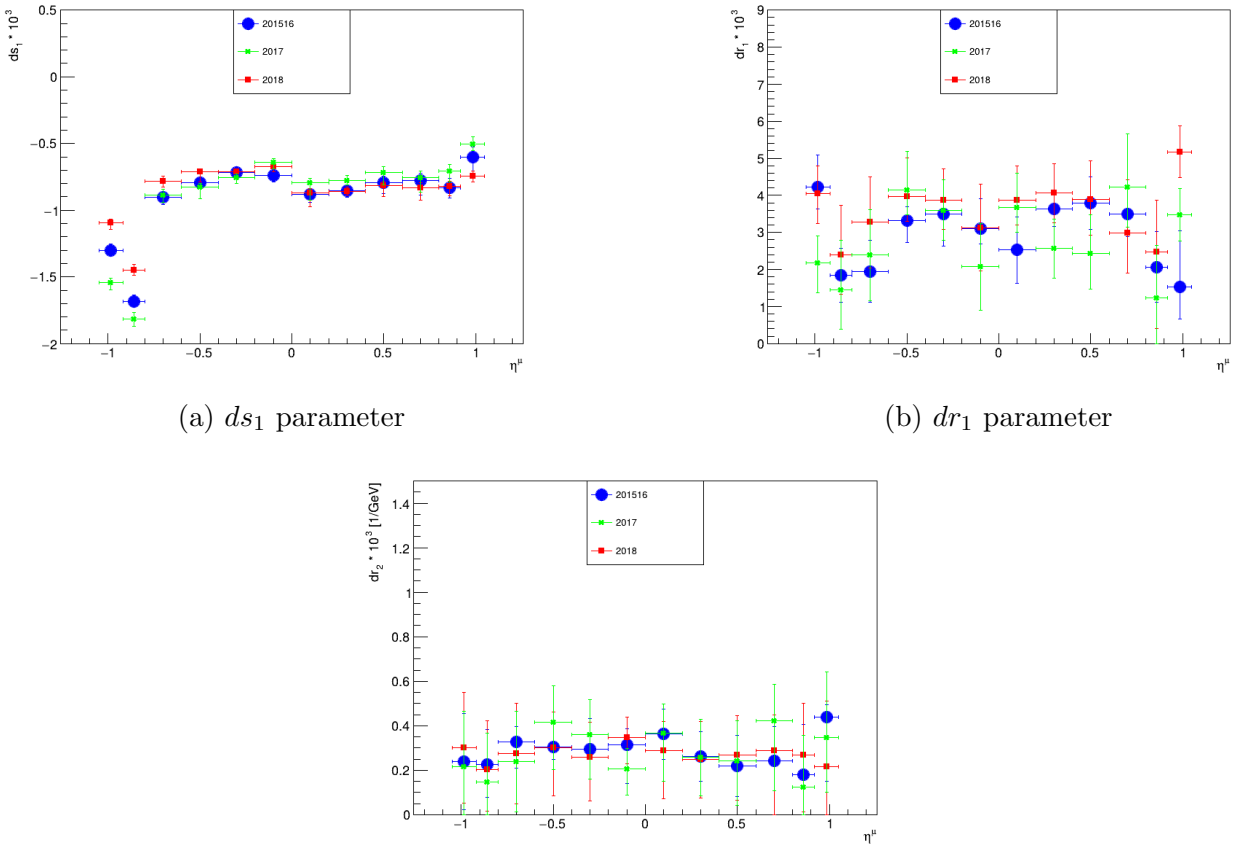

(a) ds_1 parameter

(b) dr_1 parameter

(c) dr_2 parameter

Figure 5.23: Calibration Parameters as a function of η^μ for the three campaigns and ID muons. Points are average over iterations and the error bars are systematic uncertainties for the corresponding iterations.

In the Figure 5.23 the calibration correction parameters for 2018,17,15-16 are shown with their systematic uncertainties contribution. The scale ds_1 (a) is relatively flat for the inner barrel region of $-0.8 < \eta^\mu < 0.8$ with a value $\approx 10^-3$. From 0.8 to 1.05 and from -0.8 to -1.05 scale exhibits an anti - symmetric behavior with opposite behavior in the corresponding η^μ bins. The anti-symmetric behavior, and specifically the large negative values observed in the bin -0.8 to -1.05, are likely caused by the solenoid magnetic field measurement, as mentioned in Chapter 2.2.3. Moreover, it is known that magnetic field in the intermediate region has a complex nature which requires larger corrections at the corresponding regions.

In the barrel region systematic uncertainty is $\approx 10^{-5}$ for scale parameter, for all campaigns, which is sufficient for the scope of the Z mass analysis calibration.

Additionally, the resolution parameters (b) and (c) in the barrel region are relatively flat compared to the corrections observed at higher η^μ. This behavior arises from the minimal variations in material and magnetic field within the barrel region.

The scale parameter exhibits a comparatively smaller contribution to the overall systematic

uncertainties when compared to the two resolution parameters, especially when considered in relation to their respective nominal values. The larger uncertainties in the resolution parameters do not significantly contribute to the Z mass uncertainty. Therefore, the larger error bars observed are not considered an obstacle for achieving a precise Z mass calibration. On the opposite side, the scale parameter systematic uncertainties are dominant in the Z mass measurement.

In Appendix G, in tables G.1, G.2 and G.3 the dominant systematic per η^{μ} region for the three parameters are presented for 2017 campaign. Goal of this study is to understand the main systematic contributions and their nature.

Furthermore, a crucial part of the calibration is the statistical uncertainty per iterations as the procedure is iterative. To proceed in the analysis and in the calibration the precision and stability of the parameters over iterations have to be verified. In Appendix G the average over iteration studies are presented.

5.4.0.3 Validation

For the validation two sets of plots are presented. One is the $m_{\mu\mu}$ distribution pre and post calibration. The second is the validation framework graphs as presented in 3.4.

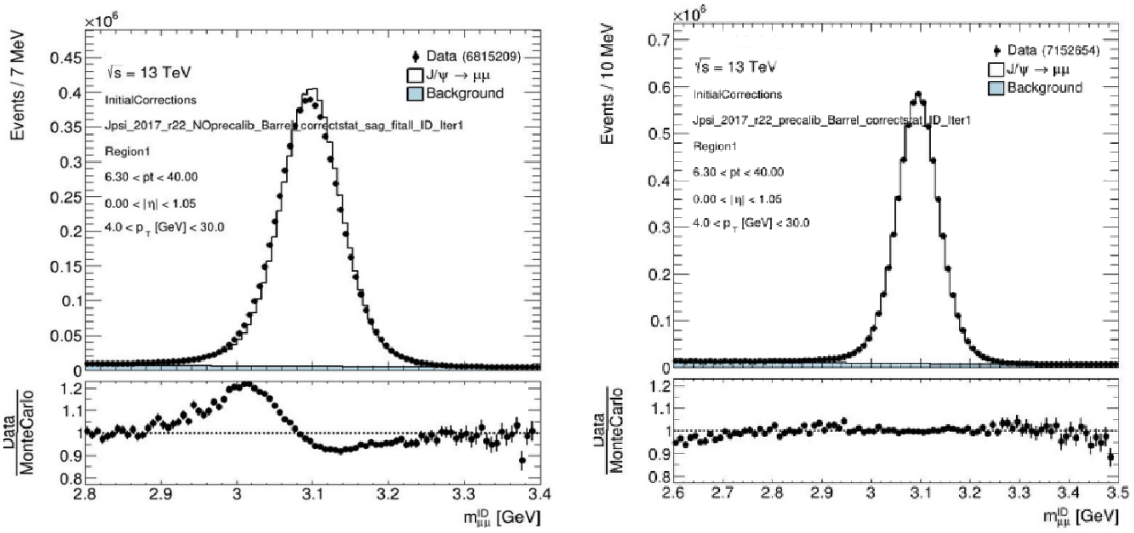

(a) Pre Calibration (b) Post Calibration

Figure 5.24: Mass distribution of J/ψ of data and simulation plus background distributions. Pre and post calibration, with muons: $6.3 < p_T^{subleading} < 30$ GeV. The samples correspond to 2017 campaign and corrected for the η^{μ} calibration presented in the Figure 5.23.

In the Figure 5.24, mass distributions of data and simulation + background are shown for muons belonging only to the barrel region, with $6.3 < p_T^{subleading} < 30$ GeV. These distributions are presented before and after the calibration corrections. An excellent accuracy of the calibration is observed. Specifically, under the J/ψ resonance peak ($\approx$ 2.9 to 3.2 GeV). In the tails there are some structures observed. This phenomenon arises from two factors: the non-closure of the resolution parameters and the p_T^{μ} dependence of the calibration parameters. The majority of muons included in the $m_{\mu\mu}$ distributions presented, are low-p_T^{μ} muons, for which the calibration is highly accurate. However, for higher p_T^{μ} muons, non-closure effects in the calibration are expected, potentially contributing to the structures observed in the post-calibration figure.

Using the validation framework, presented in Chapter 3.4, the calibration is evaluated as a function of kinematic variables. The mean and σ of $m_{\mu\mu}$ distributions from simulation and

data are compared as functions of $\eta^{leading-\mu}$, $\phi^{leading-\mu}$, and $p_T^{leading-\mu}$. These comparisons are shown before and after the calibration. The validation results for 2017 are presented here, while results for other years are included in Appendix G.3.

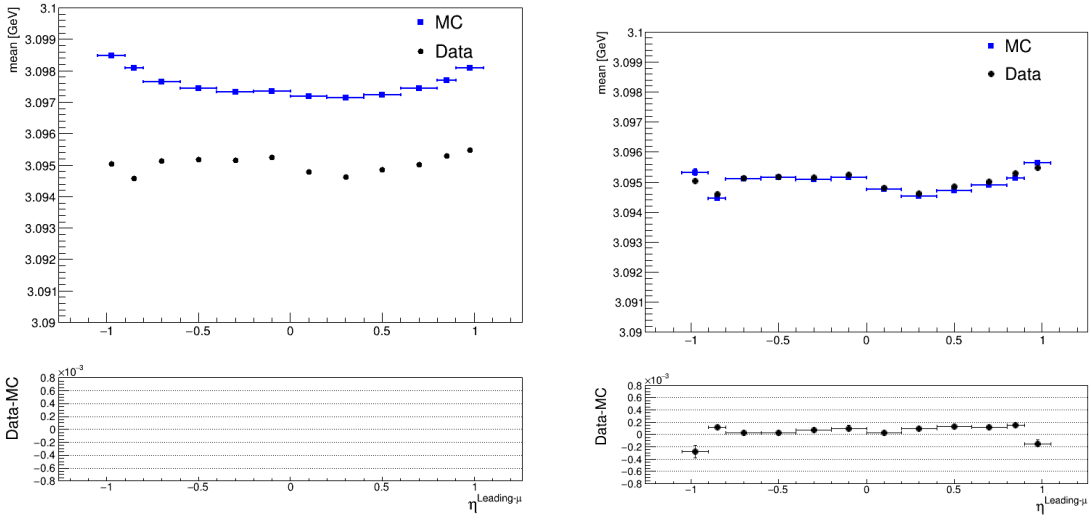

(a) Pre Calibration (b) Post Calibration

Figure 5.25: Mean of the $m_{\mu\mu}$ distribution as a function of $\eta^{leading-\mu}$ before and after calibration applied. The samples correspond to 2017 campaign, corrected for the calibration as a function of η^{μ} presented in the Figure 5.23.

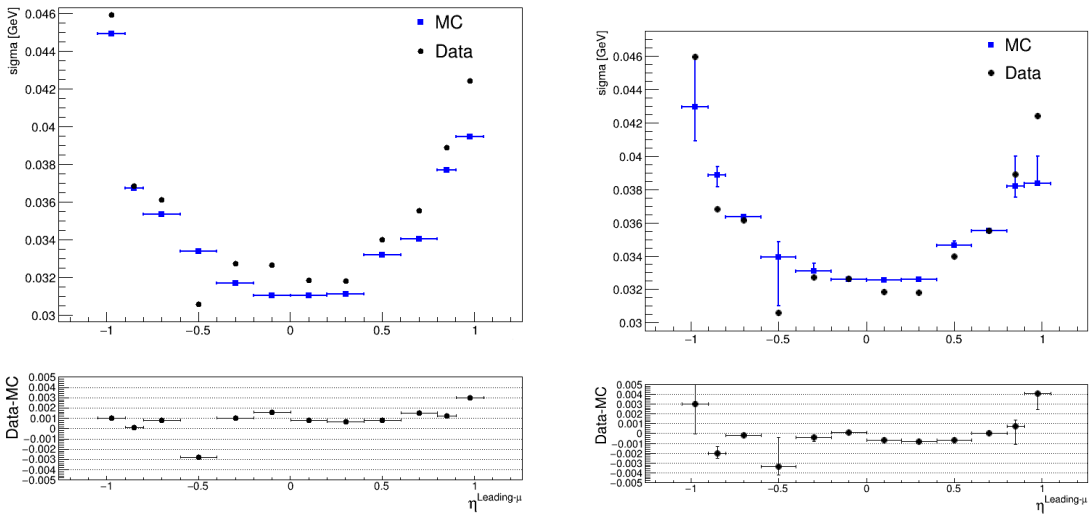

(a) Pre Calibration (b) Post Calibration

Figure 5.26: σ of the $m_{\mu\mu}$ distribution as a function of $\eta^{leading-\mu}$ before and after calibration applied. The samples correspond to 2017 campaign, corrected for the calibration as a function of η^{μ} presented in the Figure 5.23.

$\eta^{\mathbf{leading}-\mu}$: Figures 5.25 and 5.26 display the mean and σ of the $m_{\mu\mu}$ distributions as functions of $\eta^{leading-\mu}$. The validation binning is set to the same binning as the calibration.

Before the calibration, regarding the mean, there are insignificant modulations in the MC but for the data there is a clear dependence of the mean from η^{μ}. This is due to the effect of the charge independent momentum biases, present in data. It is important to note that the disagreement observed prior to calibration corresponds to the precision of the measurement of the solenoid magnetic field strength ($\approx 2\%$), as mentioned in the Chapter 2.2.3. In the data, there is an asymmetry in the mean from negative to positive η. Additionally, a clear structure appears in $-0.9 < \eta^{leading-\mu} < -0.8$ and therefore the MC needs a larger correction, in this region, to describe the data. This originates, probably, from the solenoid magnetic field measurement, which in the negative η direction was less accurate due to the dedicated technique, as mentioned in the Chapter 2.2.3.

Post calibration, the simulation aligns closely with the data. Some points exhibit a persistent, negligible difference. The most prominent ones are the bins $-1.05 < \eta^{leading-\mu} < -0.9$ and $0 < \eta^{leading-\mu} < 0.2$. These non closure effects originate in structures, present in data, with finer binning than the calibration binning.

Regarding σ, a widening of the $m_{\mu\mu}$ distributions is observed, from central barrel to outer barrel. This occurs due to the degradation of muon resolution with η. Post calibration, the agreement between data and MC reaches an accuracy of 10^{-3} GeV. There are multiple regions with reduced closure. This is due to the Gaussian smearing, which introduces additional uncertainty in the process.

$\phi^{\mathbf{leading-\mu}}$ In the Figures 5.27 and 5.28, the mean and the σ of the $m_{\mu\mu}$ distributions are shown as a function of $\phi^{leading-\mu}$.

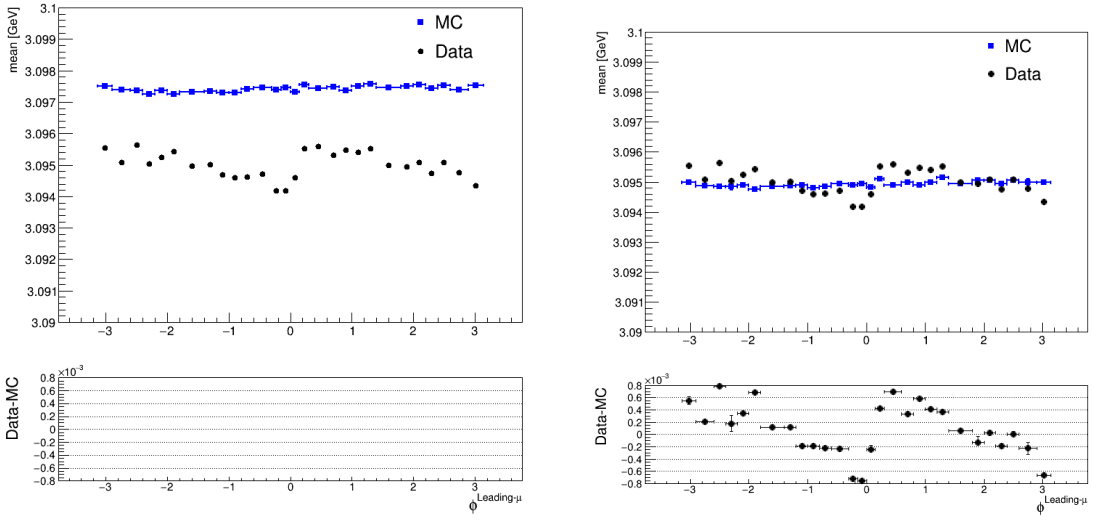

(a) Pre Calibration (b) Post Calibration

Figure 5.27: Mean of the $m_{\mu\mu}$ distribution as a function of $\phi^{leading-\mu}$ before and after calibration applied. The samples correspond to 2017 campaign, corrected for the calibration as a function of η^{μ} presented in the Figure 5.23.

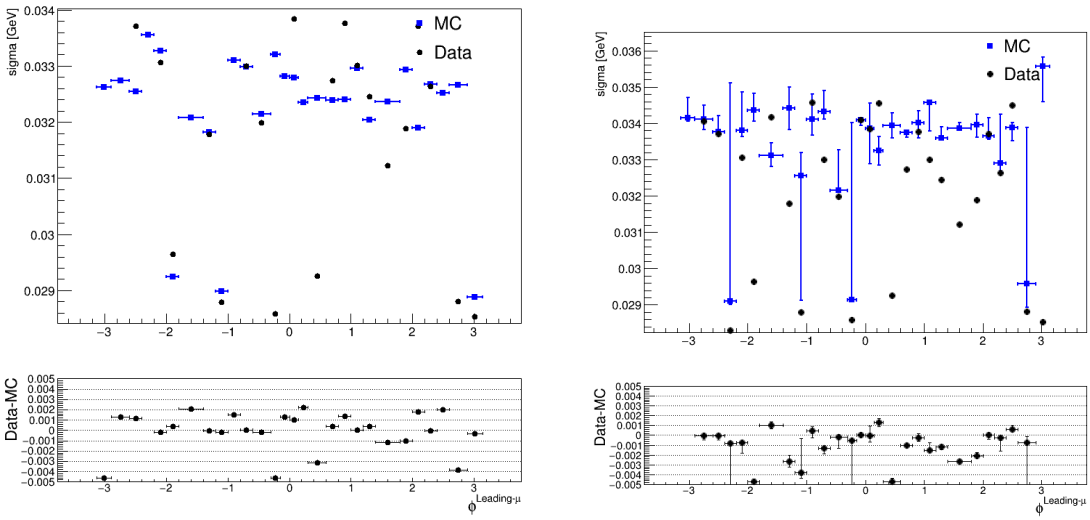

(a) Pre Calibration (b) Post Calibration

Figure 5.28: σ of the $m_{\mu\mu}$ distribution as a function of $\phi^{leading-\mu}$ before and after calibration applied. The samples correspond to 2017 campaign, corrected for the calibration as a function of η^{μ} presented in the Figure 5.23.

By comparing the mean before and after calibration, it is evident that the calibration aligns the simulation closer to the data, although it has a negligible effect on the shape of the mean as a function of $\phi^{leading-\mu}$. After the calibration, residual non-closure patterns remain, most prominently in the negative central region ($-1 < \phi^{leading-\mu} < 0$). In this area, the non-closure values reach up to 0.5×10^{-4} GeV, which constitutes a significant effect given the precision required for the Z mass measurement. The shapes observed in the data arise from deformations of the detector in the transverse plane or magnetic field residuals, which the calibration as a function of η^{μ} was unable to fully address.

The σ plots exhibit a dependence with $\phi^{leading-\mu}$. For the ID tracks, a dependence of σ with ϕ, is not expected. This effect is difficult to disentangle and is likely connected with the fact that the corresponding plot is inclusive in η. In the σ graphs there a notable improvement after the calibration, with remaining non closures. These non closure are not expected to contribute significantly in the Z mass measurement and they are ignored in the context of the thesis.

$\mathbf{p_T^{leading-\mu}}$: In the Figures 5.29 and 5.30, the mean and the σ of the $m_{\mu\mu}$ distributions are shown as a function of $p_T^{leading-\mu}$.

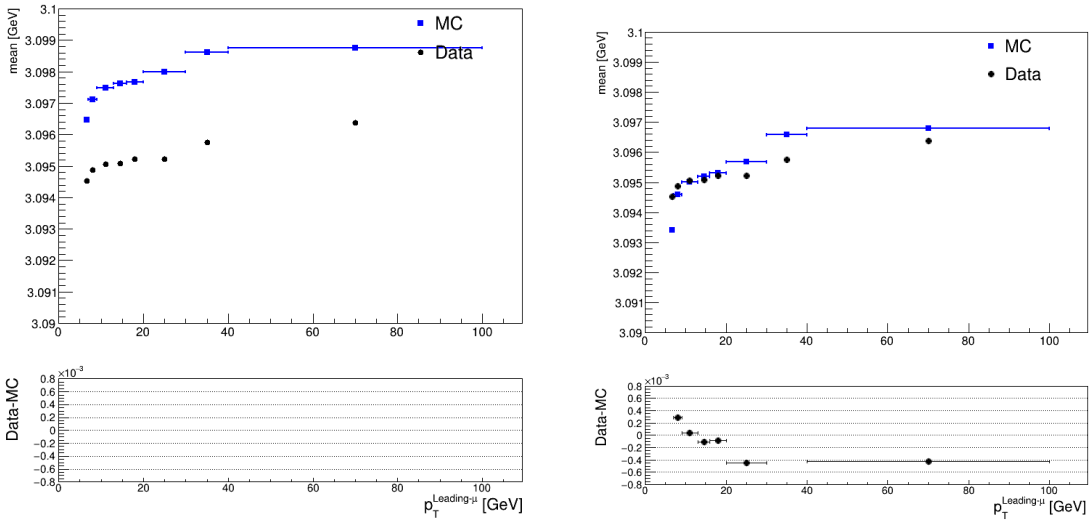

(a) Pre Calibration (b) Post Calibration

Figure 5.29: Mean of the $m_{\mu\mu}$ distribution as a function of $p_T^{leading-\mu}$ before and after calibration applied. The samples correspond to 2017 campaign, corrected for the calibration as a function of η presented in the Figure 5.23.

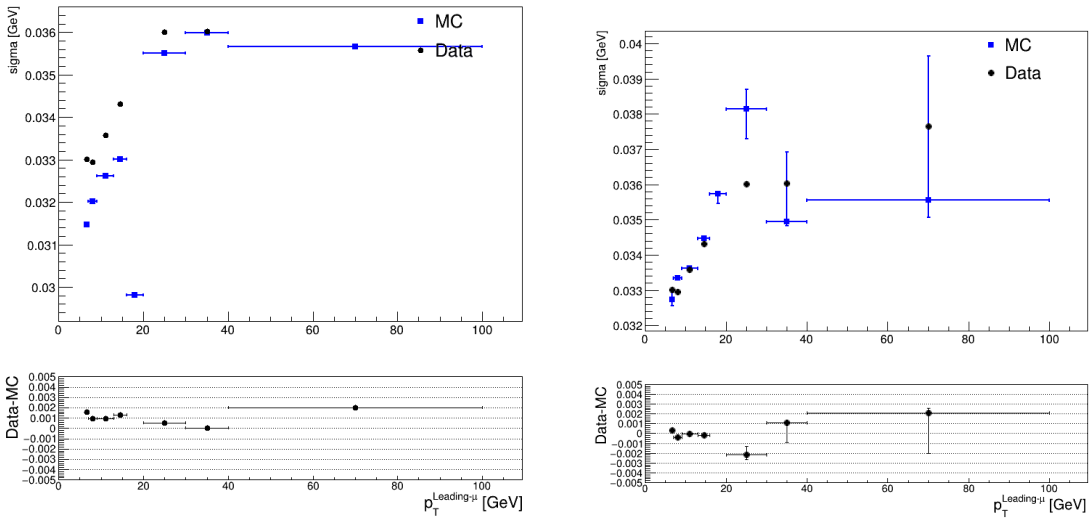

(a) Pre Calibration (b) Post Calibration

Figure 5.30: σ of the $m_{\mu\mu}$ distribution as a function of $p_T^{leading-\mu}$ before and after calibration applied. The samples correspond to 2017 campaign, corrected for the calibration as a function of η presented in the Figure 5.23.

Regarding the mean, there are structures of non-closure remaining after the calibration. Specifically, there is a trend of disagreement that grows with $p_T^{leading-\mu}$. In the first $p_T^{leading-\mu}$ bin, the difference is positive because the calibration as a function of η describes muons of average $p_T^{\mu} \approx 9-10$ GeV. For larger $p_T^{leading-\mu}$, the trend of difference between data and MC is negative, reflecting the p_T^{μ} dependence of the scale.

The σ plots reveal a widening of the mass distribution with increasing $p_T^{leading-\mu}$. This effect arises due to the deterioration of muon resolution at higher p_T^{μ}. Interestingly, in the highest $p_T^{leading-\mu}$ bin, the σ decreases. This behavior is attributed to the fact that the displayed σ

corresponds to the Crystal Ball function, where at high p_T^μ the Gauss function contribution becomes more prominent. Overall, for the σ, the calibration improves the agreement between the simulation and the data, with the highest $p_T^{leading-\mu}$ bin exhibiting a non closure.

Consequently, the calibration as a function of p_T^μ is necessary to be studied. The corresponding studies are shown in Section 5.5.

5.4.1 ϕ^μ scale residuals

To treat the non closures shown in the validation as a function of $\phi^{leading-\mu}$, in the Figure 5.27, a dedicated post calibration procedure is performed. To obtain the corrections, the samples of simulation are calibrated with the corrections obtained in the Section 5.4.0.2 and the calibration is repeated for a few iterations. The calibration was performed by integrating over η^μ and utilizing a binning in ϕ^μ. All parameters were allowed to float in the calibration fit. The resolution parameters were found to be negligible and compatible with zero. The scale residuals in ϕ^μ and the validation as a function of $\phi^{leading-\mu}$ are shown in the Figure 5.31.

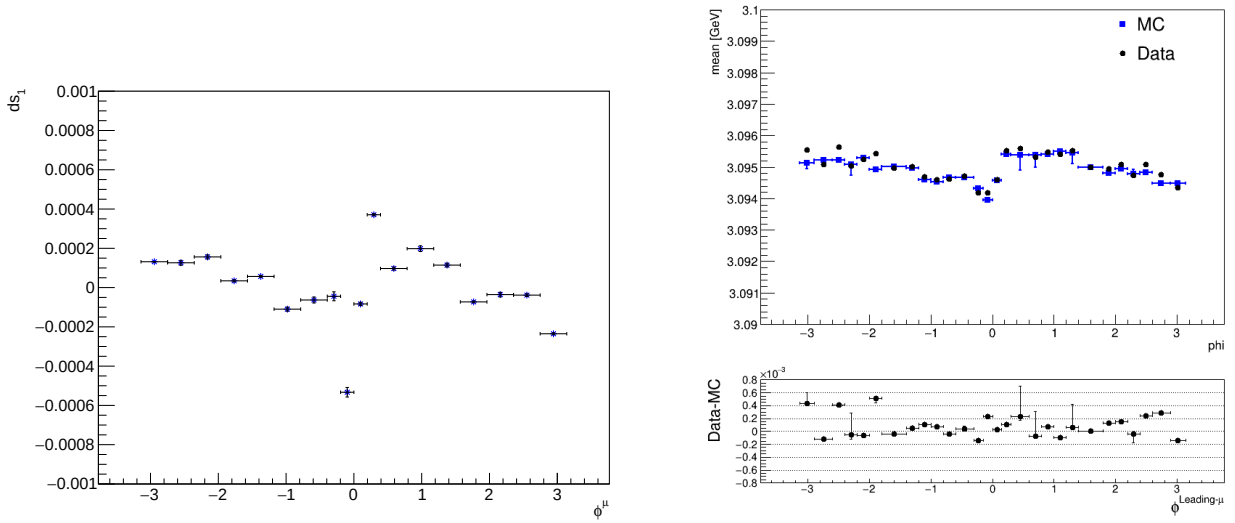

(a) ds_1 parameter

(b) mean of $m_{\mu\mu}$ as a function of $\phi^{leading-\mu}$

Figure 5.31: a) Scale parameter ds_1 as a function of ϕ^μ for $1.05 < \eta < 1.05$. b) Validation of calibration, mean of $m_{\mu\mu}$ as a function of $\phi^{leading-\mu}$ after correcting for the ϕ^μ residuals commented in 5.4.0.3.

The statistical uncertainty is of the order of 10^{-6} for the ds_1 parameter. In the validation shown in the Figure 5.31 (b), the agreement after applying the ϕ^μ residual correction is improved compared to that presented in the Figure 5.27. In most regions, the difference in the mean between data and MC is compatible with zero. However, some outliers are observed, which can be attributed to the finer binning used for validation compared to the binning chosen for calibration.

5.5 Calibration as a function of p_T^μ

In this subsection, the dependence of the calibration with p_T^μ is presented. Calibration, due to a non closure of the p_T^μ parametrization from scale and resolution parameters, has a p_T^μ dependence which is necessary to be accounted for, in order to calibrate muons originating

from Z decays. Calibration is performed in different p_T^μ bins with muons belonging to a single η^μ bin: $-1.05 < \eta^\mu < 1.05$.

The main challenge for this study is the limited size of simulated J/ψ signal. The strong dependence with p_T^μ requires as much as p_T^μ bins as possible to study the p_T^μ dependence accurately. But at the same time the individual bins need to have sufficient events to ensure calibration fits with minimal statistical uncertainty. p_T^μ binning chosen is in a way to ensure a balance between the two requirements.

5.5.0.1 Method

Calibration procedure is similar to the η^μ calibration presented in the Section 5.4. The phase space observable of interest is changed from η^μ to p_T^μ. For every p_T^μ bin, at least one of the muons, positive or negative, is required to be in the bin of interest. For each p_T^μ bin, three parameters of interest are defined: one scale parameter, ds_1, and two resolution parameters, dr_1 and dr_2.

In these calibration fits, all parameters for ID muons (ds_1, dr_1, dr_2) are allowed to float. The resolution parameter dr_1 is expected to be independent of p_T^μ, whereas ds_1 and dr_2 are more likely to show such dependence. However, primary attention is given to the ds_1 calibration with p_T^μ, as it has the most significant impact on the Z mass measurement.

An important aspect of the p_T^μ calibration is the choice of the triggers. In general, the calibration process is sensitive to the difference in the simulation and data p_T^μ distributions. Since one of the trigger's major characteristic is the p_T^μ selection they can influence the data-simulation agreement. Additionally, pre-scale trigger factors can impact the discrepancy between the two, resulting in acquiring different p_T^μ calibration results depending on the choice of trigger. Consequently different triggers choices are used to construct a systematic uncertainty from the p_T^μ extrapolation. For the corresponding study two different trigger configurations are compared. One of the general trigger list and one of the MCP one. The importance of comparing the two p_T^μ calibrations arises from the fact that the general trigger list includes several triggers which are pre-scaled and therefore influence heavily the agreement between data and simulation p_T^μ distributions. In the η^μ calibration such a study is less important since η^μ calibration is inclusive in p_T^μ and less sensitive to these effects. In both calibrations to correct for the trigger miss-simulation effect a $p_T^{\mu\mu}$ re-weighting is applied.

For 2017 and 2018 MCP triggers are almost not at all pre-scaled. On the contrary in the general trigger list there many triggers heavily pre-scaled. Trigger lists are found in the Appendix I. For the 2015-16 campaign, MCP triggers are absent in the samples processed. The general trigger list used for 2015-16 includes heavily pre-scaled triggers. This is expected to have an impact on the kinematic distributions and on the accuracy of the calibration. The p_T^μ re-weighting procedure is expected to cover efficiently the possible biases.

5.5.0.2 Results

In the Figures 5.32 to 5.34, the results for 2015-16, 2017, 2018 are presented.

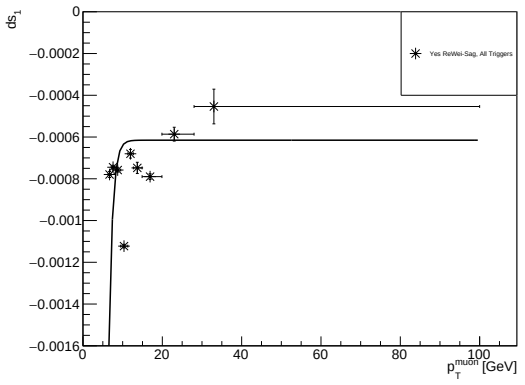

(a) ds_1 parameter

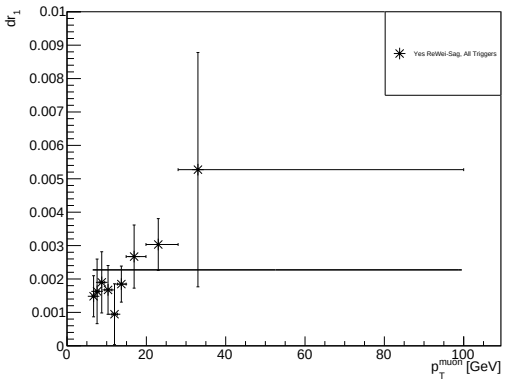

(b) dr_1 parameter

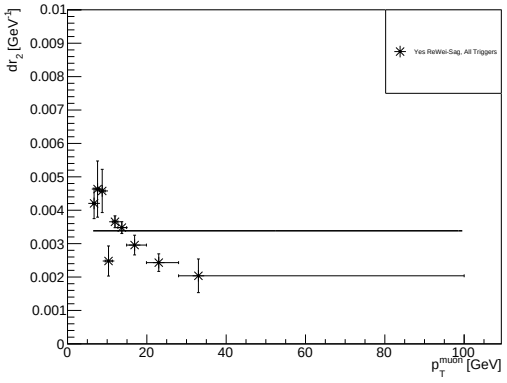

(c) dr_2 parameter

Figure 5.32: Calibration Parameters as a function of p_T^μ for the campaign 2015-16 and ID, barrel muons. Points are average over iterations 15 to 20 and the error bars are the standard deviation over iterations.

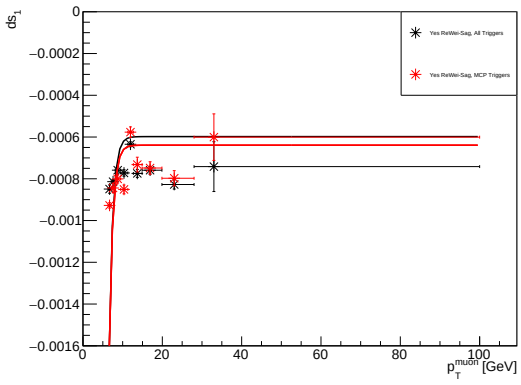

(a) ds_1 parameter

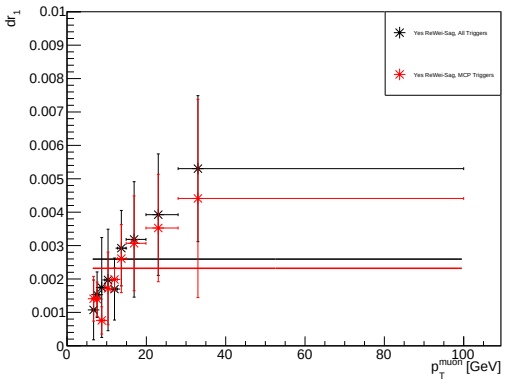

(b) dr_1 parameter

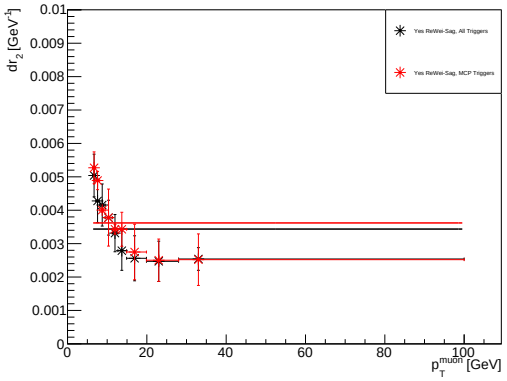

(c) dr_2 parameter

Figure 5.33: Calibration Parameters as a function of p_T^μ for the campaign 2017 and ID, barrel muons. Points are average over iterations 15 to 20 and the error bars are the standard deviation over iterations.

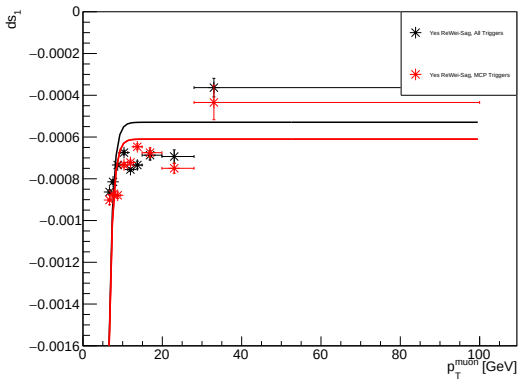

(a) ds_1 parameter

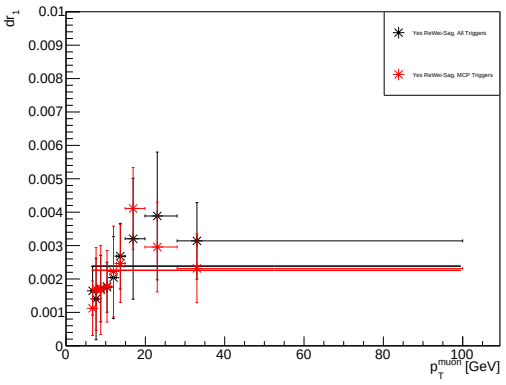

(b) dr_1 parameter

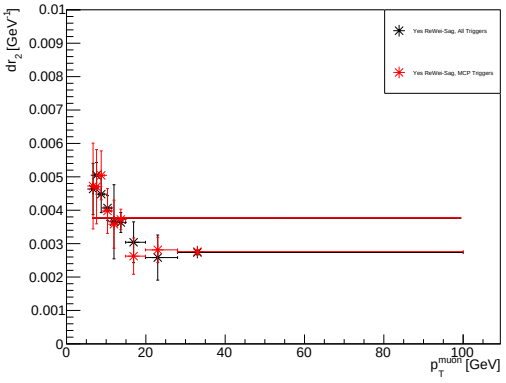

(c) dr_2 parameter

Figure 5.34: Calibration Parameters as a function of p_T^μ for the campaign 2018 and ID, barrel muons. Points are average over iterations 15 to 20 and the error bars are the standard deviation over iterations.

ds_1: In the Figures 5.32a, 5.33a and 5.34a, the scale ds_1 as a function of p_T^μ is presented for the three campaigns. Two separate calibrations are presented, one using the MCP trigger list and the other using general trigger lists (Defined in Appendix I), for the years 2017 and 2018. Depending on the campaign the difference of the two calibrations is less or more significant.

The p_T^μ dependence of ds_1 is fitted with a negative exponential one. In this model the scale that is computed from the calibration procedure, ds_1^{fitted}, is parameterized as:

$$ds_1^{fitted} = ds_1^{true} - e^{-slope \times p_T^\mu}$$

with ds_1^{true} is the true value of the scale ds_1 that is constant with p_T^μ, the exponential part is it's correction for the low p_T^μ values that do not follow a steady with p_T^μ dependence and *slope* is the exponential constant. The parametric function is plotted on the graphs with the same color as indicated for the points in the legend. It is not a function that corresponds to a specific physics based model. Rather, it is a phenomenological approach. The parametric function, does not fully describe the shape of the data points, which display fluctuations with p_T^μ, indicating unresolved mis-modeling issues beyond those currently addressed.

Additionally, it is hypothesized that trigger mis-modeling may be responsible for the outlier points, particularly in regions where the leading and sub-leading distributions diverge significantly. Another hypothesis is that in these p_T^μ ranges there is significant overlap between Physics Main and B Physics streams. These points are the fourth point for 2015-16 and 2017 campaigns. A minor study has been conducted for the outlier bin $11 < p_T^\mu < 12$ GeV of 2017

campaign. It's existence have a large impact on the dependence of ds_1 from the p_T^{mu} and it gives a non physical shape in the calibration. The main hypothesis of this study is that since the $p_T^{\mu} = 11$ GeV is a cut value for one of the main triggers: `HLT_mu11_mu6_bJpsimumu`,there is a possibility that in a minimal interval above 11 GeV the distributions of leading and sub-leading are significantly different resulting this point. To test this hypothesis a calibration has been produced with excluding muons with p_T^{μ} from 11 to 11.7 GeV from the selection. In Appendix H.1. the nominal and the hypothesis calibrations are compared for the scale parameters. The other parameters are of less importance in the extrapolation process and for this study their comparison is considered redundant. The alternative p_T^{μ} binning did not resolve the issue and the outlier point continues to exist.

In addition to ensuring agreement between the two calibrations, another critical aspect to address is the overall shape of the scale as a function of p_T^{μ}. Across all three campaigns, the overall dependence of ds_1 with p_T^{μ} exhibits a consistent pattern. The shape agrees with the validation plots produced for the calibration as a function of η^{μ} in Section 5.4.0.3, Figure 5.29. In the 2015-16 case, the p_T^{μ} dependence appears more pronounced compared to the 2017-2018 cases, as the scale shows a persistent upward trend in the final bins, increasing sharply with p_T^{μ}. In contrast, the 2017 graph indicates that the scale levels off, reaching a plateau around $p_T^{\mu} \approx 12$ GeV. The prominence of this plateau varies depending on the choice of trigger due to the last bin above 30 GeV. In the 2018 graph, the plateau is again visible at the same region. The last bin resides significantly above the bins from $p_T^{\mu}{}^{\mu} \approx 12 - 30$ GeV. The last bins in all campaigns show slow or a sharp rise with p_T^{μ}. Without additional events in the MC sample the study has reached it limits.

Consequently, a slow rise of the scale above the plateau region $p_T^{\mu} \approx 12 - 30$ GeV can not be excluded. At the same time, the extremely high values indicated in the 2015-16, 2018 campaigns for the high p_T^{μ} are believed to be results of unstable fit due to low number of events in the simulation. For this reason, in the context of this thesis the parametric function is considered to be stable above the plateau region.

The region $p_T^{\mu} < 20$ GeV is less important for this study since Z mass analysis includes muons with $p_T^{\mu} > 21$ GeV. A potential deviation in the low p_T^{μ} bins between the two calibrations does not significantly impact the Z mass analysis. In contrast, the higher p_T^{μ} bins are more important. At the last bins of the Figures 5.33a and 5.34a for 2017 and 2018 campaigns the high p_T^{μ} bin is significantly different in the two trigger selections. At this high p_T^{μ}, the number of available simulation events is low. First, the fits themselves can become unstable due to the low number of events, potentially leading to a "false" result. Secondly, the re-weighting when performed with low number of events can result to un-physical weights which influence the distributions. Moreover, as presented in the Figure 5.6, there are high values of Data/MC ratio for the $p_T^{\mu\mu}$ distributions. These values will lead to high weights and, as noted, likely originate from overlapping events between the Main Physics and BPhys streams. Lastly, an incorrect mixture of Prompt and Non Prompt J/ψ can distort significantly the high p_T^{μ} bin result, as Non Prompt is dominant in high p_T^{μ}, as shown in the Figure 5.1.

dr_1: In the Figures 5.32b, 5.33b and 5.34b, the resolution parameter dr_1 as a function of p_T^{μ} is presented for the three campaigns. This resolution parameter is characterized with an increased standard deviation over iterations relatively to it's value. It's value is considered to be constant with p_T^{μ} since values from the first to the last bin are compatible within the uncertainty margin. The parametric function is therefore a linear one. The difference between the two calibrations for the 2017 and 2018 campaigns is negligible and it is considered zero.

dr_2: In the Figures 5.32c, 5.33c and 5.34c, the resolution parameter dr_2 as a function of p_T^{μ} is presented for the three campaigns. In this parameter there is a p_T^{μ} dependence is observed. dr_2

parameter though have negligible values and in the p_T^μ regime of the J/ψ it's contribution is low. Therefore, it's value is considered constant with p_T^μ and it is fitted with a linear function. The difference between the two calibrations for the 2017 and 2018 campaigns is negligible and it is considered zero.

A key aspect to consider is the interplay between the two resolution parameters, as their correlation is significant during the fitting process. A significant p_T^μ is not expected but one is seen clearly in all the corresponding Figures for dr_1 and dr_2. Given that dr_1 increases with p_T^μ while dr_2 decreases, it is likely that this behavior is driven by their strong correlation. A good practice would be to "lock" the values of dr_1 in the η^μ calibration values and float only dr_2. This way final result would be less prone to correlation between resolution parameters.

5.6 Conclusions

First, the overall strategy was outlined, emphasizing the necessity of utilizing the J/ψ resonance. This approach facilitates the study of the p_T^μ dependence of the calibration, with particular attention given to the scale.

Afterwards, the data and simulation samples and the kinematic distributions were presented for the three campaigns, and two different trigger configurations in the Figures 5.4, 5.5 and 5.6. Different ratio's were observed in the Data/MC ratio plots depending on the trigger list choice. Most importantly a large ratio was observed for high values of $p_T^{\mu\mu}$. A possible root is the non correct mixture of Prompt and Non Prompt J/ψ in the simulation.

A study was performed to investigate selection choices on Prompt and Non Prompt J/ψ. The study's main goal was to create two separate samples with a negligible contamination between Prompt and Non Prompt. This separation is possible by using the muon d_0/σ_{d_0} and $z_0 \times \sin\theta$ or the di-muon L_{xy}. The calibration between the two samples was compared for the two different selection choices. By comparing scale ds_1 as function of η^μ for Prompt and Non Prompt two conclusions are derived:

- The Non Prompt J/ψ produced far from the interaction point are more energetic. This is reflected in the ds_1 results.
- The Non-Prompt calibration is affected by issues with fit quality. This is due to incomplete background estimation and signal simulation. Since Non Prompt includes B-meson physics, it is sensitive non perturbative QCD physics, which is hard to simulate accurately.

Since Prompt calibrations has shown a statistical uncertainty of $\approx 10^{-5}$ for the scale, the majority of Non Prompt J/ψ is decided to be dropped. Rest of the calibration studies use therefore the muons selection: $|d_0/\sigma_{d_0}| < 3$ and $|z_0 \times \sin\theta| < 0.5$ mm.

The calibration studies proceeded to a calibration as a function of η^μ for all campaigns. Scale at the inner-most barrel has almost a uniform dependence with η^μ. At the outermost barrel, scale deviates from uniformity, due to discontinuations of the detector there and the complex nature of the magnetic field in intermediate regions. Systematic variations of the calibration were produced. Relative systematic uncertainties are in the order of ≈ 0.01 for the barrel region. Resolution parameters have larger relative uncertainties but are not expected to contribute significantly in the Z mass measurement.

Validation plots demonstrated a good agreement between MC and data post-calibration, particularly for the η^μ dependence of the mean and the σ of the $m_{\mu\mu}$ distributions. However, some residual non-closure effects remain, which can be attributed to the calibration binning not being sufficiently fine. As a function of $\phi^{leading-\mu}$ and $p_T^{leading-\mu}$ there are remaining non closures after the calibration. For the case of $\phi^{leading-\mu}$ a second calibration as a function of ϕ^μ was able to address the non closures.

Finally, a calibration was presented for the barrel region as a function of p_T^μ. Scale parameter showed a rising shape with p_T^μ which is not possible to fit with a trivial parametric function, for example a linear one. The parametric function chosen to describe the scale dependence was an inverse exponential. Overall, a plateau is reached at higher p_T^μ which is important for the Z mass measurement.

Additionally, the scale dependence had a major difference when fitted with two different trigger configurations. This is considered as a systematic in the Z mass measurement. The source is likely to be connected with the overlap between the BPhys and Physics Main streams. As one of the trigger configurations use more triggers, it is possible to increase the overlap.

At the dependence of scale from p_T^μ there were two categories of outlier points. The first one, present for the 2015-16 and 2017 campaigns at intermediate $p_T^\mu < 20$ are likely to originate in trigger effects. The second type of outlier points are the ones at $p_T^\mu > 30$. Their origin comes from non physical effects. The major one being the number of simulated events, which are very low in these bins, leading to non accurate fits during calibration. Secondly the incorrect mixture of Prompt and Non Prompt J/ψ can influence greatly the agreement between data and MC p_T^μ distributions.

Resolution parameters showed a low dependence from p_T^μ but due to large statistical uncertainties they can be considered stable with p_T^μ. Specifically they showed an anti-correlating behavior which could be an effect of fit configuration. As an alternative the dr_1 could have been kept stable with p_T^μ and float only the dr_2 to avoid heavy correlation effects.

5.6.0.1 Outlook

To improve the results presented for calibration as a function of p_T^μ, a correction can be included to accurately describe Prompt and Non Prompt J/ψ ratio with p_T^μ. This is possible by studying variables with distinct behavior in Prompt and Non Prompt J/ψ. A good example is the d_0/σ_{d_0} distribution. Producing templates of d_0/σ_{d_0} for different p_T^μ bins, Prompt and Non Prompt simulation and data, as in the Figure 5.8a. By comparing the simulation templates to the data one, an accurate description of the ratio between them can be derived, as a function of p_T^μ.

Post calibration, the simulation aligns closely with the data. Some points exhibit a persistent, negligible difference. The most prominent ones are the bins $1.05 < \eta^{leading-\mu} < 0.9$ and $0 < \eta^{leading-\mu} < 0.2$. These non closure effects are believed to originate in structures, present in data, with a finer dependence than the binning chosen for the calibration.

Additionally, the calibration as a function of p_T^μ showed a dependence from the year processed. This is likely due to the overlap between data streams and a minor reconstruction error existing in the samples. With the availability of improved samples, these effect will not exist.

Furthermore, a simulation sample with more available events can provide stable fits for the high p_T^μ bins. Also a finer binning will be possible to study better the p_T^μ scale dependence.

Chapter 6

Z Mass Measurement

Contents

In this Chapter, the Z mass measurement procedure and analysis are presented. A dedicated framework is used for Negative Likelihood fits to determine the Z mass.

First, there will be an analysis of the data and simulation samples used for Z mass measurement, alongside the selection performed. The muon momentum correction choices and effect on the Z mass are going to be discussed. A dedicated weighting procedure is presented, which produce Z mass distributions for different mass and width variations. Lastly, the results of the statistical analysis are presented with the systematic uncertainties, using a blinded likelihood fit.

6.1 Data and Simulation Samples

Data samples corresponds to data taken throughout the full Run-2 for proton-proton collisions, for a total integrated luminosity 150 fb^{-1} a center of mass energy of $\sqrt{s} = 13$ TeV. Data are chosen from Main Physics stream of ATLAS for all campaigns.

For the simulation samples, dedicated MC generators were used. For the W and Z the Powheg generator was utilized, with up to Next to Leading Order (NLO) for QCD [66] - [69], using the CT10 PDF [70], interfaced to Pythia8 [51] using the AZNLO tune [72]. To add the effect of QED final state radiation the samples were interfaced with Photos++ [73]. Simulation samples [74] were processed with Geant4 [75] for the detector effects. The list of background processes are presented in Chapter 3.3.4. Simulation normalization is scaled to ATLAS luminosity values using the cross sections from PDG [2].

Trigger selection is presented in the Table 6.1.

Year	Trigger
2015	HLT_mu20_iloose_L1MU15 OR HLT_mu40
2016,17,18	HLT_mu26_ivarmedium OR HLT_mu50

Table 6.1: Trigger list used for the samples of Z mass measurement

6.1.1 Selection

Event selection is displayed in the Table 6.2.

Selection for Signal Region
Only two muons
Muon trigger matched
Muons Isolated
Opposite charge
Both $p_T^\mu > 25$ GeV
Both $\|\eta^\mu\| < 1.05$
$66 < m_{\mu\mu} < 116$ GeV

Table 6.2: Selection for Z mass measurement, data and simulation samples.

Selection of two muon events is crucial to exclude background with multiple leptons at the final stage as $t\bar{t}$ or di-boson processes. Trigger matching and passing are crucial for proper normalization, ensuring that the selected events correspond to the applied trigger conditions. Additionally, applying isolation selection on muons is essential to suppress background events where muons are produced inside jets or in association with other particles. This isolation criteria improves the purity of the sample by reducing contamination from non-prompt or secondary muons. This cut significantly reduces the background contributions, especially from $t\bar{t}$. Opposite charge is important, as $Z \to \mu^+\mu^-$ by definition must include a muon and an anti-muon. The $p_T^\mu > 25$ GeV selection removes lower-energy background processes and further tightens the event selection to signal-like events. The $|\eta| < 1.05$ selection is crucial to exclude muons that do not belong in the barrel region, as tracking systems outside the barrel region of the Inner Detector have poorer resolution. Additionally, selecting muons within the Z mass range, $66 < m_{\mu\mu} < 116$ GeV, is essential for the measurement. At this stage, the background is nearly fully suppressed, and the data event yield is accurately described by the signal plus background processes.

6.1.2 Comparison of Data and Simulation

In the Figure 6.1, the cut flow histograms are displayed for the three campaigns for data and simulation (signal and background). Cut flow histograms are normalized to luminosity of the individual years. After the opposite sign selection, at the last three bins, there is good agreement between simulation and data. Background contributes significantly in the first bin ("No cut"). As the cut flow histogram progresses to the signal region the background becomes negligible. The mass selection is reducing the background to an percentage of $\approx 1\%$.

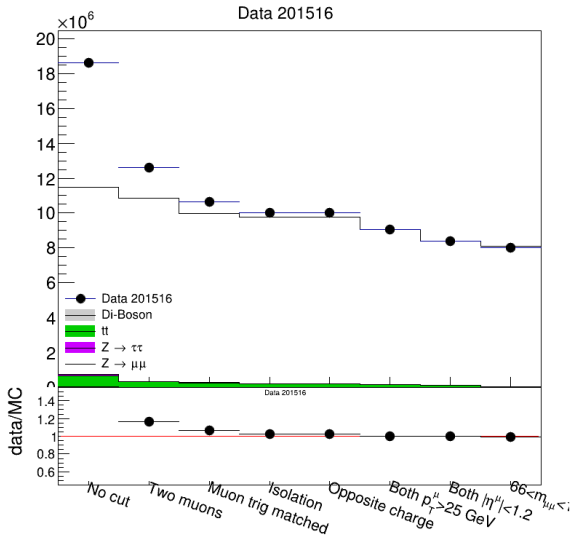

(a) 2015-16

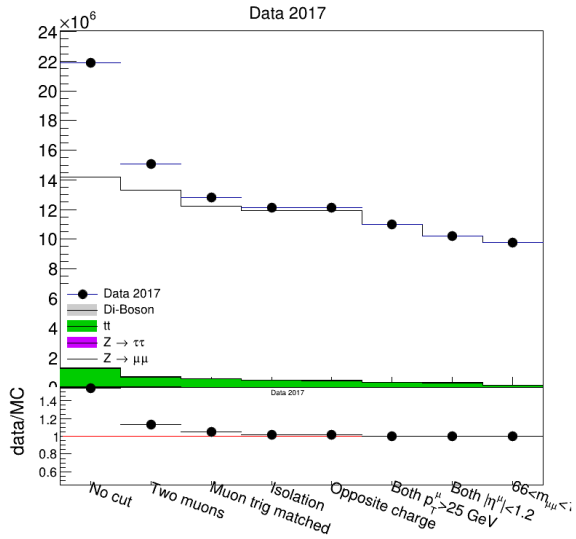

(b) 2017

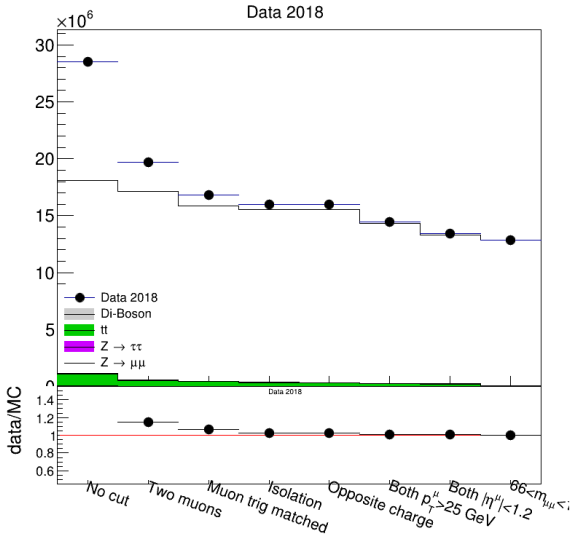

(c) 2018

Figure 6.1: Cut flow histograms for simulation (signal and background) and data.

Kinematic distributions are important to understand underlying effects and the quality of the measurement. In the Figures 6.2, 6.3, 6.4 the leading, sub-leading and di-muon p_T distributions are shown. There is a trend observed in the ratio plots of increasing disagreement towards larger values. Specifically, in the Figures leading Figures for all campaigns there is a trend which is visible at $p_T^{leading} \approx 90$ GeV. For the sub-leading, this discrepancy is relevant for pictures $p_T^{sub-leading} \approx 50$ GeV. A noticeable discrepancy is also observed at high $p_T^{\mu\mu} > 100$ GeV. These discrepancies exhibited in all p_T kinematic distributions notably increase at higher values. This is primarily attributed to the absence of higher-order diagrams at the Next-to-Next-to-Leading Order (NNLO) for the signal, which grow in significance as the energy increases.

In the Figures 6.5 and 6.6, leading η_μ and $Y_{\mu\mu}$ distributions are presented. Angle related distributions are sensitive to the lack of higher order diagrams, mis-modeling of angle kinematic variables but also deformations of the detector, not corrected at the calibration procedure. Corresponding Figures, show an excellent agreement between MC and data. Therefore, in the context of the thesis, it is concluded that there is no study needed for angle mis-modeling.

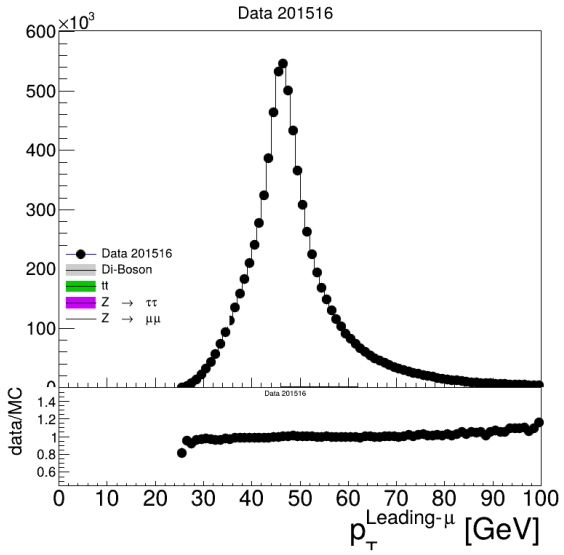

(a) 2015-16

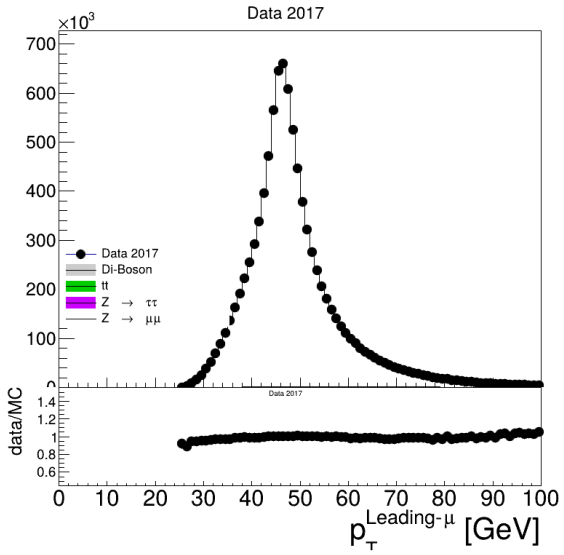

(b) 2017

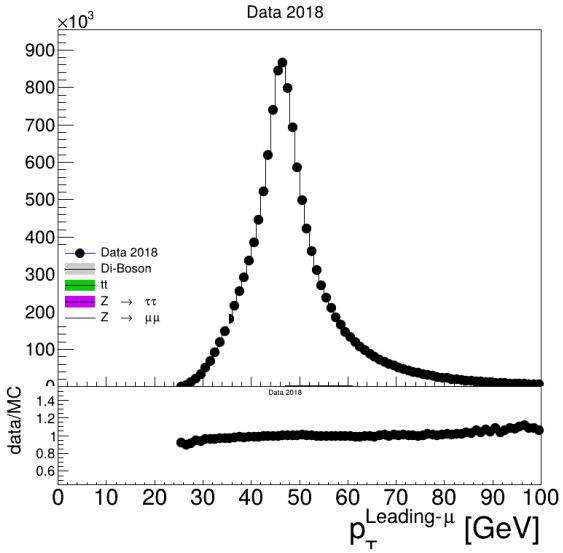

(c) 2018

Figure 6.2: $p_T^{leading-\mu}$ distributions for the three campaigns, simulation (signal+background) and data, using selection of Table 6.2. Simulation samples are scaled to Run-2 luminosity.

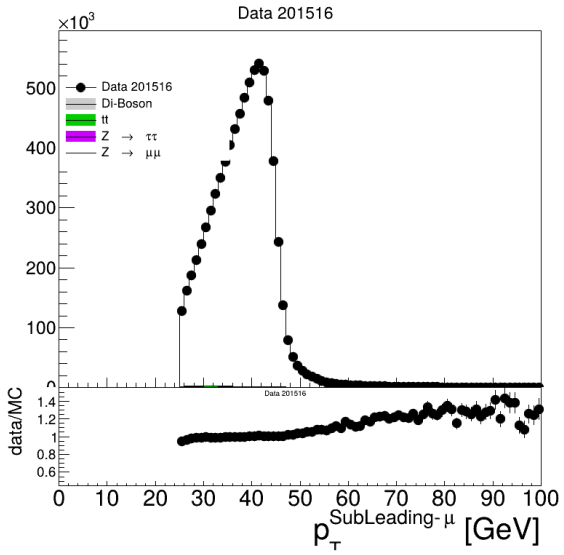

(a) 2015-16

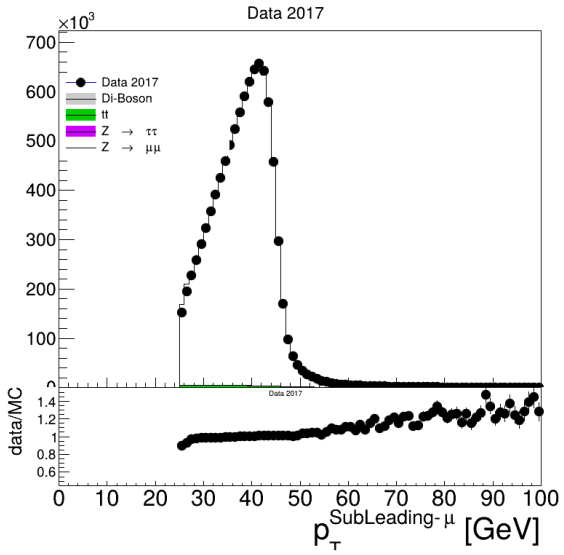

(b) 2017

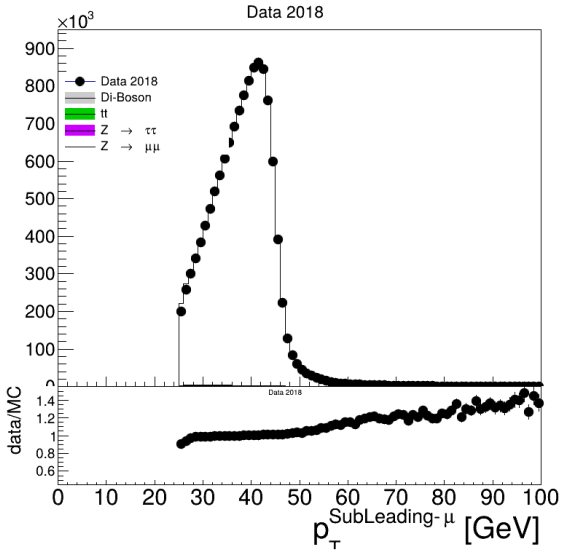

(c) 2018

Figure 6.3: $p_T^{subleading-\mu}$ distributions for the three campaigns, simulation (signal+background) and data, using selection of Table 6.2. Simulation samples are scaled to Run-2 luminosity.

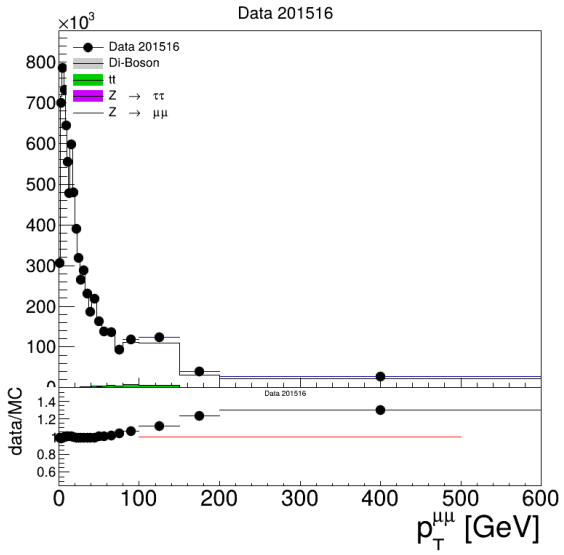

(a) 2015-16

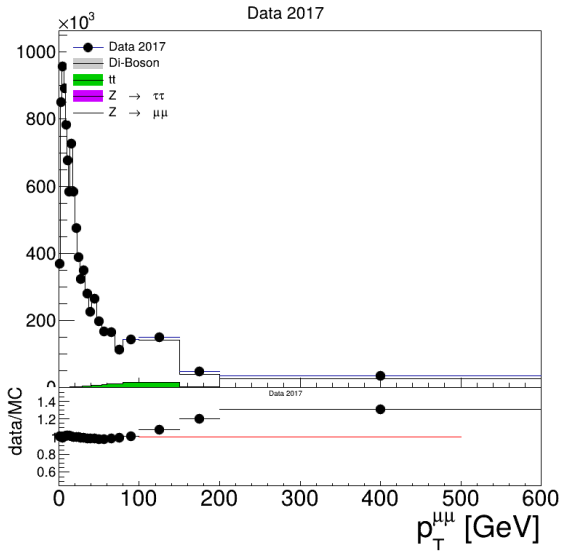

(b) 2017

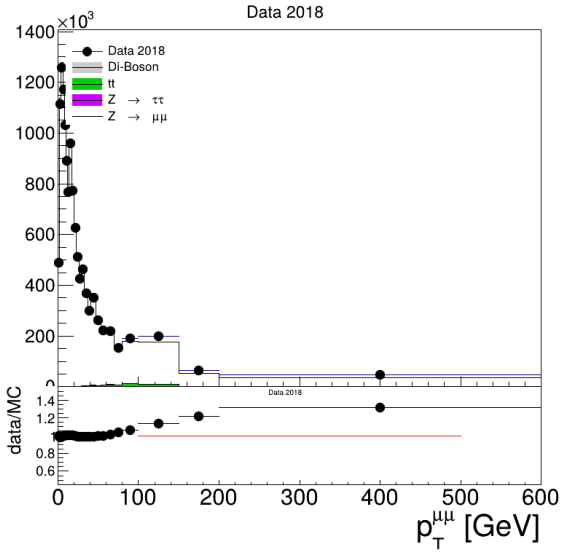

(c) 2018

Figure 6.4: $p_T^{\mu\mu}$ distributions for the three campaigns, simulation (signal+background) and data, using selection of Table 6.2. Simulation samples are scaled to Run-2 luminosity.

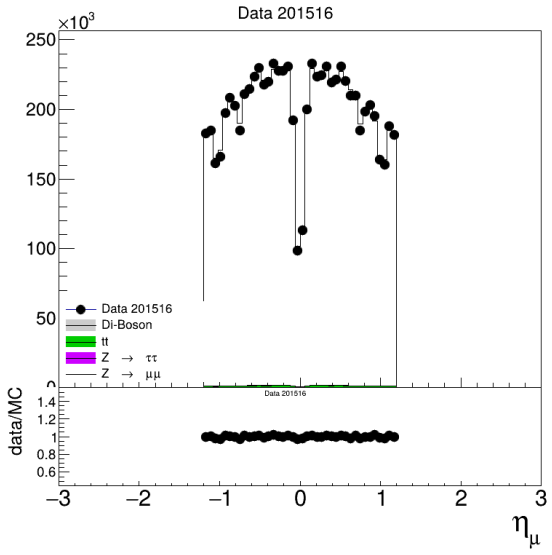

(a) 2015-16

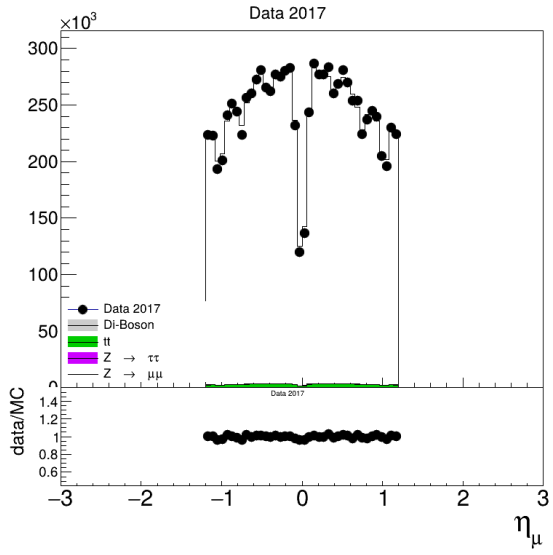

(b) 2017

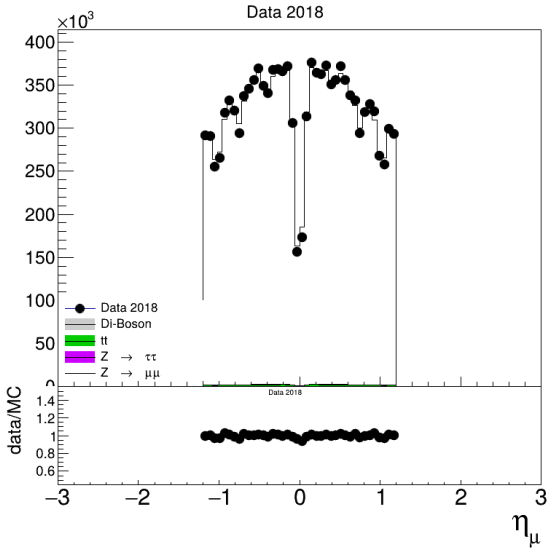

(c) 2018

Figure 6.5: $\eta^{leading-\mu}$ distributions for the three campaigns, simulation (signal+background) and data, using selection of Table 6.2. Simulation samples are scaled to Run-2 luminosity.

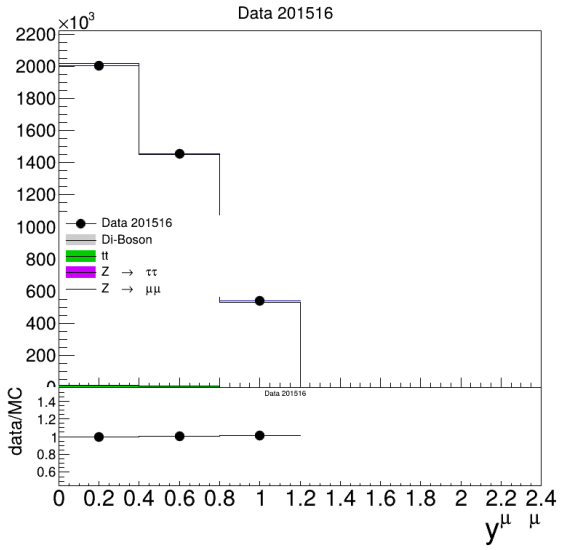

(a) 2015-16

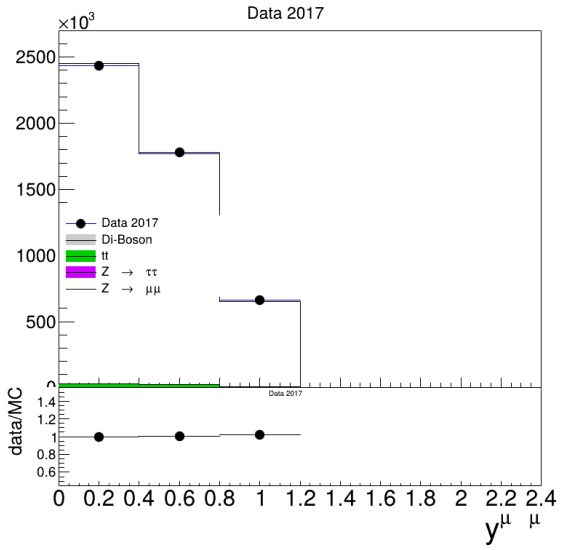

(b) 2017

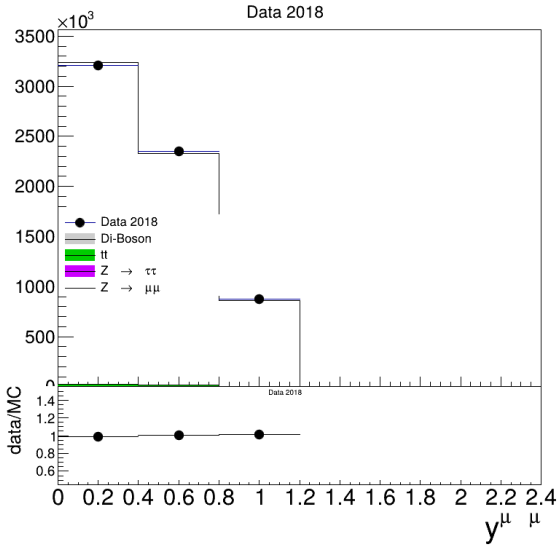

(c) 2018

Figure 6.6: Rapidity $Y^{\mu\mu}$ distributions for the three campaigns, simulation (signal+background) and data, using selection of Table 6.2. Simulation samples are scaled to Run-2 luminosity.

6.2 Systematic Uncertainties

Systematic uncertainties are a crucial part in precision measurements such as the determination of the Z boson mass. Systematic uncertainties, unlike statistical uncertainties that diminish with larger datasets or improved methods, originate from potential biases in experimental procedures or theoretical models. These uncertainties reflect limitations in the precision of measurements due to factors such as calibration errors, detector performance and modeling assumptions.

In the context of the Z mass there is a wide range of systematic uncertainties to take into account. Systematic uncertainties are evaluated by varying each source within its estimated range and observing the corresponding impact on the Z mass measurement. The magnitude of the change is taken as the systematic uncertainty for that source.

The list of systematic uncertainties applied in the analysis:

- η calibration: For the η calibration systematic uncertainties one template is created for

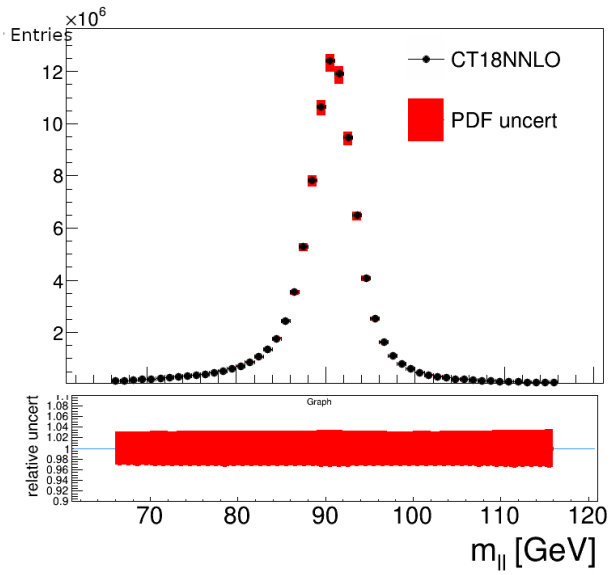

Figure 6.7: PDF uncertainty effect on the signal sample. Produced by Emilien Chapon. The red band represents the PDF uncertainty. This uncertainty is determined by comparing all PDF models to the nominal CT18NNLO and selecting the model with the largest deviation as the uncertainty estimate.

each variation of the calibration parameters. Additionally, the number of systematic uncertainties for each parameter will be equal to the number of regions used in the calibration. In each template produced for a specific η region, the strategy is to describe the parameter of interest within that region using either the up or down variation, while all other regions are modeled with the nominal parameters. This approach isolates the impact of variations in a single η region on the calibration or measurement, enabling a focused study of systematic effects. The systematic uncertainties correspond to the three calibration parameters ds_1, $dr1$ and dr_2.

- Luminosity: Luminosity is a critical aspect of the ATLAS experiment, as it directly affects the normalization of cross section measurements. There is an associated experimental uncertainty. It originates from inefficiencies of the detector LUCID [77], which measures luminosity. recorded by ATLAS has an uncertainty. Relative luminosity uncertainty for each year is displayed in Table 6.3:

Year	2015	2016	2017	2018
Lumi.Uncertainty %	1.13	0.89	1.13	1.10

Table 6.3: Relative uncertainty of Luminosity for Run-2, taken from [76]

In the Z mass fits, in the context of the thesis, a larger uncertainty is given for the luminosity to cover for additional uncertainties. Most importantly, the PDF uncertainty is included in the luminosity uncertainty, because as seen in the Figure 6.7 the PDF's change the normalization and don't influence the shape it self strongly. Since PDF uncertainties are not available in the timescale of the thesis, their contribution is considered to be covered by the luminosity uncertainty.

- Extrapolation calibration: In the Chapter 5.5.0.2, it is shown that two different choices in the trigger configuration give different extrapolation behavior. The difference between

the two is added as a symmetric systematic uncertainty. The source of this systematic is likely connected to the overlap issue between the data streams used. Therefore, it is a systematic uncertainty likely to be resolved with processing another samples for the calibration. Due to this ambiguity the results are presented with and without this systematic uncertainty.

List of systematic uncertainties not yet applied in this thesis:

- Signal and background cross section: Signal and background cross sections are associated with theoretical uncertainties that must be incorporated into the fitting procedure. These uncertainties arise mainly for missing higher order diagrams in the simulation. By including these uncertainties, the fit can appropriately scale the relevant samples and improve convergence. Due to the negligible contribution of the background, the fit cannot adequately account for luminosity, as well as signal and background cross sections. To effectively calculate the cross sections a control region is needed, which is not available in the context of the thesis. Furthermore, because of the minimal background presence, luminosity and signal cross sections effectively have the same effect. To account for the above the signal and background cross sections uncertainties are not included in the fit. Their contribution is absorbed by the luminosity uncertainty.

- NNLO: Due to missing of higher order corrections in the signal sample there is a disagreement between data and simulation as presented in the Chapter 6.1.2 for higher energies. This effect will be treated with a corresponding systematic.

- FRS: Final state radiation variations, which correspond to different Photos settings, can have an effect on the tails of the $m_{\mu\mu}$ distribution. A dedicated re-weighting can be applied to construct a corresponding systematic uncertainty.

- PDF: PDF's are a important aspect of hadron collider experiments, as analyzed in Section 1.3.1. Their contribution was studied in the context of the Z mass measurement and was found to have a minor effect on the shape itself. On the contrary main effect was on the normalization of the signal. This is shown in the Figure 6.7. Consequently the corresponding uncertainty is going be covered by the luminosity uncertainty in the context of the thesis.

- Efficiency uncertainties: Efficiency in ATLAS is prone to uncertainties which are connected to imperfections of the algorithms and limitations of the detector. Efficiency has different values for different regions of the kinematic phase space. Therefore efficiency uncertainty does not change only the normalization but possibly introduce shapes to the kinematic distributions.

In the Figure 6.8, the systematic variations of the calibration, up down and nominal, are presented. The scale variations influence mainly the mean of the histogram where the resolution change the smearing of the distribution.

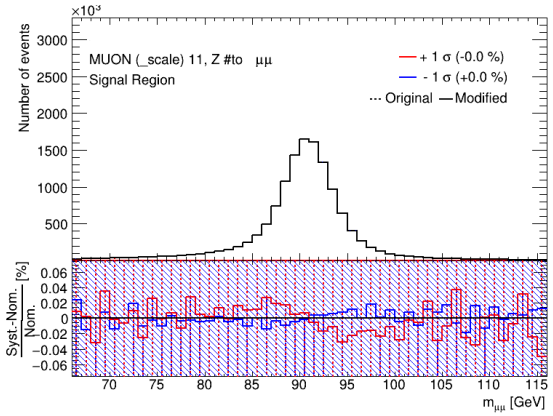

(a) Example of scale systematic, from η calibration region $0 < \eta < 0.4$.

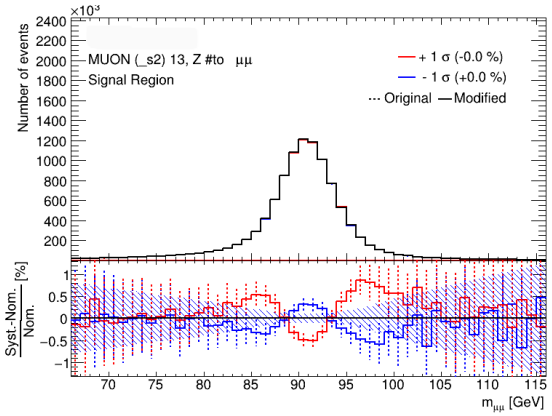

(b) Example of resolution systematic, from η calibration region $0 < \eta < 0.4$.

Figure 6.8: Example of systematic uncertainties (ds_1, dr_1, dr_2) on the signal shape.

6.3 Mass templates

In this Section, the method of template production is presented. Templates are a key feature of the measurement. By fitting a parametric function in the $m_Z - \Gamma_Z$ phase space, the fit can capture the dependence of the two parameters of interest over a continuous range of values. This allows for a more precise characterization of their relationship and provides a framework for simultaneously optimizing both parameters within the phase space.

To produce the variations the simulation at truth level is acquired. By computing the Breit-Wigner distribution for different mass and width of the Z corresponding weights are derived. The re-weighting is calculated per event and it is dependent from the mass of the boson in generator level. With these weights, variations of the mass distribution are produced.

The weight is the ratio of the cross sections for target mass and width $\sigma_{target}(M_Z^{target}, \Gamma_Z^{target})$ to the nominal one $\sigma_{nominal}(M_Z^{initial}, \Gamma_Z^{initial})$:

$$weight = \frac{\sigma_{target}(M_Z^{target}, \Gamma_Z^{target})}{\sigma_{nominal}(M_Z^{initial}, \Gamma_Z^{initial})} \tag{6.1}$$

The cross sections are derived from Equation 1.61 for the Z Line-shape of Chapter 1.5.3.1.

The shape of the Z/γ interference is plotted in the Figure 1.10, Chapter 1.5.3.2. In the Figure 6.9, variations of Z mass and width effect on the $m_{\mu\mu}$ distribution are compared. The nominal case corresponds to 91.185 GeV and 2.5 GeV. Two cases of large offset are compared. For the Z mass, an offset of 100 MeV, and for the Width, 50 MeV.

The Z mass variations have larger effect in the central bins of the histogram. The mass variations move the mean of the distribution. The width variations have a different effect. Their main effect is on the central bins of the histograms. In the high tail the effect is less significant than the low tail. Moreover, it has a large correlation with the integral of the histogram. The low tail effect is due to the natural "tilt" of the distribution at lower tail due to final state ration of the muons. It's main effect is to change the number of events in the $m_{\mu\mu}$ histogram.

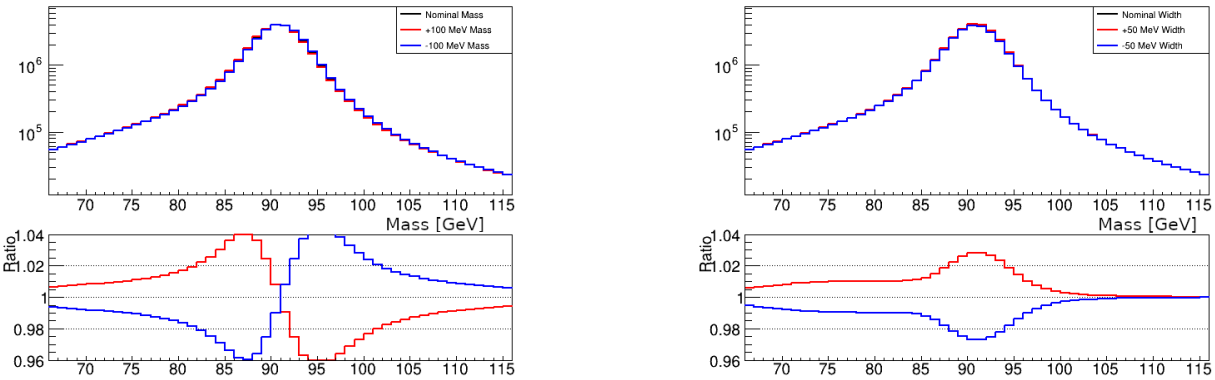

(a) m_Z variations comparison

(b) Γ_Z variations comparison

Figure 6.9: Examples of the template for Mass (a) and Width (b) variations. Width(2.5 GeV) and Mass(91.185 GeV) correspond to the nominal case. In the ratio plot the nominal to the corresponding variation case is plotted. The simulation sample used is the 2017 campaign one.

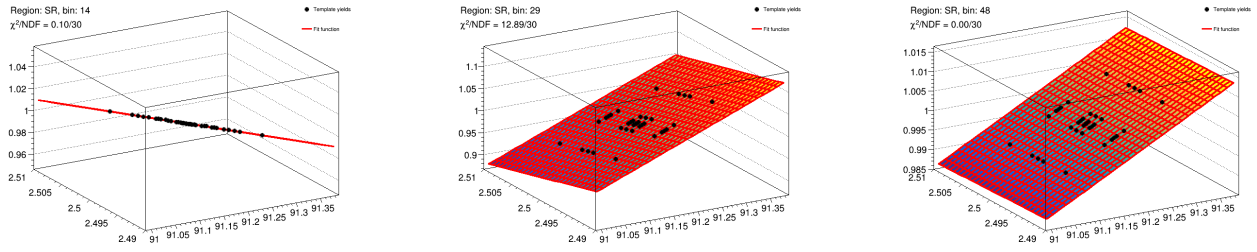

(a) $m_{\mu\mu}$ bin at the low edge

(b) $m_{\mu\mu}$ bin at the middle

(c) $m_{\mu\mu}$ bin at the high edge

Figure 6.10: Examples of the morphing for two $m_{\mu\mu}$ distribution bins relative event yield. One template is the reference template and value is fixed at 1 in the graph. The other templates are compared to the reference template. Reference template is the hypothesis: $m_Z = 91.185$ GeV $\Gamma_Z = 2.5$ GeV. On x axis is m_Z in GeV, y axis is Γ_Z in GeV, z axis is the relative event yield.

In the Figure 6.10, morphing (interpolation) examples are given for three bins of the m_Z distribution. The morphing function chosen is quadratic in the 2D phase space of m_Z and Γ_Z. No difference in the quality of fit was found with a linear function. This means that the Γ_Z and m_Z variations change linearly the template event yield in each bin. In the Figure 6.10, the three m_Z relative yield examples are from different regions of the m_Z distribution. Analyzing these morphing examples is crucial to understand the behavior of the templates. From the example at the lower edge of the distributions (a), the linear dependence is shown clearly. In the (b) example, the bin shown resides close to the central bin of the distribution. The variations of m_Z have a more significant impact on the relative event yield than those in Γ_Z. In the (c) example, the bin resides at the upper tail of the distribution. There it is clear that the m_Z has a big impact on the relative event yield, where the Γ_Z has almost no effect.

6.4 Likelihood Fit and Results

6.4.1 Likelihood Fit and method

6.4.1.1 Likelihood Function

To derive the Z mass measurement and uncertainties a likelihood fit method [78] is used. The parameters fitted are grouped into two categories according to their roles in the analysis.

Parameters of interest (POI) and **nuisance parameters** (NP). Parameters of interest are the primary parameters be determined by the fit. The fit is configured in a way to accurately determine the best-fit value of these parameters. In the context of this analysis the POI are the m_Z and Γ_Z. The nuisance parameters are proxies to systematic uncertainties. The likehood function is the function:

$$L(\vec{n}|\vec{\theta},\vec{\mu}) = \prod_{\text{bin}} P(n_{\text{bin}}|S_{\text{bin}}(\vec{\theta},\vec{\mu}) + B_{\text{bin}}(\vec{\theta},\vec{\mu})) \cdot \prod_{j} G(\theta_j), \tag{6.2}$$

where:

- $\vec{n}$ represents the observed data in each bin,
- $\vec{\theta}$ denotes the constrained nuisance parameters associated with systematic uncertainties,
- $\vec{\mu}$ contains the unconstrained parameters, including the parameters of interest and any unconstrained nuisance parameters,
- $P(n_{\text{bin}}|S_{\text{bin}} + B_{\text{bin}})$ is the Poisson probability of observing n_{bin} events in a given bin, given the expected signal $S_{\text{bin}}(\vec{\theta},\vec{\mu})$ and background $B_{\text{bin}}(\vec{\theta},\vec{\mu})$,
- $G(\theta_j)$ represents the Gaussian prior for each constrained nuisance parameter θ_j.

In Bayesian statistics, estimators are treated as random variables. This allows nuisance parameters to be marginalized (integrated out), contributing to the overall uncertainty of the parameter estimation. In contrast, within the frequentist approach, nuisance parameters must be estimated simultaneously alongside the POIs. This transforms the fitting procedure into a multi-dimensional likelihood maximization problem.

When fitting models with multiple unknown parameters, including both POIs and nuisance parameters, the profile likelihood method is commonly employed. This method is used to test a specific hypothesized value of the parameter of interest while accounting for the uncertainties in the nuisance parameters. In practice, it profiles out the nuisance parameters by maximizing the likelihood with respect to them, allowing a more accurate comparison between the hypothesized value of the parameter of interest and its alternatives.

By using prior information profile likelihood fit can constrain systematic uncertainties. The total likelihood is structured as:

$$L_{\text{total}} = L_{\text{phys}}(x_{\text{data}}|\mu,\hat{\hat{\theta}}) \times L_{\text{subs}}(\hat{\hat{\theta}}|\hat{\theta},\sigma_\theta)$$

where, $L_{\text{phys}}(x_{\text{data}}|\mu,\hat{\hat{\theta}})$ is the physical likelihood function, which depends on the data x_{data}, the parameter of interest μ, and the profiled nuisance parameters $\hat{\hat{\theta}}$. The second term, $L_{\text{subs}}(\hat{\hat{\theta}}|\hat{\theta},\sigma_\theta)$, is the subsidiary likelihood, which constrains the nuisance parameters θ using prior information (such as external measurements). The nuisance parameters θ are constrained by a Gaussian distribution with known mean $\hat{\theta}$ and uncertainty σ_θ. This reflects the prior knowledge we have about the nuisance parameters.

The procedure is the following:

Profiling over the Nuisance Parameters: The nuisance parameters θ are "profiled" by maximizing the likelihood function for each fixed value of μ, the parameter of interest. Mathematically, this means finding $\hat{\hat{\theta}} = \arg\max_\theta L_{\mu=\text{const.}}(\theta)$, the value of θ that maximizes the likelihood for a fixed μ.

Estimating the Parameter of Interest: Once the nuisance parameters are profiled, the next step is to maximize the total likelihood with respect to μ. This gives the best estimate $\hat{\mu} = \arg\max_\mu L(\mu,\hat{\hat{\theta}})$, where $\hat{\hat{\theta}}$ is the previously profiled nuisance parameter. The likelihood now depends on the profiled value of $\hat{\hat{\theta}}$.

6.4.1.2 Hessian Matrix

To calculate the correlation of the nuisance parameters and the POI a Hessian Matrix of the likelihood function is used. According to the standard Gaussian error propagation the correlation between parameters is calculated using the second derivatives.

$$\rho_{ij} = \frac{\mathrm{Cov}(\theta_i, \theta_j)}{\sqrt{\mathrm{Var}(\theta_i)\mathrm{Var}(\theta_j)}} \tag{6.3}$$

where $Var(\theta_i)$ are the diagonal elements of the covariance matrix and $\mathrm{Cov}(\theta_i, \theta_j)$ are the off diagonal terms in the covariance matrix for the elements i,j. The hessian matrix is given by:

$$H = \begin{pmatrix} \frac{\partial^2 f}{\partial \theta_1^2} & \frac{\partial^2 f}{\partial \theta_1 \partial \theta_2} & \cdots & \frac{\partial^2 f}{\partial \theta_1 \partial \theta_n} \\ \frac{\partial^2 f}{\partial \theta_2 \partial \theta_1} & \frac{\partial^2 f}{\partial \theta_2^2} & \cdots & \frac{\partial^2 f}{\partial \theta_2 \partial \theta_n} \\ \vdots & \vdots & \ddots & \vdots \\ \frac{\partial^2 f}{\partial \theta_n \partial \theta_1} & \frac{\partial^2 f}{\partial \theta_n \partial \theta_2} & \cdots & \frac{\partial^2 f}{\partial \theta_n^2} \end{pmatrix} \tag{6.4}$$

To handle the above complicated fit, dedicated minimization algorithm Minuit2, ref. [48], is utilized.

6.4.1.3 Pull Plots

To observe the quality of the fit and to compare the behavior of the nuisance parameters before and after the fit the pull plots are utilized. At the pull plots the pull $Pull_i$ for parameter i is computed:

$$\mathrm{Pull}_i = \frac{n_i^{\mathrm{obs}} - n_i^{\mathrm{fit}}}{\sigma_i} \tag{6.5}$$

where n_i^{obs} is the observed value for bin i, n_i^{fit} is the predicted value from the fit, σ_i is the uncertainty in the observed value n_i^{obs}.

A well fitted model will have the pull for all parameters distributed around zero.

6.4.2 Results

In order to to bias the analysis the m_Z is blinded in fit. This mean that the data distribution is re-weighted by the procedure described in the Section 6.3, but with the target mass unknown. The target mass resides in blinded interval of $M_Z^{PDG} \pm 50\mathbf{MeV}$.

In Figures 6.11 and 6.12, results of the fit on the $m_{\mu\mu}$ distributions are displayed, for 201516 and 2018 campaigns. In both pre-fit plots (a), a trend is observed in the tails of the distribution, which becomes evident in the ratio plot. This trend makes it challenging to interpret and attribute the pre-fit discrepancies between data and simulation to specific sources or mis-modelings. In the post-fit plots (b), the ratio appear nearly flat, indicating that the fit is successful and the model accurately describes the blinded data.

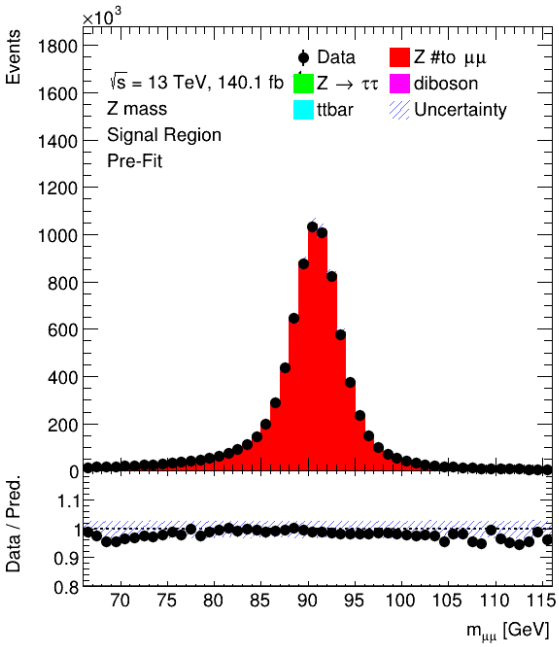

(a) Pre fit

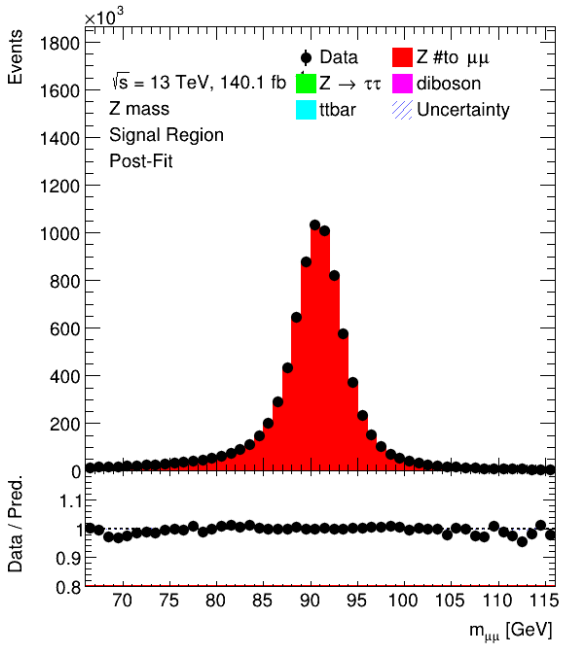

(b) Post Fit

Figure 6.11: Pre and Post fit $m_{\mu\mu}$ distributions for 201516 campaign

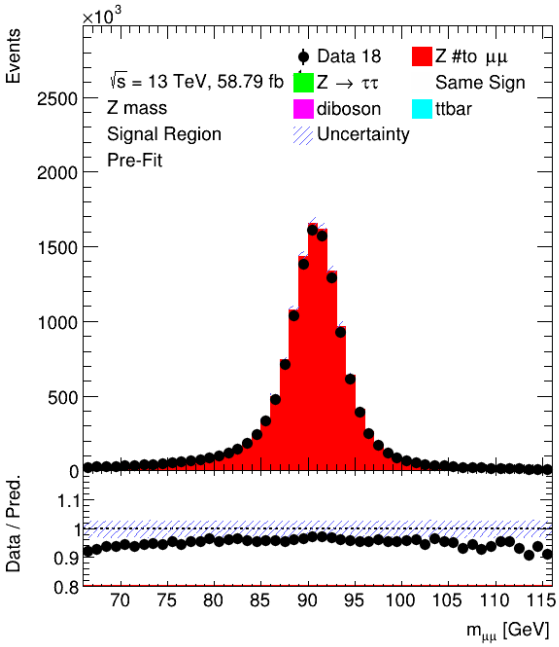

(a) Pre fit

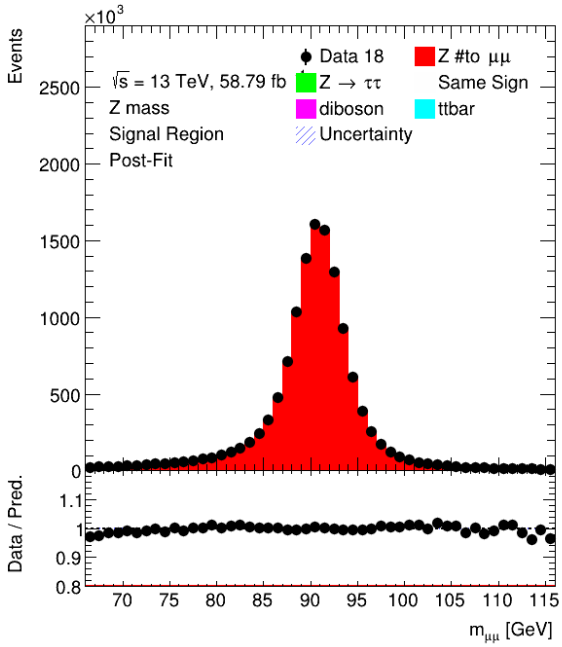

(b) Post fit

Figure 6.12: Pre and Post fit $m_{\mu\mu}$ distributions for 2018 campaign

Post fit correlation matrix between nuisance parameters and the parameters of interest is presented in the Figure 6.13. The correlation between the two parameters of interest is the most important part of the the correlation study. Notably the correlation between the two displayed is $\approx 5\%$. This this is a crucial point, as it demonstrates that a m_Z measurement is feasible without a simultaneous Γ_Z fit.

Luminosity has a large correlation with width Γ_Z. This occurs because the distribution is broadened by the width while the total number of events remains constant. As a result, when

the luminosity is used to normalize the simulation to the data, a correlation between the two parameters emerges.

Then nuisance parameters connected to the calibration have a large correlation with the two parameters of interest. For the scale nuisance parameters there is a large correlation with the m_Z. The correlation value changes depending on the η region that the nuisance parameter belongs to. There is a trend in negative η regions to have a larger correlation. For the Γ_Z there is a strong correlation with the resolution parameters nuisance parameters. By comparing Figure 6.9 (b), which illustrates the effect of width variations, with the impact of resolution parameters in the Figure 6.8, it is evident that the shape of these effects is quite similar. Consequently, this strong correlation is expected.

Moreover, a strong correlation is observed between resolution nuisance parameters of different η regions. This is an important observation since the calibration fit does not take into account correlations between the η regions of the calibration.

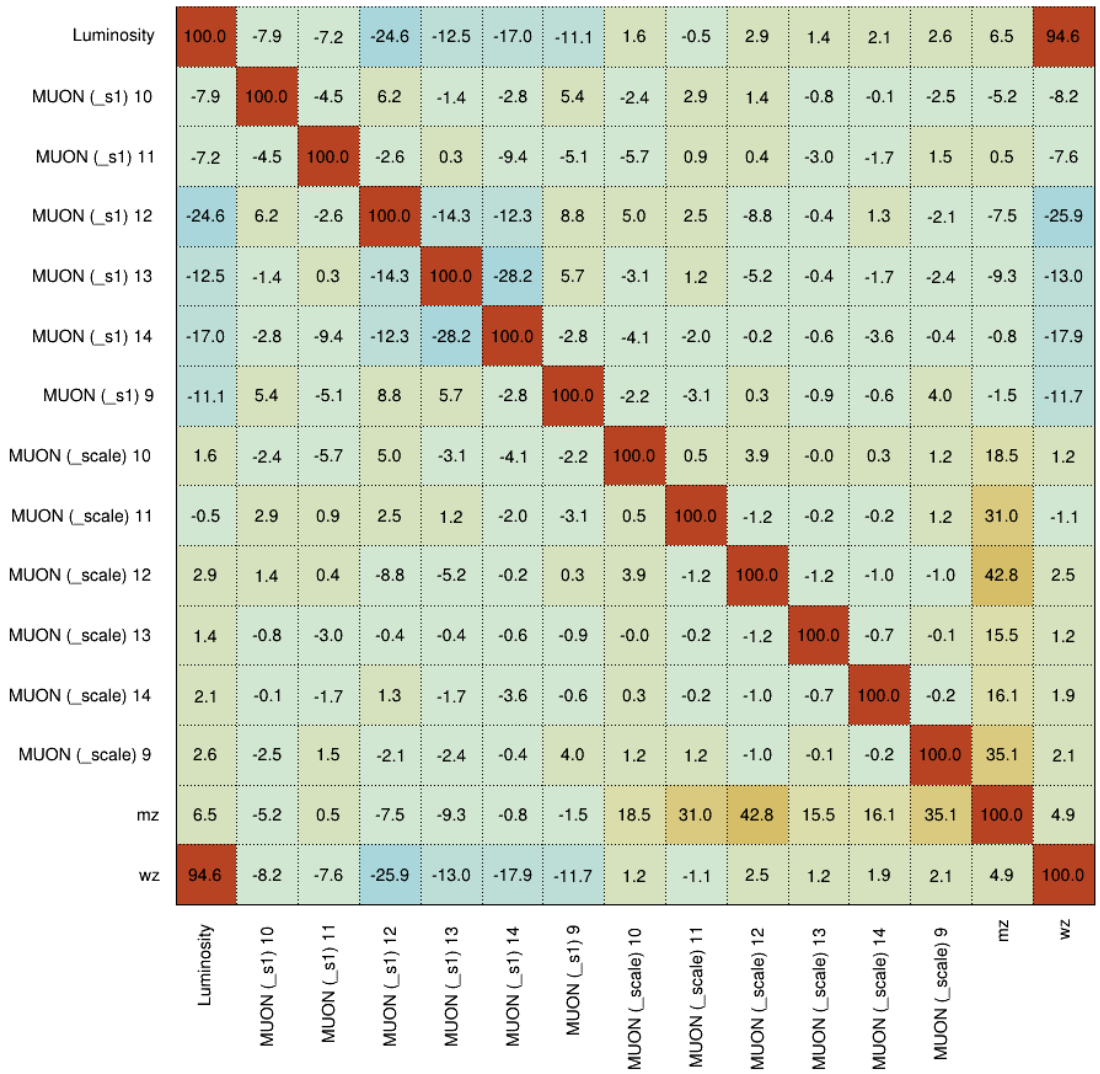

Figure 6.13: Hessian correlation matrix between the parameters of nuisance and parameters of interest

In the Table 6.4, likelihood fit results on m_Z and Γ_Z are presented for the 2015-16, 2018 campaigns. m_Z uncertainty is $\approx 2\ MeV$ for all years making the measurement an extremely accurate one with the current systematic uncertainties used. The central value is blinded. Thus, the focus is on the differences in the fit results across the years, rather than the absolute values. The fitted value of $m_Z^{ref.}$ for 2015-16 is used as a reference point for comparison.

2015-16	
m_Z	$m_Z^{ref.} \pm 0.0012(\text{stat.}) \pm 0.0011(\text{syst.})$ GeV
Γ_Z	$2.5004 \pm 0.0003(\text{stat.}) \pm 0.0003(\text{syst.})$ GeV
2018	
m_Z	$m_Z^{ref.} + 0.0075 \pm 0.0010(\text{stat.}) \pm 0.0012(\text{syst.})$ GeV
Γ_Z	$2.4952 \pm 0.0004(\text{stat.}) \pm 0.0003(\text{syst.})$ GeV

Table 6.4: $m_Z^{(blinded)}$ and Γ_Z values post fit, and systematic uncertainties from η calibration. 2015-16 fitted $m_Z^{ref.}$ value is used as a reference.

Using the BLUE combination method for uncorrelated measurements [79] a combined result is obtained:

$$m_Z^{(\text{blinded})} = m_Z^{ref.} + 0.00356 \pm 0.002\,\text{GeV},$$
$$\Gamma_Z = 2.4990 \pm 0.0003\,\text{GeV}.$$

Results are repeated with the extrapolation systematic to asses it's impact on the uncertainty of the fit. In the Table 6.5 likelihood fit results on $m_Z^{ref.}$ and Γ_Z are presented for the 2015-16, 2018 campaigns.

2015-16	
m_Z	$m_Z^{ref.} \pm 0.0012(\text{stat.}) \pm 0.0025(\text{syst.})$ GeV
Γ_Z	$2.5004 \pm 0.0003(\text{stat.}) \pm 0.0003(\text{syst.})$ GeV
2018	
m_Z	$m_Z^{ref.} + 0.0071 \pm 0.0010(\text{stat.}) \pm 0.0025(\text{syst.})$ GeV
Γ_Z	$2.4952 \pm 0.0004(\text{stat.}) \pm 0.0003(\text{syst.})$ GeV

Table 6.5: $m_Z^{(blinded)}$ and Γ_Z values post fit, and systematic uncertainties from η calibration + extrapolation systematic uncertainty. 2015-16 fitted m_Z value is used as a reference (ref.).

Using the BLUE combination method for uncorrelated measurements [79] a combined result is obtained:

$$m_Z^{(\text{blinded})} = m_Z^{ref.} + 0.00366 \pm 0.0028\,\text{GeV},$$
$$\Gamma_Z = 2.4990 \pm 0.0004\,\text{GeV}.$$

In the Figures 6.14, the ranking plots for the two POI are displayed. Results are presented only for 2018 campaign to avoid redundancy. Ranking plots display the pull and pre, post fit impact of the most significant nuisance parameters on a POI.

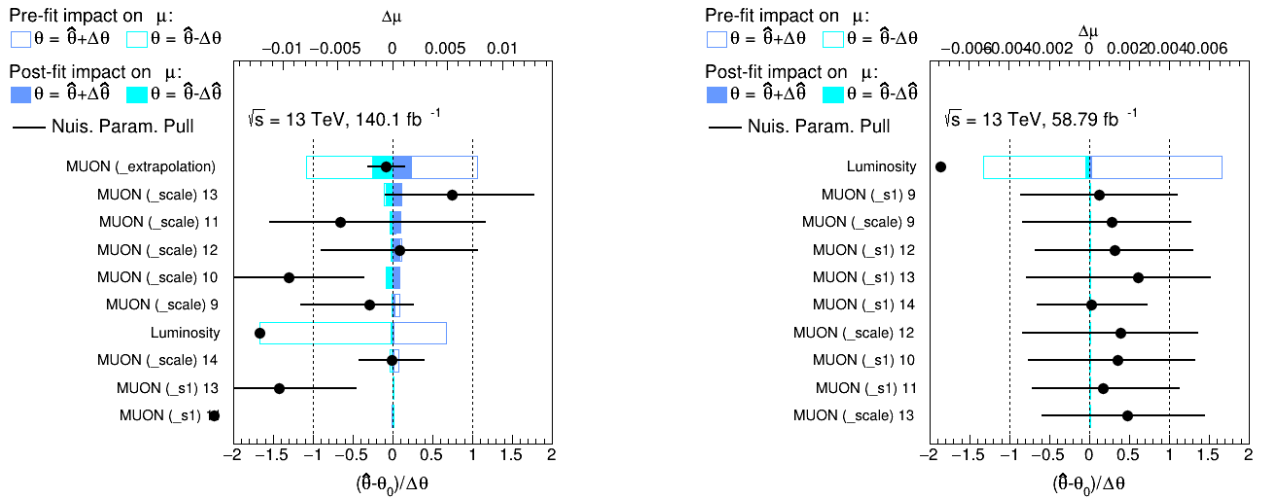

(a) m_Z (b) Γ_Z

Figure 6.14: Ranking plots for m_Z and Γ_Z POIs, 2018 campaign. Nuisance parameter numbers indicated correspond to different bins of the calibration procedure. *Scale* NPs are connected with scale parameter systematic uncertainties. $s1$ NPs are connected to resolution parameter dr_1 systematic uncertainties.

Regarding the m_Z ranking plot, there are strong pulls observed. As expected, scale NPs are dominant. First, the extrapolation NP has the largest effect on the Z mass. Post calibration though, the corresponding uncertainty is constrained. Possibly, this signals that the p_T^μ dependence of the scale is flat in the Z p_T^μ range. Some NPs, such as the *MUON* (*Scale* 10), exhibit a large pull. This phenomenon is hard to disentangle. Likely, it is connected with calibration non-closures. Luminosity, is heavily constrained and pulled post fit. This is expected as the luminosity uncertainty was inflated pre fit to incorporate additional systematic uncertainties.

Regarding the Γ_Z ranking plot, the dominating NPs are the ones connected with dr_1 calibration resolution parameter, as expected. No strong pulls are observed, but the majority of the pulls are titled to positive values. This phenomenon is hard to disentangle without further calibration studies.

6.5 Conclusions

In this Chapter the Z mass measurement is presented. First, data and simulation samples are presented. From the comparison of kinematic distributions, the effect of missing higher order corrections on the signal is presented. Notably, there is a trend of disagreement for higher values of p_T^μ and $p_T^{\mu\mu}$. By deriving signal templates and through a dedicated likelihood fit the final measurement is derived. The templates for width and the mass have distinctively different shape, allowing for a separate measurement of the two. Finally, by incorporating calibration systematic uncertainties and blinding the central value the final results are: $\mathbf{m_Z^{blinded}} = m_Z^{ref.} + 0.00356 \pm 0.002\,\text{GeV}$ and $\mathbf{\Gamma_Z} = 2.4990 \pm 0.0003\,\text{GeV}$.

The 2015-16 and 2018 years exhibit a difference between the mean values fitted. This is likely due to calibration non closures in the ϕ direction and an incorrect p_T^μ extrapolation due to known issues existing in the samples processed. With a more precise calibration a closure between the different years is expected.

Since the central value is blinded, the primary focus is on the uncertainties. The values presented here correspond to an approximation of the final calibration uncertainties on the Z mass, assuming that the extrapolation systematic is appropriately handled from the analysis.

Chapter 7

Conclusions

In this thesis the m_Z measurement was discussed using proton proton collision data from ATLAS. Main focus was given to the calibration procedure to correct for charge independent effects.

In Chapter 4, the qualification task and calibration work for ATLAS was presented. First, the calibration "pre-smearing" corrections procedure were presented. To derive the pre-smearing corrections the $\sigma_{p_T^\mu}/p_T^\mu$ was studied. Maps of $\frac{\sigma_{p_T^\mu}/p_{T\,Data}}{\sigma_{p_T^\mu}/p_{T\,MC}}$ were derived for the three muon track types: ID, CB and ME. The comparison of the three shows that the CB resembles ID in the barrel and ME at the end-cap regions. From the maps it is derived that the ME and CB tracks are sensitive to mis-modeling of the toroid magnetic field and the complex systems of the Muon Spectrometer. Structures of mis-modeling are observed in the small toroid systems and a systematic deficiency of the detector CSC. The Inner Detector, on the other hand, exhibits excellent an performance and a uniformity in ϕ. By studying the $\sigma_{p_T^\mu}/p_T$ as a function of p_T^μ and fitting the corresponding plots with an analytical function, it is derived that the $\sigma_{p_T^\mu}/p_T$ discrepancy between MC and data is increasing with p_T^μ. Finally, corrections were derived from the maps and injected into the ATLAS calibration framework. In most cases no significant improvement was found in the final result, compared to the nominal ATLAS calibration procedure.

In Chapter 5 the process of deriving calibration parameters as a function of η and p_T^μ is presented, using the J/ψ meson resonance . First a study is done for the calibration comparison of Prompt and Non Prompt J/ψ, focusing on scale ds_1 as a function of η. Separate samples of the two were produced and compared using the decay length L_{xy}. It is concluded that the Non Prompt J/ψ is sensitive to calibration non closures due to it's large background contribution and the non perturbative QCD interference in it's production. The majority of Non Prompt J/ψ are chosen to be excluded through kinematic selection from the analysis.

Secondly, the η calibration is presented. For the η calibration the innermost barrel has a uniform response where in the outermost parts it deviated from this picture. The η calibration has negligible systematic uncertainties paving the way for an accurate Z boson mass measurement.

For the p_T^μ calibration the trigger choice can influence heavily the dependence of the scale ds_1 with p_T^μ. A strong dependence is observed for the scale but for intermediate $p_T^\mu \approx 10 - 20$ GeV a plateau is reached. At higher values there is an nonphysical dependence from p_T^μ which originates in double counting of data in the Main and BPhys streams. The resolution parameters are withing statistical uncertainty in the different p_T^μ bins. Therefore, are considered to be constant with p_T^μ in the context of this thesis.

Lastly, in Chapter 6,the Z mass measurement is performed. Templates of m_Z and Γ_Z variations were produced using a Z lineshape approach. By using a dedicated likelihood fit the width and the mass were calculated simultaneously. The final combined result, with using η

calibration systematic uncertainties and a blinded mass value, is: $\mathbf{m_Z^{blinded}} = m_Z^{ref.} + 0.00356 \pm 0.002\,\text{GeV}$ and $\mathbf{\Gamma_Z} = 2.4990 \pm 0.0003\,\text{GeV}$.

The result obtained exhibits a low systematic uncertainty. In conclusion, the calibration tools of ATLAS derive an accurate calibration, with a low systematic uncertainty for the m_Z by using the J/ψ resonance. In other words, the muon reconstruction algorithms of ATLAS and specifically in the barrel of the tracker system, are proven to provide excellent and precise measurements of the p_T^μ.

Outlook

Calibration with the ATLAS tools has exhibited an excellent performance. Nevertheless, there is room for improvement and comparison with other methods.

Calibration To enhance the obtained results, it is crucial to repeat the calibration as a function of p_T^μ without data overlap. This approach will allow for a more accurate description of the scale as a function of p_T^μ. Furthermore, analyzing the relative cross sections of Prompt and Non-Prompt J/ψ can contribute to achieving a more accurate calibration for high p_T^μ.

Moreover, using a non iterative method, which calibrates all the η^μ and p_T^μ bins simultaneously, can have a better estimation on the correlation between bins, potentially leading to more accurate results.

Another interesting topic would be the use of the calibration presented in this thesis in the context of the W mass measurement. In this case, the conditions are more challenging since there is also the missing energy part of the reconstruction and increased precision is required. Additionally, the W mass measurement is performed using the whole η range, and not only in barrel, making the approach of this thesis challenging. Since Inner Detector is deteriorating in performance in forward regions, the calibration procedure used in this thesis can be potentially inadequate for a W mass measurement. Alternatively, a Combined Tracks approach could be followed in that case.

Z mass For the Z mass a major problem in this thesis is the non capability of the fit to constraint the background yield. This is not regarded as a major issue, since background is negligible. However, utilizing a control region to constrain the background could potentially improve convergence further.

Bibliography

[1] Department of Physics, University of Zurich, "The Standard Model of Particle Physics", [Online]. Available: https://www.physik.uzh.ch/en/groups/serra/outreach/StandardModel.html. [Accessed: 08-Nov-2024].

[2] Particle Data Group, "Review of Particle Physics," *Progress of Theoretical and Experimental Physics*, vol. 2020, no. 8, 2020. doi: 10.1093/ptep/ptaa104.

[3] Feynman, R. P. (1950). "Mathematical Formulation of the Quantum Theory of Electromagnetic Interaction". Physical Review. 80 (3): 440–457. doi: 10.1103/PhysRev.80.440

[4] M. Gell-Mann, "The Eightfold Way: A Theory of Strong Interaction Symmetry," United States, March 1961. doi: 10.2172/4008239.

[5] Alan D. Martin, "Proton structure, Partons, QCD, DGLAP and beyond," 2008. doi: 10.48550/arXiv.0802.0161.

[6] R. D. Ball *et al.* [NNPDF Collaboration], "Parton Distributions from High-Precision Collider Data," *Eur. Phys. J. C*, vol. 77, p. 663, 2017. doi: 10.1140/epjc/s10052-017-5199-5.

[7] Tie-Jiun Hou, et al., "New CTEQ global analysis of quantum chromodynamics with high-precision data from the LHC," *Phys. Rev. D*, vol. 103, no. 1, p. 014013, 2021. doi: 10.1103/PhysRevD.103.014013.

[8] Jun Gao, et al. "CT10 next-to-next-to-leading order global analysis of QCD," *Phys. Rev. D*, vol. 89, no. 3, p. 033009, 2014. doi: 10.1103/PhysRevD.89.033009.

[9] H. Abramowicz *et al.* [H1 and ZEUS Collaborations], "Combination of Measurements of Inclusive Deep Inelastic $e^{\pm}p$ Scattering Cross Sections and QCD Analysis of HERA Data," *Eur. Phys. J. C*, vol. 75, p. 580, 2015. doi: 10.1140/epjc/s10052-015-3710-4.

[10] S. Bailey, et al., "Parton distributions from LHC, HERA, Tevatron and fixed target data: MSHT20 PDFs," *Eur. Phys. J. C*, vol. 81, no. 4, p. 341, 2021. doi: 10.1140/epjc/s10052-021-09057-0.

[11] C. S. Wu, et al., "Experimental Test of Parity Conservation in β Decay," *Phys. Rev.*, vol. 105, pp. 1413–1414, 1957. doi: 10.1103/PhysRev.105.1413.

[12] S. L. Glashow, "Partial Symmetries of Weak Interactions," *Nucl. Phys.*, vol. 22, pp. 579–588, 1961. doi: 10.1016/0029-5582(61)90469-2.

[13] A. Salam, "Weak and Electromagnetic Interactions," *Conf. Proc. C*, vol. 680519, pp. 367–377, 1968. doi: $10.1142/9789812795915_0034$.

[14] S. Weinberg, "A Model of Leptons," *Phys. Rev. Lett.*, vol. 19, pp. 1264–1266, 1967. doi: 10.1103/PhysRevLett.19.1264.

[15] J. Goldstone, "Field theories with 'superconductor' solutions," CERN-TH-118, *Nuovo Cimento*, vol. 19, pp. 154–164, 1961. doi: 10.1007/BF02812722.

[16] J. Ellis, et al., *A Historical Profile of the Higgs Boson. An Updated Historical Profile of the Higgs Boson*, in *The Standard Theory of Particle Physics*, L. Maiani and G. Rolandi, Eds., pp. 255–274, 2016, doi: $10.1142/9789814733519_0014$.

[17] Aad, G., et al., "Observation of a new particle in the search for the Standard Model Higgs boson with the ATLAS detector at the LHC," *Physics Letters B*, vol. 716, no. 1, pp. 1–29, Sep. 2012, doi: 10.1016/j.physletb.2012.08.020.

[18] ATLAS Collaboration, "Measurement of the W-boson mass and width with the ATLAS detector using proton–proton collisions at $\sqrt{s} = 7$ TeV," *Eur. Phys. J. C*, vol. 84, no. 12, p. 1309, 2024. doi: 10.1140/epjc/s10052-024-13190-x.

[19] R. L. Workman et al. (Particle Data Group), "Review of Particle Physics," Prog. Theor. Exp. Phys. 2022, 083C01 (2022) and 2023 update.

[20] S. Bethke and A. Wagner, "The JADE experiment at the PETRA collider: history, achievements and revival," *Eur. Phys. J. H*, vol. 47, p. 16, 2022. doi: 10.1140/epjh/s13129-022-00047-8.

[21] ALEPH Collaboration, DELPHI Collaboration, L3 Collaboration, OPAL Collaboration, and the LEP Electroweak Working Group, "Combination procedure for the precise determination of Z boson parameters from results of the LEP experiments," 2001. doi: 10.48550/arXiv.hep-ex/010102.

[22] S. Mukherjee, "Data Scouting and Data Parking with the CMS High Level Trigger," in *Proceedings of Science*, p. 139, Sep. 2020. doi: 10.22323/1.364.0139.

[23] A. Gehrmann-De Ridder, et al, "Precision phenomenology with fiducial cross sections in the triple-differential Drell-Yan process," *J. High Energ. Phys.*, vol. 2023, p. 2, 2023. doi: 10.1007/JHEP05(2023)002.

[24] L. Kluberg, "Neutral Currents in Gargamelle," in *Proceedings of the 9th Rencontres de Moriond: High Energy Leptonic Interactions*, pp. 111–123, 1974.

[25] D. Denegri, "The discovery of the W and Z," *Physics Reports*, vol. 403-404, pp. 107-145, 2004, doi: 10.1016/j.physrep.2004.09.006.

[26] S. Myers, "The Large Hadron Collider 2008–2013," *International Journal of Modern Physics A*, vol. 28, no. 25, p. 1330035, 2013. doi: 10.1142/S0217751X13300354.

[27] Mobs E (2019) The CERN accelerator complex - 2019. Complexe des accélérateurs du CERN - 2019. In: General photo. https://cds.cern.ch/record/2684277

[28] Shota Tsiskaridze, "The ATLAS Experiment at the Large Hadron Collider", *Search for Flavor-Changing Neutral Current Top Quark Decays $t \to Hq$, with $H \to bb^-$, in pp Collisions at $\sqrt{s} = 8$ TeV with the ATLAS Detector* , Springer, doi: 10.1007/978-3-319-63414-2_2.

[29] G. Aad et al., *Magnet system and magnetic field*, 2008 JINST 3 S08003. `https://jinst.sissa.it/LHC/ATLAS/ch02.pdf`

[30] ATLAS Collaboration, "Measurement of the ATLAS solenoid magnetic field," *Journal of Instrumentation*, vol. 3, p. P04003, 2008. Accepted as Scientific Note SN-ATLAS-2008-068. doi: 10.1088/1748-0221/3/04/P04003.

[31] A. M. Rodriguez Vera, *ATLAS Detector Magnet System*, Photograph, 28 May 2021, https://cds.cern.ch/images/ATLAS-PHOTO-2021-029-1.

[32] ATLAS Collaboration, *ATLAS muon spectrometer: Technical Design Report*, CERN, Geneva, 1997. Technical design report. ATLAS. Link: https://cds.cern.ch/record/331068.

[33] ATLAS Collaboration, "Operation and performance of the ATLAS semiconductor tracker in LHC Run 2," *Journal of Instrumentation*, vol. 17, no. 01, p. P01013, 2022. doi: 10.1088/1748-0221/17/01/P01013.

[34] ATLAS Collaboration, "Gas gain stabilisation in the ATLAS TRT detector," *Journal of Instrumentation*, vol. 11, p. P04027, 2016. doi: 10.1088/1748-0221/11/04/P04027.

[35] ATLAS Collaboration, "Commissioning of the ATLAS Muon Spectrometer with Cosmic Rays," *Eur. Phys. J. C*, vol. 70, pp. 875–916, 2010. CERN-PH-EP-2010-045. doi: 10.1140/epjc/s10052-010-1415-2

[36] ATLAS Collaboration, "ATLAS inner detector: Technical design report. Vol. 1", CERN-LHCC-97-16.

[37] ATLAS Collaboration, "Calorimeter", CERN, [Online]. Available: https://atlas.cern/Discover/Detector/Calorimeter. [Accessed: 08-Nov-2024].

[38] ATLAS Collaboration, M. Aaboud, G. Aad, *et al.*, "Performance of the ATLAS trigger system in 2015," *European Physical Journal C*, vol. 77, no. 317, 2017. doi: 10.1140/epjc/s10052-017-4852-3.

[39] M. Mironova, "Experimental Particle Physics with the ATLAS Detector," in *Search for Higgs Boson Decays to Charm Quarks with the ATLAS Experiment and Development of Novel Silicon Pixel Detectors*, Springer Theses, Springer, Cham, 2023. doi: 10.1007/978-3-031-36220-0$_3$.

[40] A. Salzburger. The ATLAS track extrapolation package. ATL-SOFT-PUB-2007-005.

[41] A. Salvucci, "Measurement of muon momentum resolution of the ATLAS detector," *EPJ Web of Conferences*, vol. 28, p. 12039, 2012. doi: 10.1051/epjconf/20122812039.

[42] H. Bethe, "Zur Theorie des Durchgangs schneller Korpuskularstrahlen durch Materie," *Annalen der Physik*, vol. 397, no. 3, pp. 325–400, Jan. 1930. doi: 10.1002/andp.19303970303.

[43] V. L. Highland, "Some practical remarks on multiple scattering," *Nuclear Instruments and Methods*, vol. 129, no. 2, pp. 497–499, 1975. ISSN: 0029-554X. doi: 10.1016/0029-554X(75)90743-0.

[44] ATLAS Collaboration, "Muon identification and performance in the ATLAS experiment," in *Proceedings of the XXVI International Workshop on Deep-Inelastic Scattering and Related Subjects (DIS2018)*, Kobe, Japan, 2018. ATL-PHYS-PROC-2018-052.

[45] ATLAS Collaboration, "Studies of the performance of the ATLAS detector using cosmic-ray muons," *European Physical Journal C*, vol. 71, no. 1593, 2011. doi: 10.1140/epjc/s10052-011-1593-6.

[46] ATLAS Collaboration, *Studies of the muon momentum calibration and performance of the ATLAS detector with pp collisions at* $\sqrt{s} = 13$ *TeV*, Eur. Phys. J. C **83** (2023) 686, doi: 10.1140/epjc/s10052-023-11584-x.

[47] ATLAS Collaboration, "Inner Detector Alignment," ATLAS Experiment - Experiment Briefing, CERN, [Online]. Available: `https://atlas.cern/updates/experiment-briefing/inner-detector-alignment`. [Accessed: 14-Nov-2024].

[48] F. James and M. Roos, "Minuit: A System for Function Minimization and Analysis of the Parameter Errors and Correlations", *Comput. Phys. Commun.*, vol. 10, pp. 343–367, 1975, doi: 10.1016/0010-4655(75)90039-9.

[49] M. Baak, "Interpolation between multi-dimensional histograms using a new non-linear moment morphing method," *Nuclear Instruments and Methods in Physics Research Section A: Accelerators, Spectrometers, Detectors and Associated Equipment*, vol. 771, pp. 39–48, 2015. doi: 10.1016/j.nima.2014.10.033.

[50] J. E. Gaiser, *Appendix-F Charmonium Spectroscopy from Radiative Decays of the J/Psi and Psi-Prime*, Ph.D. Thesis, SLAC-R-255 (1982). (205 pages, function defined on p. 178.)

[51] T. Sjöstrand, et al. "A brief introduction to PYTHIA 8.1," *Computer Physics Communications*, vol. 178, no. 11, pp. 852–867, 2008. doi: 10.1016/j.cpc.2008.01.036.

[52] ATLAS Collaboration, "Alignment of the ATLAS Inner Detector in Run-2", *Eur. Phys. J. C*, vol. 80, no. 12, p. 1194, 2020. CERN-EP-2020-108. doi: 10.1140/epjc/s10052-020-08700-6.

[53] W. Barter, M. Pili, and M. Vesterinen, "A simple method to determine charge-dependent curvature biases in track reconstruction in hadron collider *Eur. Phys. J. C*, vol. 81, no. 3, p. 251, 2021, doi:10.1140/eujc/s10052-021-09016-9.

[54] P. Nason, "A new method for combining NLO QCD with shower Monte Carlo algorithms," *JHEP* **11** (2004) 040, 10.1088/1126-6708/2004/11/040.

[55] S. Frixione, P. Nason, and C. Oleari, "Matching NLO QCD computations with parton shower simulations: the POWHEG method," *JHEP* **11** (2007) 070, 10.1088/1126-6708/2007/11/070.

[56] S. Alioli, P. Nason, C. Oleari, and E. Re, "NLO vector-boson production matched with shower in POWHEG," *JHEP* **07** (2008) 060, 10.1088/1126-6708/2008/07/060.

[57] S. Alioli, *et al.*, "A general framework for implementing NLO calculations in shower Monte Carlo programs: the POWHEG BOX," *J. High Energ. Phys.*, vol. 2010, no. 43, 2010. doi: 10.1007/JHEP06(2010)043.

[58] H.-L. Lai et al., "New parton distributions for collider physics," *Phys. Rev. D*, vol. 82, no. 7, p. 074024, Oct. 2010. doi: 10.1103/PhysRevD.82.074024.

[59] P. Golonka and Z. Was, "PHOTOS Monte Carlo: a precision tool for QED corrections in Z and W decays," *Eur. Phys. J. C*, vol. 45, pp. 97–107, 2006. doi: 10.1140/epjc/s2005-02396-4.

[60] ATLAS Collaboration, "Measurement of the Z/γ^* boson transverse momentum distribution in *pp* collisions at $\sqrt{s} = 7$ TeV with the ATLAS detector," *J. High Energ. Phys.*, vol. 2014, no. 145, 2014. doi: 10.1007/JHEP09(2014)145.

[61] ATLAS Collaboration,"The ATLAS Simulation Infrastructure," *Eur. Phys. J. C*, vol. 70, pp. 823–874, 2010. doi: 10.1140/epjc/s10052-010-1429-9.

[62] S. Agostinelli *et al.* [GEANT4], "GEANT4 - A Simulation Toolkit," Nucl. Instrum. Meth. A **506** (2003), 250-303 doi:10.1016/S0168-9002(03)01368-8

[63] ATLAS Collaboration, "Luminosity determination in pp collisions at $\sqrt{s} = 13$ TeV using the ATLAS detector at the LHC," *Eur. Phys. J. C*, vol. 81, no. 10, 2021. doi: 10.1140/epjc/s10052-021-09751-3.

[64] ATLAS Collaboration, "Performance of the LUCID detector for luminosity measurement in the ATLAS experiment," *JINST*, vol. 10, no. 06, p. P06001, 2015. doi: 10.1088/1748-0221/10/06/P06001.

[65] Cowan, G., et al. Asymptotic formulae for likelihood-based tests of new physics. Eur. Phys. J. C 71, 1554 (2011). 10.1140/epjc/s10052-011-1554-0

[66] P. Nason, "A new method for combining NLO QCD with shower Monte Carlo algorithms," *JHEP* **11** (2004) 040, 10.1088/1126-6708/2004/11/040.

[67] S. Frixione, P. Nason, and C. Oleari, "Matching NLO QCD computations with parton shower simulations: the POWHEG method," *JHEP* **11** (2007) 070, doi: 10.1088/1126-6708/2007/11/070].

[68] S. Alioli, P. Nason, C. Oleari, and E. Re, "NLO vector-boson production matched with shower in POWHEG," *JHEP* **07** (2008) 060, doi: 10.1088/1126-6708/2008/07/060.

[69] Alioli S., et al. A general framework for implementing NLO calculations in shower Monte Carlo programs: the POWHEG BOX. J. High Energ. Phys. 2010, 43 (2010). doi: 10.1007/JHEP06(2010)043

[70] H. L. Lai et al., "New parton distributions for collider physics," *Phys. Rev. D*, vol. 82, no. 7, p. 074024, Oct. 2010. doi: 10.1103/PhysRevD.82.074024.

[71] Golonka, P., Was, Z. PHOTOS Monte Carlo: a precision tool for QED correctionsin Z and W decays. Eur. Phys. J. C 45, 97–107 (2006). doi: 10.1140/epjc/s2005-02396-4

[72] ATLAS Collaboration, "Measurement of the Z/γ^* boson transverse momentum distribution in pp collisions at $\sqrt{s} = 7$ TeV with the ATLAS detector", *J. High Energ. Phys.*, vol. 2014, p. 145, 2014. doi: 10.1007/JHEP09(2014)145.

[73] Golonka, P., Was, Z. PHOTOS Monte Carlo: a precision tool for QED corrections in Z and W decays. Eur. Phys. J. C 45, 97–107 (2006). doi: 10.1140/epjc/s2005-02396-4.

[74] ATLAS Collaboration, "The ATLAS Simulation Infrastructure," *Eur. Phys. J. C*, vol. 70, pp. 823–874, 2010. doi: 10.1140/epjc/s10052-010-1429-9.

[75] S. Agostinelli *et al.*, "Geant4 – a simulation toolkit," *Nucl. Instrum. Meth. A* **506** (2003) 250.

[76] ATLAS Collaboration, "Luminosity determination in pp collisions at $\sqrt{s} = 13$ TeV using the ATLAS detector at the LHC", *Eur. Phys. J. C*, vol. 81, no. 10, 2021. doi: 10.1140/epjc/s10052-021-09751-3.

[77] ATLAS Collaboration, "Performance of the LUCID detector for luminosity measurement in the ATLAS experiment", *JINST*, vol. 10, no. 06, p. P06001, 2015. doi: 10.1088/1748-0221/10/06/P06001.

[78] G. Cowan, K. Cranmer, E. Gross, and O. Vitells, "Asymptotic formulae for likelihood-based tests of new physics", *Eur. Phys. J. C*, vol. 71, p. 1554, 2011. doi: 10.1140/epjc/s10052-011-1554-0.

[79] Luca Lista, "Combination of measurements and the BLUE method", *EPJ Web Conf.*, vol. 137, p. 11006, 2017. doi: 10.1051/epjconf/201713711006.

Appendix A

Fermions EW Couplings

Fermion	**Q**	$\boldsymbol{I_W^3}$	$\boldsymbol{C_L}$	$\boldsymbol{C_R}$	$\boldsymbol{C_V}$	$\boldsymbol{C_A}$
ν_e, ν_μ, ν_τ	0	$+\frac{1}{2}$	$+\frac{1}{2}$	0	$+\frac{1}{2}$	$+\frac{1}{2}$
e^-, μ^-, τ^-	-1	$-\frac{1}{2}$	-0.27	0.23	-0.04	$-\frac{1}{2}$
u, c, t	$+\frac{2}{3}$	$+\frac{1}{2}$	0.35	-0.15	$+0.19$	$+\frac{1}{2}$
d, s, b	$-\frac{1}{3}$	$-\frac{1}{2}$	-0.42	0.08	-0.35	$-\frac{1}{2}$

Table A.1: Values of C_R, C_L, Q, and I_W^3 for different fermions.

Appendix B

Calibration Iteration Scheme

Calibration ATLAS algorithm utilizes an iteration scheme. An outline of this scheme is described in the following:

- First Iteration: Only muons that belong to the same region are selected. This way an independent calibration is derived for each region.
- Second Iteration: Since there is a calibration correction for all available phase space, from the first iteration, now muons are allowed to belong to different regions. The regions used can be finer in this iteration. For the second muon of the pair the procedure is a bit different. If it belongs to the region of interest then it is also fitted, but if it belongs to another region of the phase space, then the corrections for it are injected from the first iteration.
- Third Iteration: The procedure is the same but now the phase space binning can be even finer. For an ID calibration the same binning will be kept for all the other iterations.
- Fourth Iteration: For the official ATLAS calibration, for the MS and CB calibrations ϕ dependence is introduced, which corresponds to the Large and Small Sectors.
- Fifth Iteration: Advanced template likelihood method is used for the minimization.

Appendix C

Calibration Systematics

Below the list of systematic uncertainties for the ATLAS calibration procedure is analysed:

- J/ψ and Z p_T range: changing the nominal p_T range selection for the templates produced.

Decay Process	**Nominal Range**	**Modified Range**
J/ψ decay	$6.3 < p_T^{S.L.} < 9$ GeV $9 < p_T^{Sub-Leading} < 20$ GeV	$6.3 < p_T^{S.L.} < 8$ GeV $8 < p_T^{S.L.} < 20$ GeV $6.3 < p_T^{S.L.} < 12$ GeV - $12 < p_T^{S.L.} < 20$ GeV
Z decay	$20 < p_T^{L.} < 50$ GeV $50 < p_T^{L.} < 300$ GeV	$20 < p_T^{L.} < 40$ GeV $40 < p_T^{L.} < 300$ GeV $20 < p_T^{L.} < 80$ GeV - $80 < p_T^{L.} < 300$ GeV

Table C.1: Comparison of the nominal and modified p_T ranges for muons from J/ψ and Z decays.

- J/ψ and Z mass range: templates with different $M_{\mu\mu}$ windows.

  For the J/ψ this is essential as the background is more dominant at the tails and it is an exponential falling function. Therefore the region further from the $M_{\mu\mu}$ peak is influenced from the background domination and the specific choises of the MC generators used in the simulation of the process J/ψ. Also on the upper side of the J/ψ nominal template range of $M_{\mu\mu} = 3.5$ GeV there is a minor contribution of J/ψ 2S which also can contribute variations of the background shape fitted. The template window is shifted as: 2.75 ¡ $M_{\mu\mu} < 3.4$ GeV.

  For the Z this is essential as the regions farther from the peak is sensitive from Initial and Final State Radiation and the running of the α_Z^{EM} which can influence at the tails the shape of the signal. The template model is changed to: 75 ¡ $M_{\mu\mu} < 115$ GeV.

- J/ψ background model: different model for the fit of J/ψ background shape. The nominal exponential model is altered with a chebysev polynominal of the second order.

- J/ψ signal modeling: changing the signal modeling during the data driven method of background calculation. The nominal model of Crystal Ball and Gauss is replaced with a sum of two Crystal Balls. The signal model fitted, influences the final background shape fitted resulting to a systematic in the calibration.

- Histogram Templates Binning: number of bins of templates changes, for J/ψ from 90 to 60 bins and for Z from 200 to 150 bins.

- J/ψ and Z separate scale calibration: produces two different calibrations using only J/ψ and Z. This is essential as the calibration is not accounting properly the p_T dependence of scale. To account for this a systematic is defined where only the scale parameter ds_1 is allowed to float during two different calibrations, one using only J/ψ and another one using only Z.

- Z p_T re-weighting: templates of $M^Z_{\mu\mu}$ are produced by using a different p_T distribution of the Z from the nominal one(produced by Powheg + Pythia), the one produced by Sherpa. The nominal p^Z_T distribution is re-weighted to the Sherpa one by deriving a weight. This weight is multiplied to the total weight of the signal Z MC. This systematic covers Z related theory uncertainties.

Appendix D

Pre-Smearing Studies

D.1 J/ψ and Z σ_{p_T} distributions

In this section $\sigma^{\mu}_{p_T}$ distributions are displayed for simulation and data, CB tracks. Muons originate from di-muon decays for J/ψ:$2.9 < m_{\mu\mu} < 3.3$ and Z:$77 < m_{\mu\mu} < 110$. Examples are displayed for barrel, intermediate and end-cap region. CB tracks have similar behavior to ID tracks in barrel region and to ME tracks in the end-cap.

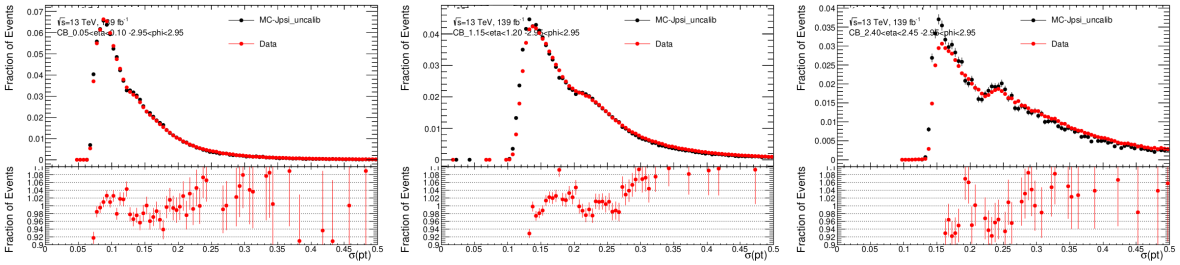

(a) J/ψ CB Barrel (b) J/ψ CB Intermediate (c) J/ψ CB end-cap

Figure D.1: J/ψ CB

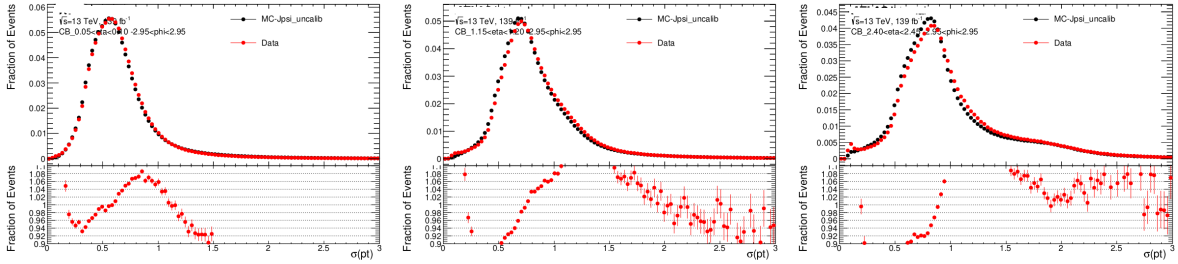

(a) Z CB Barrel (b) Z CB Intermediate (c) Z CB EndCaps

Figure D.2: Z CB

D.2 J/ψ and Z p_T distributions

In this section p^{μ}_{T} distributions are displayed for simulation and data, CB tracks. Muons originate from di-muon decays for J/ψ:$2.9 < m_{\mu\mu} < 3.3$ and Z:$77 < m_{\mu\mu} < 110$. Examples are displayed for barrel, intermediate and end-cap region. CB tracks have similar behavior to ID tracks in barrel region and to ME tracks in the end-cap.

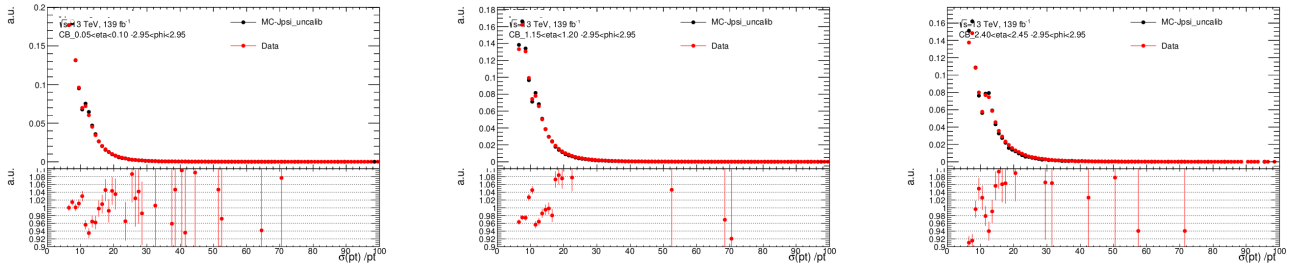

(a) J/ψ CB Barrel (b) J/ψ CB Intermediate (c) J/ψ CB EndCaps

Figure D.3: p_T^μ distributions for CB muon tracks. Muons are required to be in the J/ψ mass range: $2.9 < m_{\mu\mu} < 3.3$.

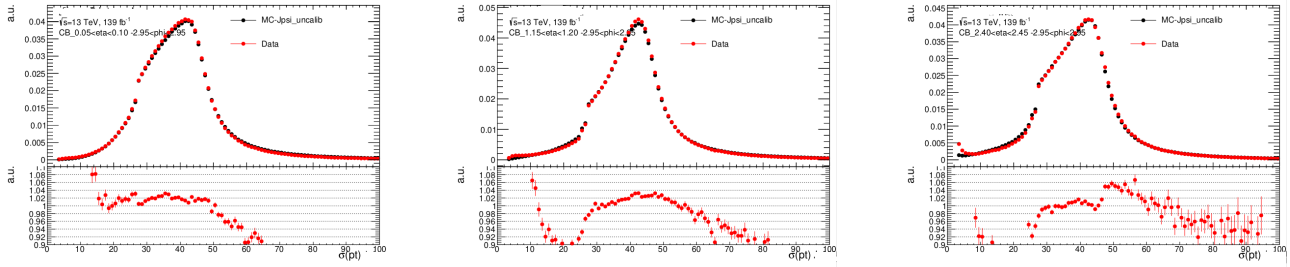

(a) Z CB Barrel (b) Z CB Intermediate (c) Z CB EndCaps

Figure D.4: p_T^μ distributions for CB muon tracks. Muons are required to be in the Z mass range: $77 < m_{\mu\mu} < 110$.

D.3 Fits of Relative Uncertainty

In this Section, examples of relative p_T^μ uncertainty parametric fits are presented, according to the Relation 2.7, for ID muon traks. The section is complementary to the Chapter 4.1.3. In the Tables D.1 and D.2, the pulls for r_1 and r_2 are presented for ID muon tracks for several η bins. The pulls are derived from fitting Relation 2.7 to graphs of relative p_T^μ uncertainty as a function of p_T^μ, for simulation and Data.

In this case, the pull for the parameter r_2 is larger in most bins, and mainly in larger η. Signaling a signal data disagreement growing with p_T^μ. Furthermore, compared to the ME Tables 4.1 - 4.2 the pulls of r_2 in the ID tables are significantly lower. This is due to the better knowledge of the magnetic field in the central solenoid system compared to the more complex nature of the Toroid one of the Muon Spectrometer.

Bin	$\frac{r_1^{MC}-r_1^{Data}}{r_1^{Data}}\%$	$\frac{r_2^{MC}-r_2^{Data}}{r_2^{Data}}\%$
$0.05< \eta <0.10$	0	0
$0.10< \eta <0.15$	2	2
$0.15< \eta <0.20$	1	2
$1.20< \eta <1.25$	0	5
$1.25< \eta <1.30$	0	4
$1.30< \eta <1.35$	1	4
$2.45< \eta <2.50$	0	0
$2.50< \eta <2.55$	0	1
$2.55< \eta <2.60$	0	6

Table D.1: Pull of parametrization fits in MC and data for ID muons coming from Z resonance decay

Bin	$\frac{r_1^{MC}-r_1^{Data}}{r_1^{Data}}\%$	$\frac{r_2^{MC}-r_2^{Data}}{r_2^{Data}}\%$
$0.05< \eta <0.10$	1	11
$0.10< \eta <0.15$	0	8
$0.15< \eta <0.20$	0	9
$1.20< \eta <1.25$	0	3
$1.25< \eta <1.30$	0	10
$1.30< \eta <1.35$	0	5
$2.45< \eta <2.50$	0	0
$2.50< \eta <2.55$	2	5
$2.55< \eta <2.60$	2	31

Table D.2: Pull of parametrization fits in MC and data for ID muons coming from J/ψ resonance decay

Appendix E

Validation of CB tracks - J/ψ

$\eta^{\textbf{leading}-\mu}$: In Figures E.1 and E.2 the mean and the σ of the distributions are displayed as a function of $\eta^{leading-\mu}$.

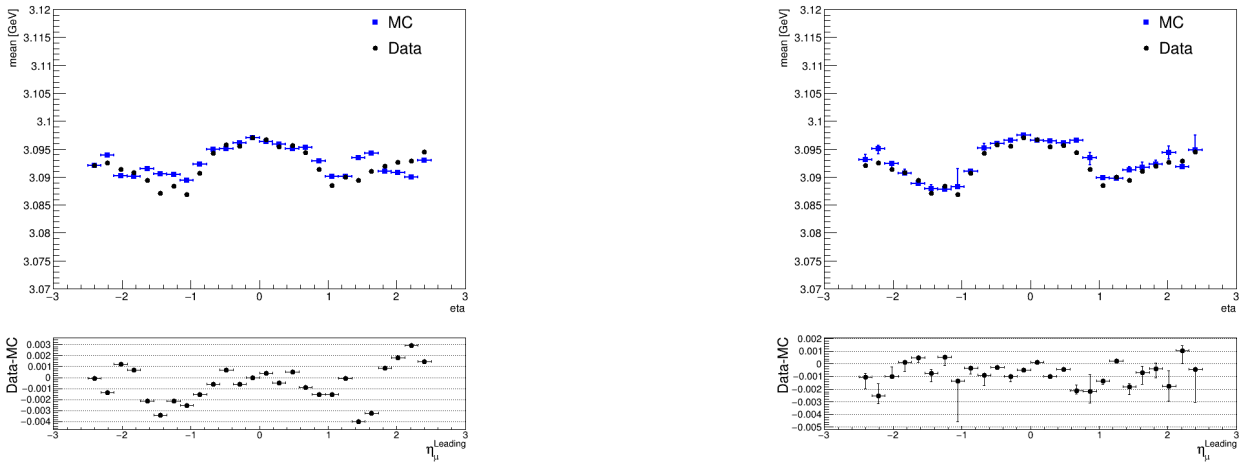

(a) Pre-calibration

(b) Post-calibration

Figure E.1: Pre and post calibration mean of $m_{\mu\mu}$ distribution ($2.8 < m_{\mu\mu} < 3.3$ GeV) as a function of $\eta^{leading-\mu}$.

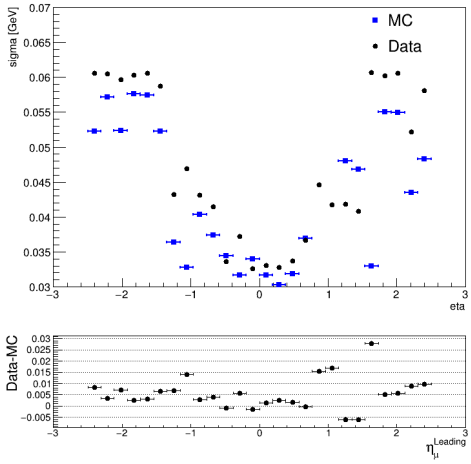

(a) Pre-calibration

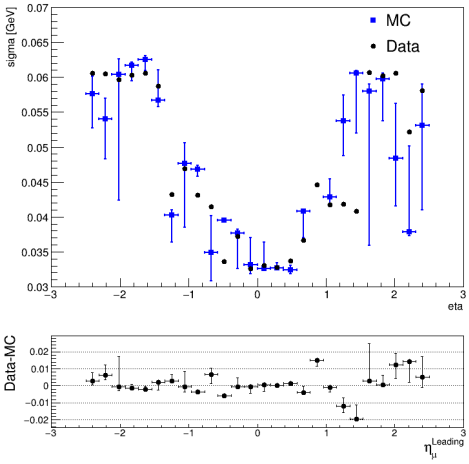

(b) Post-calibration

Figure E.2: Pre and post calibration σ_{CR} of $m_{\mu\mu}$ distribution ($2.8 < m_{\mu\mu} < 3.3$ GeV) as a function of $\eta^{leading-\mu}$.

For the mean and σ plots, the shape as a function of $\eta^{leading-\mu}$ is similar to the Z case, Figure 4.34 and 4.35.

For the mean, the agreement between MC and data after the calibration is in the order of 10^{-3} GeV. For the σ the agreement is again in the order 10^{-3} GeV. Some outliers are in the order of 10^{-2} GeV.

$\phi^{\mathbf{leading-\mu}}$: In Figures E.3 and E.4 the mean and the σ of the distributions are displayed as a function of $\phi^{leading-\mu}$.

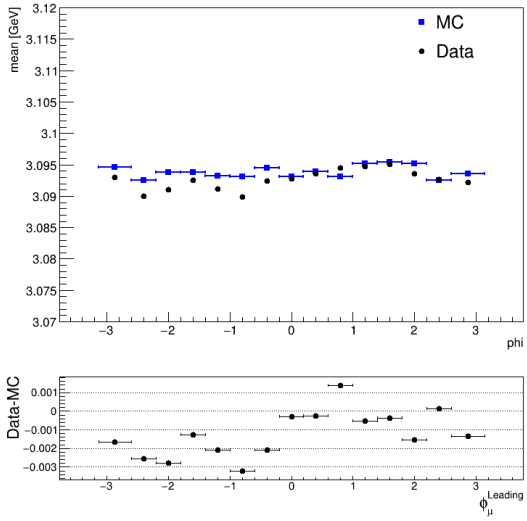

(a) Pre-calibration

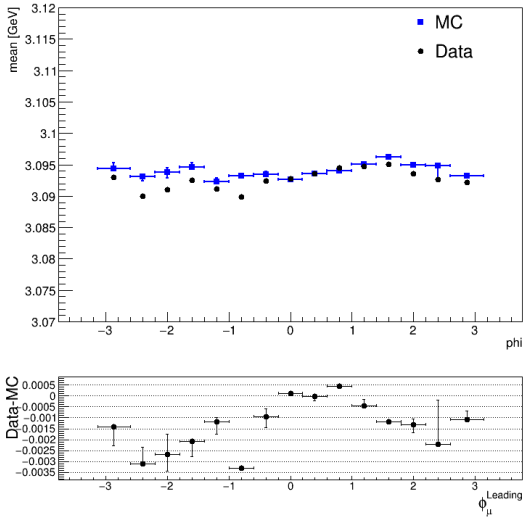

(b) Post-calibration

Figure E.3: Pre and post calibration mean of $m_{\mu\mu}$ distribution ($2.8 < m_{\mu\mu} < 3.3$ GeV) as a function of $\phi^{leading-\mu}$.

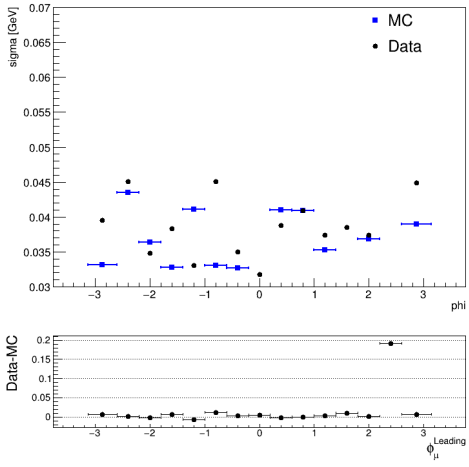

(a) Pre-calibration

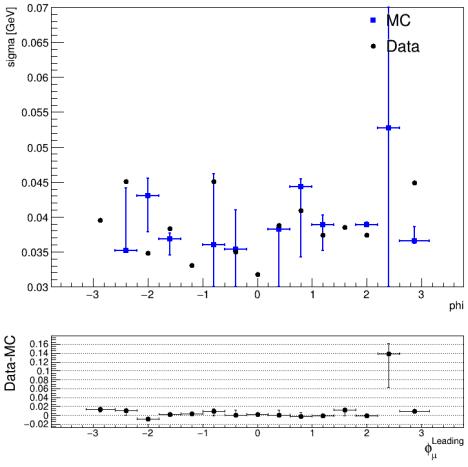

(b) Post-calibration

Figure E.4: Pre and post calibration σ_{CR} of $m_{\mu\mu}$ distribution ($2.8 < m_{\mu\mu} < 3.3$ GeV) as a function of $\phi^{leading-\mu}$.

For the mean and σ plots, the shape as a function of $\phi^{leading-\mu}$ is similar to the Z case, Figures 4.36 and 4.37.

For the mean there is an excellent agreement between data and MC, in the order of 10^{-3} GeV. In the σ there is large outlier point, which is deemed as non physical and further investigation is needed. Apart from that, the agreement is excellent at the order of 10^{-3} GeV.

$\mathbf{p^{leading-\mu_T}}$: In Figures E.5 and E.6 the mean and the σ of the distributions are displayed as a function of $p^{leading-\mu_T}$.

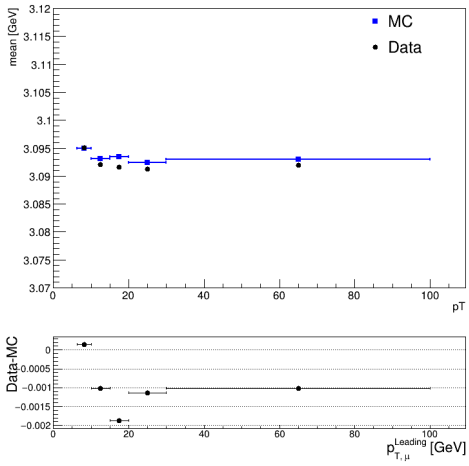

(a) Pre-calibration

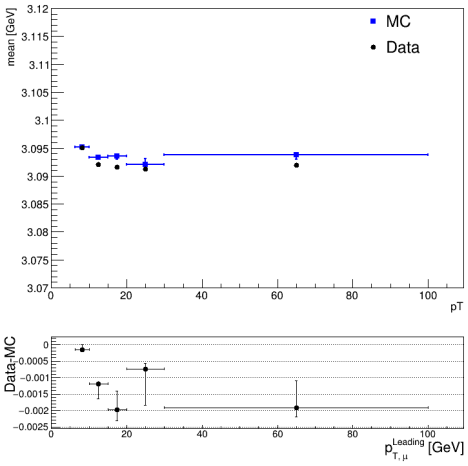

(b) Post-calibration

Figure E.5: Pre and post calibration mean of $m_{\mu\mu}$ distribution ($2.8 < m_{\mu\mu} < 3.3$ GeV) as a function of $p_T^{leading-\mu}$.

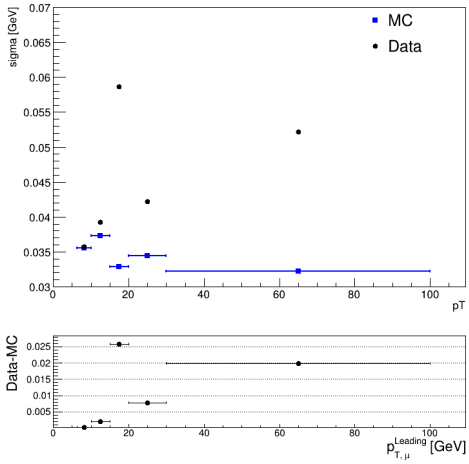

(a) Pre-calibration

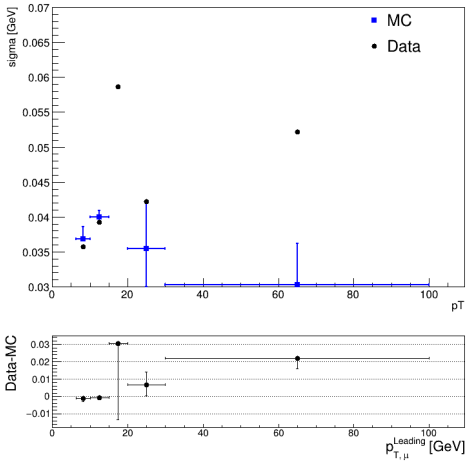

(b) Post-calibration

Figure E.6: Pre and post calibration σ_{CR} of $m_{\mu\mu}$ distribution ($2.8 < m_{\mu\mu} < 3.3$ GeV) as a function of $p_T^{leading-\mu}$.

The calibration is inclusive in p_T^{μ}. Due the Z simulation sample which has more available events, the fit converges closer to the Z values. The p_T^{μ} of the scale ds_1 parameter creates a slope of disagreement seen in the mean plot as a function of $p_T^{leading-\mu}$. The expected behavior, post calibration, is the slope to start from positive values and the agreement to increase as the momentum of the muons is closer to the momentum of the muons coming from Z. In contrast, at the subtraction plot there is an ever increasing of a negative slope. This happens likely due an known problem of kinematic distributions in the J/ψ data samples and it is considered as non physical, as mentioned in Section 4.2.1.

Appendix F

Non Prompt Studies

In this Apprendix section complementary figures and studies on the Prompt - Non Prompt calibration comparison are presented.

F.1 Resolution parameters for Prompt-Non Prompt Calibration

In Figures F.1a, F.1b the resolution parameters for Prompt and Non Prompt J/ψ , as they are defined in Table 5.3 in the Lxy studies, are compared. Their behavior is less essential for the Z mass measurement analysis but it is investigated for completeness. The dr_1 parameter is showing no clear trend between the two calibrations. For Non Prompt J/ψ again the error bars, which correspond to standard deviation over iterations, are larger. In the barrel region the agreement resides within the statistical uncertainty. At endcaps there are points which show a substantial difference between two calibrations. In these regions the background fit is challenged even more and the simulation statistics are substantially lower compared to the central ones and therefore these difference are regarded as fit non closures. dr_2 n parameter has a similar behavior, there is good agreement in central and intermediate regions and within the uncertainties.

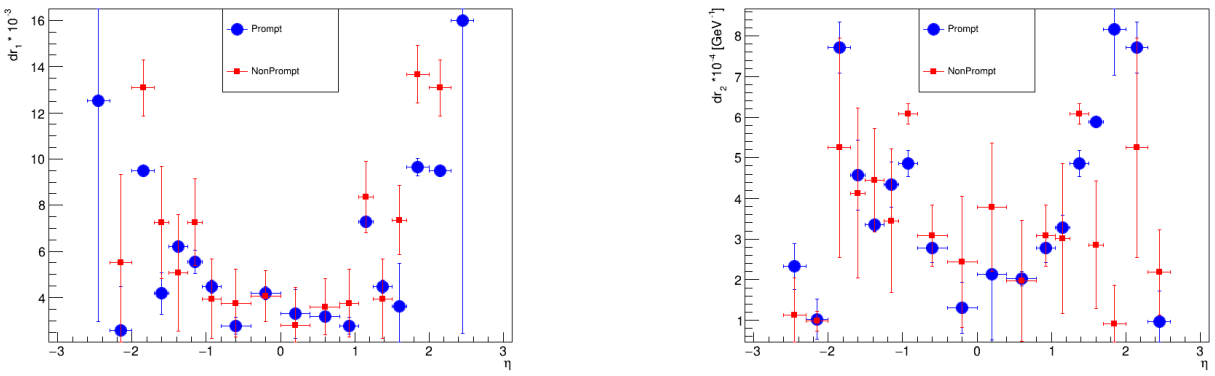

(a) dr_1 parameter

(b) dr_2 parameter

Figure F.1: Resolution parameters and χ^2/(Degrees of Freedom) comparison for calibrations of Prompt and Non Prompt J/ψ as they are defined in Chapter 5.3

.

F.2 Background studies

For the background shape fit non closure a minor study has been done. Technical details and χ^2, scale and resolution as a function of η can be found in Apprendix F. The main goal of this short study is to observe if an alternative model for the background with more flexibility in the slope can lead a more stable and accurate calibration for the Non Prompt case. The hypothesis is that a more complex background model with more flexibility could describe better the background distribution as the nominal exponential model has only one slope variable. Adding though additional parameters to the fit should be handled with care as more parameters have to be fitted per region per iteration and therefore possibly increasing instability of calibrations with iterations. The χ^2 as a function of η for the iterations 6-12 is going to be compared for two cases. One case is the nominal exponential background model and a new one which can be more flexible in shape. For this study a Chebysev polynomial of the third order is used as new model. The signal is kept at the nominal model (the sum of a Crystal Ball and a Gaussian distribution). The samples used for this minor study is the Non Prompt one, as it is defined by the Lxy selection of Table 5.6. In Figure F.3 of χ^2 of the two calibrations as a function of η in Apprendix F the two central η bins at the Chebysev polynomial model case have decreased χ^2, but in the rest of the barrel regions the two calibrations are compatible in the statistical uncertainty margin. There there is no indication that this effect reduces significantly χ^2 in all barrel and therefore for the rest of the studies to be made the nominal background model is used for the Non Prompt.

In Figure F.2, a scale comparison is presented for the two Non-Prompt sample calibrations, each utilizing different background models. In the central barrel region ($|\eta| < 0.4$), the two calibrations show complete agreement. However, in the intermediate and outermost barrel regions ($0.4 < |\eta| < 1.05$), the scale for the Chebyshev model begins to shift towards the ds_1. values of the Prompt nominal calibration. This trend is further illustrated in Figure F.4, where ds_1, is plotted for the Prompt (using the exponential background model) and Non-Prompt (using the Chebyshev background model) samples. There the Prompt and Non Prompt calibration are closer compared to the one presented in Figure 5.15a. The observed differences between the two calibrations remain, though certain regions with the new background model show a tendency to align more closely with the Prompt calibration values.

In the following Figures two calibrations with two different background models are compared. The one is with exponential background model and the other one is with a Chebysev of third order polynomial:

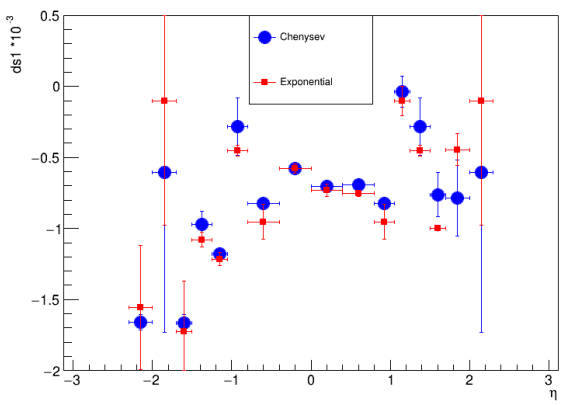

Figure F.2: Scale ds_1 as a function of η for two different calibrations for Chebysev and Exponential background models

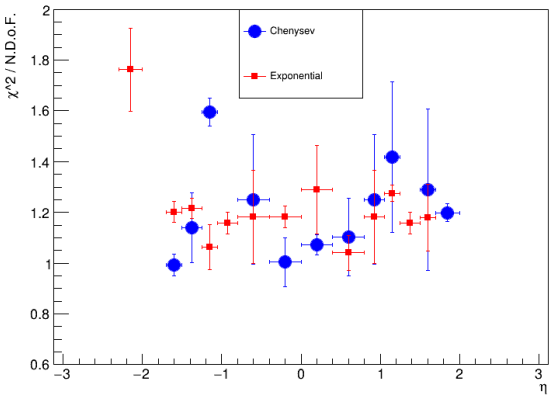

Figure F.3: χ^2/(Degrees of Freedom as a function of η for two different calibrations for Chebysev and Exponential background models

The points used Figures F.3 and F.2 are from iteration 5 to iteration 12. Points are the mean and the error bars are the standard deviation.

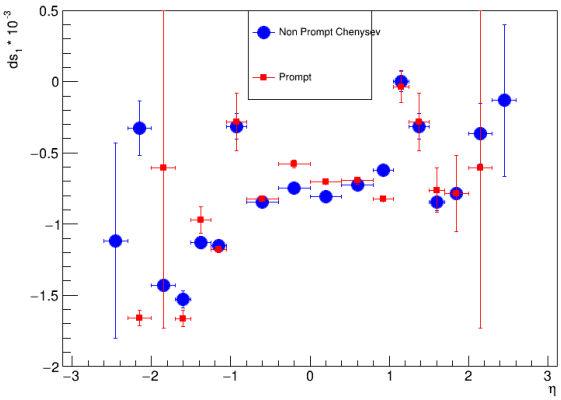

Figure F.4: Scale ds_1 as a function of η for two different calibrations for Non Prompt (Chebysev for background model) and Prompt (exponential for background model)

Appendix G

eta Calibration results

G.1 Calibration Parameters, Statistical uncertainty 2017

In Figure G.1 the calibration parameters for ID, 2017 are presented as they are fitted between Iteration 15 and Iteration 20. Points are mean over iterations and error bars are standard deviation over iterations:

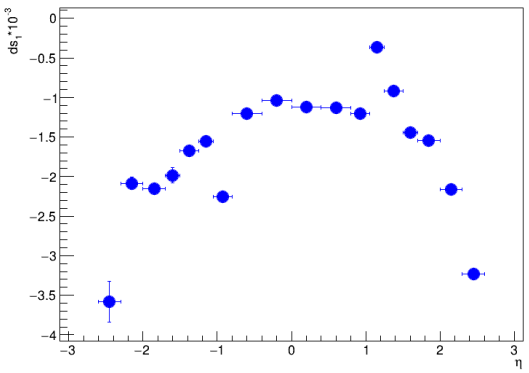

(a) ds_1 parameter

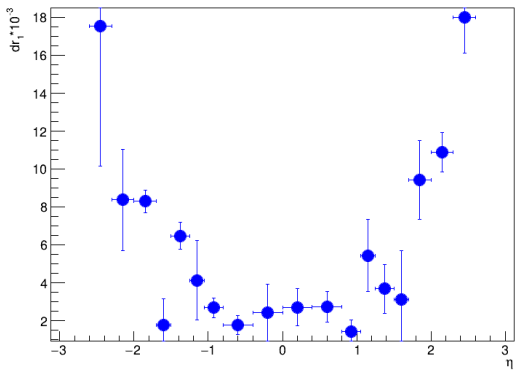

(b) dr_1 parameter

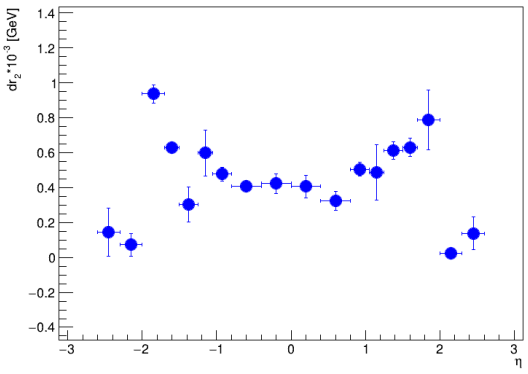

(c) dr_2 parameter

Figure G.1: Calibration Parameters for the campaign 2017 and ID muons. Points are average over iterations 15 to 20 and the error bars are standard deviation over the corresponding iterations.

In Figure G.1 in Appendix G the points are the average over iterations and the error bars are the Standard Deviation over iterations. The scale parameter in Figure G.1 a) is the most stable

in barrel region compared to the resolution parameters in Figures G.1 b) and c). The standard deviation for the scale parameter is $\approx 1 \times 10^{-6}$ for the central barrel region ($0 < \eta < 0.8$) and at the outer barrel ($0.8 < |\eta| < 1.05$) is reaching $\approx 1 \times 10^{5}$. The statistical uncertainty for the scale is excellent for the precision required and it's contribution is almost half than the systematic contribution for most of the barrel regions.

G.2 Table of Dominant Systematics

For the scale parameter all the regions are shown for completeness and for the resolution parameters only the barrel regions are kept. The systematic with the larger distance from the parameter in a given η region is regarded as the positive or negative systematic variation. As mentioned the most significant systematic uncertainties for the Z mass calibration analysis are the scale ones. Therefore there is a focus in analysing the corresponding uncertainties. At the Table G.1 the dominant systematic contributions for the scale ds_1 are shown for the down and up contribution. Dominating systematic in the down variation, which is the larger one compared to the up variation, are the background and signal modeling ones as observed in Figure 5.23a. In the barrel region ($-1.05 < \eta$¡1.05) the dominant ones are the ones related to the J/ψ p_T binning and the background analytical ones. This signals an imperfect modeling of the signal and shape of J/ψ. At the resolution parameters in the $-1.05 < \eta < 1.05$ regions the dominant systematic uncertainties are the ones connected to p_T binning of the sub-leading muon. Therefore the choice of the p_T binning is expected to influence more the tails of the mass signal distributions where the background model and signal model can have a significant impact on the scale.

Tables of dominant systematic contribution for the calibration parameters defined in Equation 3.2, Chapter 3.3 for the ID tracks are presented in the Tables G.1, G.1 and G.3.

η **Bin**	**Down Systematic Contribution**	**Up Systematic Contribution**
$-2.6 < \eta < -2.3$	Background Parameterization	J/ψ p_T Up
$-2.3 < \eta < -2.0$	Background Parameterization	J/ψ p_T Up
$-2.0 < \eta < -1.7$	Background Technique	J/ψ p_T Up
$-1.7 < \eta < -1.5$	Background Technique	J/ψ Bins Reduce
$-1.5 < \eta < -1.25$	Background Technique	Background Parameterization
$-1.25 < \eta < -1.05$	Background Technique	J/ψ p_T Up
$-1.05 < \eta < -0.8$	J/ψ Bins Reduce	Background Parameterization
$-0.8 < \eta < -0.4$	Background Technique	Background Parameterization
$-0.4 < \eta < 0.0$	J/ψ p_T Up	J/ψ p_T Down
$0.0 < \eta < 0.4$	J/ψ Bins Down	Background Parameterization
$0.4 < \eta < 0.8$	Background Parameterization	J/ψ p_T Up
$0.8 < \eta < 1.05$	J/ψ Bins Down	J/ψ Bins Reduce
$1.05 < \eta < 1.25$	Background Technique	J/ψ p_T Up
$1.25 < \eta < 1.5$	Background Technique	J/ψ p_T Up
$1.5 < \eta < 1.7$	Background Technique	J/ψ p_T Up
$1.7 < \eta < 2.0$	Background Technique	J/ψ p_T Up
$2.0 < \eta < 2.3$	Background Technique	J/ψ p_T Up
$2.3 < \eta < 2.6$	Background Parameterization	J/ψ p_T Up

Table G.1: Systematic contributions for the η bins used in calibration for the scale parameter ds_1. 2017 campaing

η Bin	Down Systematic Contribution	Up Systematic Contribution
$-1.05 < \eta < -0.8$	J/ψ p_T Down	J/ψ Bins Down
$-0.8 < \eta < -0.4$	Background Parameterization	J/ψ Bins Reduce
$-0.4 < \eta < 0.0$	J/ψ p_T Down	J/ψ p_T Up
$0.0 < \eta < 0.4$	J/ψ p_T Up	J/ψ Bins Down
$0.4 < \eta < 0.8$	J/ψ Bins Reduce	J/ψ Bins Down
$0.8 < \eta < 1.05$	J/ψ Bins Reduce	J/ψ p_T Down
$1.05 < \eta < 1.25$	J/ψ Bins Reduce	J/ψ p_T Down

Table G.2: Systematic contributions for the η bins used in calibration for the scale parameter dr_1. 2017 campaing

η Bin	Down Systematic Contribution	Up Systematic Contribution
$-1.05 < \eta < -0.8$	J/ψ Bins Down	J/ψ p_T Up
$-0.8 < \eta < -0.4$	J/ψ Bins Reduce	Background Parameterization
$-0.4 < \eta < 0.0$	J/ψ Bins Down	J/ψ p_T Down
$0.0 < \eta < 0.4$	Background Technique	J/ψ p_T Up
$0.4 < \eta < 0.8$	Background Technique	J/ψ Bins Reduce
$0.8 < \eta < 1.05$	J/ψ Pt Down	J/ψ p_T Up
$1.05 < \eta < 1.25$	J/ψ Pt Down	J/ψ p_T Up

Table G.3: Systematic contributions for the η bins used in calibration for the scale parameter dr_2. 2017 campaing

G.3 Validation for η, Z mass Calibration

In this Section, validation plots of calibration are presented as a function of muon kinematic observables. The calibration is performed as a function of η, presented in Chapter 5.4. In Chapter 5.4.0.3, the validation is presented for the 2017 campaign. Here are presented complementary plots from 2015-16 and 2018 campaigns.

The validation plots presented in this section exhibit behavior consistent with those discussed in the main text. To avoid redundancy, the commentary on these plots is kept minimal.

G.3.1 $\eta^{leading-\mu}$

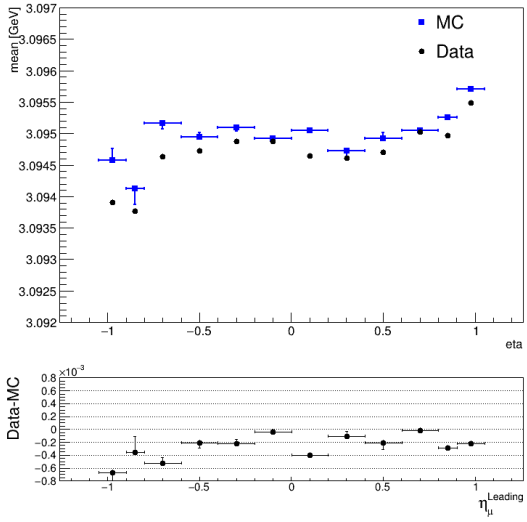

(a) Mean as a function of $\eta^{\text{leading-}\mu}$

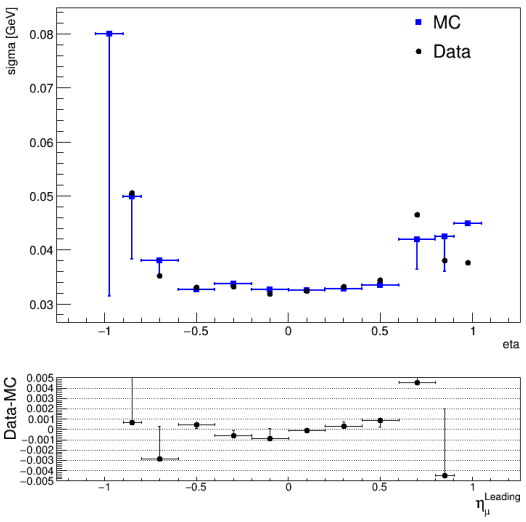

(b) Variance as a function of $\eta^{\text{leading-}\mu}$

Figure G.2: Mean and variance as a function of $\eta^{\text{leading-}\mu}$ after calibration has been applied. The samples used are from **2015-16** and are corrected for the η calibration presented in Figure 5.23.

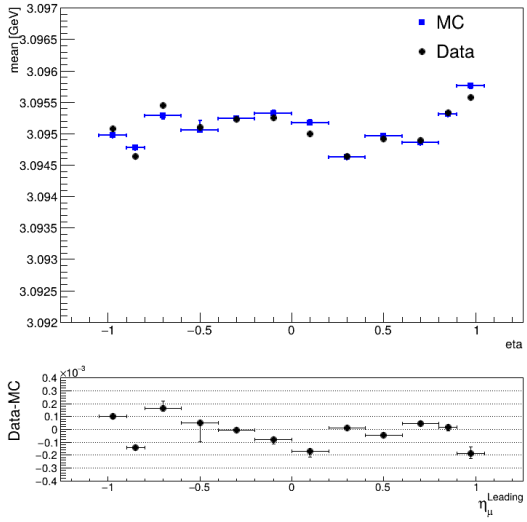

(a) Mean as a function of $\eta^{\text{leading-}\mu}$

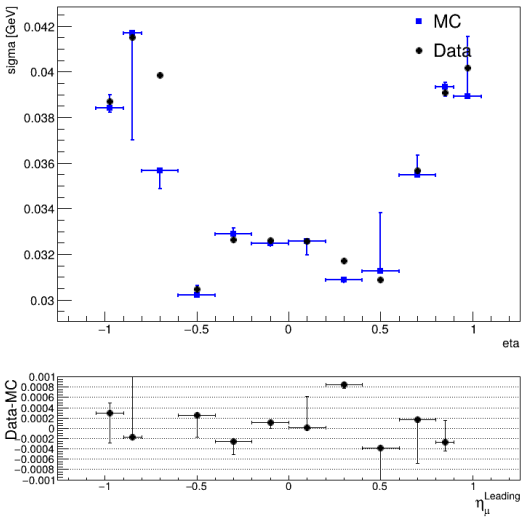

(b) Variance as a function of $\eta^{\text{leading-}\mu}$

Figure G.3: Mean and variance as a function of $\eta^{\text{leading-}\mu}$ after calibration has been applied. The samples used are from **2018** and are corrected for the η calibration presented in Figure 5.23.

In Figures G.2, G.3 the mean and the σ are displayed as a function of $\eta^{\text{leading-}\mu}$, for 2015-16 and 2018 respectively. In both cases the agreement is in the order of 10^{-4} for the mean 10^{-3} for the σ. In 2015-16 there is a shape of non closure in negative $\eta^{\text{leading-}\mu} > -0.5$. Since there is a known error in the samples used, it is hard to disentangle the effect. With another sample used for the calibration, in the future, the non closure is expected to be treated.

G.3.2 $\phi^{leading-\mu}$

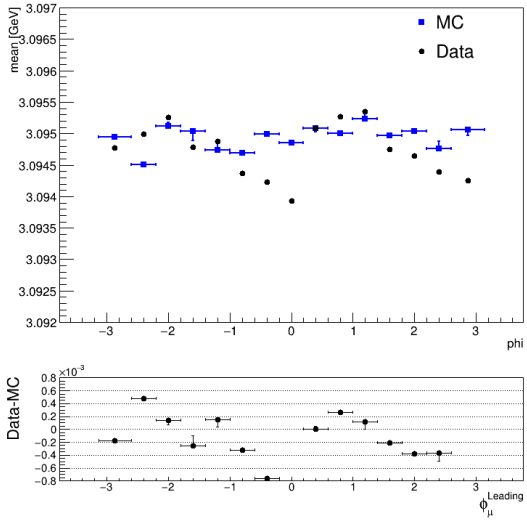

(a) Mean as a function of $\phi^{\text{leading-}\mu}$

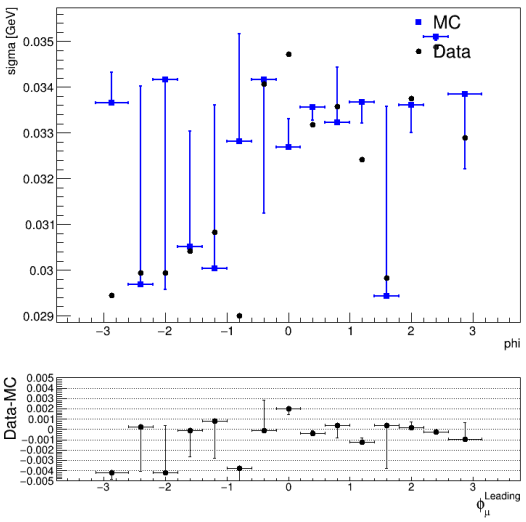

(b) Variance as a function of $\phi^{\text{leading-}\mu}$

Figure G.4: Mean and variance as a function of $\phi^{\text{leading-}\mu}$ after calibration has been applied. The samples used are from **2015-16** and are corrected for the η calibration presented in Figure 5.23.

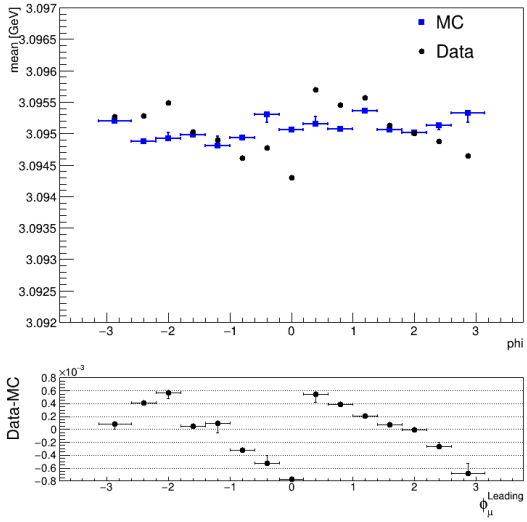

(a) Mean as a function of $\phi^{\text{leading-}\mu}$

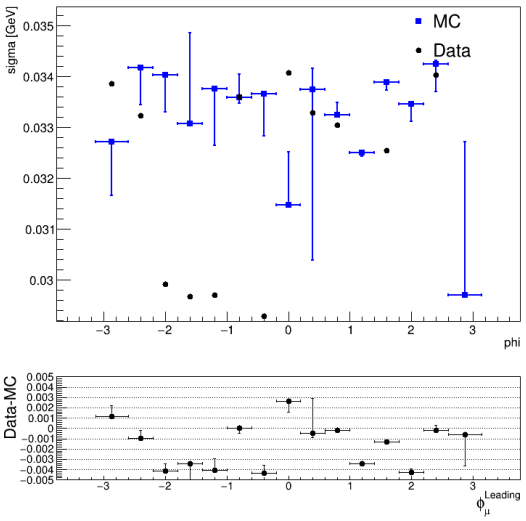

(b) Variance as a function of $\phi^{\text{leading-}\mu}$

Figure G.5: Mean and variance as a function of $\phi^{\text{leading-}\mu}$ after calibration has been applied. The samples used are from **2018** and are corrected for the η calibration presented in Figure 5.23.

In Figures G.4, G.5 the mean and the σ are displayed as a function of $\phi^{\text{leading-}\mu}$, for 2015-16 and 2018 respectively. The structures seen are in data and simulation are similar to the ones already discussed for the 2017 case, presented in Chapter 5.4.0.3.

G.3.3 $p_T^{leading-\mu}$

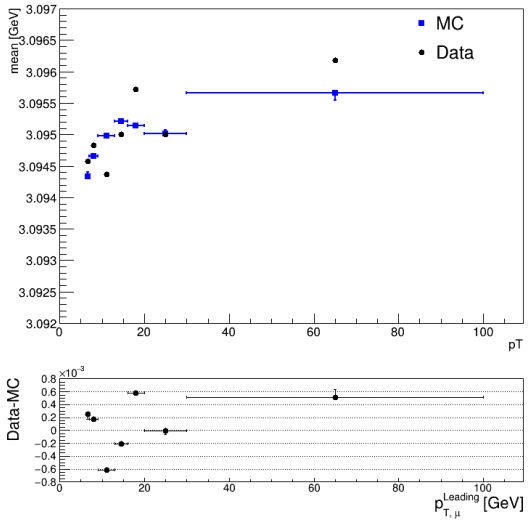

(a) Mean as a function of $p_T^{\text{leading-}\mu}$

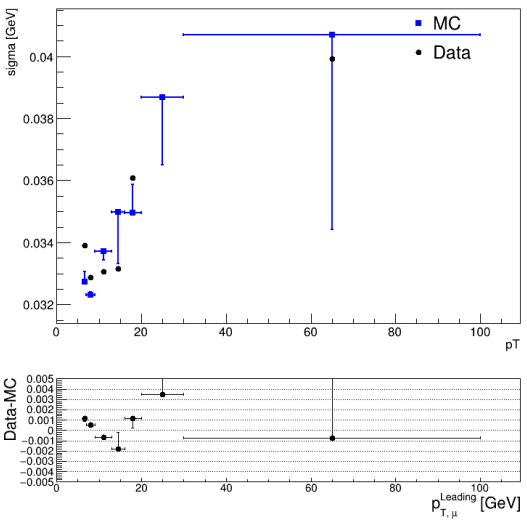

(b) Variance as a function of $p_T^{\text{leading-}\mu}$

Figure G.6: Mean and variance as a function of $p_T^{\text{leading-}\mu}$ after calibration has been applied. The samples used are from **2015-16** and are corrected for the η calibration presented in Figure 5.23.

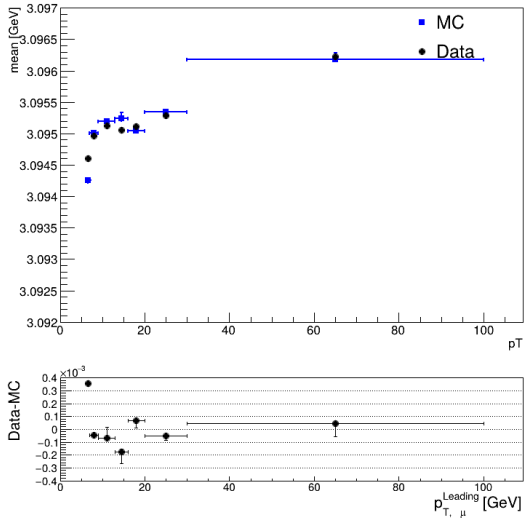

(a) Mean as a function of $p_T^{\text{leading-}\mu}$

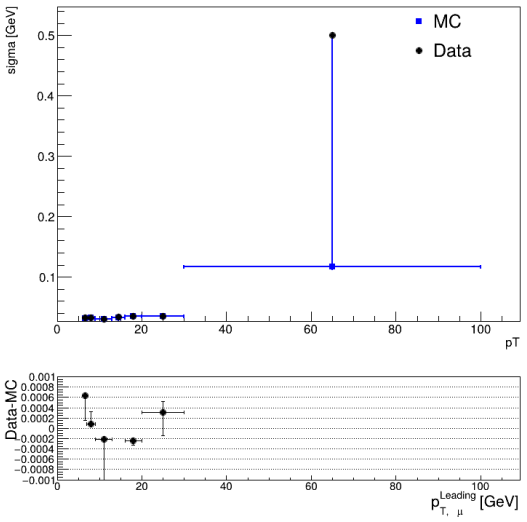

(b) Variance as a function of $p_T^{\text{leading-}\mu}$

Figure G.7: Mean and variance as a function of $p_T^{\text{leading-}\mu}$ after calibration has been applied. The samples used are from **2018** and are corrected for the η calibration presented in Figure 5.23.

In Figures G.6, G.7 the mean and the σ are displayed as a function of $p_T^{\text{leading-}\mu}$, for 2015-16 and 2018 respectively.

The mean agreement between MC and data differs significantly for all years. Specifically for the 2015-16 the disagreement is rising with $p_T^{\text{leading-}\mu}$, where for the 2018 there is the opposite effect. In the bins $p_T^{\text{leading-}\mu} > 10$ GeV there is absolute agreement between MC and data. This

effect is likely connected to the data overlap between the BPhys and Physics Main stream, which can be affected from the year processed in the samples.

At the σ plots similar behavior is seen to the 2017 Figures presented in Chapter 5.4.0.3. In the 2018 case there is a data outlier point, this is regarded as the outcome of a failed parametric fit to the di-muon mass distribution.

Appendix H

p_T Extrapolation

H.1 Fifth Bin 2017

In this chapter a minor study of the 2017 calibration revisits the results with a different configuration. Goal is to remove the outlier fifth bin presented at the Figure 5.33a. This outlier makes the extrapolation of the scale with p_T more challenging and deviates from a smooth extrapolation shape. The hypothesis of this study is that the outlier point arises from the `HLT_mu11_mu6_bJpsimumu` trigger, which is used in both the MCP and the general trigger list. Since the trigger applies a cut of $p_T^{\mu} = 11$ GeV for the leading muon, the outlier may result from the significant difference between the leading and sub-leading muon distributions at the threshold where the trigger becomes effective. Since these studies are sensitive to changes and miss simulations of the p_T^{μ} distribution by excluding a negligible window in p_T around the trigger effect region ≈ 11 GeV. Therefore a second calibration is presented with a window in p_T^{μ} where the muons are excluded. This region is the $p_T^{\mu} = 11 - 11.7$ GeV. The two calibration results presented in the Figure H.1 correspond to the iterations 5 - 9. The points are the mean over iterations and the error bars correspond to standard deviation over iterations. The two calibration use slight different bin configuration for the fifth and the sixth bin since in the trial one there is the exclusion window.

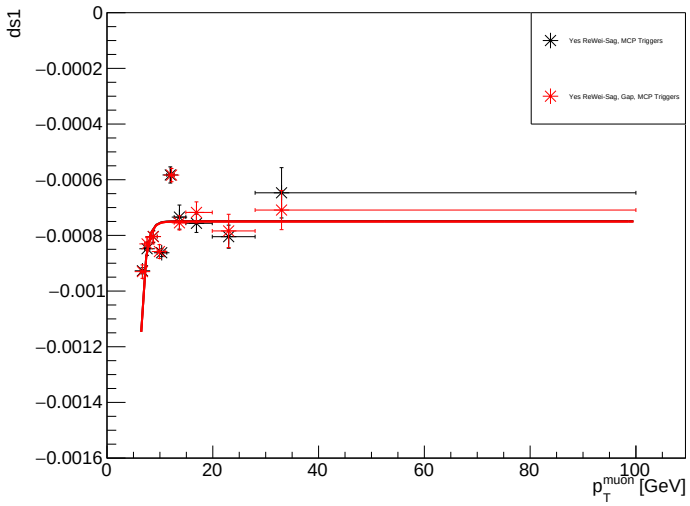

Figure H.1: Enter Caption

In Figure H.1 the calibration with the gap is compared to the nominal used for 2017 with MCP trigger list. In both calibrations there is $p_T^{J/\psi}$ re-weighting used and sagitta corrections.

The problem with the fifth bin is not fixed but there is a visible difference between the two calibrations.The calibration with the gap (red points) converges to a smoother configuration in the final bins compared to the nominal calibration (black points). Notably, the seventh and eighth bins are closer in the gap trial calibration. The red line in Figure H.1 is a parametric fit of an inverse exponential and corresponds to the red points. It is overlapping with the black line corresponding to the black points.

Ultimately the two calibrations are close. The fifth bin outlier is not treated with this study. It is not excluded that a wider gap in the p_T^μ would resolve this issue but a detailed study of this is out of the timescale and scope of the thesis.

Appendix I

Trigger lists

The choice of trigger is important for the calibration procedure. As presented in section 5 of Chapter 5.5.0.2 the trigger list used can have a direct impact on the calibration result. In section 2 of the Chapter 5.2.2 also kinematic distributions on muons are presented for the different choice of trigger. In this Apprendix section are presented the trigger lists used this thesis.

One is called MCP trigger list. It is the trigger list used by ATLAS official group for the J/ψ samples in muon momentum calibration and is shown in Table I.1

MCP trigger list (2017, 2018)
HLT_mu11_mu6_bJpsimumu
HLT_2mu6_bJpsimumu_Lxy0_L1BPH_2M9_2MU6_BPH_2DR15_2MU6

Table I.1: MCP trigger list

The main advantage of this trigger list is that it includes non pre-scaled triggers which ensure a better agreement between data and MC in the kinematic distributions of the muons. Though it includes only two triggers therefore excluding some di-muon events.

In order to get more muons coming from J/ψ candidates another trigger list, which in the context of the thesis is called general trigger list. This list includes more triggers relevant for J/ψ studies but the disadvantage is that some triggers are heavily pre-scaled, which could lead to increased disagreement in muon kinematic distributions. Since trigger configurations and the pre-scale factors change per campaign there different general trigger lists for 2015-16 and 2017-2018. In general trigger lists the ATLAS recommended ones are included.

The general trigger list for **2017** and **2018** campaigns is presented at the Table I.2

General Trigger List for 2017/2018
HLT_mu22_mu8noL1
HLT_mu20_2mu4_JpsimumuL2
HLT_mu20_2mu2noL1_JpsimumuFS
HLT_2mu6_bBmumux_BpmumuKp_L1BPH_dash_2M9_dash_2MU6_BPH_dash_2DR15_dash_2MU6
HLT_mu11_mu6_bJpsimumu_Lxy0
HLT_mu11_mu6_bDimu_Lxy0
HLT_mu11_mu6_bDimu
HLT_mu11_mu6_bJpsimumu
HLT_2mu6_bJpsimumu_Lxy0_L1BPH_dash_2M9_dash_2MU6_BPH_dash_2DR15_dash_2MU6
HLT_2mu6_bJpsimumu_L1BPH_dash_2M9_dash_2MU6_BPH_dash_2DR15_dash_2MU6

Table I.2: List of HLT Triggers

The general trigger list for the **2015-16** campaign is shown at I.3.

General Trigger List for 2015-16
HLT_mu10_mu6_bJpsimumu_delayed
HLT_2mu14
HLT_mu6_mu4_bJpsimumu
HLT_2mu10
HLT_mu22_mu8noL1
HLT_mu20_2mu4_JpsimumuL2
HLT_mu20_2mu2noL1_JpsimumuFS
HLT_2mu6_bBmumux_BpmumuKp_L1BPH_dash_2M9_dash_2MU6_BPH_dash_2DR15_dash_2MU6
HLT_mu11_mu6_bJpsimumu_Lxy0
HLT_mu11_mu6_bDimu_Lxy0
HLT_mu11_mu6_bDimu
HLT_mu11_mu6_bJpsimumu
HLT_2mu6_bJpsimumu_Lxy0_L1BPH_dash_2M9_dash_2MU6_BPH_dash_2DR15_dash_2MU6
HLT_2mu6_bJpsimumu_L1BPH_dash_2M9_dash_2MU6_BPH_dash_2DR15_dash_2MU6

Table I.3: General trigger list for 2015-16